Modelling the dynamics of the upper ocean in the Eastern Tropical Pacific and its interactions with the tropical atmosphere

LIZDENIA ARCE-MARENCO

SUBMITTED TO THE UNIVERSITY OF NEWCASTLE UPON TYNE IN PARTIAL FULFILLMENT OF THE REQUIREMENTS FOR THE DEGREE OF DOCTOR OF PHILOSOPHY

School of Natural and Environmental Sciences

May 2021

Abstract

The physical behaviour of the central and eastern tropical Pacific regions is characterized by a complex variety of multi-scale interacting processes. The Madden-Julian Oscillation (MJO) is the primary mode of intraseasonal variability in the tropical atmosphere. Although convection, together with related cloudiness and precipitation, tends to dissipate east of the 180º meridian, the MJO wind signal continues to progress eastward across the eastern Pacific and South America and into the tropical Atlantic.

This research explores numerically the response of the upper ocean in the central and eastern tropical Pacific regions to MJO forcing. We use a global, intermediate resolution configuration of the Nucleus for European Modelling of the Ocean (NEMO) framework version 3.6, referred to as ORCA1-LIM3, forced with daily atmospheric forcing from the Coordinated Oceanic Reference Experiments (CORE) dataset version 2, for the period 1990 to 2000.

The results show a strong influence of the MJO on temperature, salinity, zonal currents, and vertical currents in the first 300 m of depth, particularly at the equator. The intraseasonal wind is the key forcing factor that modulates the impact of the MJO. This is except for the temperatures at the mixed layer depth, the halocline, and the pycnocline, in the regions of the Central American Pacific coast and the southwestern Mexican coast where the influence of the MJO can be observed even in the absence of intraseasonal wind forcing.

The impact of the MJO on the ocean's internal intraseasonal variability is analysed in the case of tropical instability waves. We show that the barotropic and baroclinic conversion terms that control the eddy kinetic energy levels in the region vary in magnitude with the phases of the MJO. These results have ramifications for understanding ocean intraseasonal variability, which is a critical step towards improving our ability to make more reliable mid-range ocean weather and ocean climate forecasts for the region.

Acknowledgements

There are people with whom I am sincerely grateful, without them this work would not have been possible. First, my deep thanks to my supervisor Dr Miguel Angel Morales Maqueda for his constant guidance, mentoring, support, patience, and for being so generous with his time. I also would like to extend my gratitude to Prof Andrew Willmott for the discussion of this manuscript and his invaluable comments.

A special thanks to Mr John Garside, not only for the grammatical corrections of this thesis but also for his weekly visits and his concern for my well-being beyond the academic considerations.

My thanks to the Ministry of Science, Technology, and Communications of Costa Rica for their financial support and to the Newcastle University for its computer resources essential for the development of this project.

I am very grateful to my many Newcastle local friends and to the Latino friends; they both made undertaking this PhD an enjoyable experience.

I keep my warmest words for my family, for their loving support and unconditional encouragement. To my sisters, Josy and Ily for always being there. To my husband Danny, thank you from the bottom of my heart for your patience and love. Lastly, I would like to give my most sincere gratitude to my parents, to whom this thesis is dedicated.

Abbreviations and Acronyms

Abbreviation or Acronym	Definition
AGCM	atmospheric general circulation model
BCL	conversion of mean potential energy to EKE
BTR-KH	conversion of mean kinetic energy to EKE
CMCC	Euro-Mediterranean Center on Climate Change
C-GLORS	CMCC Global Ocean Reanalysis System
CGCM	coupled general circulation model
CISK	Conditional Instability of the Second Kind
CLIVAR	Climate Variability and Predictability
CMIP	Coupled Model Intercomparison Project
CORE	Coordinated Oceanic Reference Experiments
EKE	eddy kinetic energy
ENSO	El Niño Southern Oscillation
EOF	empirical orthogonal function
EPE	eddy potential energy
EUC	Equatorial Undercurrent
GFDL	Geophysical Fluid Dynamics Laboratory
GMSL	Global Monthly Mean Sea Level
GSM	general circulation model
IAF	Interannual Forcing
II	Simulation IAF-Atmospheric forcing and IAF Wind forcing
IN	Simulation IAF-Atmospheric forcing and NYF Wind forcing
ISKw	intraseasonal Kelvin Wave
ITCZ	Intertropical Convergence Zone
MJO	Madden-Julian Oscillation
MLD	mixed layer depth
NCAR	National Center for Atmospheric Research
NEC	North Equatorial Current
NECC	North Equatorial Countercurrent
NEMO	Nucleus for European Modelling of the Ocean
NI	Simulation NYF-atmospheric forcing and IAF wind forcing
NN	Simulation NYF-atmospheric forcing and NYF wind forcing
NN-	Simulation NYF-atmospheric forcing and NYF-50% wind forcing
NN+	Simulation NYF-atmospheric forcing and NYF+50% wind forcing
NYF	Normal Year Forcing
ORAS4	Ocean ReAnalysis System
OLR	Outgoing Longwave Radiation

PC	Principal Components
PDO	Pacific Decadal Oscillation
PSMSL	Permanent Service for Mean Sea Level
RMM	Real-time Multivariate
SEC	South Equatorial Current
SODA	Simple Ocean Data Assimilation
SPCZ	South Pacific Convergence Zone
SSH	Sea Surface Height
SSS	Sea Surface Salinity
SST	Sea Surface Temperature
STD	standard deviation
TIW	Tropical Instability Wave
TIWE	Tropical Instability Wave Experiment
TKE	Turbulent Kinetic Energy
TMI	Microwave Imager
TRMM	Tropical Rainfall Measuring Mission
TVD	Total Variance Dissipation
WGOMD	Working Group on Ocean Model Development
WISHE	Wind-Induced Surface Heat Exchange

Table of Contents

Abstract ..... **i**

Acknowledgements ..... **ii**

Abbreviations and Acronyms ..... **iii**

Table of Contents ..... **v**

List of Figures ..... **ix**

List of Tables ..... **xx**

Chapter 1 General Introduction **1**

1.1 Equatorial Pacific oceanography **1**

1.1.1 Equatorial waves ***3***

1.1.1.1 Kelvin waves ***3***

1.1.1.2 Tropical instability waves ***5***

1.1.2 Temporal variability ***6***

1.2 The Madden-Julian Oscillation **6**

1.2.1 MJO Structure ***6***

1.2.2 MJO Theories ***8***

1.2.3 MJO Index ***10***

1.2.4 Modelling the MJO ***12***

1.2.5 The MJO in the Eastern Tropical Pacific Ocean ***13***

1.3 Objective of the thesis **14**

1.4 Thesis outline **14**

Chapter 2 Data and Methods **16**

2.1 Introduction **16**

2.2 The NEMO Model **16**

2.2.1 The ORCA1_LIM3 configuration ***18***

2.2.1.1 CORE forcing *20*

2.2.2 Numerical experiments *26*

2.3 Statistics **27**

2.3.1 Anomaly calculations *28*

2.3.2 Filtering data *28*

2.3.3 Wavelet analysis *28*

2.3.4 Empirical orthogonal function analysis *28*

2.3.5 Composite technique *29*

2.3.6 Pattern Correlation *29*

2.3.7 Granger Causality *29*

2.3.8 Distributed lag model *30*

2.4 General model performance **31**

Chapter 3 The Madden-Julian Oscillation's impact on the upper ocean in the central and eastern regions of the tropical Pacific **38**

3.1 Introduction **38**

3.2 Identification of intraseasonal variability **39**

3.3 Dominant patterns and spectral analysis of intraseasonal variability **41**

3.3.1 Sea surface height intraseasonal variability *41*

3.3.3 Sea surface salinity intraseasonal variability *45*

3.3.4 Sea surface zonal velocity intraseasonal variability *47*

3.3.5 Non-solar heat flux intraseasonal variability *49*

3.3.6 Solar heat flux intraseasonal variability *51*

3.3.7 Evaporation intraseasonal variability *53*

3.3.8 Precipitation intraseasonal variability *55*

3.4 Connection with the MJO **57**

3.5 Lagged linear regression and Granger causality analysis **67**

3.6 Summary **68**

Chapter 4 The Madden-Julian Oscillation's impact below the ocean surface in the central and eastern regions of the tropical Pacific....70

4.1 Introduction....70

4.2 Upper ocean vertical structure....70

4.3 Spatial patterns of intraseasonal variability....72

4.4 Intraseasonal oceanography vertical structure....75

4.4.1 Temperature....75

4.4.2 Salinity....81

4.4.3 Zonal Currents....84

4.4.4 Meridional Currents....87

4.4.5 Vertical Currents....90

4.5 Potential links with the MJO....93

4.6 Lagged linear regression and Granger causality analysis....98

4.7 Summary....103

Chapter 5 The influence of the Madden-Julian Oscillation on Tropical Instability Waves in the eastern tropical Pacific....105

5.1 Introduction....105

5.2 Identification of TIWs....106

5.3 Dominant factors in the TIW energy transformation process....111

5.3.1 BRT-KH....112

5.3.2 BCL....115

5.4 Connection with the MJO....117

5.5 Summary....128

Chapter 6 General Discussion....130

6.1 Oceanographic surface variability and its response to the MJO....130

6.1.1 Dominant patterns of the surface intraseasonal variability....130

6.1.2 MJO surface composites....132

6.1.3 Lagged linear regression and Granger causality analysis....133

6.2 Oceanographic subsurface variability and its response to the MJO 134

6.2.1 Vertical sections of intraseasonal variability 135

6.2.2 MJO related subsurface composites 136

6.2.3 Lagged linear regression and Granger causality analysis 138

6.3 TIWs and their response to MJO 139

6.3.1 TIWs energy transformation 140

6.3.2 MJO composites 141

6.4 Limitations 142

6.4.1 Statistical Methods 142

6.4.2 Model Resolution 143

6.4.3 Coupled Model 143

Chapter 7 Conclusions and future work 145

7.1 Synthesis of key findings 145

7.2 Opportunities for future research 147

References 148

Appendices 163

Appendix A 163

Appendix B 165

List of Figures

Figure 1.1. Schematic circulation in the tropical Pacific. The arrows indicate the flow direction of the currents. Colour shading represent different water depths (data from GEBCO_2014 Grid, version 20141112).....2

Figure 1.2. Upwelling and downwelling Kelvin waves. Figure reproduced from Cushman-Roisin and Beckers (2011).....4

Figure 1.3. Tropical instability waves seen in 3-days average-composites maps of SST from the Tropical Rainfall Measuring Mission (TRMM) Microwave Imager (TMI) for the periods 11–13 July 1998 (upper) and 14–16 November 1998 (lower). Figure reproduced from Chelton et al. (2000).....5

Figure 1.4. Schematic of the MJO longitudinal advance across the Indian and Pacific oceans. Time progresses downward, the relative height of the tropopause is indicated in the upper part of each panel and the average anomaly surface pressure is represented in the lower part of each panel, with negative (positive) anomalies in red (blue). Cloudiness associated with the convection centre and arrows represent the zonal circulation. Adapted from Madden and Julian (1972).....7

Figure 1.5 Schematic diagrams of the MJO theories a) Wave-CISK and b) wind-induced surface heat exchange (WISHE). The cloud symbol indicates the location of the convective centre. Arrows represent the anomalous winds and the grey oval the region of maximum convergence. Adapted from Flatau *et al.* (1997). 10

Figure 1.6. The spatial structure of the combined EOFs of OLR and zonal winds at 850hPa and 200 hPa. Fields are equatorially averaged between latitudes 15°N and 15°S. Figure reproduced from Wheeler and Hendon (2004). 11

Figure 1.7. Phase space diagram defined by RMM1 and RMM2. RMM1 corresponds to the x-axis and RMM2 corresponds to the y-axis Different geographical locations are labelled indicating where the convection signal of the active MJO is taking place. Also shown is the weak MJO at the centre of the phase space diagram. Figure reproduced from Wheeler and Hendon (2004).....12

Figure 2.1. Arrangement of the variables and their computation points in an Arakawa C-grid. T defines the scalar points of temperature, salinity, density, pressure and horizontal divergence. u, v and w-points define the horizontal components of the velocity components,

and f indicates the relative and planetary vorticities on the f-points (Madec et al., 1997). 18
Figure 2.2. Horizontal distribution of restoring coefficients (1/s) at the depth of 9.55 m. 19
Figure 2.3. MJO composites of zonal winds anomalies (m/s). 22
Figure 2.4. MJO composites of meridional winds anomalies (m/s). 23
Figure 2.5. MJO composites of air temperature anomalies (°C). 23
Figure 2.6. MJO composites of specific air humidity anomalies (kg/kg). 24
Figure 2.7. MJO composites of incoming shortwave radiation anomalies (W/m^2). 25
Figure 2.8. MJO composites of incoming longwave radiation anomalies (W/m^2). 25
Figure 2.9. Left panels show time mean of sea surface height (m) between 1990 to 2000 for a) model, b) GLORS data, c) ORA data and d) SODA data. Right panels show the differences between model and reanalysis from e) GLORS data, f) ORA data and g) SODA data. 33
Figure 2.10. Left panels show time mean of sea surface temperature (°C) between 1990 to 2000 for a) model, b) GLORS data, c) ORA data and d) SODA data. Right panels show the differences between model and reanalysis from e) GLORS data, f) ORA data and g) SODA data. 33
Figure 2.11. Left panels show vertical sections of time mean of temperature (°C) averaged over the latitudinal band 2°S – 2°N between 1990 to 2000 for a) model, b) SODA data and c) ORA data. The bold line denotes the 20°C isotherm. Right panels show the differences between model and reanalysis from d) SODA data and f) ORA data, the bold line denotes 0°C. 34
Figure 2.12. Left panels show time mean of sea surface salinity (psu) between 1990 to 2000 for a) model, b) GLORS data, c) ORA data and d) SODA data. Right panels show the differences between model and reanalysis from e) GLORS data, f) ORA data and g) SODA data. 35
Figure 2.13. Left panels show time mean sea surface zonal current (m/s) between 1990 to 2000 for a) model, b) GLORS data, c) ORA data and d) SODA data. Right panels show the differences between model and reanalysis from e) GLORS data, f) ORA data and g) SODA data. 36
Figure 2.14. Left panels show vertical sections of time mean of equatorial currents (m/s, eastward in red and westward in blue) at 125°W between 1990 to 2000 for a) model, b) SODA data and c) ORA data. The bold line denotes the equator. Right panels show the

difference between model and reanalysis from d) SODA data and e) ORA data bold line denotes the equator. 36
Figure 2.15. Left panels show time mean of surface meridional current (m/s) between 1990 to 2000 for a) model, b) GLORS data, c) ORA data and d) SODA data. Right panels show the difference between model and reanalysis from e) GLORS data, f) ORA data and g) SODA data. 37
Figure 3.1. Bathymetry (in metres) of the tropical Pacific region (data from ETOPO1 (Amante and Eakins, 2009)). 39
Figure 3.2. Shaded regions denote the total variance of a field and the black contours reflect the intraseasonal (10-120 day) variance as a percent of the total variance of **a)** sea surface height (m), **b)** sea surface temperature ($^{\circ}$C), **c)** sea surface salinity (psu), **d)** sea surface zonal current (m/s), **e)** non-solar heat flux (W/m^2), **f)** solar heat flux (W/m^2), **g)** evaporation (mm/day) and **h)** precipitation (mm/day) where each is expressed in units of standard deviation. Percentage contour interval is 20%.....40
Figure 3.3. First (a) and second (b) leading EOF modes of SSH intraseasonal anomalies. The percentage of variance explained by each EOF mode is given at the top of each panel. 42
Figure 3.4. The fraction of the intraseasonal variance (%) explained by the two leading EOF modes of SSH anomalies.....42
Figure 3.5. Wavelet analysis of PC1 and PC2 of the SSH intraseasonal anomalies. Panels (a) and (b) show the corresponding wavelet power spectrums. The thick black contours indicate the 95% confidence level, and the thin black line indicates the border of the cone of influence (all data below this line are unreliable). Panel (c) shows the global wavelet spectrums. The thin lines represent the 95% confidence level. 43
Figure 3.6. First (a) and second (b) leading EOF modes of SST intraseasonal anomalies. The percentage of variance explained by each EOF mode is given at the top of each panel. 44
Figure 3.7. The fraction of the intraseasonal variance (%) explained by the two leading EOF modes of the SST anomalies. 44
Figure 3.8. Wavelet analysis of PC1 and PC2 of the SST intraseasonal anomalies. Panels (a) and (b) show the corresponding wavelet power spectrums. The thick black contours indicate the 95% confidence level, and the thin black line indicates the border of the cone of influence (all data below this line are unreliable). Panel (c) shows the global wavelet spectrums. The thin lines represent the 95% confidence level. 45

Figure 3.9. First (a) and second (b) leading EOF modes of SSS intraseasonal anomalies. The percentage of variance explained by each EOF mode is given at the top of each panel. 46
Figure 3.10. The fraction of the intraseasonal variance (%) explained by the two leading EOF modes of the SSS anomalies. 46
Figure 3.11. Wavelet analysis of PC1 and PC2 of the SSS intraseasonal anomalies. Panels (a) and (b) show the corresponding wavelet power spectrums. The thick black contours indicate the 95% confidence level, and the thin black line indicates the border of the cone of influence (all data below this line are unreliable). Panel (c) shows the global wavelet spectrums. The thin lines represent the 95% confidence level. 47
Figure 3.12. First (a) and second (b) leading EOF modes of sea surface zonal velocity intraseasonal anomalies. The percentage of variance explained by each EOF mode is given at the top of each panel. 48
Figure 3.13. The fraction of the intraseasonal variance (%) explained by the two leading EOF modes of the sea surface zonal velocity anomalies. 48
Figure 3.14. Wavelet analysis of PC1 and PC2 of the sea surface zonal velocity intraseasonal anomalies. Panels (a) and (b) show the corresponding wavelet power spectrums. The thick black contours indicate the 95% confidence level, and the thin black line indicates the border of the cone of influence (all data below this line are unreliable). Panel (c) shows the global wavelet spectrums. The thin lines represent the 95% confidence level. 49
Figure 3.15. First (a) and second (b) leading EOF modes of non-solar heat flux intraseasonal anomalies. The percentage of variance explained by each EOF mode is given at the top of each panel. 50
Figure 3.16. The fraction of the intraseasonal variance (%) explained by the two leading EOF modes of the non-solar heat flux anomalies. 50
Figure 3.17. Wavelet analysis of PC1 and PC2 of the non-solar heat flux intraseasonal anomalies. Panels (a) and (b) show the corresponding wavelet power spectrums. The thick black contours indicate the 95% confidence level, and the thin black line indicates the border of the cone of influence (all data below this line are unreliable). Panel (c) shows the global wavelet spectrums. The thin lines represent the 95% confidence level. 51
Figure 3.18. First (a) and second (b) leading EOF modes of solar heat flux (W/m^2) intraseasonal anomalies. The percentage of variance explained by each EOF mode is given at the top of each panel. 52

Figure 3.19. The fraction of the intraseasonal variance (%) explained by the two leading EOF modes of the solar heat flux anomalies. 52
Figure 3.20. Wavelet analysis of PC1 and PC2 of the solar heat flux intraseasonal anomalies. Panels (a) and (b) show the corresponding wavelet power spectrums. The thick black contours indicate the 95% confidence level, and the thin black line indicates the border of the cone of influence (all data below this line are unreliable). Panel (c) shows the global wavelet spectrums. The thin lines represent the 95% confidence level.....53
Figure 3.21. First (a) and second (b) leading EOF modes of evaporation anomalies. The percentage of variance explained by each EOF mode is given at the top of each panel. ..54
Figure 3.22. The fraction of the intraseasonal variance (%) explained by the two leading EOF modes of the evaporation anomalies. 54
Figure 3.23. Wavelet analysis of PC1 and PC2 of the evaporation intraseasonal anomalies. Panels (a) and (b) show the corresponding wavelet power spectrums. The thick black contours indicate the 95% confidence level, and the thin black line indicates the border of the cone of influence (all data below this line are unreliable). Panel (c) shows the global wavelet spectrums. The thin lines represent the 95% confidence level.....55
Figure 3.24. First (a) and second (b) leading EOF modes of precipitation (mm/day) anomalies. The percentage of variance explained by each EOF mode is given at the top of each panel.....56
Figure 3.25. The fraction of the intraseasonal variance (%) explained by the two leading EOF modes of the precipitation anomalies.....56
Figure 3.26. Wavelet analysis of PC1 and PC2 of the precipitation intraseasonal anomalies. Panels (a) and (b) show the corresponding wavelet power spectrums. The thick black contours indicate the 95% confidence level, and the thin black line indicates the border of the cone of influence (all data below this line are unreliable). Panel (c) shows the global wavelet spectrums. The thin lines represent the 95% confidence level.....57
Figure 3.27. MJO composites of the SSH anomalies from the entire dataset (as a percent change from standard deviation SSH). The thick black lines show 95% significance.....58
Figure 3.28. MJO composites of the sea surface zonal current velocity anomalies from the entire dataset (as a percent change from standard deviation sea surface zonal velocity). The thick black lines show 95% significance. 60
Figure 3.29. MJO composites of the SST anomalies from the entire dataset (as a percent change from standard deviation SST). The thick black lines show 95% significance. 61

Figure 3.30. MJO composites of the solar heat flux anomalies from the entire dataset (as a percent change from standard deviation sea surface zonal velocity). The thick black lines show 95% significance. 62
Figure 3.31. MJO composites of the non-solar heat flux anomalies from the entire dataset (as a percent change from standard deviation sea surface zonal velocity). The thick black lines show 95% significance. 63
Figure 3.32. MJO composites of the zonal winds anomalies (shading) and of surface wind stress (vector). 63
Figure 3.33. MJO composites of the evaporation anomalies from the entire dataset (as a percent change from standard deviation sea surface zonal velocity). The thick black lines show 95% significance. 64
Figure 3.34. MJO composites of the SSS anomalies from the entire dataset (as a percent change from standard deviation SSS). The thick black lines show 95% significance. 66
Figure 3.35. MJO composites of the precipitation anomalies from the entire dataset (as a percent change from standard deviation sea surface zonal velocity). The thick black lines show 95% significance. 66
Figure 3.36. Variance (%) explained by lagged linear regression model for filtered anomalies of a) SSH, b) SST, c) SSS, d) sea surface zonal current, e) non-solar heat flux, f) solar heat flux, g) evaporation and h) precipitation, regressed against RMM1 and RMM2. The hatched regions are those where Granger causality is significant at a 99% confidence level. 67
Figure 4.1. Time means of vertically averaged (between 10 and 260 m) **a)** temperature (˚C), **c)** salinity (psu), **e)** zonal current (m/s), **d)** meridional current (m/s) and **e)** vertical current (m/s). Longitude-depth sections of the same time means of **b)** temperature (˚C), **d)** salinity (psu), **f)** zonal current (m/s), **g)** meridional current (m/s) and **h)** vertical current (m/s). 71
Figure 4.2. Time means of a) mixed layer depth (m), b) thermocline depth (m), c) halocline depth (m) and d) pycnocline depth (m).....72
Figure 4.3. Shaded regions denote the total variance and the black contour lines are the fraction of the intraseasonal (10-120 day) variance to the total variance of a) temperature (°C), b) salinity (psu), c) zonal current (m/s), d) meridional current (m/s), e) vertical current (m/s), where each are averaged between 10-260 m. And f) mixed layer depth (m), g) thermocline depth (m), h) halocline depth (m) and i) pycnocline depth (m) where each is

expressed in units of standard deviation. Percent contours are plotted every 30, starting at 0 except for temperature where contours are plotted every 20, starting at 0. 74
Figure 4.4. Longitude-depth vertical sections of standard deviation filtered temperature (°C) at a) 7°N, b) 5°N, c) 2°N, d) equator, e) 2°S and f) 5°S, from the coast (right edge) to 150°E in the upper 300 m. Dotted, dashed, solid black and solid red lines denote the corresponding mean thermocline, mean halocline, mean pycnocline and mean mixed layer depths, respectively. The thin black line denotes the 20°C isotherm. Crosses denote the locations for which power spectra were computed and are presented in Figure 4.5. 76
Figure 4.5. Power spectrums for intraseasonal temperature time series for depths indicated in Figure 4.4 at latitudes 7°N, 5°N, 2°N, equator, 2°S and 5°S and longitudes 160°E, 175°W, 150°W, 125°W and 105°W. The dashed curves denote the 95% significance level. 77
Figure 4.6. Longitude-depth vertical sections of standard deviation (in 10^{-7} °C/s) of temperature time derivative, zonal advection, meridional advection, and vertical advection of temperature at latitudes 7°N, 5°N, 2°N, equator, 2°S and 5°S from the coast (right edge) to 150°E in the upper 300 m. Dotted, dashed and solid black lines denote the corresponding mean thermocline, mean halocline and mean pycnocline, respectively. 80
Figure 4.7. Longitude-depth vertical sections of standard deviation filtered salinity (psu) at a) 7°N, b) 5°N, c) 2°N, d) equator, e) 2°S and f) 5°S, from the coast (right edge) to 150°E in the upper 300 m. Dotted, dashed and solid black lines denote the corresponding mean thermocline, mean halocline and mean pycnocline depths, respectively. Crosses denote the locations for which power spectra were computed and are presented in Figure 4.8. 82
Figure 4.8. Power spectrums for intraseasonal salinity time series for depths indicated in Figure 4.7 at latitudes 7°N, 5°N, 2°N, equator, 2°S and 5°S and longitudes 160°E, 175°W, 150°W, 125°W and 105°W. The dashed curves denote the 95% significance level. 83
Figure 4.9. Longitude-depth vertical sections of standard deviation filtered zonal currents (m/s) at a) 7°N, b) 5°N, c) 2°N, d) equator, e) 2°S and f) 5°S, from the coast (right edge) to 150°E in the upper 300 m. Dotted, dashed and solid black lines denote the corresponding mean thermocline, mean halocline and mean pycnocline depths, respectively. Crosses denote the locations for which power spectra were computed and are presented in Figure 4.10.....85
Figure 4.10. Power spectrums for intraseasonal zonal currents time series for depths indicated in Figure 4.9 at latitudes 7°N, 5°N, 2°N, equator, 2°S and 5°S and longitudes 160°E, 175°W, 150°W, 125°W and 105°W. The dashed curves denote the 95% significance level.....86

Figure 4.11. Longitude-depth vertical sections of standard deviation filtered meridional currents (m/s) at a) 7°N, b) 5°N, c) 2°N, d) equator, e) 2°S and f) 5°S, from the coast (right edge) to 150°E in the upper 300 m. Dotted, dashed and solid black lines denote the corresponding mean thermocline, mean halocline and mean pycnocline depths, respectively. Crosses denote the locations for which power spectra were computed and are presented in Figure 4.12.....88
Figure 4.12. Power spectrums for intraseasonal meridional currents time series for depths indicated in Figure 4.11 at latitudes 7°N, 5°N, 2°N, equator, 2°S and 5°S and longitudes 160°E, 175°W, 150°W, 125°W and 105°W. The dashed curves denote the 95% significance level.....89
Figure 4.13. Longitude-depth vertical sections of standard deviation filtered vertical currents (m/s) at a) 7°N, b) 5°N, c) 2°N, d) equator, e) 2°S and f) 5°S, from the coast (right edge) to 150°E in the upper 300 m. Dotted, dashed and solid black lines denote the corresponding mean thermocline, mean halocline and mean pycnocline depths, respectively. Crosses denote the locations for which power spectra were computed and are presented in Figure 4.14.....91
Figure 4.14. Power spectrums for intraseasonal vertical currents time series for depths indicated in Figure 4.13 at latitudes 7°N, 5°N, 2°N, equator, 2°S and 5°S and longitudes 160°E, 175°W, 150°W, 125°W and 105°W. The dashed curves denote the 95% significance level.....92
Figure 4.15. Longitude-depth sections showing MJO composites of temperature anomalies relative to total standard deviation (in %) at 2°N, the equator, and 2°S, from the coast (right edge) to 150°E in the upper 300 m. The thick black lines show 95% significance. The dashed lines indicate the corresponding mean thermocline depth.....94
Figure 4.16. Longitude-depth sections showing MJO composites of salinity anomalies relative to total standard deviation (in %) at 2°N, the equator, and 2°S, from the coast (right edge) to 150°E in the upper 300 m. The thick black lines show 95% significance. The dotted and dashed lines indicate the corresponding mean halocline and thermocline, respectively. 95
Figure 4.17. Longitude-depth sections showing MJO composites of zonal current anomalies relative to total standard deviation (in %) at 2°N, the equator, and 2°S, from the coast (right edge) to 150°E in the upper 300 m. The thick black lines show 95% significance. The dashed lines indicate the corresponding mean thermocline depth. 96

Figure 4.18. Longitude-depth sections showing MJO composites of meridional currents anomalies relative to total standard deviation (in %) at 2°N, the equator, and 2°S, from the coast (right edge) to 150°E in the upper 300 m. The thick black lines show 95% significance. The dashed lines indicate the corresponding mean thermocline depth. 97
Figure 4.19. Longitude-depth sections showing MJO composites of vertical currents anomalies relative to total standard deviation (in %) at 2°N, the equator, and 2°S, from the coast (right edge) to 150°E in the upper 300 m. The thick black lines show 95% significance. The dashed lines indicate the corresponding mean thermocline depth. 98
Figure 4.20. Variance (%) explained by the lagged linear regression model for filtered temperature anomalies at the mixed layer depth (a, e, and i), the mean thermocline depth (b, f, and j), the mean halocline depth (c, g, and k) and the mean pycnocline depth (d, h, and l) regressed against RMM1 and RMM2, based on II (left), IN (centre) and NI (right) output. The hatched regions indicate a significant Granger causality test. Significance is assessed at a 99% confidence level.....100
Figure 4.21. Variance (%) explained by the lagged linear regression model for filtered salinity anomalies at the mixed layer depth (a, e, and i), the mean thermocline depth (b, f, and j), the mean halocline depth (c, g, and k) and the mean pycnocline depth (d, h, and l) regressed against RMM1 and RMM2, based on II (left), IN (centre) and NI (right) output. The hatched regions indicate a significant Granger causality test. Significance is assessed at a 99% confidence level. 100
Figure 4.22. Variance (%) explained by the lagged linear regression model for filtered zonal current anomalies at the mixed layer depth (a, e, and i), the mean thermocline depth (b, f, and j), the mean halocline depth (c, g, and k) and the mean pycnocline depth (d, h, and l) regressed against RMM1 and RMM2, based on II (left), IN (centre) and NI (right) output. The hatched regions indicate a significant Granger causality test. Significance is assessed at a 99% confidence level.....101
Figure 4.23. Variance (%) explained by the lagged linear regression model for filtered meridional current anomalies at the mixed layer depth (a, e, and i), the mean thermocline depth (b, f, and j), the mean halocline depth (c, g, and k) and the mean pycnocline depth (d, h, and l) regressed against RMM1 and RMM2, based on II (left), IN (centre) and NI (right) output. The hatched regions indicate a significant Granger causality test. Significance is assessed at a 99% confidence level.....102
Figure 4.24. Variance (%) explained by the lagged linear regression model for filtered vertical current anomalies at the mixed layer depth (a, e, and i), the mean thermocline depth

(b, f, and j), the mean halocline depth (c, g, and k) and the mean pycnocline depth (d, h, and l) regressed against RMM1 and RMM2, based on II (left), IN (centre) and NI (right) output. The hatched regions indicate a significant Granger causality test. Significance is assessed at a 99% confidence level. 103

Figure 5.1. Hovmöller diagrams of 0 to 5°N averaged, filtered EKE [m^2/s^2] from the II, NFY1, NN+ and NN- simulations. The x-axis is longitude, and the y-axis is time. The red and blue boxes correspond to the occurrence of the Niño and Niña events, respectively. 107

Figure 5.2. Hovmöller diagrams of filtered EKE [m^2/s^2] at 0, 1°N, 2°N, 3°N, 4°N and 5°N from II, NFY1, NN+ and NN- simulations. The x-axis is longitude, and the y-axis is time in for 11 years. 108

Figure 5.3. Time mean EKE [m^2/s^2] averaged in the upper 100 m in the II, NN, NN+ and NN- simulations between 1990 to 2000. The red box (2°S-6°N, 100°W-150°W) represents the region where the EKE data density is relatively high in II. 109

Figure 5.4. Longitude-depth vertical sections of mean filtered EKE [m^2/s^2] averaged between 0 to 5°N in the II, NN, NN+ and NN- simulations between 1990 to 2000, from the coast (right edge) to 150°E in the upper 150 m. 110

Figure 5.5. Increase factor in mean filtered EKE [m^2/s^2] in the NN+ (red) and the NN- (blue) simulations regionally averaged between 0 to 5°N and in the upper 150 m, from the coast (right edge) to 150°E. 111

Figure 5.6. Time mean barotropic conversion term [10^{-8} m^2/s^3] averaged in the upper 100 m in the II, NN, NI and IN simulations. 113

Figure 5.7. Time mean barotropic conversion term [10^{-8} m^2/s^3]. Top group: longitude-depth vertical sections averaged between 2°S to 6°N. Bottom group: latitude-depth vertical sections averaged between 100°W to 150°W in the II, NN, NI and IN simulations in the upper 150 m. 114

Figure 5.8. Time mean baroclinic conversion term [10^{-8} m^2/s^3] averaged in the upper 100 m in the II, NN, NI and IN simulations. 115

Figure 5.9. Time mean baroclinic conversion term [10^{-8} m^2/s^3]. Top: longitude-depth vertical sections averaged between 2°S to 6°N. Bottom: latitude-depth vertical sections averaged between 100°W to 150°W in the II, NN, NI and IN simulations in the upper 150 m. 116

Figure 5.10. Time series of a) barotropic [10^{-8} m^2/s^3] and b) baroclinic conversion term [10^{-8} m^2/s^3] averaged between 2˚S to 7˚N and 100˚W to 150˚W over 0-100 m, from the II (red), NN (yellow), IN (blue) and NI (green) simulations. 117
Figure 5.11. MJO composites of barotropic conversion term [10^{-8} m^2/s^3] averaged between 2˚S to 7˚N and over 0-100 m, from the II, NI, and IN simulations. 119
Figure 5.12. MJO composites of baroclinic conversion term [10^{-8} m^2/s^3] averaged between 2˚S to 7˚N and over 0-100 m, from the II, NI, and IN simulations. 120
Figure 5.13. Depth-time plots of BTR-KH components a-c) $-u'v'\partial U\partial y$ (m^2/s^3), d-f) $-v'v'\partial V\partial y$ (m^2/s^3), g-i) $-u'w'\partial U\partial z$ (m^2/s^3) and j-l) $-v'w'\,\partial V\partial z$ (m^2/s^3) averaged between 2˚S to 7˚N and 100˚W to 150˚W in the upper 180 m, from the II (left panel), the NI (centre panel) and the IN (right panel) simulations. The three dotted, dashed and solid lines indicate the corresponding mixed layer depth, 20˚C isotherm and the depth of the EUC core, respectively. 122
Figure 5.14. Depth-time plots of Reynolds stress components a-c) $u'v'$ (m^2/s^2), d-f) $v'v'$ (m^2/s^2), g-i) $u'w'$ (m^2/s^2) and j-l) $v'w'$ (m^2/s^2) averaged between 2˚S to 7˚N and 100˚W to 150˚W in the upper 180 m, from the II (left panel), the NI (centre panel) and the IN (right panel) simulations. The three dotted, dashed and solid lines indicate the corresponding mixed layer depth, 20˚C isotherm and the depth of the EUC core, respectively. Note the colorbar for each row of panels is different. 123
Figure 5.15. Depth-time plots of a-c) meridional shear of the zonal velocity (s^{-1}), d-f) meridional shear of the meridional velocity (s^{-1}), g-i) vertical shear of the zonal velocity (s^{-1}), j-l) vertical shear of the meridional velocity (s^{-1}), and m-o) meridional gradient of temperature (Cm^{-1}) averaged between 2˚S to 7˚N and 100˚W to 150˚W in the upper 180 m, from the II (left panel), the NI (centre panel) and the IN (right panel) simulations. The three dotted, dashed and solid lines indicate the corresponding mixed layer depth, 20˚C isotherm and the depth of the EUC core, respectively. Note the colorbar for each row of panels is different. 124
Figure 5.16. MJO composites of Reynolds stress components a) $u'v'$, b) $v'v'$, c) $u'w'$, d) $v'w'$, and e) meridional shear of the zonal velocity, f) meridional shear of the meridional velocity, g) vertical shear of the zonal velocity, h) vertical shear of the meridional velocity and i) meridional gradient of temperature averaged between 2˚S to 7˚N and 100˚W to 150˚W in the upper 100 m for MJO active (solid) and MJO inactive (dashed), from the II (red), NI (green) and IN (blue) simulations. Note the different vertical scale. 127

List of Tables

Table 2.1. Summary of the main model parameterizations.....18
Table 2.2. Atmospheric variables provided by CORE II. 20
Table 2.3. Number of days for MJO composite analysis from 1st January 1975 to 31st December 2009. 21
Table 2.4. Characteristics of the numerical experiments. 27
Table 2.5. Description of the reanalysis data products used in the validation of the model. 31
Table 3.1. Number of days for MJO composite analysis from 1st January 1990 to 31st December 2000. 58
Table 3.2. Maximum pattern correlation for each variable for each MJO phases. The dark gray shading indicates the highest values. 59
Table 5.1. Time mean of each of the barotropic terms and the baroclinic term [10^{-8} m^2/s^3] averaged over 2°S-6°N and 100°W-150°W (red box Figure 5.3) at the surface. 112
Table 5.2. Number of days for MJO composite analysis from the TIWs season (July to December) for years 1990 to 2000.....118

Chapter 1

General Introduction

1.1 Equatorial Pacific oceanography

The equatorial Pacific Ocean covers a large geographic area roughly within the limits of the west coast of the American continent and ~ 150°E in the zonal direction and within the parallels ~ 10°S - 10°N in the meridional direction. In this region, the main dynamic processes are the result of the ocean-atmosphere coupling (Amador *et al.*, 2006). These ocean-atmosphere interactions give great relevance to the region because they contribute to the regulation of the planet's climate, influence the development of phenomena such as El Niño Southern Oscillation (ENSO) and also create unique conditions for high biological productivity (Fiedler and Lavín, 2006).

In this geographic region surface winds and currents have a strong seasonal cycle mainly modulated by the meridional migration of the Intertropical Convergence Zone (ITCZ). The ITCZ located on average at 5°N is a region a few hundred kilometres wide where the northeast and southeast trade winds converge, generating an area of weak winds, heavy rains, and heavy cloud cover (Tomczak and Godfrey, 1994). During the austral spring and winter, from July to November, the ITCZ remains north of 10°N. The south-easterly trade winds become stronger and therefore the equatorial divergence intensifies, connecting the cold equatorial waters with the upwelling waters from the Peru Current and resulting in the so-called equatorial cold tongue (Kessler, 2006). Conversely, during the austral summer and autumn, from December to May, the trade winds from the northeast are intense and the equatorial upwelling is minimal, so the cold tongue is absent. This cold tongue is centred on the equator and extends up to 120°W from western South America, with sea surface temperature (SST) below 24°C (Fiedler and Talley, 2006) (Figure 1.1).

The tropics are also characterized by being a great reservoir of heat. This region receives a large amount of energy from the sun annually. The intense solar radiation, atmospheric convection and surface winds dominate the variability in the thermohaline structure of the basin. The mean distribution of SST for the Pacific basin shows that the minimum temperatures are located in the easternmost side of the basin while the maximum

temperatures are located in the western sector. Nevertheless, in the eastern Pacific, there is also a region with relatively high SST values (>27.5 ˚C): the eastern Pacific warm pool. This warm pool is a consequence of the combination of large net heat flux and weak wind mixing (Wang and Enfield, 2001) (Figure 1.1). Given these factors, this warm pool is a highly stratified region with a strong vertical temperature gradient and therefore a permanent shallow thermocline. The Gulf of Panama, in the eastern warm pool, shows the lowest salinity values of 29-31 psu, due to the extreme local rainfall and river runoff (Fiedler and Talley, 2006).

Another region of high relevance, especially from the point of view of its biology, in the eastern warm pool, is the open-ocean upwelling Costa Rica Dome. In this dome, the thermocline forms a persistent cyclonic eddy centred at 9˚N and 90˚W and this thermocline can be located very close to the surface at approximately 30 m (Xie *et al.*, 2005). Among the factors conspiring to cause the dome are the ITCZ, coastal wind jets and the terminus of the equatorial current system (Fiedler, 2002). The coastal eddies in this region are generated by three intense and narrow wind jets blowing through gaps in the mountains in southern Mexico and Central America towards the sea. The Tehuantepec Jet, the Papagayo Jet and the Panama Jet develop only from November to April (Willett *et al.*, 2006).

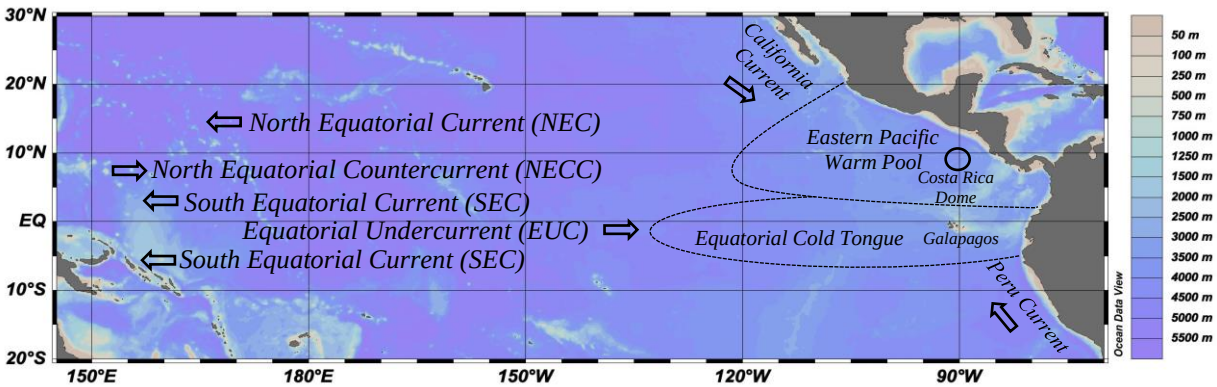

Figure 1.1. Schematic circulation in the tropical Pacific. The arrows indicate the flow direction of the currents. Colour shading represent different water depths (data from GEBCO_2014 Grid, version 20141112).

The oceanic circulation in the tropical Pacific Ocean is driven by ITCZ-related wind forcing and the dynamics of the tropical anticyclonic gyres. This circulation system consists mainly of three surface currents: The South Equatorial Current (SEC), the North Equatorial Countercurrent (NECC) and the North Equatorial Current (NEC) (Figure 1.1). The

westward SEC generated by mean easterly winds extends approximately from 10°S to 3°N. The SEC is divided into two main branches centred roughly at 3°N and 3°S. This current develops over the top 200 m and transports warm water to the western Pacific with a maximum velocity of 1 m/s (Philander, 1990; Kessler, 2006). The NECC flows from west to east between latitudes 3°N to 10°N. This narrow current has a typical velocity of 0.5 m/s and it is strongest from August to January. North of the 10°N with a displacement towards the west is located the NEC. The NEC is fed by both the NECC and the California Current at different times of the year and its speeds do not exceed 0.2 m/s (Philander, 1990; Kessler, 2006).

Below the surface is located the Equatorial Undercurrent (EUC), travelling east between 2°S and 2°N. The EUC, also called the Cromwell Current, is generated by the pressure difference between the eastern and western ends of the Pacific basin. This current flows below the thermocline; at 125°W its core is positioned at about 80 m and has an average speed near to 1 m/s (Pedlosky, 1996; Kessler, 2006). When the EUC approaches the Galapagos Islands it decelerates and splits into two branches, penetrating beyond the islands towards the coasts of South America (Eden and Timmermann, 2004; Kessler, 2006).

1.1.1 Equatorial waves

1.1.1.1 Kelvin waves

In 1966, Matsuno developed a theoretical framework to explain the dynamics of equatorially trapped waves. He formulated a set of shallow water equations (SWEs) derived from the primitive Navier-Stokes equations on a linearised equatorial β-plane. For a detailed review see Matsuno (1966). These SWEs result from a single layer model where it is assumed that there is no vertical shear of horizontal velocity. The fluid layer of depth h has a constant density, that is, it is an incompressible fluid. The equatorially trapped waves are zonally propagating solutions of the SWEs. Kelvin waves are a particular solution of the SEW in which the meridional component of the velocity equals zero. The phase speed (c) (1.1) and the dispersion relation (1.2) for frequency ω, wave number k and acceleration of gravity $g = 9.81$ m/s^2 are given by the following equations:

$$c = \sqrt{gh}, \tag{1.1}$$

$$\omega = k\sqrt{gh} \tag{1.2}$$

In the equatorial Pacific, anomalous winds are primarily responsible for the generation of Kelvin waves. These waves play an important role in the redistribution of energy in the region, particularly between latitudes 5°S and 5°N (Fedorov and Brown, 2009). The oceanic Kelvin waves in addition to being triggered by wind anomalies can also arise from the reflection of Rossby waves as they arrive in the western Pacific boundary. Kelvin waves are non-dispersive waves, that is, their speed of propagation does not depend on their wavelength (1.1), which implies that the energy of the wave moves at the velocity of the wave itself.

Kelvin waves travel eastward along the equator with an average velocity between 2 m/s and 3 m/s. Their zonal wavelength is about 13000–14000 km with a period near to 70 days (Hendon *et al.*, 1998). Kelvin waves can be divided into two types: Downwelling Kelvin waves and Upwelling Kelvin waves (Figure 1.2). The downwelling (upwelling) Kelvin waves are characterized by deepening (raising) of the thermocline and consequently increasing (decreasing) SSTs and sea level (Zhang, 2001; McPhaden, 2002). When a Kelvin wave reaches the coasts of South America, a part of the wave continues travelling north and south as a coastal trapped Kelvin wave. The remaining part is reflected, becoming a Rossby wave travelling west (Stewart, 2008). Similar to Kelvin waves, Rossby waves can be classified into two types, upwelling and downwelling, as these waves also cause disturbances in the depth of the thermocline (Fedorov and Brown, 2009).

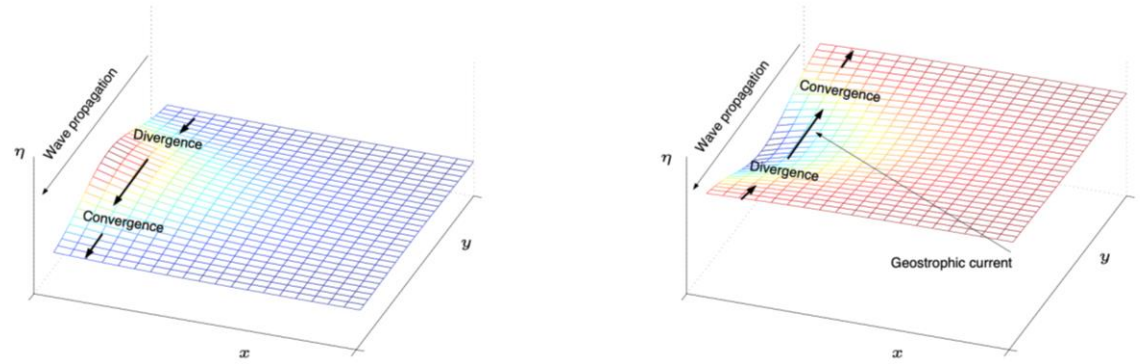

Figure 1.2. Upwelling and downwelling Kelvin waves. Figure reproduced from Cushman-Roisin and Beckers (2011).

1.1.1.2 Tropical instability waves

In the 1970s, tropical instability waves (TIWs) were first documented in the Atlantic by Düing *et al.* (1975) and in the Pacific by Legeckis (1977). These synoptic waves are easy to recognize in SST patterns between latitudes ~ 5°S and ~ 10°N (Figure 1.3) (Chelton *et al.*, 2000). TIWs have also been detected by variations in salinity, sea level and current velocity through both observations and model simulations (e.g., Qiao and Weisberg, 1995; Masina and Philander, 1999; Lee *et al.*, 2012). TIWs propagating westward with a typical phase speed of ~ 0.5 m/s are characterized by a wavelength of 1000-2000 km and a period of 20-40 days (Qiao and Weisberg, 1995; Willett *et al.*, 2006).

TIWs are generated by instabilities caused by intense vertical and horizontal shears from the equatorial current system and/or by variations in the meridional gradient of SST (Yu *et al.*, 1995; Masina *et al.*, 1999). More details on the mechanisms that cause TIWs are discussed in Chapter 5. Since TIWs depend on the background conditions these waves are seasonal and related to strong easterly trade winds. In the Pacific, TIWs are most intense during July to December, when the equatorial currents shear is strongest. TIWs also show interannual variability related to the ENSO phases. During El Niño years, the Pacific cold tongue is weakened and TIWs are suppressed, and, conversely, during the La Niña years, TIWs are the most energetic (Contreras, 2002).

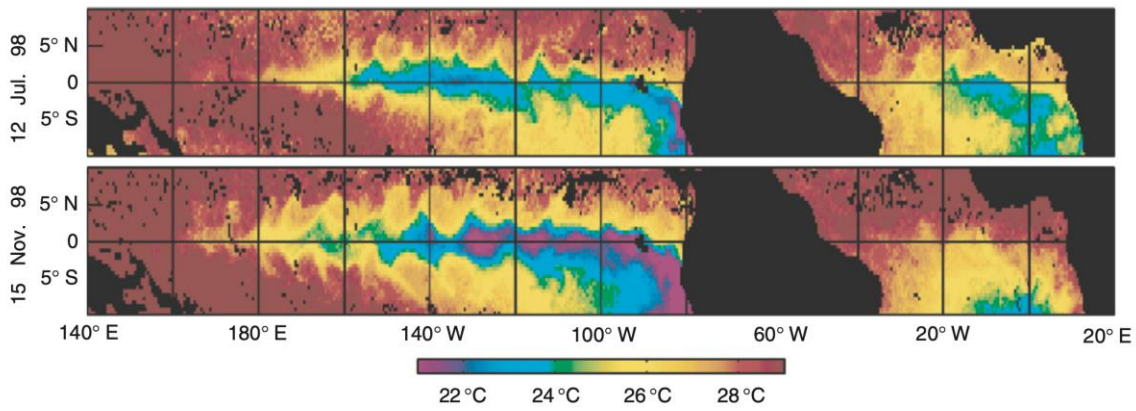

Figure 1.3. Tropical instability waves seen in 3-days average-composites maps of SST from the Tropical Rainfall Measuring Mission (TRMM) Microwave Imager (TMI) for the periods 11–13 July 1998 (upper) and 14–16 November 1998 (lower). Figure reproduced from Chelton *et al.* (2000).

1.1.2 Temporal variability

The temporal variability of the ocean-atmosphere conditions of the tropical Pacific can be decomposed into oscillations with periods of weeks (intraseasonal), months (seasonal), years (interannual) and decades (interdecadal). On the interannual scale, variability in the region is dominated by El Niño-Southern Oscillation (ENSO). The dynamics of this phenomenon is directly related to Rossby and Kelvin waves. This phenomenon has a strong impact on rainfall and thermal structure affecting marine ecosystems and the local economy (Wang and Fiedler, 2006). The leading mode of interdecadal variability in the North Pacific, the Pacific Decadal Oscillation (PDO), with decadal periods between 20 to 30 years is reviewed in Mestas-Nuñez and Miller (2006). In the intraseasonal variability band (periods between 10 and 90 days), the Madden-Julian Oscillation (MJO) has been identified as the most important mode that operates on the intraseasonal time scale in the tropical atmosphere (Madden and Julian, 1972). This work focuses on the intraseasonal variability of the tropical Pacific Ocean.

1.2 The Madden-Julian Oscillation

The MJO was accidentally discovered by Roland Madden and Paul Julian through observations of zonal winds and surface pressure at Canton Island in the Pacific Ocean (Madden and Julian, 1971). They noticed in the co-spectrum of zonal winds at 150 and 850 hPa a pronounced spectral peak with periods of 41 to 53 days, suggesting that this is due to a long air-mass circulation of thousands of kilometres near the equator (Madden and Julian, 1971). In a subsequent study, Madden and Julian (1972) expanded the number of observation stations and locations to study the spatial and temporal structure of the MJO. In summary, the MJO was characterised by the eastward propagation of a region of deep atmospheric convection from India to the Pacific with a speed of 5 m/s confined within a band of latitudes between 10°S to 10°N.

1.2.1 MJO Structure

Figure 1.4 shows a schematic of the MJO behaviour described in Madden and Julian (1972). At the initiation stage of a typical MJO event, the emergence of a convective anomaly is observed in the equatorial Indian Ocean, at the same time as a weak positive SST develops. This convective anomaly strengthens (as does the SST anomaly) and slowly

propagates eastward with an average phase speed of 5 m/s. The convective centre, called the active phase region of the MJO (marked in red in the schematic), experiences anomalous convergence of zonal winds in the lower troposphere and anomalous divergence in the upper troposphere. Suppressed or inactive convective conditions (indicated in blue in the schematic) are related to regions of decreased zonal circulation (Zhang, 2005). The amplitude of the deep convection system reduces over the Maritime Continent and begins to weaken at about the dateline. The reduced convective anomaly in the western Pacific continues to travel eastward with an increased velocity of 10 m/s (Hendon and Salby, 1994).

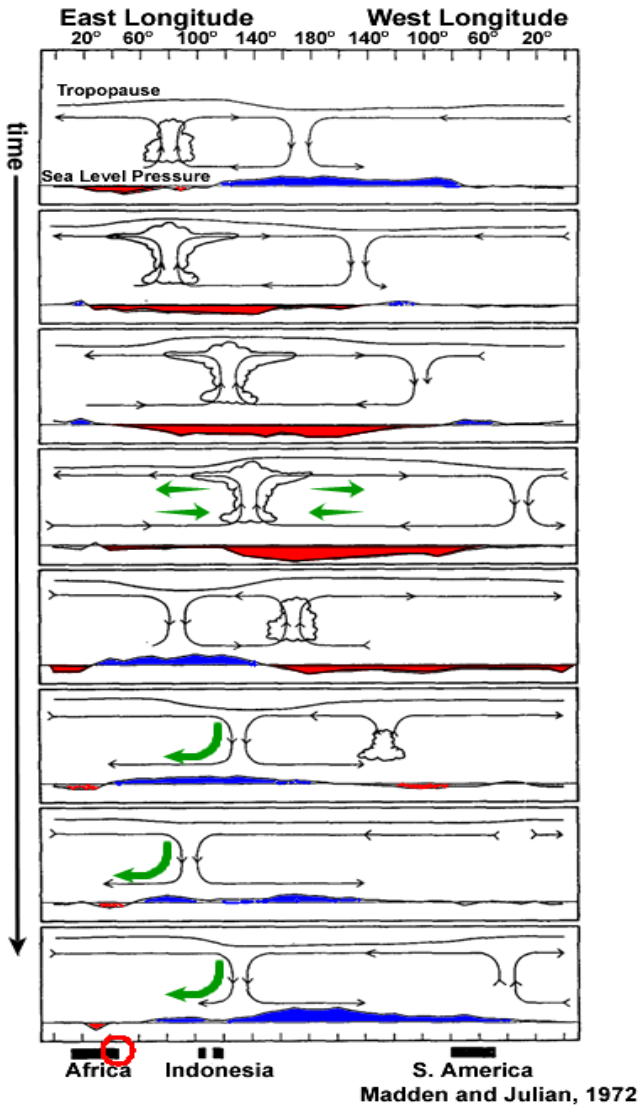

Figure 1.4. Schematic of the MJO longitudinal advance across the Indian and Pacific oceans. Time progresses downward, the relative height of the tropopause is indicated in the upper part of each panel and the average anomaly surface pressure is represented in the lower part of each panel, with negative (positive) anomalies in red (blue). Cloudiness associated with the convection centre and arrows represent the zonal circulation. Adapted from Madden and Julian (1972).

The internal structure of the active phase of the MJO is associated with masses of convective clouds. Nakazawa (1988) using outgoing longwave radiation (OLR) observations identified the clustering of convective clouds (super cloud clusters) during the active phase of the MJO. These clusters, of the order of 10^3 km, originate in the Indian Ocean and propagate eastward to the Pacific Ocean.

1.2.2 MJO Theories

A theoretical model that fully explains all the observed features of the MJO is difficult to derive and none is yet universally accepted. For example, the source of energy required for triggering the MJO is still under debate. There are basically two types of explanations proposed for its origin: external forcing theories and internal forcing theories. The latter examines the idea that the MJO produces its own source of energy, through a local feedback process associated with the MJO itself and the former portrays the MJO as the result of independent external forcing (Zhang, 2005).

Three theories with external forcing stand out. 1. Intraseasonal fluctuations of the Asian summer monsoon. In this theory, during monsoon rainfall, a stationary oscillation occurs as a result of the interaction between evaporation, convection and radiation (Hu and Randall, 1995). 2. Stochastic forcing. This theory proposes as a possible mechanism energy generation from the local convection (Salby and Garcia, 1987). 3. Forcing from the midlatitudes. According to this theory, the MJO might be amplified, if not generated, by baroclinic disturbances at higher latitudes (Frederiksen and Frederiksen, 1997).

The two most important theories relying on internal forcing are presented below.

- Wave-CISK: The term Conditional Instability of the Second Kind (CISK) introduced by Charney and Eliassen (1964) to explain the growth of tropical cyclones has been the basis of subsequent MJO theories. Broadly speaking, convection at the mesoscale level is generated by the convergence of the boundary layer moisture into a low-pressure region (Lindzen, 1974) (Figure 1.5a). This theory invokes the interaction between the convergence of moisture in the boundary layer atmospheric instability leading to the creation of Kelvin waves to explain the MJO. Although this theory, among other deficiencies, produces a convection structure

with a phase velocity faster than observations, modified versions of this approach are still relevant today.

- Intraseasonal modification of surface fluxes – WISHE: This theory proposed by Neelin *et al.* (1987) and Emanuel (1987) simultaneously but separately is referred to as 'wind-induced surface heat exchange' (WISHE). Unlike the previous theory, here convection is linked to surface evaporation rather than to the transport of moisture from other regions. In this theory, the convection vertically redistributes moisture and heat from the ocean that have been advected into the region by the trade winds (Figure 1.5b). Among the weaknesses of this theory is the assumption that the mean surface winds are easterlies and that the maximum evaporation is located east of the region of maximum intensity of the MJO. Despite these shortcomings, this theory, that uses idealized zonal wind and temperature distributions, is able to represent reasonably the structure and realistic eastward propagation phase speed of the MJO (Emanuel, 1987; Neelin *et al.*, 1987).

Each of these theories makes use of some of the multiple factors that could affect the MJO, among them surface wind patterns, upper-troposphere wind, upper-troposphere temperature structure, sources of convective instability and SST. But none of them delivers a complete explanation of the phenomenon. Nevertheless, they are the basis for many modern theories. Examples of these are Large-scale convective vortex (Hayashi and Itoh, 2017), Nonlinear solitary wave (Yano and Tribbia, 2017), Gravity wave (Yang and Ingersoll, 2013), Skeleton (Majda and Stechmann, 2009) and Trio-interaction (Wang *et al.*, 2016a). We recommend the reader to consult Lau *et al.* (2012) and Jiang *et al.* (2020) for a detailed conceptual and mathematical review of the MJO theories.

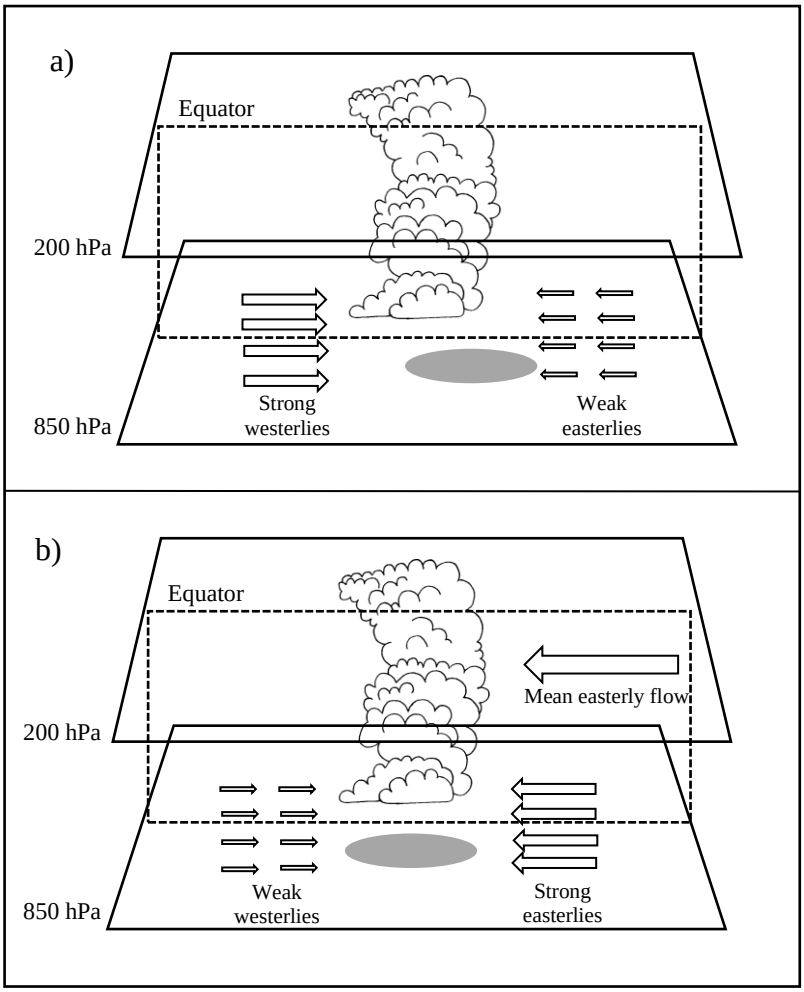

Figure 1.5 Schematic diagrams of the MJO theories a) Wave-CISK and b) wind-induced surface heat exchange (WISHE). The cloud symbol indicates the location of the convective centre. Arrows represent the anomalous winds and the grey oval the region of maximum convergence. Adapted from Flatau *et al.* (1997).

1.2.3 MJO Index

Wheeler and Hendon (2004) introduced a real-time multivariate index to monitor MJO conditions which will be used extensively in this thesis. The Wheeler-Hendon index describes the MJO cycle through the leading components of the multivariate empirical orthogonal function (EOF) analysis of the zonal winds at 850 hPa and 200 hPa and OLR between latitudes 15˚N and 15˚S. The combination of the first two EOFs accounts for 25% of the combined variance of the aforementioned atmospheric fields, while the third component only explains about 6.1% (Figure 1.6).

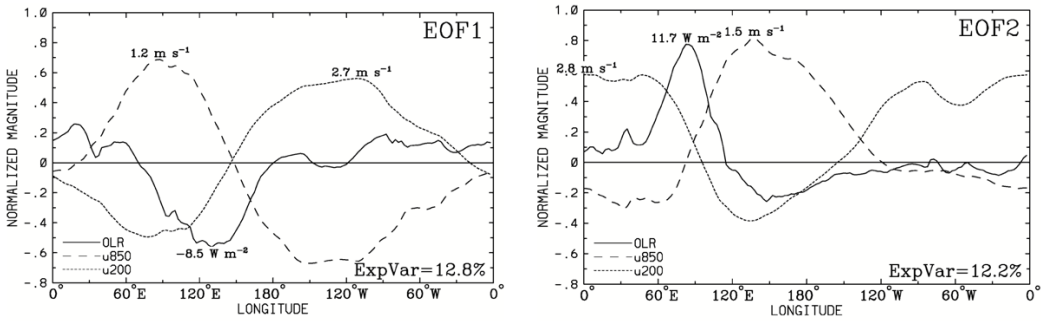

Figure 1.6. The spatial structure of the combined EOFs of OLR and zonal winds at 850hPa and 200 hPa. Fields are equatorially averaged between latitudes 15˚N and 15˚S. Figure reproduced from Wheeler and Hendon (2004).

The evolution of the MJO can be described based on the two principal components (PC) of the two leading EOF modes, referred as the Real-time Multivariate MJO series 1 (RMM1) and 2 (RMM2) (Wheeler and Hendon, 2004). If RMM2 is plotted against RMM1, the eastward progression of MJO enhanced convection is indicated by an anticlockwise rotation. From the amplitude (strength) and the angle of these two RMMs, each MJO event can be classified using the following equations:

$$\text{Amplitude} = \sqrt{(\text{RMM1})^2 + (\text{RMM2})^2} \tag{1.3}$$

$$\text{Angle} = \tan^{-1}\left({}^{\text{RMM2}}/_{\text{RMM1}}\right) \tag{1.4}$$

An MJO event is considered strong if its amplitude is greater than or equal to one, but if its amplitude is less than one it is classified as a weak MJO event (Wheeler and Hendon, 2004). Figure 1.7 shows a diagram that conceptually divides the MJO trajectory in the phase space spanned by RMM1 and RMM2 into eight different phases across the Indian and Pacific Oceans. The trajectory of weak events is confined within the central circle of the diagram. In phases 2 and 3 convection is located over the Indian Ocean, in phases 1 and 8 it occurs in the Western Hemisphere and Africa, in phases 6 and 7 it happens in the Western Pacific, and in phases 4 and 5 it occurs over the Maritime Continent of the Pacific Ocean. In this study, only days with an MJO amplitude larger than one will be considered.

MJOs do not occur in regular temporal patterns. There is the possibility that one MJO event will occur immediately after another, as there may also be extended periods with little or no MJO activity. Matthews (2008) defined MJO primary events as those that are not preceded by an MJO event, and MJO successive events as those that occur in succession.

With these definitions, he classified the MJO events from 1974 to 2005. He found that 40% of the events were primary events. Furthermore, the frequency of the MJO episodes is variable, this oscillatory phenomenon has frequencies in the range of 30 to 90 days (Zhang, 2005).

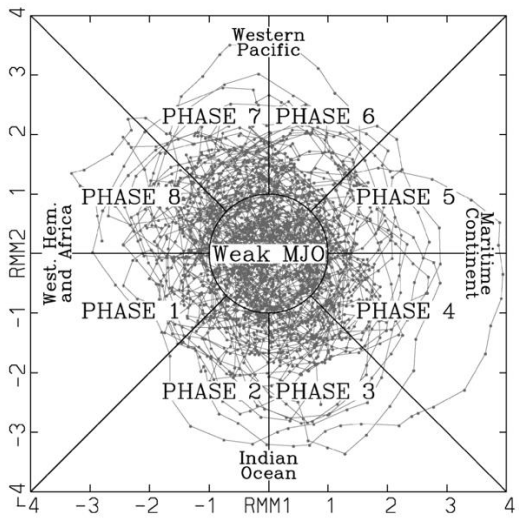

Figure 1.7. Phase space diagram defined by RMM1 and RMM2. RMM1 corresponds to the x-axis and RMM2 corresponds to the y-axis Different geographical locations are labelled indicating where the convection signal of the active MJO is taking place. Also shown is the weak MJO at the centre of the phase space diagram. Figure reproduced from Wheeler and Hendon (2004).

1.2.4 Modelling the MJO

Representing the observed behaviour of the MJO and its teleconnections in numerical models has been a difficult challenge in the last decades. In the 1980s, the first MJO simulations in atmospheric general circulation models (AGCMs) focused on the generation of MJO signals at upper wind levels (Hayashi and Golder, 1986; Lau and Lau, 1986; Swinbank *et al.*, 1988). Although these simulations were able to adequately reproduce the eastward propagation of the MJO, they showed deficiencies emulating other MJO features. And these remain an ongoing problem. In particular, the simulated period is generally too short, and the propagation amplitude is too weak. Models also often fail to adequately simulate the eastward propagation of the convective signal from the Indian Ocean across the Maritime Continent and the seasonality of the oscillation, which is strongest in the boreal winter (Slingo *et al.*, 1996). Hung *et al.* (2013) investigated the ability of 20 models from the Coupled Model Intercomparison Project phase 5 (CMIP5) to represent the MJO. While deficiencies related to the aforementioned problems were reported, significant advances were found compared to previous models.

According to Zhang (2005), ongoing efforts to improve the MJO representation in models should focus mainly on four factors. First, the convective parameterization schemes. For example, a more realistic representation of the MJO has been observed when the parameterisation of cumulus is improved (e.g., Klingaman and Woolnough, 2014). Second, model resolution. Although increasing the model resolution does not necessarily imply better modelling of the MJO (e.g., Liess and Bengtsson, 2004), some research has reported improvements in MJO representation compared to low-resolution experiments (e.g., Crueger *et al.*, 2013). Third, model basic state. Zhang *et al.* (2006) showed that the background state of the mean precipitation, low-level zonal wind, and boundary-layer moisture convergence can affect the accuracy of MJO simulations. Finally, air-sea coupling. The role of the ocean has been theorized in the initiation and maintenance of the MJO (Flatau *et al.*, 1997). The incorporation of the air-sea coupling in MJO simulations has shown improvements in terms of space-time structure, amplitude, a more realistic representation of SSTs and OLR, and strengthening of convection (e.g., Kim *et al.*, 2010; Crueger *et al.*, 2013). However, the effect including air-sea interactions in other experiments was minimal or none (e.g., Hendon, 2000).

1.2.5 The MJO in the Eastern Tropical Pacific Ocean

The MJO is an atmospheric phenomenon characterized by a convection region that propagates from the Indian Ocean to the tropical western Pacific. Although related cloudiness and precipitation tend to dissipate east of the 180° meridian, the MJO wind signal continues to move eastward across the eastern Pacific and South America into the tropical Atlantic (Zhang 2005). For this reason, the number of studies investigating the relationship between the MJO and intraseasonal variability in the eastern tropical Pacific has increased in recent decades.

Barlow and Salstein (2006), using daily rainfall data, observed that precipitation in Mexico and Central America is modulated by the MJO. They reported that in some stations the precipitation was double depending on the phase of the MJO. Maloney *et al.* (2008) found significant SST variations during an MJO event in boreal winter. Furthermore, they also estimated that the MJO is responsible for about 30-40% of the intraseasonal SST variance

in the east warm pool. A relationship has also been found between the MJO and hurricanes and tropical storms in the eastern Pacific (Maloney and Hartmann, 2000).

It has been observed that other variables also undergo modulations due to the MJO, among them surface heat fluxes, boreal summer winds, sea surface height and mixed layer depth (e.g., Zhang, 2001; McPhaden, 2002; Zhang *et al.*, 2009).

1.3 Objective of the thesis

The main objective of this thesis is to study the intraseasonal variability of the eastern Pacific Ocean forced by the MJO, both on the surface and in the subsurface. To this end, an ocean model with prescribed atmospheric fields is used. We note that, since the atmospheric component is imposed, only the ocean response to the MJO, but not air-ocean interactions resulting from the MJO are investigated here.

1.4 Thesis outline

This thesis manuscript is organized as follows:

- Chapter 2, after a brief introduction, (2.1), describes the main characteristics of the Nucleus for European Modelling of the Ocean (NEMO) model, the atmospheric forcing and the sensitivity experiments (2.2). The relevant statistical methods employed are outlined in Section 2.3. Finally, the model validation is provided in Section 2.4.
- Chapter 3 discusses the dominant patterns of intraseasonal variability on the ocean's surface. Surface MJO composites are also introduced and a Granger causality analysis using the MJO index as a predictor is included.
- Chapter 4 examines the vertical distributions of intraseasonal variability of temperature, salinity, and ocean currents. In addition, the MJO cycles of these variables at different latitudes are examined.
- Chapter 5 explores the response of tropical instability waves to the different phases of the MJO.

- Chapter 6 gives a summary and discussion of all key findings from Chapters 3 to 5.
- Finally, conclusions, along with recommendations for future work are outlined in Chapter 7.

Chapter 2

Data and Methods

2.1 Introduction

This chapter provides a description of the main characteristics of the numerical model that has been used here, together with the configurations and simulations that were set-up for the purpose of this study. It also describes the methodology that has been used in order to analyse, validate and evaluate the model output, from the definition and calculation of the various observed anomalies through to the application of elaborate analysis techniques such as Empirical Orthogonal Functions (EOF) (von Storch and Zwiers, 2001) and the Granger causality analysis (Granger, 1969). Finally, the model's general performance is presented and discussed at the end of this chapter.

2.2 The NEMO Model

The Nucleus for European Modelling of the Ocean (NEMO) framework version 3.6 is used in this study. Specifically, the NEMO-OPA ocean model, which is a component of NEMO, simulates the three-dimensional patterns of ocean currents and of the distribution of dynamic tracers, namely temperature and salinity. The reader is referred to the NEMO Ocean Engine User Manual (Madec and NEMO-team, 2016) for full and comprehensive details. However, for report completeness, we described in the following text those aspects of the model that are most relevant for our various discussions contained in subsequent chapters.

The NEMO model solves the three-dimensional ocean primitive equations, which amongst other relatively lesser assumptions, adopt the Boussinesq and hydrostatic approximations. The instantaneous horizontal momentum balance equation for any point within the fluid can be expressed as:

$$\frac{\partial \boldsymbol{u_h}}{\partial t} = -\left((\nabla \times \boldsymbol{u}) \times \boldsymbol{u} + \frac{1}{2}\nabla(\boldsymbol{u}^2)\right)_h - f\,\boldsymbol{k} \times \boldsymbol{u_h} - -\frac{1}{\rho_0}\nabla_h P + F_{\boldsymbol{u}}, \qquad (2.1)$$

where $\boldsymbol{u_h}$ is the horizontal components of the $\boldsymbol{u}$ 3D velocity vector, f = 2Ωsin(φ) is the Coriolis parameter, Ω is the Earth's angular velocity vector at any point, φ is the local latitude, ρ_0 is a constant reference density, P is the hydrostatic pressure and $\boldsymbol{F_u}$ encapsulates all the friction terms.

(2.2) and (2.3) express the time evolution of temperature (T) and salinity (S) at any given point, with F_T and F_S representing the horizontal and vertical turbulent terms for temperature and salinity, respectively.

$$\frac{\partial T}{\partial t} = -u\frac{\partial T}{\partial x} - v\frac{\partial T}{\partial y} - w\frac{\partial T}{\partial z} + F_T, \tag{2.2}$$

$$\frac{\partial S}{\partial t} = -u\frac{\partial S}{\partial x} - v\frac{\partial S}{\partial y} - w\frac{\partial S}{\partial z} + F_S. \tag{2.3}$$

ρ is the in-situ density given by:

$$\rho = \rho(T, S, P). \tag{2.4}$$

The vertical component of the momentum equation is reduced, under the hydrostatic approximation, to a balance between the buoyancy force and the vertical pressure gradient given by:

$$\frac{\partial P}{\partial z} = -\rho g. \tag{2.5}$$

It is assumed that the fluid is incompressible, that is the divergence of the velocity vector is zero, namely,

$$\nabla \cdot \boldsymbol{u} = 0 \tag{2.6}$$

The equations are discretized on an Arakawa three-dimensional orthogonal cuboid C-grid (Figure 2.1) at fixed vertical levels below the water surface (z-coordinates). According to the discretisation, temperature, salinity, density, pressure, and horizontal divergence are each individually defined at the T-points. The three components of the local current are located at u, v, and w points, respectively. The Coriolis acceleration and vorticities are indicated on f-points. For computational efficiency, NEMO solves the free-surface equation and the barotropic velocity equation using the split-explicit free surface formulation proposed by Shchepetkin and McWilliams (2005).

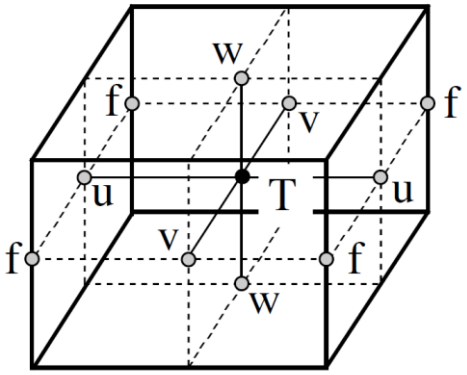

Figure 2.1. Arrangement of the variables and their computation points in an Arakawa C-grid. T defines the scalar points of temperature, salinity, density, pressure and horizontal divergence. u, v and w-points define the horizontal components of the velocity components, and f indicates the relative and planetary vorticities on the f-points (Madec et al., 1997).

The bathymetry dataset that was used in the simulations was the ETOPO1 (Amante and Eakins, 2009) with partial steps (the assumed thickness of the bottom level varies depending on the specific geographic location in the ocean) in order to better represent the seafloor topography. The Total Variance Dissipation (TVD) scheme with the approach of Zalesak (1979), was used for the advection of the tracers. For this study, the lateral diffusion of the moment is parameterized with a Laplacian operator (Redi, 1982). Additionally, the TKE (Turbulent Kinetic Energy) turbulent closure model of Gaspar *et al.* (1990) is implemented for the parametrization of vertical mixing processes. Other important features are summarized in Table 2.1.

Table 2.1. Summary of the main model parameterizations

Variable/Parameterization	**Value**
Horizontal diffusivity for tracers (T, S) Laplacian / iso-neutral	1000 m^2/s
Horizontal eddy diffusivity for tracers (T, S)	1000 m^2/s
Horizontal Laplacian eddy viscosity	20000 m^2/s
Vertical eddy viscosity	1.2×10^{-4} m^2/s
Vertical eddy diffusivity	1.2×10^{-5} m^2/s

2.2.1 The ORCA1_LIM3 configuration

A global ocean model configuration with a general horizontal resolution of 1° in both the longitude and latitude directions, was selected with, however, a local meridional symmetric refinement of up to 1/3° around the Equator being made. This configuration called

ORCA1_LIM3 is the coupling of the Louvain-la-Neuve sea ice model (LIM) with the NEMO ocean engine. It has a total of 42 vertical levels with 13 of these being uniformly spaced in the upper 200 m of the overall body of water. The time step for the integration was approximately 2880 seconds. The salinity and temperature restoration data are taken from the World Ocean Atlas (Locarnini *et al.*, 2013; Zweng *et al.*, 2013). No surface restoring was applied for either the temperature or the salinity. However, in the water column, the restoration coefficient is only made to be zero at the equator, then it has a smooth linear transition in the latitudinal band of 20 degrees either side from these north and south latitudes, where the restoration coefficient reaches the full values. An example of the horizontal distribution of restoring coefficients below the surface, specifically at a depth of 9.55 m, is as shown in Figure 2.2.

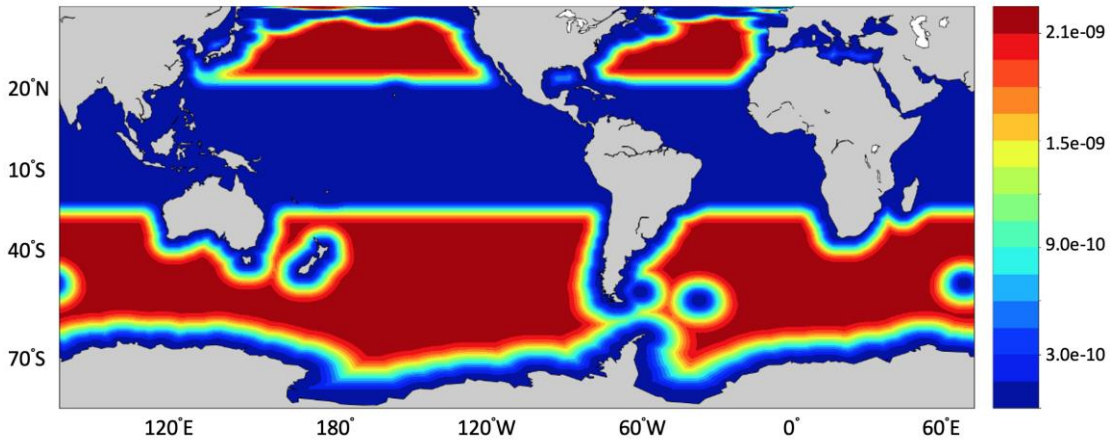

Figure 2.2. Horizontal distribution of restoring coefficients (1/s) at the depth of 9.55 m.

A newly available program option was implemented in the NEMO routine *sbc_fwb*, that controls the freshwater budget, in order to ensure that an unrealistic drift of the global mean sea level upwards trends does not develop. The effective freshwater budget of the model is corrected for the difference between the global sea surface height as estimated by the model and the global monthly mean sea level (GMSL) obtained from the CSIRO web site (http://www.cmar.csiro.au/sealevel/sl_data_cmar.html). The sea level was reconstructed for the period 1870-2015 and is the product of a combination of TOPEX / Poseidon, Jason-1 and the monthly-mean tide gauge data acquired from the Permanent Service for Mean Sea Level (PSMSL) database (Woodworth and Player, 2003) as described in Church and White (2011).

2.2.1.1 CORE forcing

The atmospheric interannual forcing of the ocean model is taken from the Coordinated Ocean-ice Reference Experiments (CORE-II) (Large and Yeager, 2008) dataset version 2, which is available through https://data1.gfdl.noaa.gov/nomads/forms/core/COREv2.html. The CORE forcing was proposed by the Climate Variability and Predictability (CLIVAR) Working Group on Ocean Model Development (WGOMD) with the support of the National Center for Atmospheric Research (NCAR) and the Geophysical Fluid Dynamics Laboratory (GFDL).

The CORE-II data sets include the eight input fields that are required in the model namely: (1) six-hourly values of specific humidity, (2) air temperature, and (3, 4) i-component and j-component of the air wind velocity, with all four values located at a reference height of 10 m above sea level, (5, 6) daily downwelling shortwave and longwave solar radiation and (7, 8) monthly values of solid precipitation and total (liquid + solid) precipitation, with all being summarized in the following table:

Table 2.2. Atmospheric variables provided by CORE II.

Variable	Frequency
Specific humidity	6 h
Air temperature	6 h
i-component of the air velocity	6 h
j-component of the air velocity	6 h
Downwelling shortwave radiation	1 day
Downwelling longwave radiation	1 day
Solid precipitation	1 month
Total precipitation.	1 month

CORE provides for two types of forcing namely: Interannual Forcing (IAF) and Normal Year Forcing (NYF) (Large and Yeager, 2004; Large and Yeager, 2008). The IAF is a forcing that varies from year to year, while the NYF is an individual annual cycle that is derived from the recorded climatological conditions over 43 years of elapsed time (1958–2000) interannual forcing. It is intended that after the application of NYF that the resulting fluxes may represent the climatological observed fluxes from the closest possible way, that

is to say, in order to remove the effects of interannual variability. For the formulation of NYF Large and Yeager (2004) established some criteria, such as NYF has a smooth transition from the end to the beginning of the year, in order to avoid jumps between years when a year is repeated.

It is important to realise that NEMO is by definition an ocean-sea ice model only. Therefore, any modes of variability resulting from interactions between the atmosphere and the ocean, such as the ENSO, cannot be properly represented in the model, where only the oceanic response to the atmospheric signatures of such modes of variability can be simulated by the model. At present, however, it is initially not clear whether air-sea fluxes or internal ocean processes can trigger the MJO (Moum *et al.*, 2016), therefore, it is not entirely inappropriate to investigate MJO's impact on the ocean with an uncoupled model. Thus, we next investigated how the MJO is represented in the atmospheric forcing.

The evaluation was carried out for the period 1975-2009 for which the MJO index (as explained in Chapter 1) is available. The various atmospheric variables that were evaluated were those having a frequency equal to or smaller than 24 hours since the MJO index is itself a daily event. Composites were constructed from the daily anomalies of each field. The anomalies were obtained as the differences between the value of the variable on a specific day and the average value of the variable for that same calendar day over 35 years elapsed time period. For example, the anomaly for January 17, 1990, was calculated taking as a comparison parameter the average value of all January 17 dates between 1975 to 2009. The results are presented by eight phases of the MJO and these should be read in the various figures in an anticlockwise direction following the numbering sequence. The number of days for each MJO phase with amplitudes that are greater than 1 are summarized in Table 2.3.

Table 2.3. Number of days for MJO composite analysis from 1st January 1975 to 31st December 2009.

MJO phase	**1**	**2**	**3**	**4**	**5**	**6**	**7**	**8**	**MJO all**	**% days on MJO**
Number of days	1015	1028	916	889	1024	981	931	924	7708	61%

For example, the zonal winds anomalies for each of the eight phases of the MJO cycle are shown in Figure 2.3. They exhibit a dipole structure with eastward propagation which begins in the Indian Ocean and moves to the tropical Pacific region. For example, it is observed that negative anomalies begin to appear during phases 7 and 8 in the Indian Ocean. These negative anomalies then move through the tropical Pacific, that is, the strength of the prevailing trade winds in the east increases. On the other hand, positive anomalies begin to be seen in phases 3 and 4 in the Indian Pacific and these move eastward during the rest of the phases (5→2). The variability range of the zonal wind anomalies is approximately 5 m/s, which represents a 30% change if it is compared to the time-mean zonal wind state (not shown here). The repetitive nature of the MJO cycle can be recognized in the similarities that are presented by phases 1 and 8 and it is for this reason that the sets of eight figures of this section the MJO phases are deliberately presented with an anticlockwise pattern.

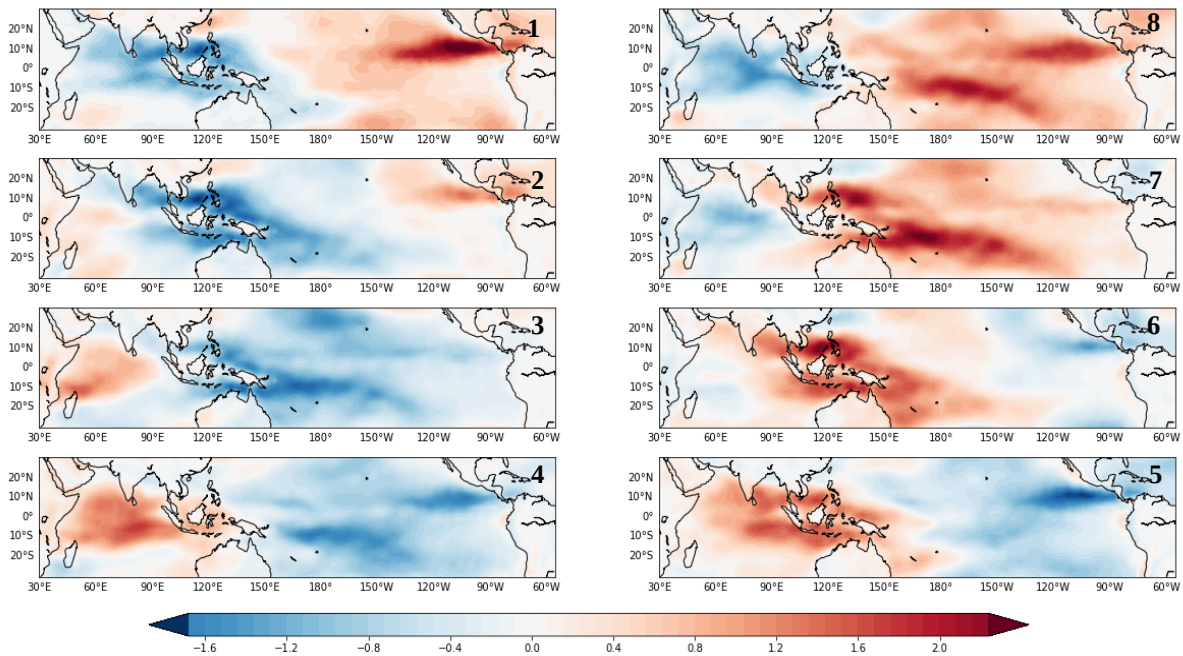

Figure 2.3. MJO composites of zonal winds anomalies (m/s).

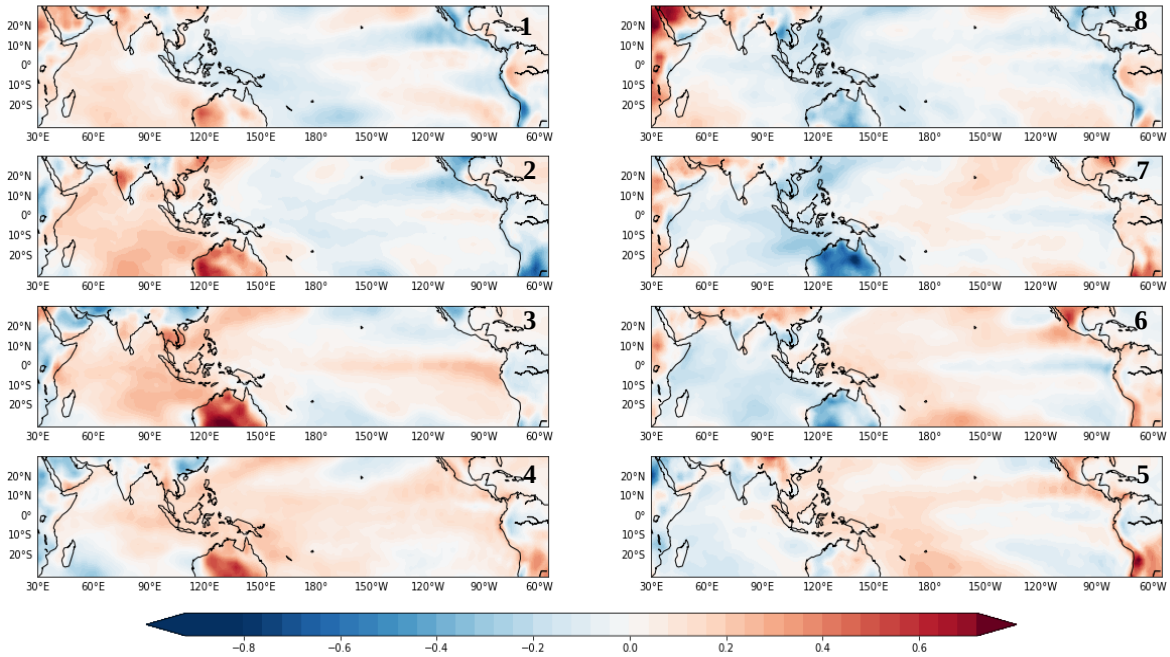

Figure 2.4. MJO composites of meridional winds anomalies (m/s).

From Figure 2.4 where the meridional winds anomalies are illustrated, a clear differentiation can be made between phases 1, 2, 3, and 4 which present positive anomalies in the Indian Ocean and with phases 5, 6, 7, and 8 which present negative anomalies in the same region. In the tropical Pacific region, wind convergence or divergence patterns can be observed as a result of the position and strength of the ITCZ.

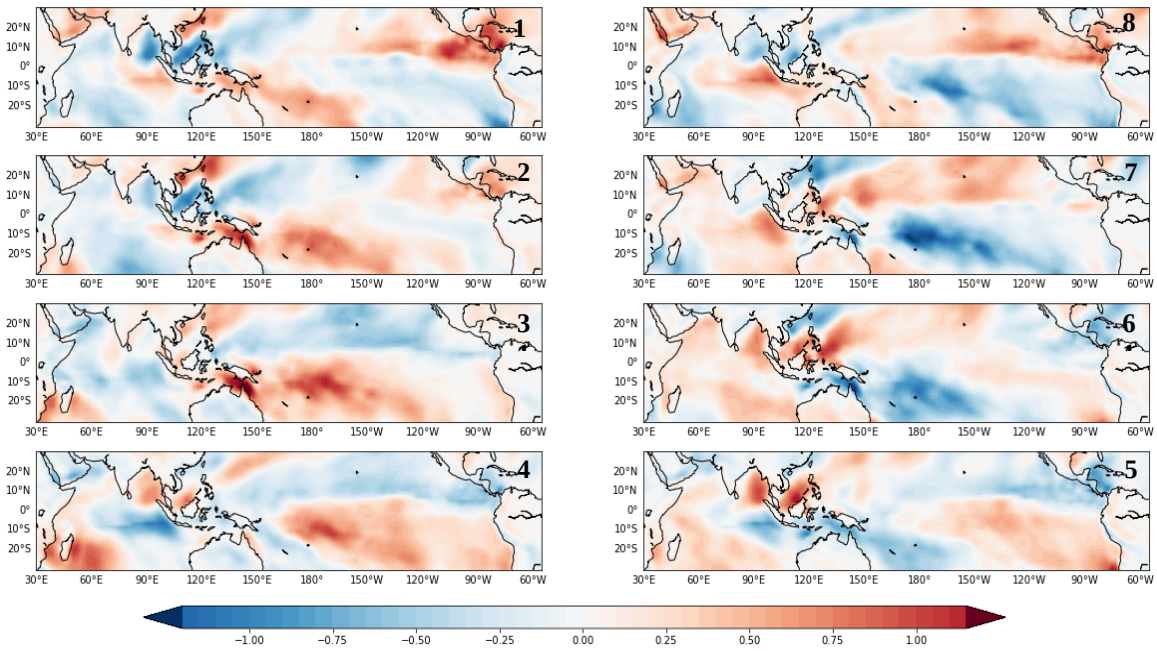

Figure 2.5. MJO composites of air temperature anomalies (˚C).

The MJO patterns of the anomalies in air temperature at 10 m above sea level and of humidity in the air also at 10 m above sea level are shown in Figures 2.5 and 2.6, respectively. In the tropical Pacific region, it is observed that positive (negative) temperature anomalies are associated with positive (negative) anomalies in specific humidity. It is what is to be expected since warm air holds more water vapour than does cold air. Peak to peak temperature variations during the MJO life cycle are approximately 2°C, while the humidity is about 0.001 kg/kg over the tropical Pacific region.

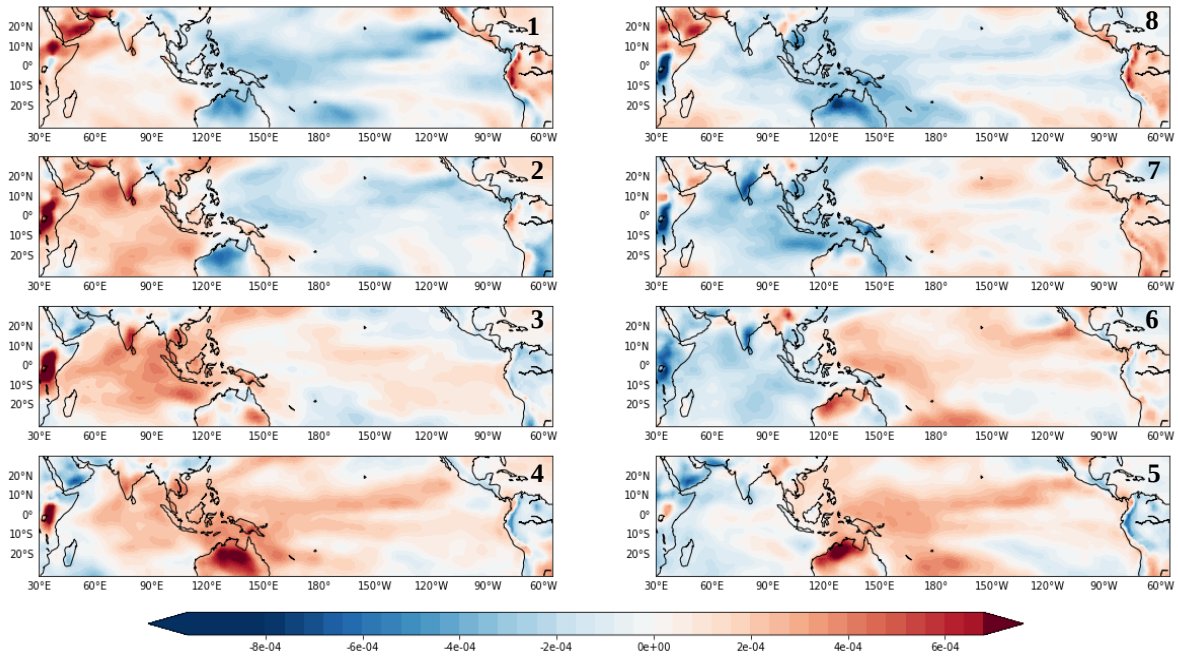

Figure 2.6. MJO composites of specific air humidity anomalies (kg/kg).

Similarly, cyclic behaviour is observed both in the Indian Ocean and in the Pacific Ocean in terms of the incoming shortwave radiation anomalies and of the incoming longwave radiation anomalies, shown in Figures 2.7 and 2.8, respectively. Both MJO composites are consistent with the previously noted humidity anomalies, that is to say, that if there is an excess of water vapour in the air then there will be positive incoming longwave radiation anomalies and consequently negative anomalies of incoming shortwave radiation. The latter shows a wide range of variability of approximately 40 W/m^2, while the variability range of the incoming longwave radiation anomalies is approximately 8 W/m^2.

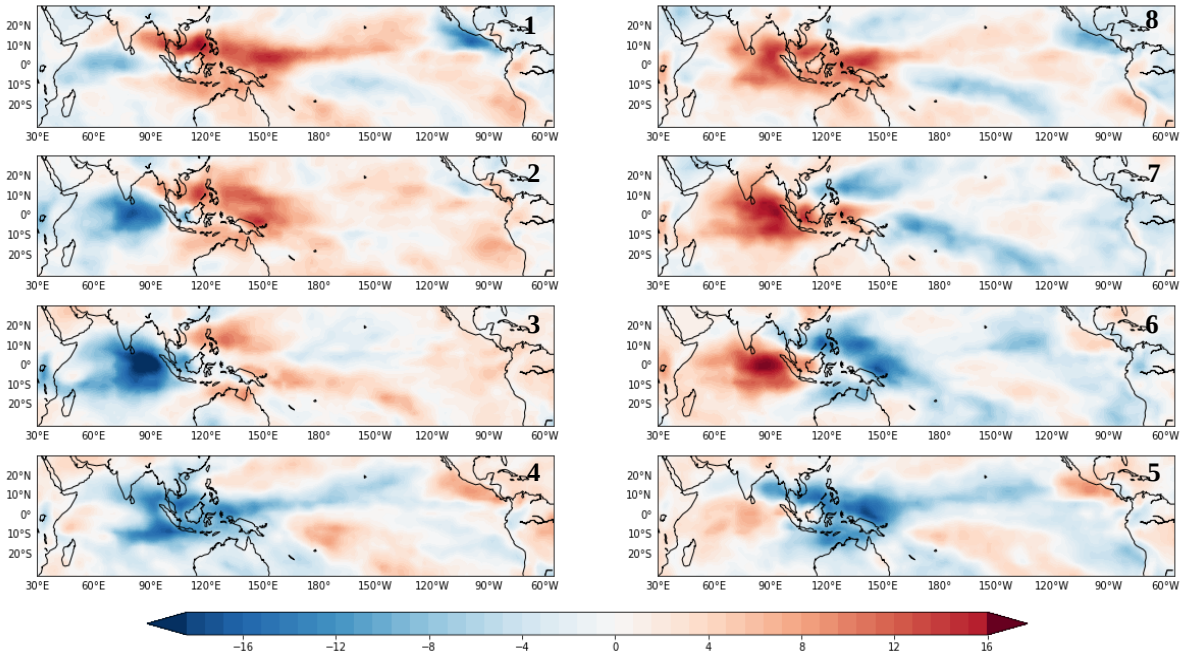

Figure 2.7. MJO composites of incoming shortwave radiation anomalies (W/m^2).

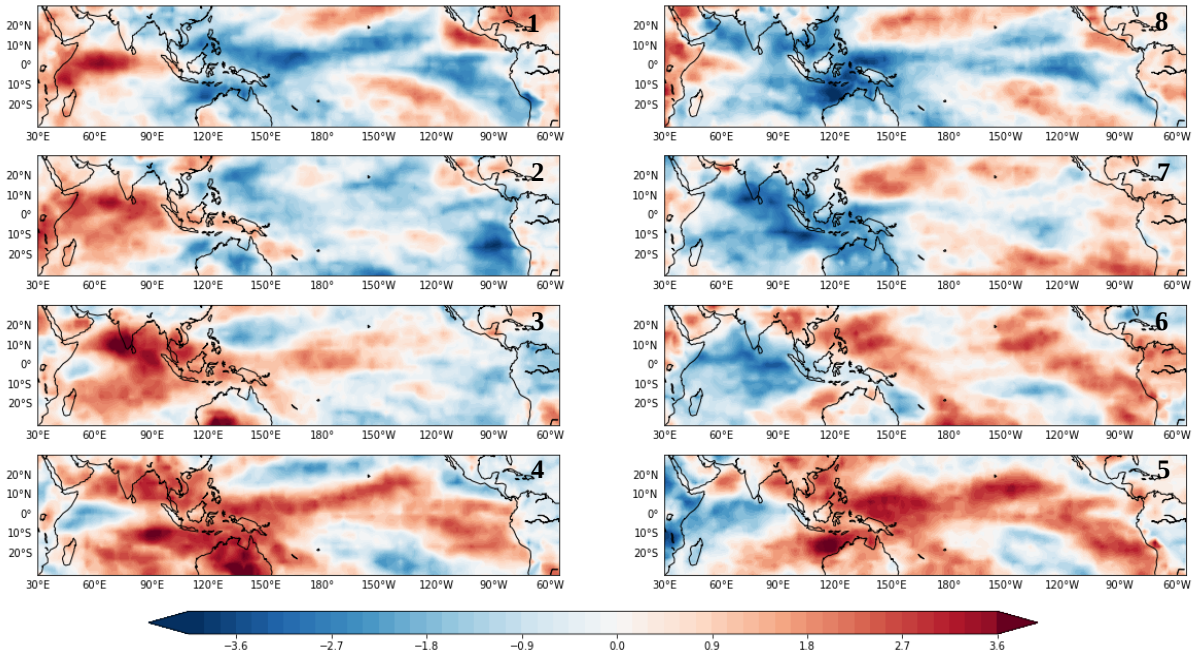

Figure 2.8. MJO composites of incoming longwave radiation anomalies (W/m^2).

In conclusion, the CORE atmospheric forcing represents well the MJO conditions and the corresponding MJO phases in the equatorial/tropical Pacific region providing confidence in employing the CORE forcing in this study.

2.2.2 Numerical experiments

The results of this thesis are based on the output of two spin-up simulations and six additional experiments, four of which are sensitivity integrations. The first experiment, labelled NN5, covers a continuous data collection period of 42 years with the repeat CORE-II NYF. This forcing has a seasonal cycle but any signature of MJOs has been largely removed by the use of long-term historical data averaging. The second main experiment, labelled II5, was carried out using the CORE-II full interannual atmospheric varying forcing and spans the years 1948 to 1989. Integrations labelled NN5 and II5 were carried out in order to bring the simulated global ocean data to spin up states to be used subsequently as the initial conditions for further numerical experiments.

In the following chapters, the results of the six simulations are used to analyse the various modes of intra-annual variability specifically in the Equatorial and Tropical Pacific regions and their interrelations. The principal differences between one simulation run and another resides in the particular atmospheric forcing approach that is used in each simulation, and these are summarized for clarify in Table 2.4 and further outlined below. The first letter in the simulation name indicates atmospheric forcing excluding winds and the second letter refers to wind forcing.

- **NN** This experiment starts from the restart files of the last year of NN5. The atmospheric forcing is the normal year forcing, NYF, as in NN5, and the simulation spans 11 consecutive years from 1990 to 2000.

- **II** In this experiment, the system behaviour is forced by the interannual varying atmospheric forcing, IAF, as in II5. This run is initiated from the restart output for 1989 from II5 and is integrated for an elapsed period of 11 consecutive years from 1990 to 2000.

- **IN** This experiment is essentially the same as II except for the wind forcing, which is taken from the CORE II normal year forcing.

- **NI** This is the same as NN except that the wind stress is taken from the IAF dataset between 1990 and 2000. All other atmospheric boundary conditions are the same as in the NYF.

- **NN+** Both this run, and the following run used NYF in which the winds, however, are modified as being boundary conditions. The near surface wind was arbitrarily increased by 50%, between latitudes 30°N and 30°S, and then gradually returning to NYF values north and south of these latitudes. The run was started from the restart files of the last year of NN5. After a 15-year spin-up, the experiment was continued for another 11 years of integration and these 11 years are used for the subsequent analyses.

- **NN-** Similar to NN+ but in which the wind speed was arbitrarily decreased by 50% in the tropical regions.

Table 2.4. Characteristics of the numerical experiments.

Name	Atmospheric forcing excluding winds	Wind forcing
NN	**N**YF	**N**YF
II	**I**AF	**I**AF
IN	**I**AF	**N**YF
NI	**N**YF	**I**AF
NN+	**N**YF	**N**YF +50%
NN-	**N**YF	**N**YF -50%

2.3 Statistics

The ocean is a highly complex and variable system, where many processes interact with each other simultaneously and on different scales of both time and space. Therefore, characterizing the intraseasonal variations of each of the different climatic variables requires working with quite large amounts of both spatial and temporal information. Different statistical techniques are thus used not only to examine and control data quality but also to identify complex patterns and to synthesize information on climate variability. In the following subsections, an overview is provided for each of the principal statistical techniques that have been applied throughout this study.

2.3.1 Anomaly calculations

An anomaly is the difference between the value of a specific variable at a given instance in time and a time-averaged value of the same variable. In our experiments, we have stored daily values of all variables of interest and have calculated a daily climatology over the eleven years of interest to us. Daily anomalies are thus calculated with reference to this daily climatology.

2.3.2 Filtering data

As this work focuses on specific intraseasonal variability, a time filter has been applied to select signals with frequencies that are only within the intraseasonal band. A bandpass zero-phase Butterworth filter (Butterworth, 1930) was thus implemented which retains only signals having periods that are between 10 and 120 days.

2.3.3 Wavelet analysis

Wavelet Transform is a technique that extracts information on the temporal evolution of the energy (essentially, it is the time integral of the square of the specific signal) that is associated with different frequencies. In this time-frequency based approach, a wavelet analysis permits the identification of the dominant modes of variability and of the temporal variation of these modes (Torrence and Compo, 1998). For this study, the so-called Morlet wavelet was used as the Mother Wavelet. The Morlet wavelet applies a Gaussian-modulated sinusoid form:

$$\psi_0 = \pi^{-1/4} e^{i\omega_0 t} e^{-t^2/2}. \quad (2.7)$$

where ψ_0 is the wavelet value at non-dimensional time t and ω_0 is the wavenumber.

2.3.4 Empirical orthogonal function analysis

The widely used method of Principal Components (PC)-Empirical Orthogonal Functions (EOF) (von Storch and Zwiers, 2001) was employed in order to find the patterns of variability that can be obtained through the decomposition of the covariance matrix of a dataset into orthogonal modes. These individual modes contain unique information that is

not correlated with that of other modes. The original data can then be, with reasonable accuracy, reconstructed from the combination of a certain number of modes that collectively explains up to a certain acceptable percentage of the variance of the specific variable of concern (von Storch and Frankignoul, 1998).

2.3.5 Composite technique

The composite technique consists in the estimation of the average of a variable for certain days that meet a certain condition. In this work, the MJO index of Wheeler and Hendon (2004) is used for the calculation of MJO composites, and only those days with an amplitude equal to or greater than one will be used in the average. Details of the number of days for each of the eight MJO phases will be provided in each chapter.

2.3.6 Pattern Correlation

Pattern correlation coefficients are used in the chapter that follows to intercompare the EOFs of key variables and the corresponding MJO phase composites. The pattern correlation coefficient is nothing by the Pearson's linear correlation (the covariance of two variables, divided by the product of their standard deviations) between the values of two variables with the same spatial domain, for example, two charts representing the latitude-longitude distribution of the variables. These charts can correspond to different depths or different times. Correlation coefficients are in the range of -1 to 1, being ± 1 when that data are perfectly correlated and zero, when no correlation exist between the variables (Yoo and Cho, 2018).

2.3.7 Granger Causality

Another way to study the interactions between variables is through causality (relation of cause and effect). The fact that two variables are correlated does not necessarily imply that there is causality between them. There are several tests of causality including Granger (1969), Geweke *et al.* (1983), or Toda and Yamamoto (1995). For this study, we will use the Granger causality test. Granger (1969) was the first to propose a causality test, stating that x is Granger causing y if the prediction of y improves when the information from x is used. Granger causality can be mathematically expressed as being the combination of two

regressions, that are the autoregression of y (2.8) and the inclusion of lagged values of x to the autoregression of y (2.9):

$$y_t = c_0 + c_1 y_{t-1} + c_2 y_{t-2} + \cdots + c_s y_{t-s} + e_t. \quad (2.8)$$

$$y_t = \alpha_0 + \alpha_1 y_{t-1} + \cdots + \alpha_s y_{t-s} + \beta_1 x_{t-1} + \cdots + \beta_s x_{t-s} + e_t. \quad (2.9)$$

where y_t is the t-th observation on the dependent variable y, x_t denotes the t-th observation on the independent variable x. In (2.8) c_0 is the intercept and $c_1, c_2, \dots, c_s$ are lagged coefficients of y_t while in (2.9) α_0 is the intercept and $\alpha_1, \dots, \alpha_s$ and $\beta_1, \dots, \beta_s$ are lagged coefficients of y_t and x_t respectively. (2.8) is known as being the "baseline model" and (2.9) as being the "full model". It is said that x Granger causes y if when comparing both models, the full model explains significantly more variance than does the baseline autoregressive model.

The results of sections 3.5 and 4.5 follow this methodology. Firstly, a Granger causality analysis was carried out by using the RMM indices to linearly predict the selected, filtered oceanic variables and to determine in which areas of the domain there is a possible causal relation between the MJO and the variable response. The model coefficients in (2.8) and (2.9) are determined through a vector autoregressive model (VAR) analysis, and the lag s, was selected by employing the Schwarz, or Bayesian, criterion (Schwarz, 1978).

2.3.8 Distributed lag model

The distributed lag model is a dynamic model that shows the linear relationship between a specified dependent variable and one or more independent variables over a period of time. (2.10) shows a distributed lag model with an independent variable:

$$y_t = \alpha + \beta_0 x_t + \beta_1 x_{t-1} + \cdots + \beta_s x_{t-s} + e_t. \quad (2.10)$$

where y_t is the t-th observation on the dependent variable y, x_t denotes the t-th observation on the independent variable x, α is the intercept and $\beta_0, \beta_1, \dots, \beta_s$ are the current and lagged coefficients of x_t. In Section 3.5 and 4.5, a distributed lag model was assessed using the

RMM indices as independent variables and the same lag s used in the Granger Causality analysis. The variance was calculated for each point of the grid omitting lag zero.

2.4 General model performance

In order to assess the ability of the overall mathematical model to reproduce the observed spatial and temporal patterns of the selected key ocean variables, three different data sets, namely, G-GLORS, ORAS4, and SODA, as described in Table 2.5, have been taken into account. There is a variety of other currently available reanalysis data, however, the aforementioned datasets were carefully selected for this evaluation procedure because each of them contains the following important variables: sea surface height (SSH), salinity, temperature, zonal current and meridional current in the tropical Pacific region.

Table 2.5. Description of the reanalysis data products used in the validation of the model.

Product	**Description**
C-GLORS	The CMCC Global Ocean Reanalysis System (Storto and Masina, 2016) integrates both in situ and satellite ocean observations into a general circulation ocean model (NEMO3.2) for the period 1980-2015. The reanalysis is performed at 1/4° spatial resolution and 50 vertical levels. C-GLORS uses the European Centre for Medium-Range Weather Forecasts (ECMWF) ERA-Interim (Dee *et al.*, 2011) as forcing and the three dimensional variational (3DVAR) scheme named OceanVar (Dobricic and Pinardi, 2008) as the data assimilation system.
ORAS4	The ECMWF Ocean ReAnalysis System (Balmaseda *et al.*, 2013) spans the period 1958 to 2015. The version 3.0 of the NEMO model is operated with a resolution of 1°x 1° and 42 levels in the vertical. ORAS4 is forced by direct surface fluxes data provided by ERA40 reanalysis (Uppala *et al.*, 2005) and ERA-Interim reanalysis. The data assimilation system used in ORAS4 is the NEMOVAR (Mogensen *et al.*, 2012).
SODA	The Simple Ocean Data Assimilation (Carton and Giese, 2008) version 2.2.4 covers a period from 1958 to 2009. The SODA is based on the Parallel Ocean Program physics (Smith *et al.*, 1992) version 2.0.1, with a horizontal resolution of 0.4°x 0.25° and 40 vertical levels. The atmospheric data set was taken from 20CRv2 (Whitaker *et al.*, 2004; Compo *et al.*, 2006; Compo *et al.*, 2011) as surface boundary conditions in the ocean model.

Model validation that was performed for the simulation is called II, as noted earlier during the integration period (1990-2000). Figure 2.9 (a, b, c, d) displays the time mean of SSH

from the model and associated the reanalysis products. The general geographical patterns of SSH are qualitative well captured by the model and this indirectly reflects a realistic system of simulated equatorial zonal currents. However, there are some quantitative differences. In the right-hand panel of the figure, which shows the differences between the model and the reanalysis data, we observe positive values of up to 0.5 m for the Pacific Ocean. In particular, the difference is greater to the north of the equator in a latitudinal band around 10°N. Any biases in terms of SSH representation could have several reasons. These could be due to differences in wind forcing between the CORE dataset (the forcing used in the model NEMO) and those that are used to conduct the reanalyses. For example, Griffies *et al.* (2014) assessed the regional sea level in CORE II simulations between 1993-2007. In his study, a rise in sea level was observed in the western Pacific region and a fall in the eastern Pacific region associated with wind trends.

A cursory validation of the simulated mean sea surface temperature (SST) and of the vertical structure temperature is made in Figures 2.10 and 2.11. The modelled SST and SST from reanalysis are generally coherent in magnitude and their spatial patterns are qualitatively similar. Nevertheless, there is a cold bias in the equatorial cold tongue region of the NEMO model, and it extends further westward than in the reanalysis. This is possibly caused by the observation that the coastal upwelling along the Peruvian coast is overestimated in the model by around 1.5°C. This bias has been related to excessively strong trade winds (Vannière *et al.*, 2013).

Despite these discrepancies, the main temperature patterns of the region were successfully simulated in the model, notably the equatorial temperature front and in the intrusion of cold waters through the Humboldt current, suggesting that the model is able to capture SST patterns with some degree of realism. Regarding the vertical temperature distribution in the equator, the model agrees better with the structure of SODA than with that of ORAS4. However, we could not obtain non-surface data for C-GLORS. The left panels of Figure 2.11 show that the simulated thermocline is shallower and sharper than is the thermocline from the ORA reanalysis.

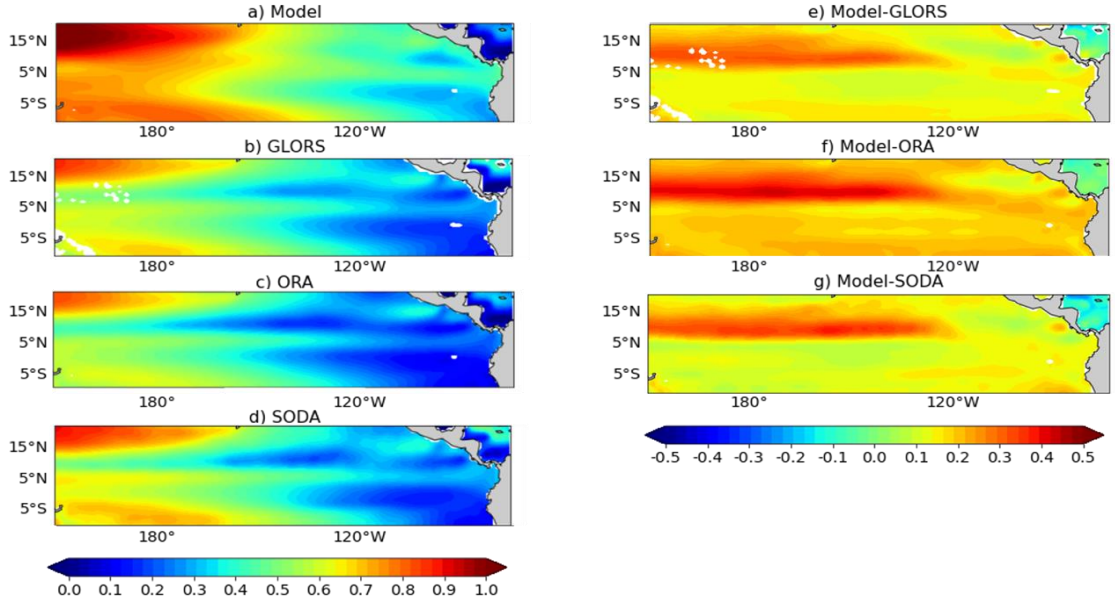

Figure 2.9. Left panels show time mean of sea surface height (m) between 1990 to 2000 for a) model, b) GLORS data, c) ORA data and d) SODA data. Right panels show the differences between model and reanalysis from e) GLORS data, f) ORA data and g) SODA data.

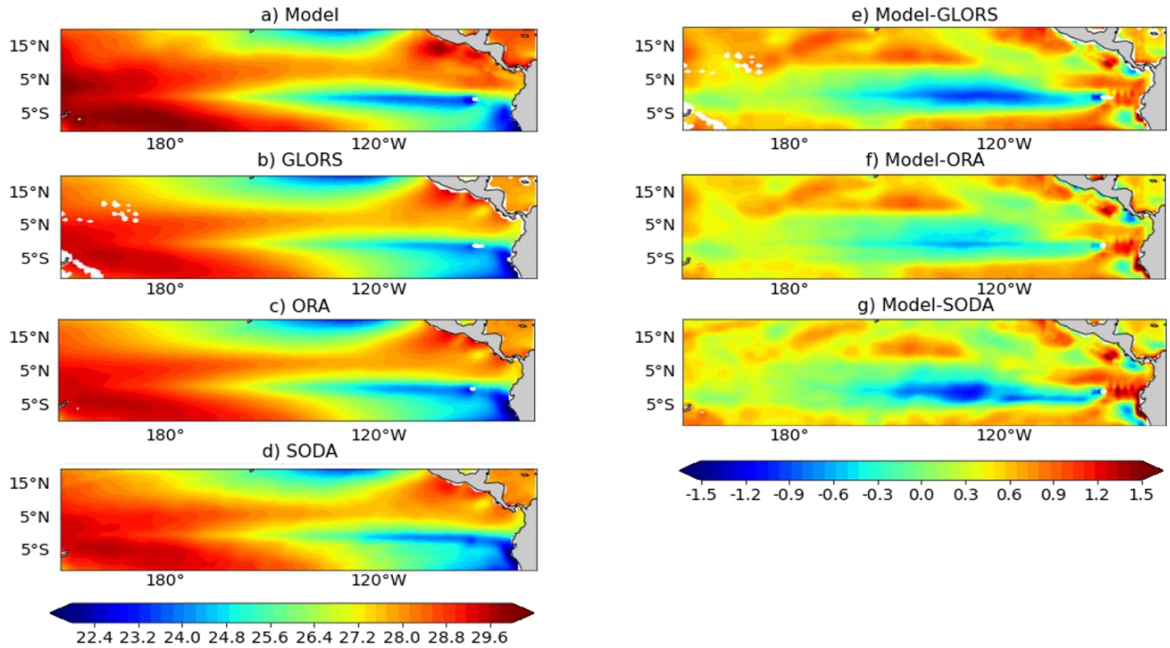

Figure 2.10. Left panels show time mean of sea surface temperature (˚C) between 1990 to 2000 for a) model, b) GLORS data, c) ORA data and d) SODA data. Right panels show the differences between model and reanalysis from e) GLORS data, f) ORA data and g) SODA data.

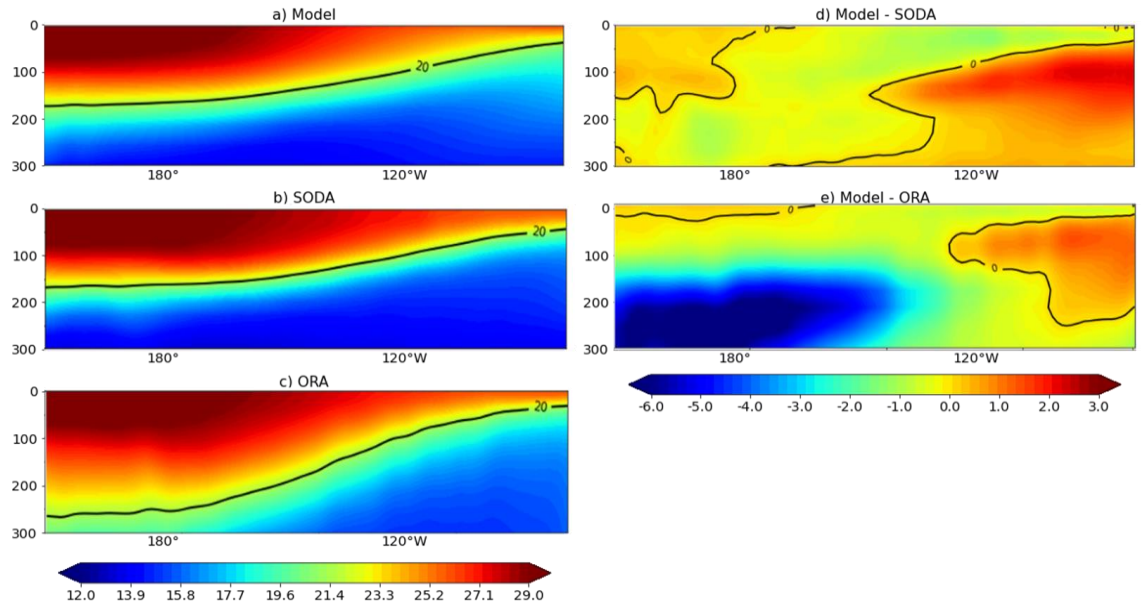

Figure 2.11. Left panels show vertical sections of time mean of temperature (˚C) averaged over the latitudinal band 2˚S – 2˚N between 1990 to 2000 for a) model, b) SODA data and c) ORA data. The bold line denotes the 20˚C isotherm. Right panels show the differences between model and reanalysis from d) SODA data and f) ORA data, the bold line denotes 0˚C.

The sea surface salinity (SSS) patterns are shown in Figure 2.12 (a, b, c, d). These are qualitatively and quantitatively consistent between the model and the reanalysis data. The greatest salinity disparities occur in the Panama Basin region (Figure 2.12 e, f, g) since the surface salinity in this region is controlled by the incoming freshwater flows that are associated with the position of the intertropical convergence zone, i.e., regions of high precipitation rates and that are usually poorly represented in many climatic models (Lin, 2007). In addition, the contribution of river input is around 30% of the total contribution of the freshwater inflow into the Panama Basin (Alory *et al.*, 2012), however, the runoff used for this region contains large data gaps, since the record length is only 20 to 40 years (Dai *et al.*, 2009).

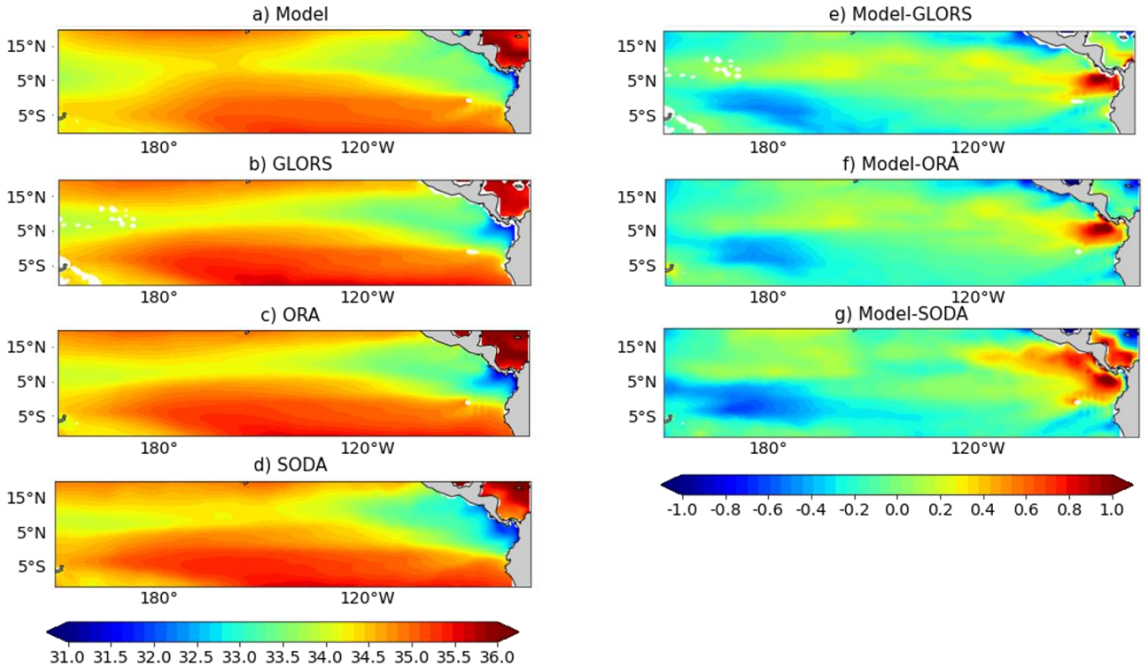

Figure 2.12. Left panels show time mean of sea surface salinity (psu) between 1990 to 2000 for a) model, b) GLORS data, c) ORA data and d) SODA data. Right panels show the differences between model and reanalysis from e) GLORS data, f) ORA data and g) SODA data.

One further comparison between the model and reanalysis products is given in Figure 2.13, which displays the sea surface zonal currents in the model and in the reanalyses. The main difference is in the representation of the North Equatorial Current (NEC), which in the model is underestimated by 0.3 m/s compared to the GLORS data. When comparing with the ORA or the SODA data, the differences increase to an approximate underestimate of 0.4 m/s and 0.6 m/s respectively. It is likely that the biases are largely due to the use of different sources of wind forcing and in their resolution. Zhou et al. (2019), when comparing different wind sources (NCEP/NCAR, ERA-Interim, CCMP, and QSCAT), concluded that the confidence of a realistic ocean circulation simulation in the tropical Pacific is linked to the wind forcing that is used.

The mean vertical distribution of the equatorial currents from both the model and the reanalyses are shown in Figure 2.14. The flow structure for the model agrees quite well with both reanalyses. For example, the eastward Equatorial Undercurrent (EUC) is centred at the equator at a depth of 80 m. However, the modelled EUC is too weak. The two main branches of the South Equatorial Current (SEC) are located at about to 3°N and 3°S in the model as for the SODA data and the ORA data. The core of the North Equatorial

Countercurrent (NECC) is located slightly further to the north and is weaker than in the reanalysis. The Equatorial Subsurface Countercurrent, or the Tsuchiya Jets, are not fully resolved in the model.

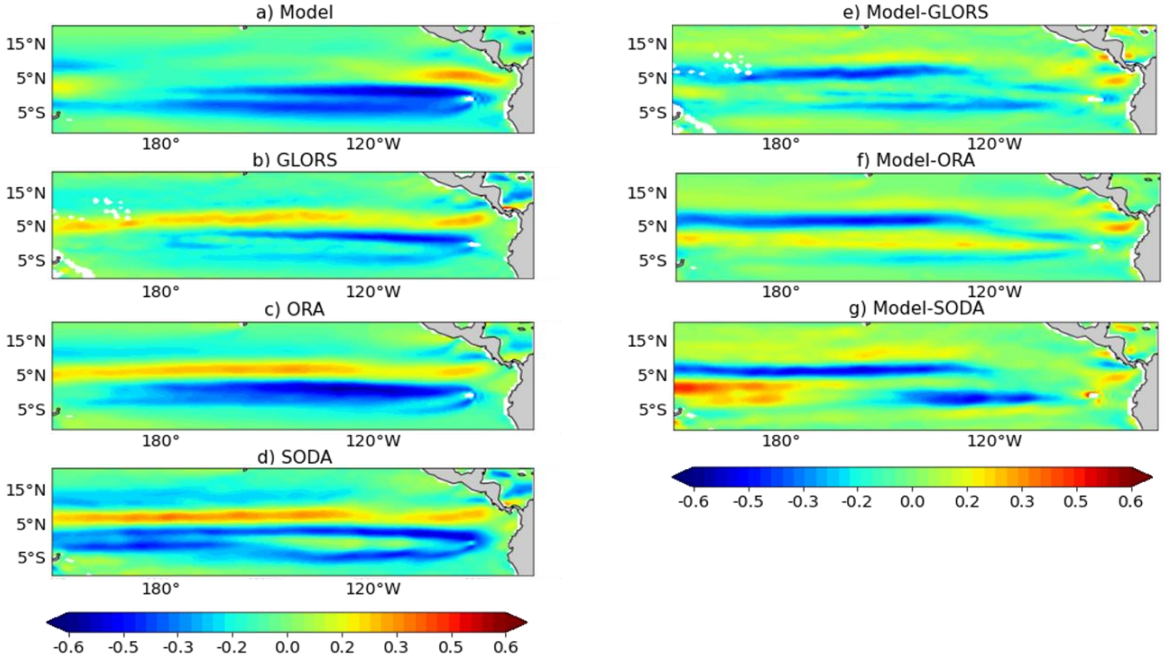

Figure 2.13. Left panels show time mean sea surface zonal current (m/s) between 1990 to 2000 for a) model, b) GLORS data, c) ORA data and d) SODA data. Right panels show the differences between model and reanalysis from e) GLORS data, f) ORA data and g) SODA data.

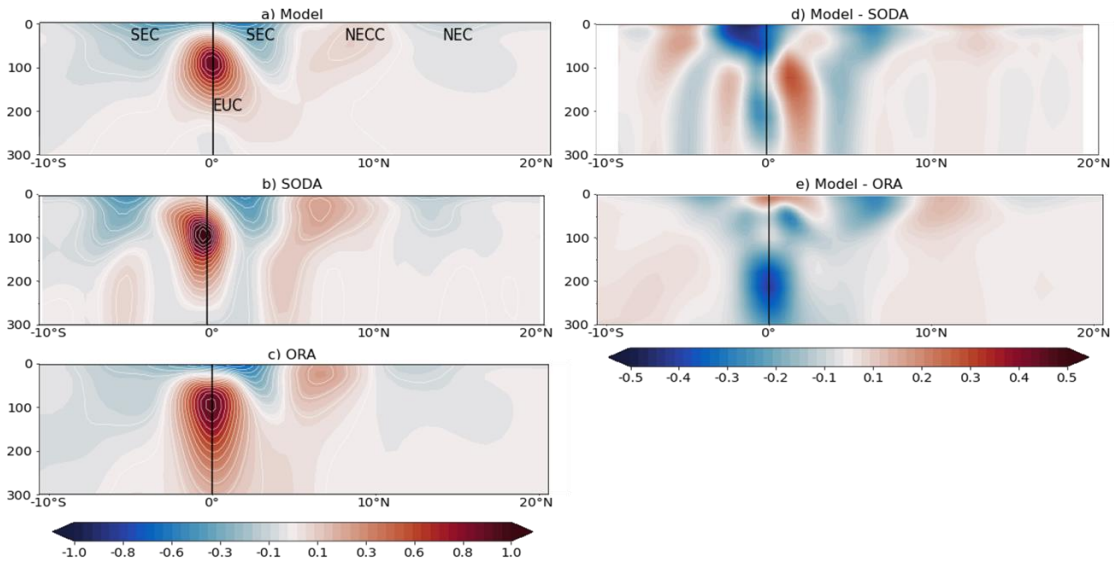

Figure 2.14. Left panels show vertical sections of time mean of equatorial currents (m/s, eastward in red and westward in blue) at 125˚W between 1990 to 2000 for a) model, b) SODA data and c) ORA data. The bold line denotes the equator. Right panels show the difference between model and reanalysis from d) SODA data and e) ORA data bold line denotes the equator.

Finally, the validation process is completed by comparing surface meridional currents as modelled with the sea surface meridional currents from reanalysis data (Figure 2.15). Although all the left panels show a similar divergence pattern and therefore an upwelling front that is close to the equator, a significant discrepancy is evident in the SEC regions. The possible cause could be related to wind forcing. It is to be noted that the calculations of the Sverdrup and Ekman transports show significant differences when using various wind sources with different resolutions (Zhou *et al.*, 2019).

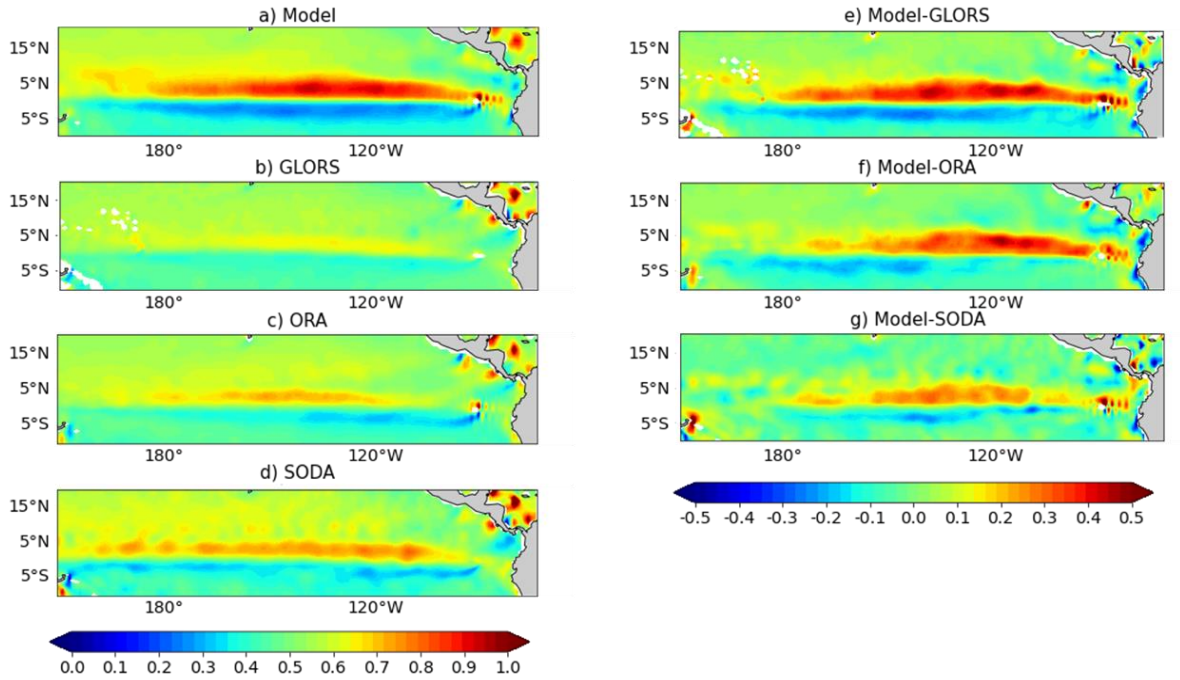

Figure 2.15. Left panels show time mean of surface meridional current (m/s) between 1990 to 2000 for a) model, b) GLORS data, c) ORA data and d) SODA data. Right panels show the difference between model and reanalysis from e) GLORS data, f) ORA data and g) SODA data.

In summary, the mathematical model and the corresponding reanalysis data agree and suggests that the ORCA1-LIM3 simulations capture the leading features of the hydrography and the ocean dynamics in the Tropical Pacific region. Thus, the model can be employed with a good measure of confidence for this research.

Chapter 3

The Madden-Julian Oscillation's impact on the upper ocean in the central and eastern regions of the tropical Pacific

3.1 Introduction

The physical behaviour of the central and eastern tropical Pacific region is characterized by a complex variety of multi-scale interacting processes. Therefore, an understanding of the intraseasonal variability in oceanic surface fluxes is a critical step towards improving our ability to make more reliable mid-range ocean weather and ocean climate forecasts for the region. In the past few years, there have been a number of studies that have sought to describe the ocean's response to the Madden-Julian Oscillation (MJO) (e.g., Miyakawa *et al.*, 2017; Pariyar *et al.*, 2019)

The main goal of this chapter is to explore numerically the response of the ocean surface in the Central and Eastern Tropical Pacific regions to MJO forcing. In order to carry out this analysis, eight key surface model outputs, which illustrate the basic oceanography of the Tropical Pacific, have been chosen. The surface heat flux response is provided by two fields, namely, the non-solar part of the heat flux (Q_{ns}), that is, the sum of the latent heat, the sensible heat and the net longwave radiation, and the solar, shortwave part of the heat flux (Q_{sr}). The surface freshwater budget is described by both evaporation and precipitation components. The remaining fields are sea surface temperature (SST), sea surface salinity (SSS), sea surface height (SSH) and surface zonal currents. The other components of the ocean currents are not discussed in this chapter. Meridional currents and vertical currents will be discussed in detail in Chapter 4.

The analysis is carried out in the rectangular model subdomain between 150°E and 74°W and between 10°S to 20°N (Figure 3.1). The chapter is organized as follows: the identification of intraseasonal variability and its relation to the total variance for each variable as presented in Section 3.2. Section 3.3 shows the dominant patterns of the intraseasonal variability. Effects of the MJO on the high frequency variabilities of the upper

ocean are quantified in Section 3.4. In section 3.5, the Granger causality and lagged linear methods have been applied to investigate the interactions between the MJO index and ocean surface. A summary of the various results is given in Section 3.6.

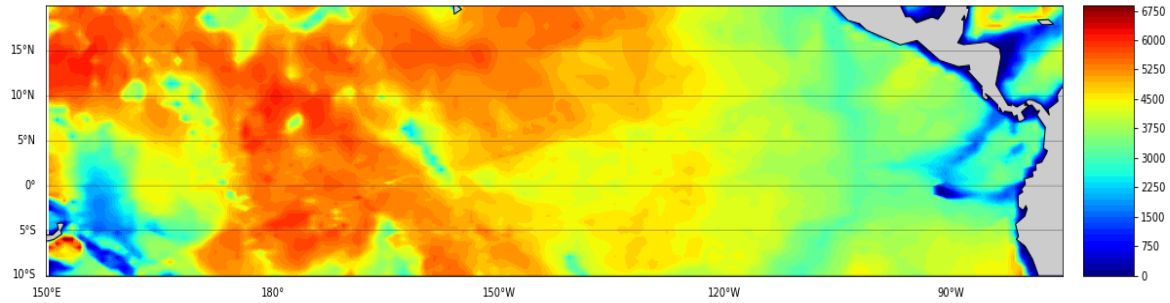

Figure 3.1. Bathymetry (in metres) of the tropical Pacific region (data from ETOPO1 (Amante and Eakins, 2009)).

3.2 Identification of intraseasonal variability

It is appropriate to first examine the contribution to the intraseasonal variability of each of the different variables with respect to the corresponding total variability. For this, the following methodology has been applied. The mean, the annual cycle, and any linear trend were first removed for each variable of the II simulation between the years 1990-2000. Then the variance was calculated, and this is called the total variance. Next, a 10-120-day bandpass Butterworth filter (as described earlier in Chapter 2) was applied to the detrended fields and the variance of the filtered time series was determined to quantify the intraseasonal variability.

Figure 3.2 shows the total variance and the percentage that the intraseasonal variance is of the total variance for each of the eight variables. For example, the intraseasonal variance of the SSH (Figure 3.2a) can be as high as 60% of the total variance. The region of the greatest variance of the unfiltered data is located near 10°S and between 180° and 150°E. In contrast, the highest intraseasonal variance occurs in the central Pacific region a few degrees north of the equator. This enhanced intraseasonal variability is believed to be caused by the occurrence of the tropical instabilities waves (TIWs) (Zhang *et al.*, 2009).

The maximum intraseasonal SST variance percentages can be seen to be located in three regions (Figure 3.2b), with a first maximum being in the western Pacific, where several

areas collectively represent about 40-60% of the total variance. Another maximum region (~ 40%) is concentrated near to the Pacific coasts of southern Mexico and Central America, on the so-called Costa Rica Dome. A third maximum variation, between 40-60%, occurs on the cold tongue, a zonal band with relatively cold surface waters, centred at the equator (Fiedler and Talley, 2006). Two possible sources for this intraseasonal variability are equatorial Kelvin waves originated in the western Pacific (Zhang, 2001) and the tropical instability waves (Legeckis, 1977). These same mechanisms can explain the high intraseasonal variances of the SSS and of the surface zonal current (Figure 3.2c and d) that explain up to 60% in each case.

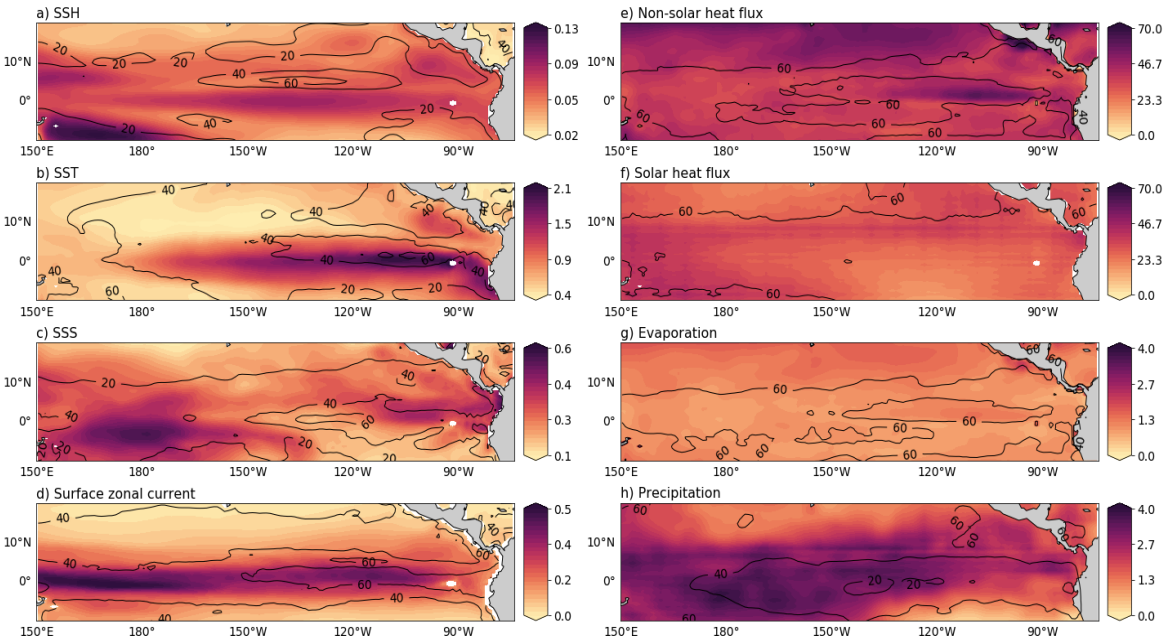

Figure 3.2. Shaded regions denote the total variance of a field and the black contours reflect the intraseasonal (10-120 day) variance as a percent of the total variance of **a)** sea surface height (m), **b)** sea surface temperature (˚C), **c)** sea surface salinity (psu), **d)** sea surface zonal current (m/s), **e)** non-solar heat flux (W/m^2), **f)** solar heat flux (W/m^2), **g)** evaporation (mm/day) and **h)** precipitation (mm/day) where each is expressed in units of standard deviation. Percentage contour interval is 20%.

The ratio of the intraseasonal non-solar heat flux variance to the total variance is displayed in Figure 3.2e. Although the non-solar surface heat flux is the combination of several heat components, as explained above, clearly the regions where there are the highest values of relative intraseasonal variance (60%) coincide with those having the highest evaporation values (Figure 3.2g). According to Grodsky *et al.* (2009), the intraseasonal variability of the latent heat in the Pacific Ocean, which is proportional to evaporation, is due to both

wind and humidity disturbances that are caused by the MJO. In contrast, the intraseasonal variance of incoming shortwave radiation follows the same general pattern of the annual mean in the region, being maximum in a region that lies north of 10°N.

The chart of the variance of the intraseasonal precipitation (Figure 3.2h) shows a good agreement with the position of the Intertropical Convergence Zone (ITCZ) band of high rainfall. Specifically, up to 40% of the total precipitation variance is observed to be occurring in the intraseasonal time scale. This is in agreement with the observation of Raymond *et al.* (2006) that the MJO has a strong influence on ITCZ variability. In the forthcoming subsections, the dominant patterns of intraseasonal variability within the ocean surface are reviewed and discussed.

3.3 Dominant patterns and spectral analysis of intraseasonal variability

This section presents the results of the empirical orthogonal function (EOF) analysis of each of the eight bandpass filtered variables introduced above. The two orthogonal modes of each variable with the highest variance were selected. We present and discuss the spatial EOF patterns and, for the two associated principal components, a wavelet analysis is performed to identify the main periodicities of the corresponding time series.

3.3.1 Sea surface height intraseasonal variability

The EOF analysis was conducted on 10-120-day bandpass filtered daily SSH anomalies spanning the period 1990-2000. The first two EOF modes are shown in Figure 3.3. According to the criterion of North *et al.* (1982), the EOF1 and EOF2 modes are found to be statistically distinguishable from each other. The leading mode explains 9.5% of the total intraseasonal variance of the SSH over the chosen domain. The high spatial amplitude region matches with the local maximum total variance over the equator that is seen in Figure 3.2a. The second EOF accounts for a slightly smaller value of 8.9% of the total intraseasonal variance. The maximum correlation between the two PCs (r=0.64) is observed when PC1 leads PC2 by 13 days. Therefore, the anomalies that are ascribed to EOF2 could be associated with those of EOF1 after an elapsed period of 13 days. These two EOFs thus appear to capture the slow eastward propagation of the intraseasonal SSH anomalies along the equator associated with trapped Kelvin waves (Rydbeck *et al.*, 2019).

These first two modes explain more than 80% of the overall intraseasonal variance in some areas of the equatorial Pacific (Figure 3.4).

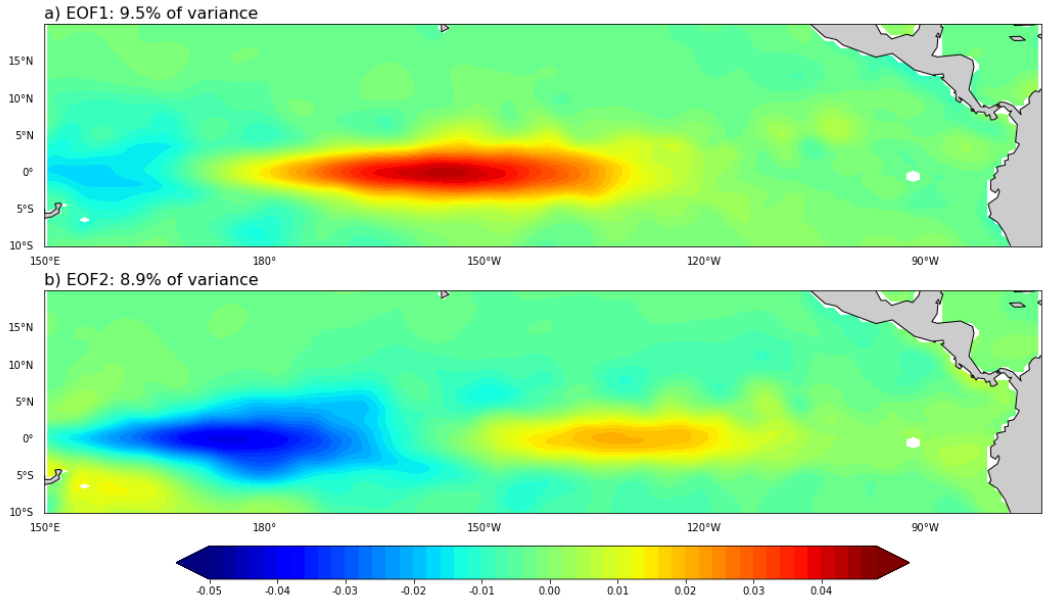

Figure 3.3. First (a) and second (b) leading EOF modes of SSH intraseasonal anomalies. The percentage of variance explained by each EOF mode is given at the top of each panel.

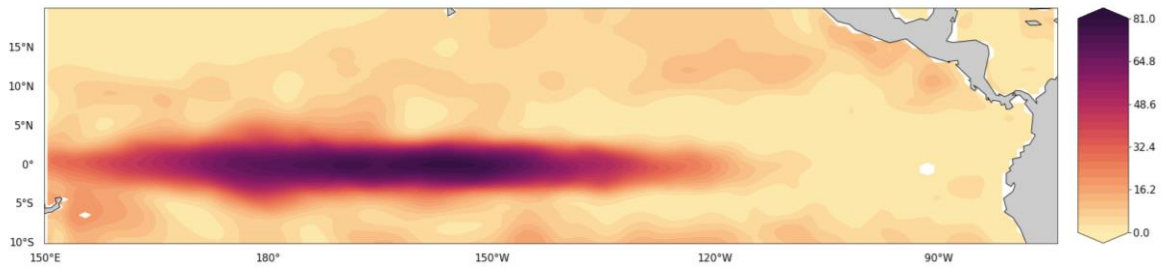

Figure 3.4. The fraction of the intraseasonal variance (%) explained by the two leading EOF modes of SSH anomalies.

A wavelet analysis has been carried out on each of the two corresponding PCs. Figure 3.5c reveals that the variance of both PCs is significant within the period interval from 46 to 91 days. In both wavelet spectrums (Figure 3.5a-b), this broad intraseasonal spectral peak is present throughout the chosen study period, with, however, greater intensity occurring in the years 1992 and 1997, both of which were El Niño years. The relationship between intraseasonal Kelvin waves and ENSO has been well documented in the literature (e.g., Benestad *et al.*, 2002; Mosquera-Vásquez *et al.*, 2014; Rydbeck *et al.*, 2019). For example,

Benestad *et al.* (2002) indicated that the intraseasonal Kelvin waves amplitudes and their phase velocity are larger during El Niño events compared to La Niña episodes.

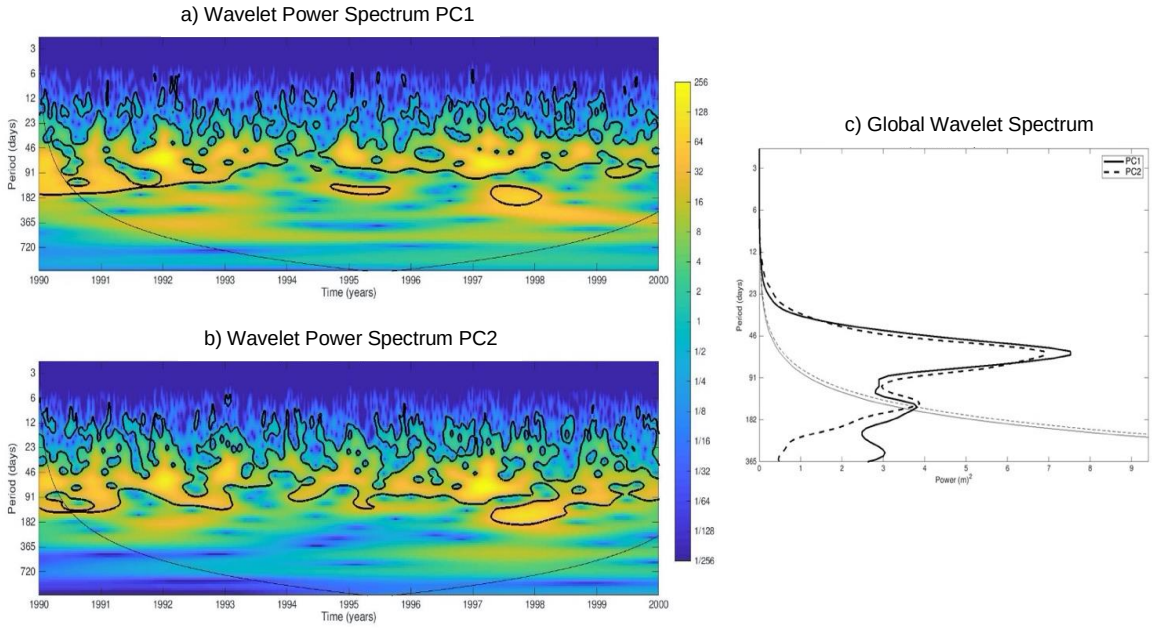

Figure 3.5. Wavelet analysis of PC1 and PC2 of the SSH intraseasonal anomalies. Panels (a) and (b) show the corresponding wavelet power spectrums. The thick black contours indicate the 95% confidence level, and the thin black line indicates the border of the cone of influence (all data below this line are unreliable). Panel (c) shows the global wavelet spectrums. The thin lines represent the 95% confidence level.

3.3.2 Sea surface temperature intraseasonal variability

The two leading modes of SST filtered anomalies were isolated by EOF analysis. These modes explain 12.2% and 5.5% respectively of the intraseasonal variance (Figure 3.6a and b). They are non-degenerate according to the North *et al.* (1982)'s criterion referred to earlier. The maximum lag correlation between both PCs is very weak around 0.17 at lag 8, which suggests that, unlike the first two EOFs of the SSH, these are two truly different modes of variability. Both EOFs are effectively confined to the eastern tropical Pacific and centred mostly on the equator. However, EOF 2 also has a large component in the area of the Costa Rica Dome. These two EOFs map well onto the patterns of greatest intraseasonal variability shown in Figure 3.2b, and they collectively represent up to 62% of the total intraseasonal variance along the eastern equatorial region (Figure 3.7). These patterns of SST intraseasonal variability in the eastern Pacific region have been related to Kelvin waves (e.g., McPhaden, 2002). Zhang (2001) observed modifications in vertical

temperature gradients due to changes in the thermocline depth associated with the oceanic Kelvin waves.

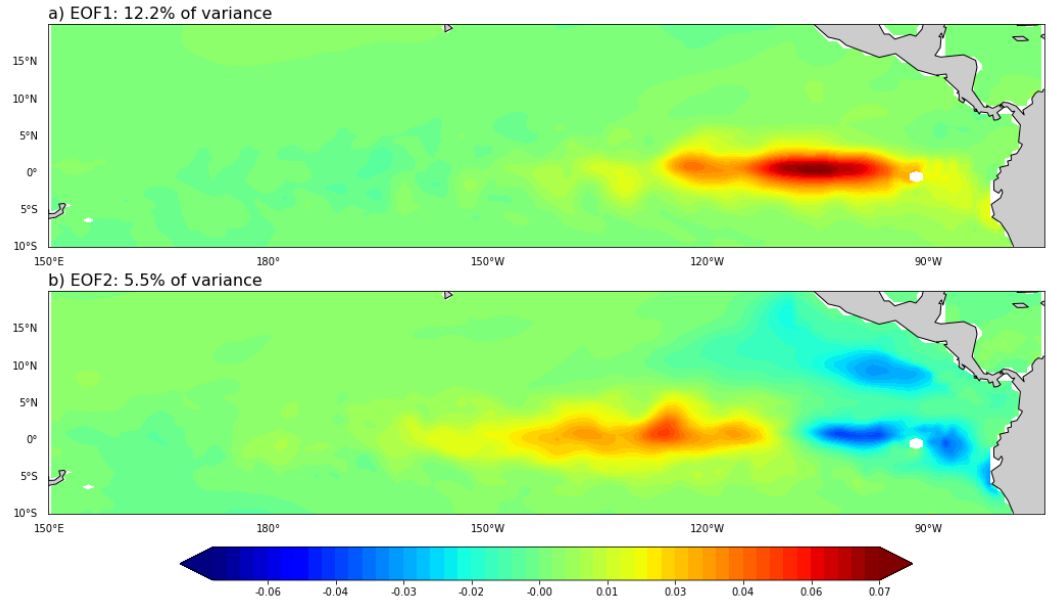

Figure 3.6. First (a) and second (b) leading EOF modes of SST intraseasonal anomalies. The percentage of variance explained by each EOF mode is given at the top of each panel.

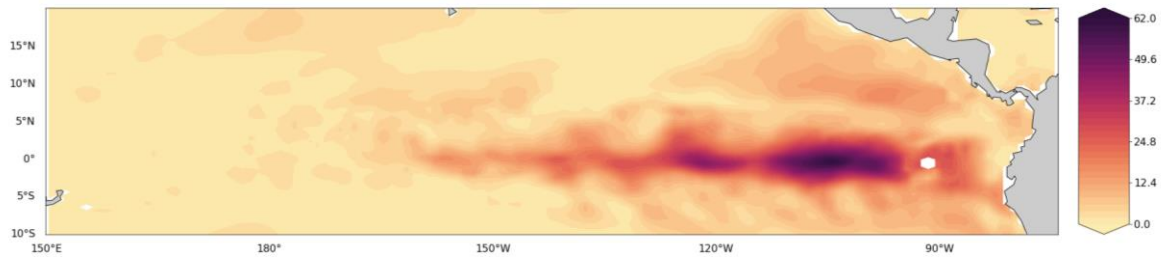

Figure 3.7. The fraction of the intraseasonal variance (%) explained by the two leading EOF modes of the SST anomalies.

Wavelet analysis of PC1 and PC2 (Figure 3.8) reveals some intermittency in the signals. For example, during late 1997 and early 1998. The spectral energy analysis shows a wider frequency range for PC1 (between 45 to 70 days) than for PC2, the latter exhibiting a well-defined peak a period of around 70 days.

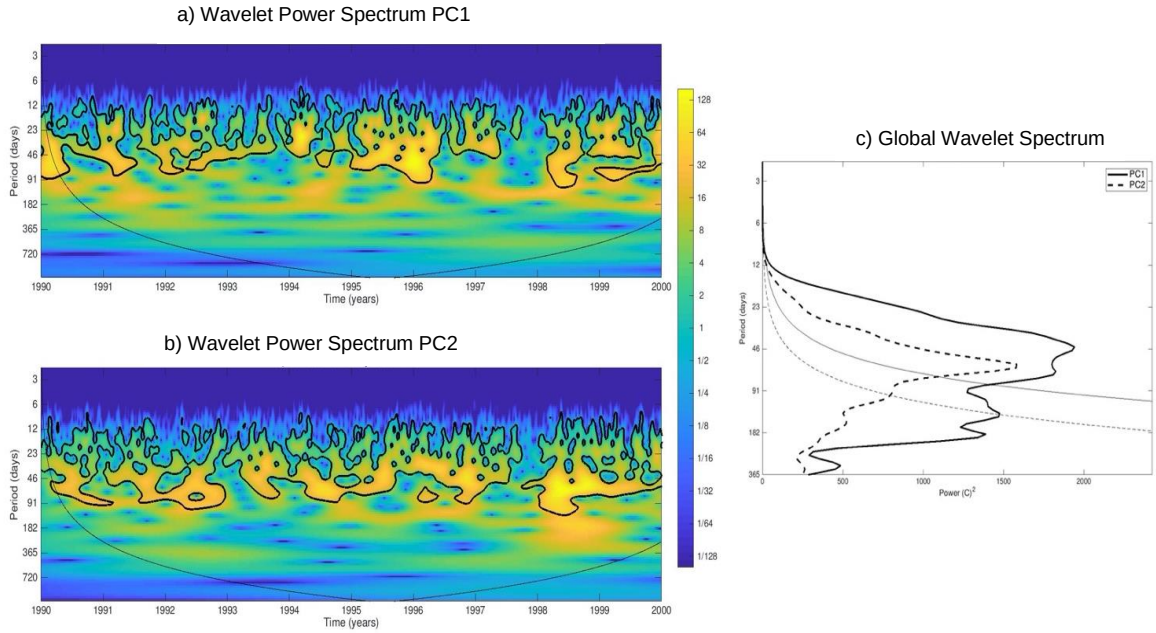

Figure 3.8. Wavelet analysis of PC1 and PC2 of the SST intraseasonal anomalies. Panels (a) and (b) show the corresponding wavelet power spectrums. The thick black contours indicate the 95% confidence level, and the thin black line indicates the border of the cone of influence (all data below this line are unreliable). Panel (c) shows the global wavelet spectrums. The thin lines represent the 95% confidence level.

3.3.3 Sea surface salinity intraseasonal variability

Figure 3.9 displays the first two EOF modes of the intraseasonal SSS variability, which together account for 9.6% of the total intraseasonal variance. These two modes are well separated statistically (according to the North *et al.* (1982) rule), the lag correlation of their respective PCs being only 0.16 at lag 43. EOF1 is very similar to the first EOF mode of SST, with a large footprint on the eastern equatorial region west of the Galapagos Archipelago (Figure 3.6a). Matthews *et al.* (2010) identified that SSS variability in the equatorial eastern Pacific is related to anomalous horizontal zonal advection. The EOF2 mode largest values are also located in the equatorial band but are centred further west, near the dateline. These two modes collectively represent up to 65% of the total amount of intraseasonal variance in these regions (Figure 3.10).

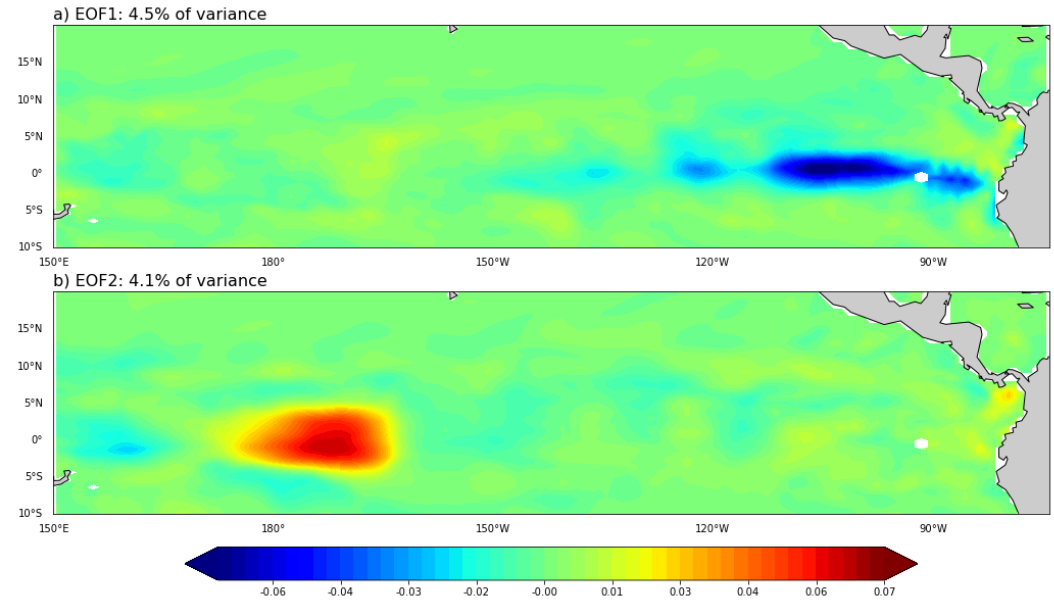

Figure 3.9. First (a) and second (b) leading EOF modes of SSS intraseasonal anomalies. The percentage of variance explained by each EOF mode is given at the top of each panel.

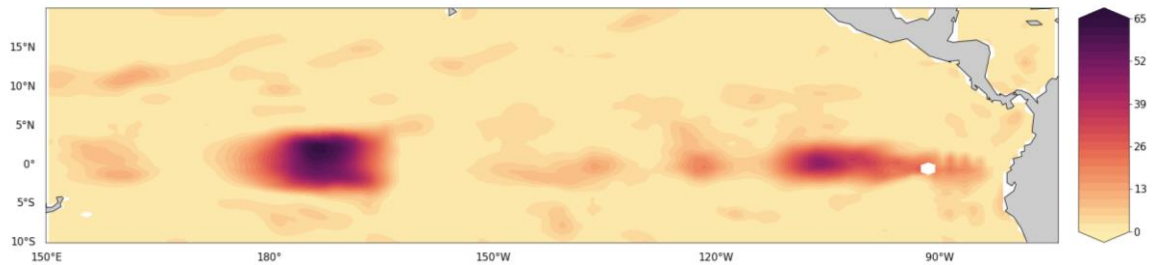

Figure 3.10. The fraction of the intraseasonal variance (%) explained by the two leading EOF modes of the SSS anomalies.

Figure 3.11 shows the wavelet power spectra during the period 1990-2000 for the two PCs. It can be observed, in particular for PC1, that four periods, albeit not equal, present an SSS variance that is above the corresponding values in other periods. For PC1 the signal that is located between 1998 and 1999 particularly stands out. However, for PC2 the power spectrum is fairly continuous throughout the overall study period. The global spectrum diagram (Figure 3.11c) identifies the main periodicity for PC2 between 90-days and 150-days elapsed time. Similarly, the presence of two other oscillations can be seen with periods that are of the order of 46 to 90 days for PC1.

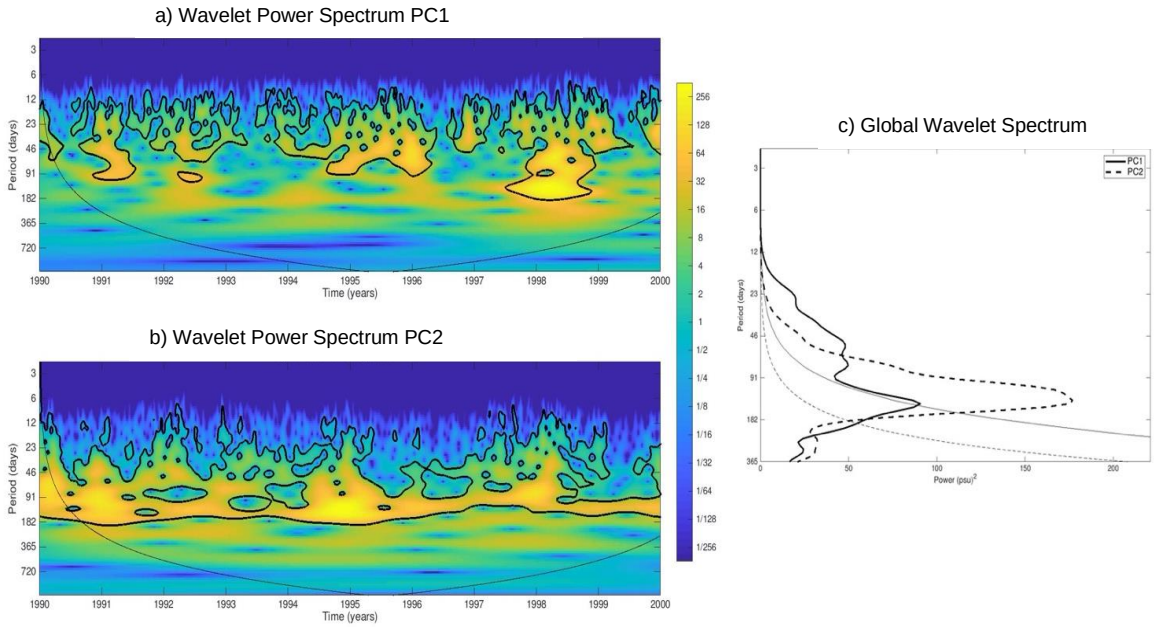

Figure 3.11. Wavelet analysis of PC1 and PC2 of the SSS intraseasonal anomalies. Panels (a) and (b) show the corresponding wavelet power spectrums. The thick black contours indicate the 95% confidence level, and the thin black line indicates the border of the cone of influence (all data below this line are unreliable). Panel (c) shows the global wavelet spectrums. The thin lines represent the 95% confidence level.

3.3.4 Sea surface zonal velocity intraseasonal variability

Figure 3.12 shows the spatial structures of the first two EOF modes of the sea surface zonal velocity anomalies for the same elapsed time period (1990-2000). The North *et al.* (1982) criterion indicates that these first two modes are statistically distinguishable from each other. Together they explain about 16% of the overall intraseasonal variance in the region. The lag correlation between the two PCs is at a maximum (r=0.61) when PC1 tends to lead PC2 by about 14 days, therefore, both represent a signal that propagates eastward. The maximum lag correlation value between the PC1 (PC2) of surface zonal velocity and the PC1 (PC2) of SSH is 0.72 (0.71) at lag 11 (9) days, which suggests that the variability of both fields could be caused by the same phenomenon.

The maximum variance of these two modes occurs in a band that is located between 150°E and 130°W and centred on the equator. The high variability in the eastern and central Pacific zonal currents is related to zonal winds forced by the MJO (Zhang *et al.*, 2010). These first two EOF modes of sea surface zonal velocity collectively represent up to 67% of the intraseasonal variance in the equatorial band between 150°E to 150°W (Figure 3.13).

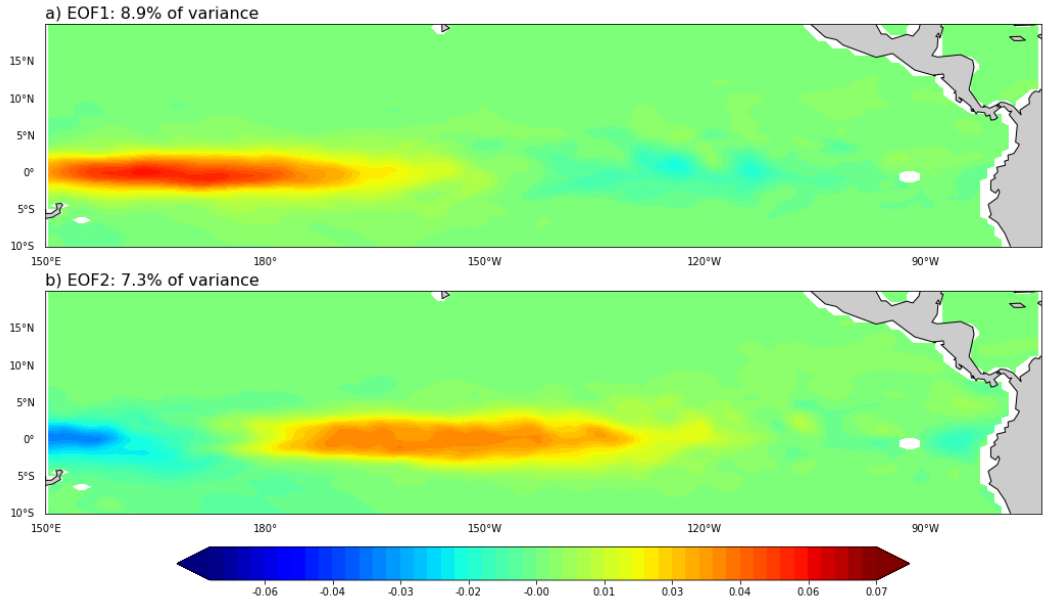

Figure 3.12. First (a) and second (b) leading EOF modes of sea surface zonal velocity intraseasonal anomalies. The percentage of variance explained by each EOF mode is given at the top of each panel.

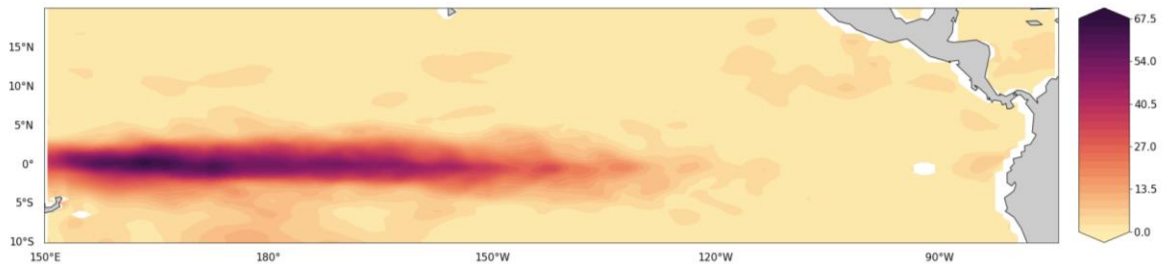

Figure 3.13. The fraction of the intraseasonal variance (%) explained by the two leading EOF modes of the sea surface zonal velocity anomalies.

Figure 3.14 shows the presence of intraseasonal waves in the study area, with an approximate periodicity of between 50 and 90 days for the time series of both PCs. It should be noted that, as in the variability of SSH, the periods with the highest power spectrum are located in the recognized El Niño years 1991-1992 and 1997-1998.

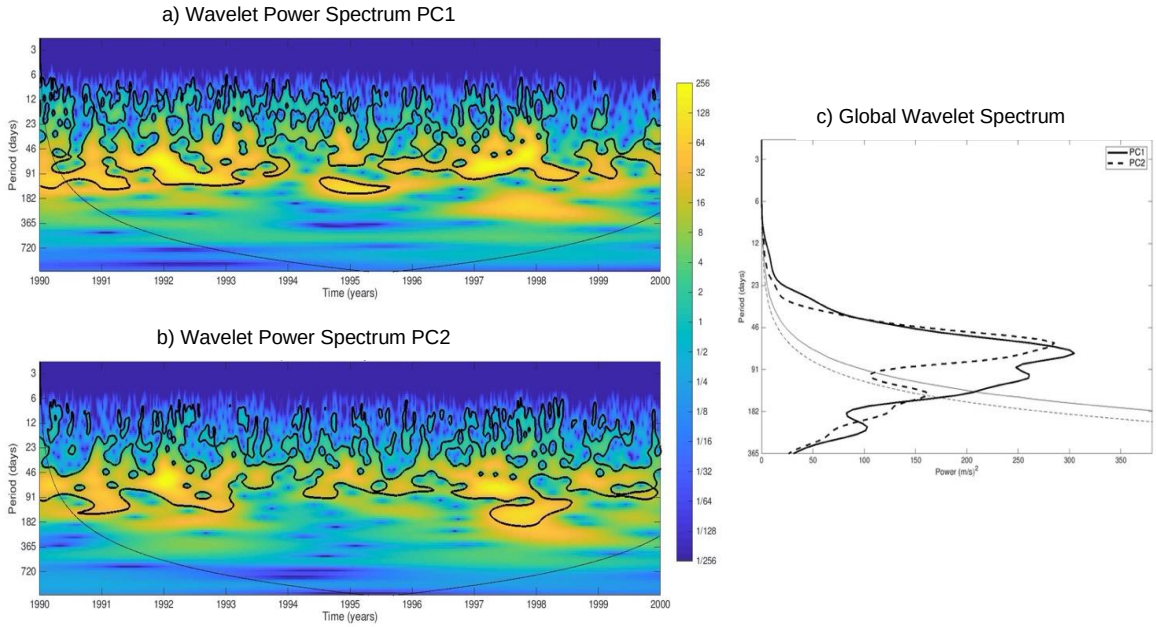

Figure 3.14. Wavelet analysis of PC1 and PC2 of the sea surface zonal velocity intraseasonal anomalies. Panels (a) and (b) show the corresponding wavelet power spectrums. The thick black contours indicate the 95% confidence level, and the thin black line indicates the border of the cone of influence (all data below this line are unreliable). Panel (c) shows the global wavelet spectrums. The thin lines represent the 95% confidence level.

3.3.5 Non-solar heat flux intraseasonal variability

In the case of the filtered anomalies of the non-penetrating part of the heat flux, the first two modes of the EOF analysis are presented in Figure 3.15. It was determined by applying the North *et al.* (1982) criterion that both modes are well separated from each other. The first EOF explains 9.2% of the overall variance while the second EOF accounts for about 6%. A lag correlation analysis of the two PCs suggests that both EOF modes are essentially different modes since their maximum correlation is only 0.17 at lag 8. The spatial structure of the variations of the non-solar heat flux closely follows the variations of the first two EOFs of the evaporation behaviour (Figure 3.21). Therefore, these results suggest that the main component of the non-solar heat flux is the latent heat.

The first two EOFs, predominantly reflecting latent heat flux effects, show maximum anomalies of the non-solar heat flux developing in a region that is above latitude 10°N. This is consistent with the work of Grodsky *et al.* (2009), who determined, based on satellite observations, that the intraseasonal variability of the latent heat flux was weak in the tropics and stronger towards the mid-latitudes. Both EOFs collectively represent up to 60% of the intraseasonal variance in the region mentioned above (Figure 3.16).

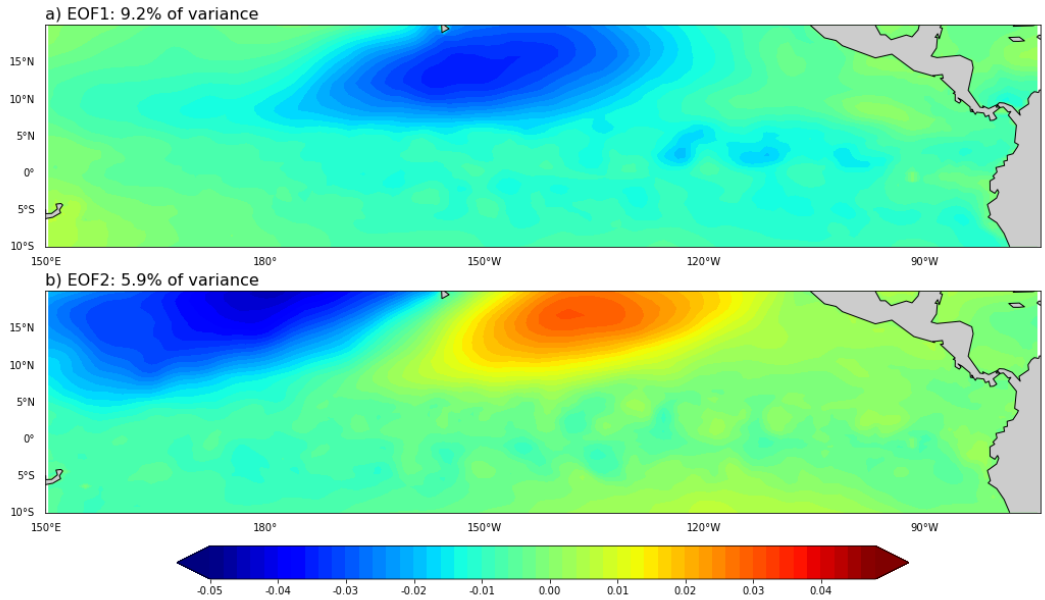

Figure 3.15. First (a) and second (b) leading EOF modes of non-solar heat flux intraseasonal anomalies. The percentage of variance explained by each EOF mode is given at the top of each panel.

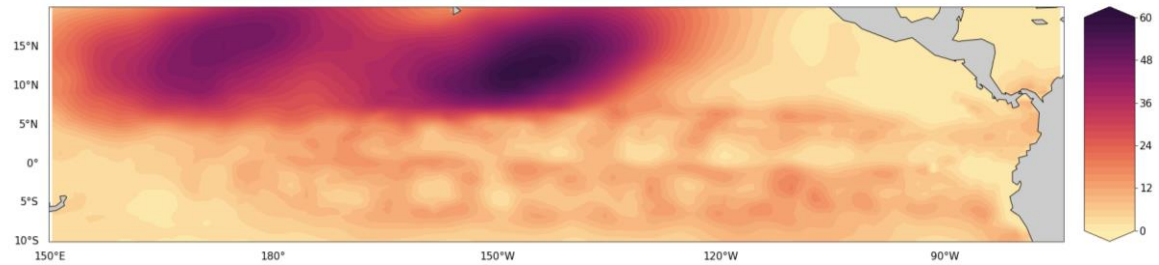

Figure 3.16. The fraction of the intraseasonal variance (%) explained by the two leading EOF modes of the non-solar heat flux anomalies.

In the wavelet analysis, Figure 3.17a and b show that the intraseasonal variance of the two PCs is significant mostly during the northern hemisphere winter and that this variability has a period below 60 days. This intraseasonal variability embedded in seasonal variations is related to the position of ITCZ (Thandlam and Rahaman, 2019). In the global wavelet spectrum, this can be distinguished in the 30-40 days spectral peak for both time series (Figure 3.17c).

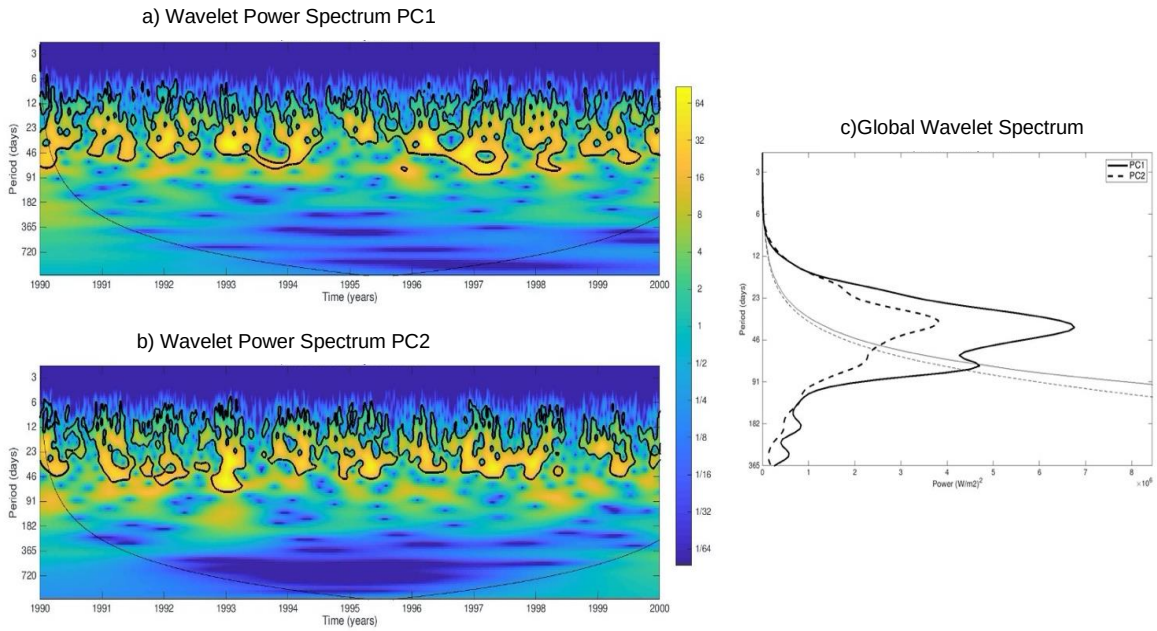

Figure 3.17. Wavelet analysis of PC1 and PC2 of the non-solar heat flux intraseasonal anomalies. Panels (a) and (b) show the corresponding wavelet power spectrums. The thick black contours indicate the 95% confidence level, and the thin black line indicates the border of the cone of influence (all data below this line are unreliable). Panel (c) shows the global wavelet spectrums. The thin lines represent the 95% confidence level.

3.3.6 Solar heat flux intraseasonal variability

The two leading modes of the solar heat flux intraseasonal variability anomalies were identified by conducting an EOF analysis. These two EOFs modes are ones that collectively explain a total of 18.2% of the intraseasonal variance and are shown in Figure 3.18. According to the North *et al.* (1982) rule, these two modes are well separated statistically, therefore both EOFs modes are treated as being two different modes. The PCs of these two leading modes have a maximum correlation of 0.17 at lag 30. The spatial patterns of the maximum anomalies of the shortwave radiation flux are located in the area west of 150°W, in the western Pacific. This is consistent with the work of Thandlam and Rahaman (2019) where they identified that the variability of the penetrating part of the heat in the central and eastern Pacific regions was seasonal, while, however, in the western Pacific region the variability was considered to be intraseasonal. This intraseasonal variability is associated with the presence of high clouds (cirrus, cirrostratus, and deep convective clouds) located in the deep and moist convective regions (Tian and Ramanathan, 2002). In the western Pacific region, the first two EOF modes collectively determine up to 75% of the intraseasonal variance as can be seen in Figure 3.19.

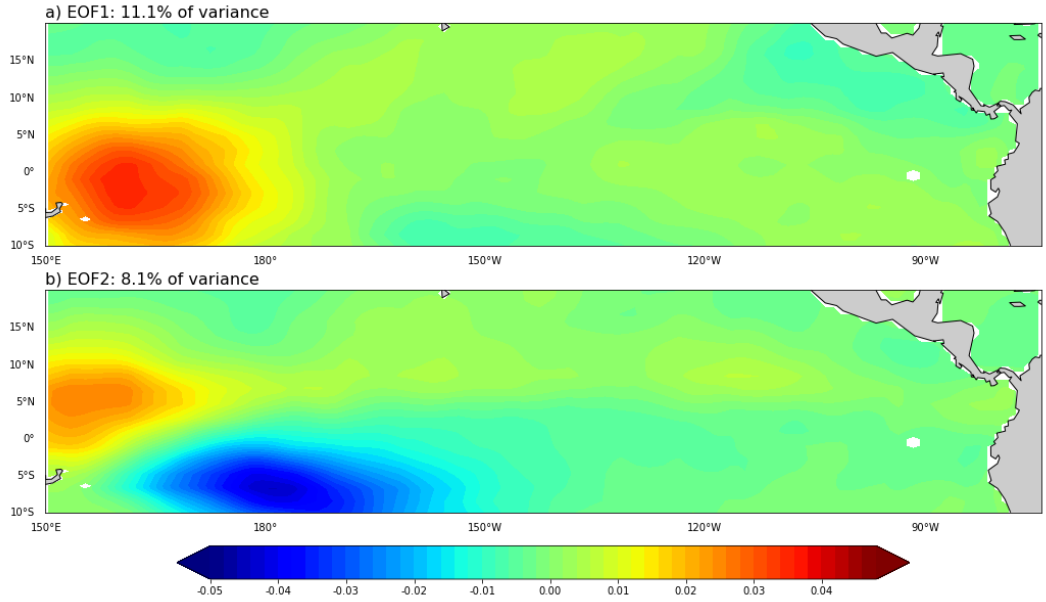

Figure 3.18. First (a) and second (b) leading EOF modes of solar heat flux (W/m^2) intraseasonal anomalies. The percentage of variance explained by each EOF mode is given at the top of each panel.

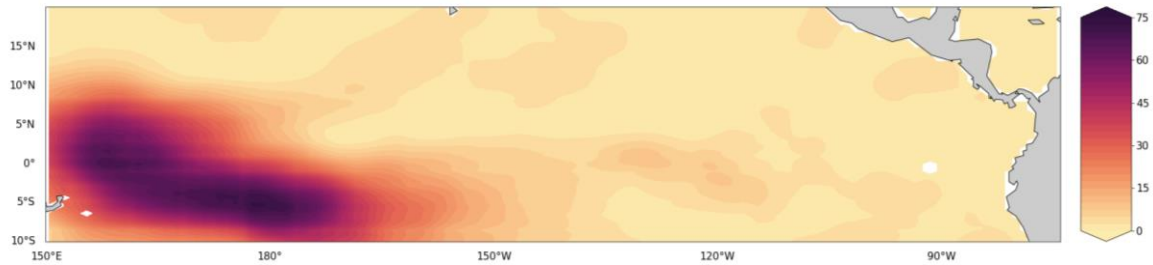

Figure 3.19. The fraction of the intraseasonal variance (%) explained by the two leading EOF modes of the solar heat flux anomalies.

The results of the wavelet analysis of the two PCs time series of the solar heat flux anomalies are presented in Figure 3.20. The global wavelet spectrum for PC1 has a significant peak at approximately 55 days, whilst the other hand, PC2 presents a peak at about 46 days. These cycles are considered to be related to the MJO (Shinoda and Hendon, 1998).

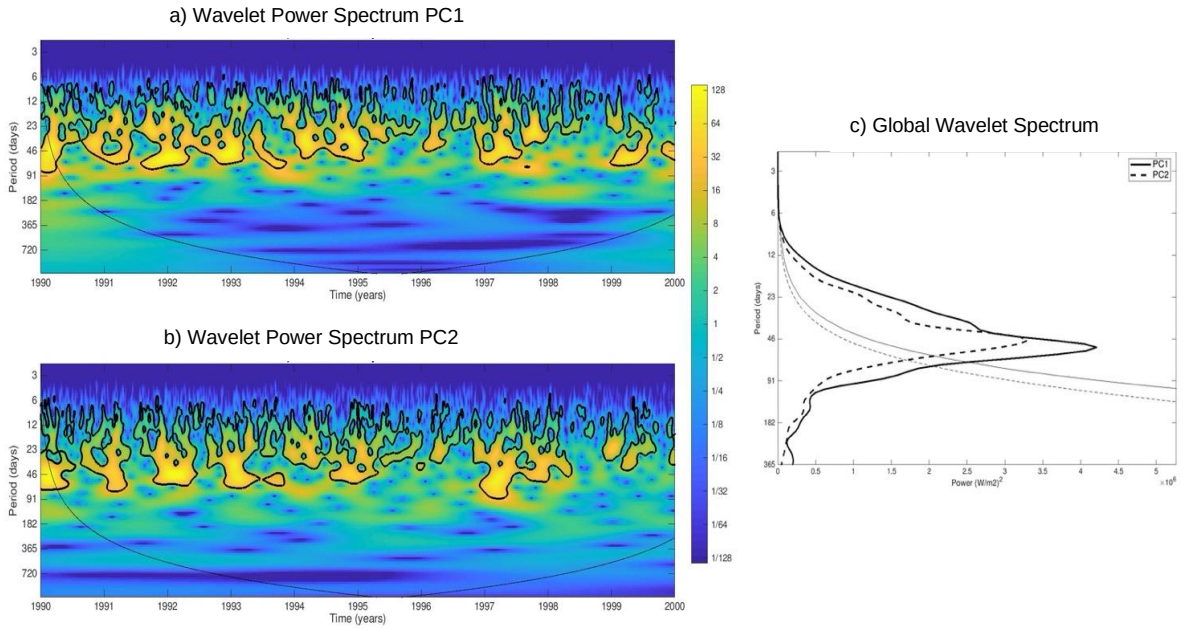

Figure 3.20. Wavelet analysis of PC1 and PC2 of the solar heat flux intraseasonal anomalies. Panels (a) and (b) show the corresponding wavelet power spectrums. The thick black contours indicate the 95% confidence level, and the thin black line indicates the border of the cone of influence (all data below this line are unreliable). Panel (c) shows the global wavelet spectrums. The thin lines represent the 95% confidence level.

3.3.7 Evaporation intraseasonal variability

The first two EOF modes for the filtered evaporation anomalies are presented in Figure 3.21. These two leading EOFs modes explain 8.8% and 6.5% respectively of the variance. Both modes, according to North's rule, are statistically distinguishable from each other. The maximum lag correlation of their respective PCs is only 0.12 at lag 92. As mentioned earlier, the spatial structure of these two modes is very similar to those found and given in Figure 3.15, corresponding to the filtered anomalies of the non-solar heat flux. This behaviour is considered to reside in the proportional relationship that exists between the latent heat flux and the evaporation. Small *et al.* (2011) through scaling analysis, identified that the intraseasonal evaporation variability in the Pacific is largely due to anomalies in the speed of the winds. Similarly, the fraction of the intraseasonal variance as shown in Figure 3.22 represented by the two leading modes is comparable in percentage (approximately 60%) and location to those found in Figure 3.16 for the non-solar heat flux.

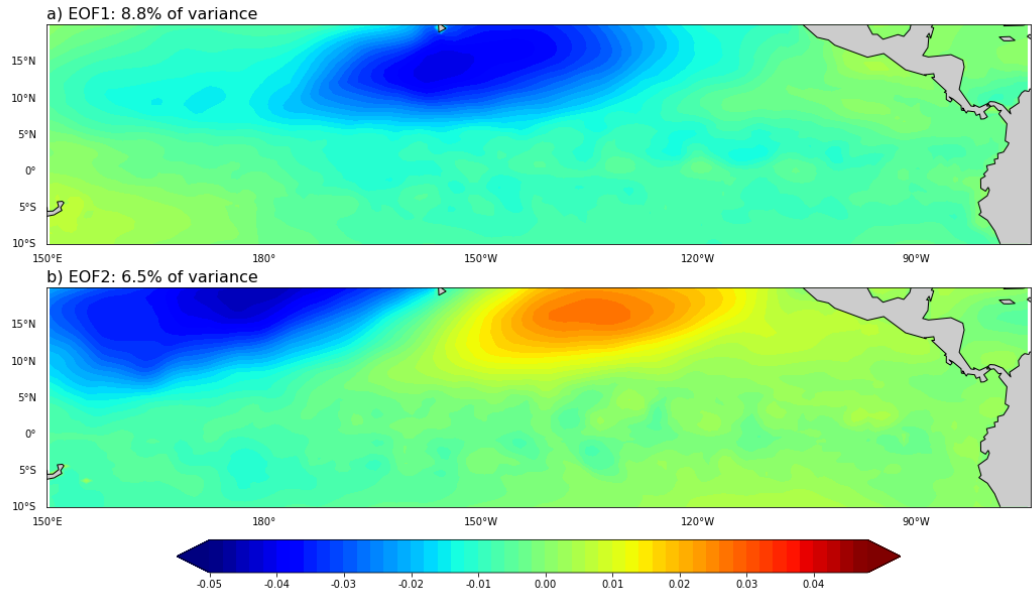

Figure 3.21. First (a) and second (b) leading EOF modes of evaporation anomalies. The percentage of variance explained by each EOF mode is given at the top of each panel.

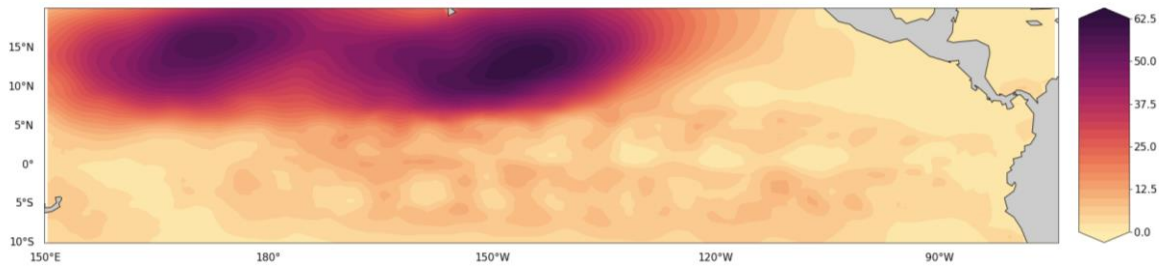

Figure 3.22. The fraction of the intraseasonal variance (%) explained by the two leading EOF modes of the evaporation anomalies.

Figure 3.23 shows the results of the wavelet spectrum analysis of PC1 and PC2 of the evaporation intraseasonal anomalies. The variations are not seen to be continuous throughout the overall study period although they are seen to be present in all years. These apparent seasonal variations could be related to the seasonal migration north-south of the ITCZ (Amador *et al.*, 2006). The obvious peaks are from 25 days to 45 days, centred around 35 days as observed in the global wavelet spectrum results.

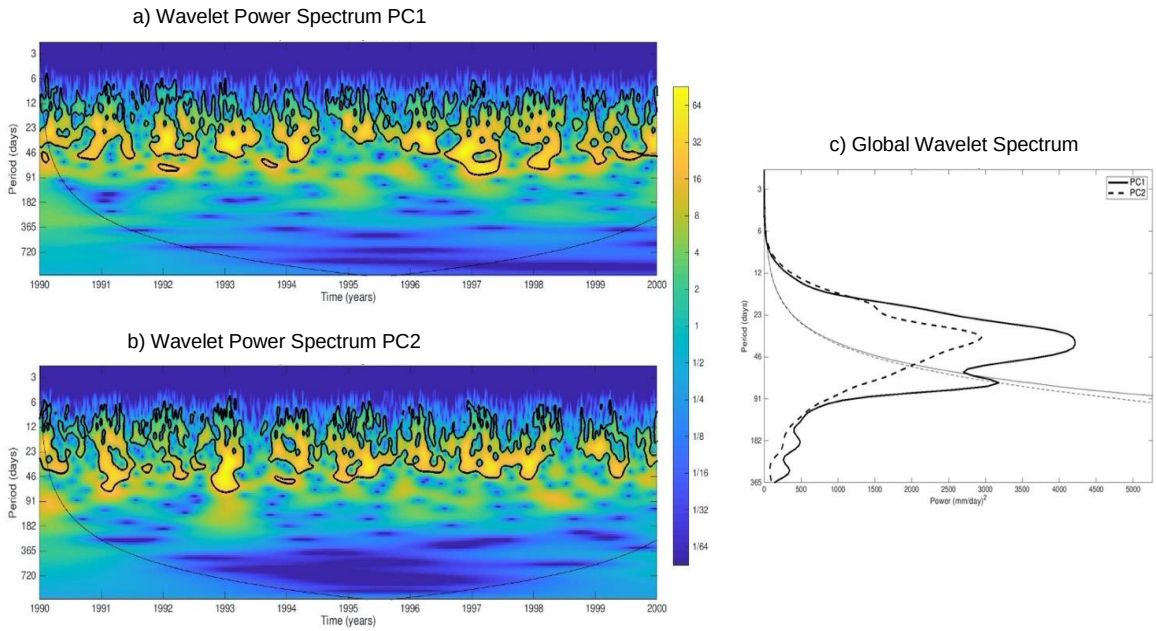

Figure 3.23. Wavelet analysis of PC1 and PC2 of the evaporation intraseasonal anomalies. Panels (a) and (b) show the corresponding wavelet power spectrums. The thick black contours indicate the 95% confidence level, and the thin black line indicates the border of the cone of influence (all data below this line are unreliable). Panel (c) shows the global wavelet spectrums. The thin lines represent the 95% confidence level.

3.3.8 Precipitation intraseasonal variability

The EOF analysis for the filtered precipitation resulted in the first two modes shown in Figure 3.24. The EOF1 mode explains 15.8% of the total variance within the domain shown, as compared to 10.5% for the EOF2 mode. These two leading modes are statistically distinguishable according to the rule of thumb postulated by North *et al.* (1982). The maximum correlation between the two PCs is 0.45 at lag 181. The anomalies associated with precipitation EOF1 have a maximum over the western Pacific region centred at latitude 3°N, while the EOF2 mode has the highest anomalies centred around 5°S and near the international dateline. These patterns of intraseasonal precipitation variability are consistent with those observed by Pariyar *et al.* (2019), which showed significant correlations with the MJO. Collectively EOF1 and EOF2 explain up to 81% of the total intraseasonal variance in the western Pacific, however, they only account for about 30% in other regions in the overall central and eastern Pacific (Figure 3.25).

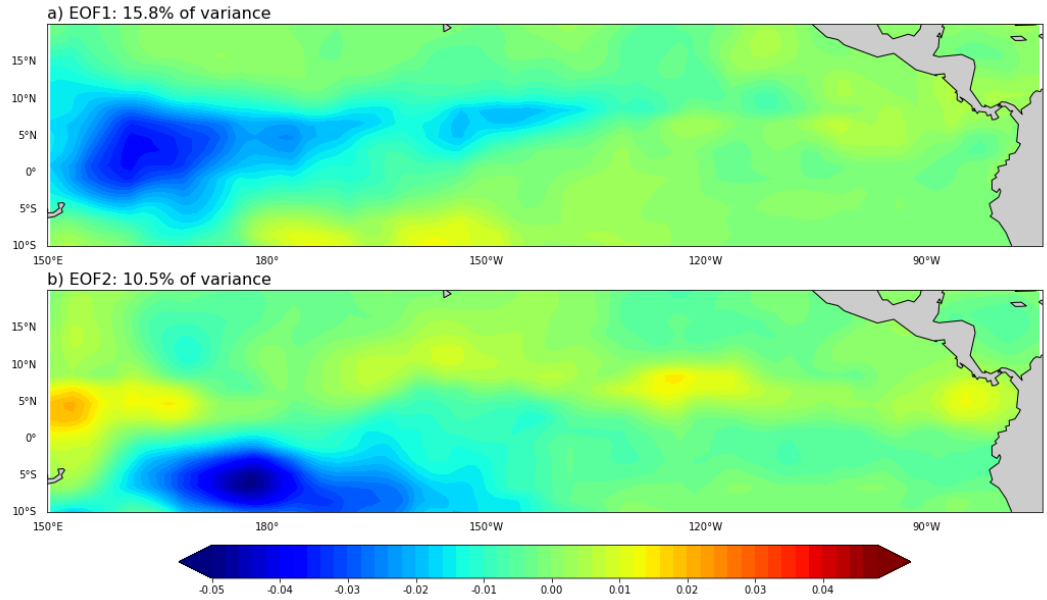

Figure 3.24. First (a) and second (b) leading EOF modes of precipitation (mm/day) anomalies. The percentage of variance explained by each EOF mode is given at the top of each panel.

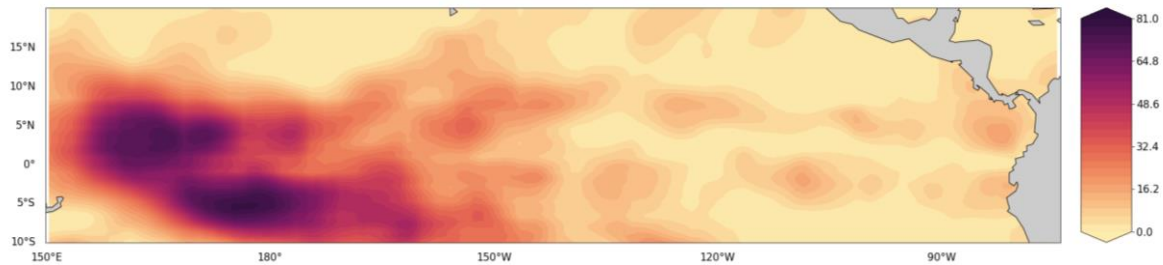

Figure 3.25. The fraction of the intraseasonal variance (%) explained by the two leading EOF modes of the precipitation anomalies.

The wavelet spectrum analysis was applied to the PCs of the intraseasonal precipitation data. The global spectrum of the wavelets revealed the presence of a significant periodic mode of 60-90 days (Figure 3.26c). The wavelet power spectrum of the PCs showed that this cycle was not present in the entire eleven-year time series (Figure 3.26a). Since the dominant patterns of precipitation variability are located in the mean position of the South Pacific convergence zone (SPCZ), the results observed in 3.26a-b are related to the interannual variability of the SPCZ (Pariyar *et al.*, 2019). ENSO modulates the interannual variability of the SPCZ, and therefore of the precipitation (Brown *et al.*, 2011). For example, Haffke and Magnusdottir (2013) observed negative SPCZ anomalies during the years 1998, 1999 and 2000 (La Niña season).

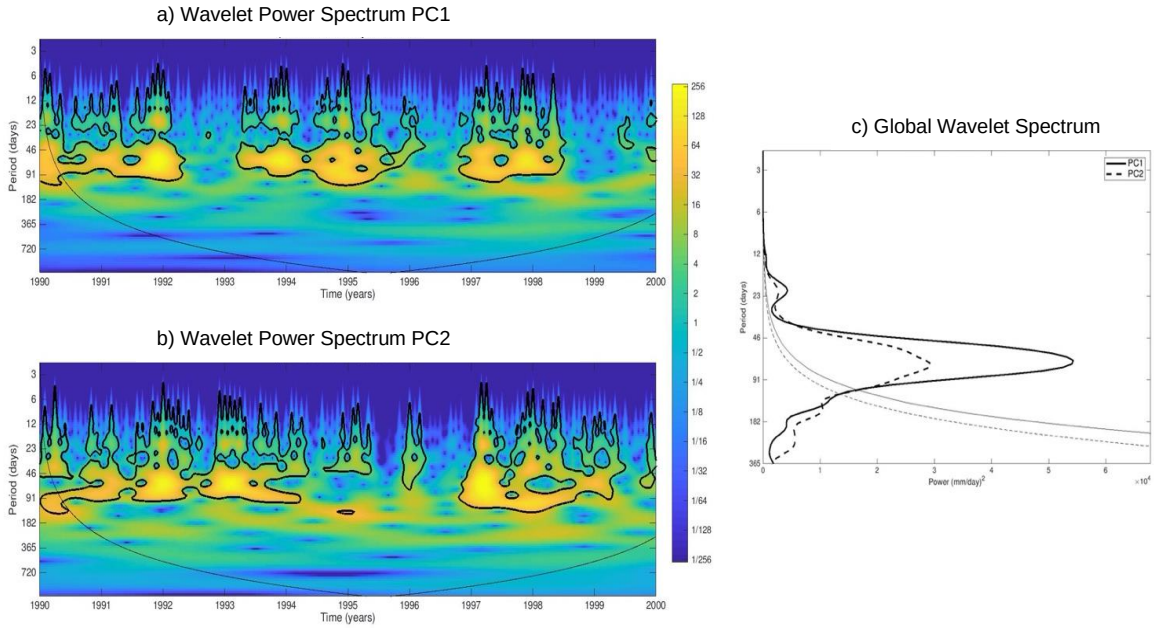

Figure 3.26. Wavelet analysis of PC1 and PC2 of the precipitation intraseasonal anomalies. Panels (a) and (b) show the corresponding wavelet power spectrums. The thick black contours indicate the 95% confidence level, and the thin black line indicates the border of the cone of influence (all data below this line are unreliable). Panel (c) shows the global wavelet spectrums. The thin lines represent the 95% confidence level.

3.4 Connection with the MJO

In order to assess in what way, the intraseasonal variability of each of the previously discussed eight variables are connected with the MJO and the spatial patterns of these relationships, a composite technique has been used for all eight MJO phases. The MJO composites technique was described in Chapter 2. In the following figures, the panels corresponding to each of the MJO phases are read in an anticlockwise manner. The results are presented as percentages of change from the standard deviation of the entire time series, henceforth we call this standard deviation STD. A significance test (Student's t-test) was then undertaken on each set of composites presented in this chapter.

The life cycle of the MJO and the determination of various phases are defined based on the time index that was proposed by Wheeler and Hendon (2004), which was described earlier in Chapter 1. The numbers of days for each MJO phase with amplitudes that are greater than 1 are summarized in Table 3.1.

Table 3.1. Number of days for MJO composite analysis from 1st January 1990 to 31st December 2000.

MJO phase	**1**	**2**	**3**	**4**	**5**	**6**	**7**	**8**	**MJO all**	**% days on MJO**
Number of days	340	304	286	305	333	283	280	282	2413	60%

A composite of all eight MJO phases for the SSH anomalies is shown in Figure 3.27. Positive anomalies begin to be present in the western Pacific during phases 5 and 6. These are considered to be related to the downwelling component of the Kelvin wave, which, as mentioned above, can be produced by anomalous westerlies MJO surface winds. These SSH positive anomalies gradually propagate eastwards, reaching up to 30% above of the STD (relative to the standard deviation of the whole unfiltered time series) as given in phase 1. Then, these waves gradually decrease in their intensity until they almost disappear shown in phase 4. Subsequently, the SSH negative anomalies (the upwelling component of the Kelvin wave) follow positive signals and during phases 5 and 6 these reach values of up to about 30 % below of the STD in the equatorial band.

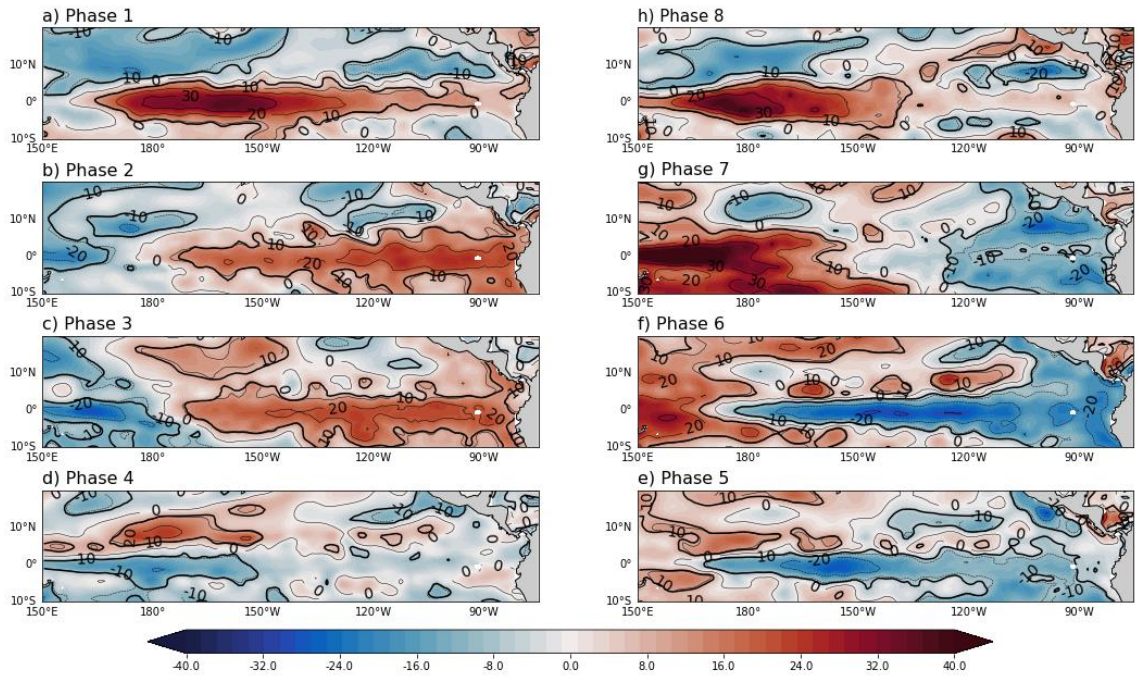

Figure 3.27. MJO composites of the SSH anomalies from the entire dataset (as a percent change from standard deviation SSH). The thick black lines show 95% significance.

A pattern correlation analysis (Section 2.3.6) was used to compare the phases of the MJO cycle (Figure 3.27) and the EOF patterns (Figure 3.3), to identify which phases of the MJO are closer to the EOF modes. It was determined that EOF1 mode presents a maximum pattern correlation of ~ 0.8 with the MJO phase 1 and of ~ -0.7 with MJO phase 5 SSH anomalies composite (Table 3.2). This is consistent with the cycle present in the MJO, where, as befits an oscillation, phases come in pairs in which spatial patterns are similar but of opposite signs (phases 1-5, 2-6, 3-7, and 4-8). On the other hand, the EOF2 pattern has the highest negative correlation with MJO phase 7 SSH anomalies composite (r ~ -0.6).

Table 3.2. Maximum pattern correlation for each variable for each MJO phases. The dark gray shading indicates the highest values.

MJO Phases		**1**	**2**	**3**	**4**	**5**	**6**	**7**	**8**
SSH	**EOF1**	0.8	0.6	0.6	-0.3	-0.7	-0.6	0.1	0.5
	EOF2	-0.2	0.2	0.3	0.3	0.1	-0.3	-0.6	-0.5
Zonal Velocity	**EOF1**	0.6	-0.1	-0.6	-0.8	-0.7	-0.4	0.7	0.8
	EOF2	0.6	0.8	0.7	0.0	-0.5	-0.8	-0.4	0.0
SST	**EOF1**	0.2	0.7	0.6	-0.4	-0.6	-0.6	-0.7	0.2
	EOF2	0.6	0.5	0.3	-0.5	-0.5	-0.5	-0.2	0.7
Solar Heat Flux	**EOF1**	0.6	0.8	0.4	-0.2	0.6	-0.6	-0.5	0.0
	EOF2	0.4	0.1	-0.3	-0.7	-0.3	-0.2	0.3	0.6
SSS	**EOF1**	-0.1	0.4	0.3	0.2	-0.1	-0.2	-0.4	-0.4
	EOF2	0.1	-0.1	-0.6	-0.3	0.0	0.4	0.1	0.2
No-Solar Heat Flux	**EOF1**	0.5	0.8	0.9	0.4	-0.6	-0.8	-0.9	-0.2
	EOF2	0.6	0.4	0.3	0.0	-0.4	-0.2	-0.2	-0.1
Evaporation	**EOF1**	-0.2	-0.7	-0.8	-0.5	0.3	0.7	0.9	0.4
	EOF2	-0.5	-0.3	-0.2	0.0	0.3	0.1	0.2	0.2
Precipitation	**EOF1**	0.4	0.5	-0.1	-0.5	-0.6	-0.2	-0.4	-0.1
	EOF2	-0.2	-0.1	0.2	0.5	0.2	0.2	0.0	-0.5

The zonal current velocities anomalies for the MJO cycle are shown in Figure 3.28. The eastwards propagation of the zonal current positive anomalies during phases 7, 8, 1, 2 and 3 is consistent with those that are presented in the previous results of the SST anomalies. The positive anomalies of the zonal current can reach values of up to 40% above of the STD in the western Pacific where the MJO winds are the strongest (Zhang *et al.*, 2009). However, in phase 3 the positive values of these anomalies are slowly weakened and subsequently, during phase 4 there is a transition to then becoming negative anomalies, which subsequently develop and strengthen in phases 5 and 6. To determine which of these phases resembled the EOF modes presented in the previous section (Figure 3.12),

correlation pattern coefficients were computed. The EOF1 mode can be associated with two MJO phases of zonal velocities anomalies (Figure 3.28). The same correlation value but with opposite signs, phase 8 (r ~ 0.8) and phase 4 (r ~ -0.8). Similarly, in Table 3.2, the EOF2 mode is identified with the MJO phases 2 and 6 with maximum correlation values of ~ 0.8 and ~ -0.8, respectively.

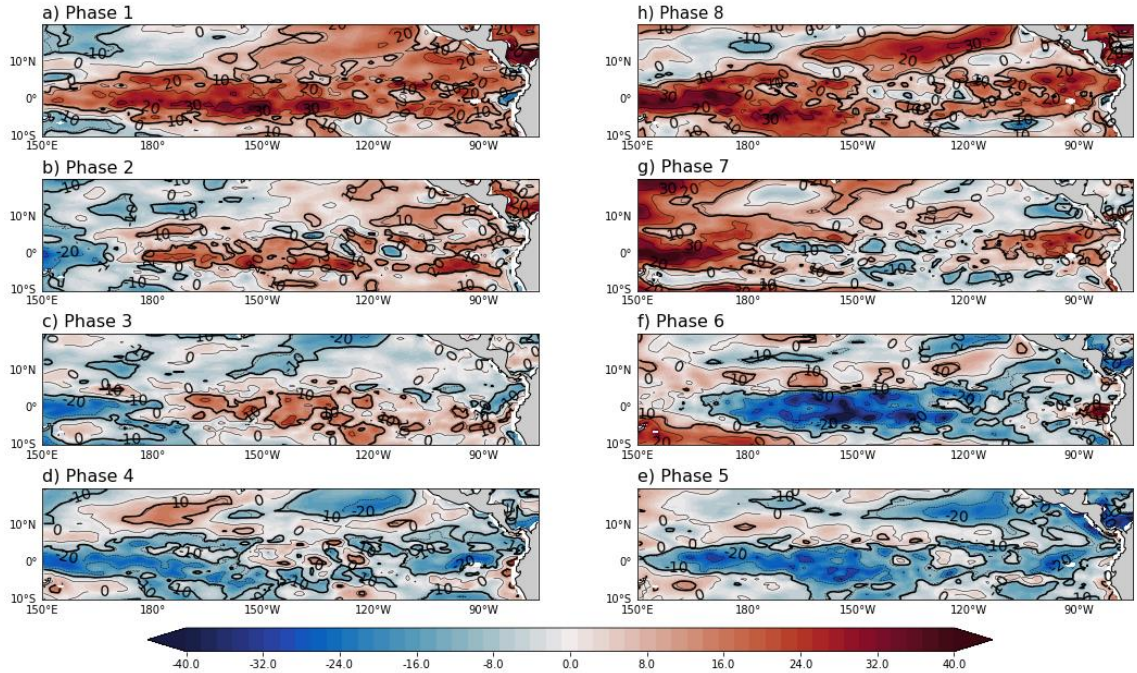

Figure 3.28. MJO composites of the sea surface zonal current velocity anomalies from the entire dataset (as a percent change from standard deviation sea surface zonal velocity). The thick black lines show 95% significance.

The SST cycle of the MJO was examined next (Figure 3.29). Relatively warm anomalies originate in the western Pacific during phase 4. These SST positive anomalies then propagate along the equator from west to east during subsequent phases, reaching their greatest amplitude of 30% of the STD in phase 2. Regions of cold anomalies are located in the central and eastern Pacific regions during phases 5-7. These SST negative anomalies are approximately -35% of the STD (phase 6). These results are similar to those found by Maloney and Kiehl (2002), who noted that the region of the Costa Rica dome has opposite anomalies when compared to those that are located in the equatorial region. These opposite positive and negative patterns of anomalies can be observed in all of the other phases except in phases 3 and 7 (Figure 3.29). Maloney and Kiehl (2002) suggest that warm pool SST anomalies may be regulated by latent heat fluxes and by surface shortwave radiation

variations, hence, we have also considered the composites of surface heat fluxes that are shown in Figure 3.30 and Figure 3.31.

The patterns of the solar heat flux anomalies (Figure 3.30) show consistency with the ones that are observed in the composite of the SST anomalies in the eastern tropical Pacific. Positive (negative) solar heat flux anomalies are associated with corresponding warm (cool) SST anomalies. This is not, however, the case in the western Pacific. Here, it is during phases 5 and 6, when warmer temperatures occur concurrently with negative solar radiation anomalies. This suggests that at least one other process may be primarily responsible for some of the SST anomalies that are observed in the western and central Pacific regions. This will be discussed later in Chapter 4, where the vertical structure of temperature anomalies, as well as the roles of both thermocline dynamics and advection, will be reviewed and further analysed.

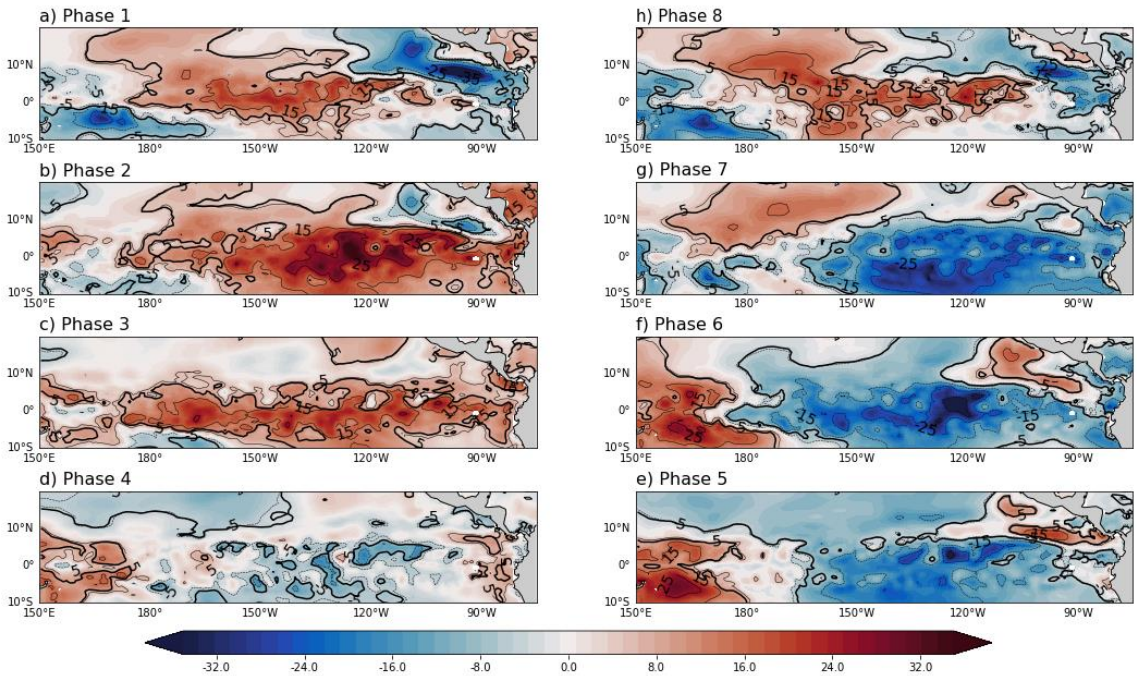

Figure 3.29. MJO composites of the SST anomalies from the entire dataset (as a percent change from standard deviation SST). The thick black lines show 95% significance.

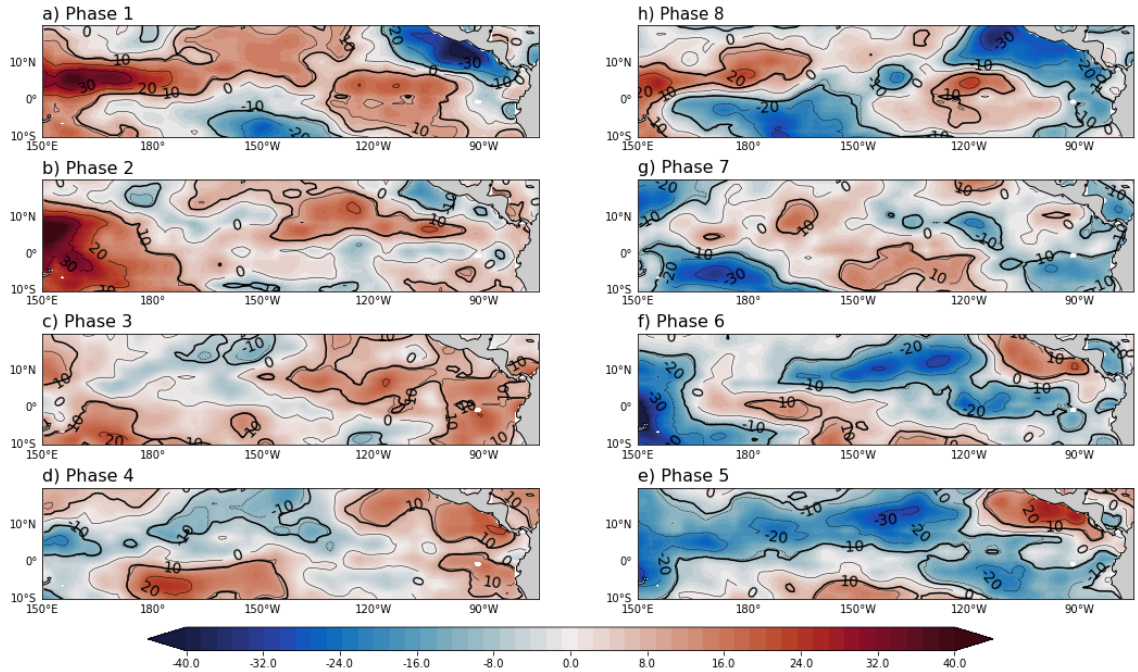

Figure 3.30. MJO composites of the solar heat flux anomalies from the entire dataset (as a percent change from standard deviation sea surface zonal velocity). The thick black lines show 95% significance.

The spatial pattern correlations between each of the eight MJO phases (Figure 3.29) and the EOF modes of SST (Figure 3.6) indicate that EOF1 has the two highest correlations with the MJO phase 2 (r ~ 0.7) and phase 7 (r ~ -0.7). The EOF2 mode shows a maximum correlation with the MJO phase 8 SST composite (r ~ 0.7). Meanwhile, for the MJO composites of the solar heat flux anomalies (Figure 3.30), it was found that for the corresponding EOF1 and EOF2 modes (Figure 3.18) the highest pattern correlations among all eight MJO phases are with phase 2 (r ~ 0.8) and with phase 4 (r ~ -0.7), respectively (Table 3.2).

Figure 3.31 summarise the modulation of non-solar heat flux anomalies by the MJO. In phase 1 of the MJO, statistically significant negative anomalies of this flux can be found mostly in the equatorial band. During phases 2 and 3 these anomalies reach negative peak values of -40% of the STD. In phase 4, positive anomalies appear which prevail until phase 7, extending initially throughout the equatorial band and expanding poleward subsequently. Values of more than 50% of the STD are attained. These spatial patterns of positive and negative anomalies are consistent with those of the wind speed anomalies (Figure 3.32), with westerlies (easterlies) anomalies prevail positive (negative) non-solar heat flux

anomalies mainly in phases 3 and 7, as has been pointed out in other studies (e.g., Batstone *et al.*, 2005).

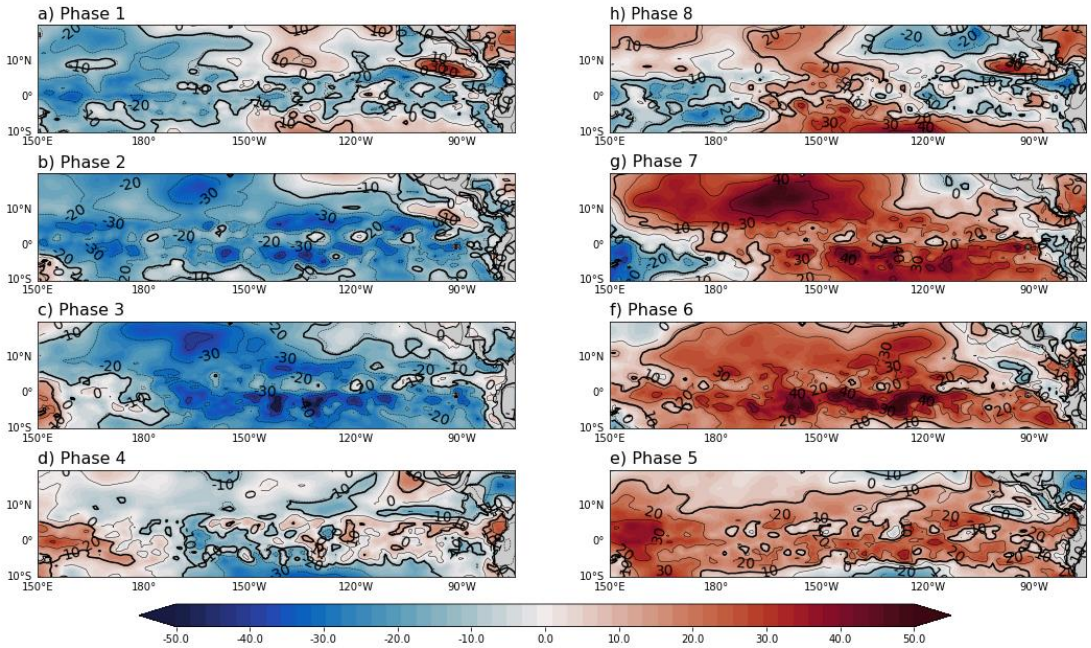

Figure 3.31. MJO composites of the non-solar heat flux anomalies from the entire dataset (as a percent change from standard deviation sea surface zonal velocity). The thick black lines show 95% significance.

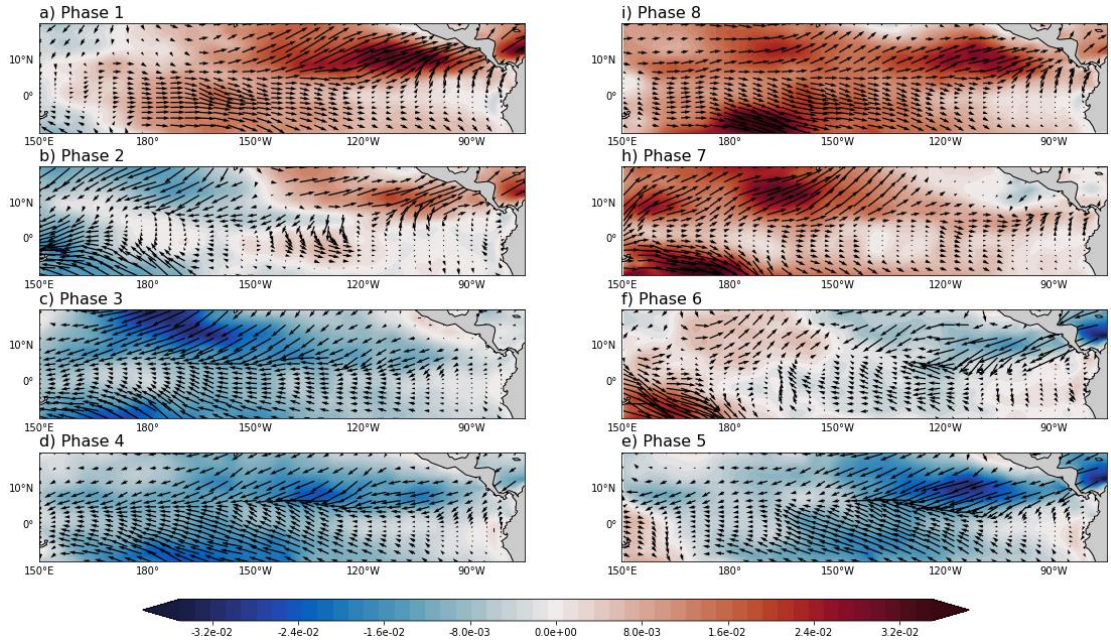

Figure 3.32. MJO composites of the zonal winds anomalies (shading) and of surface wind stress (vector).

Figure 3.33 shows the MJO composites for evaporation anomalies. When comparing these with the corresponding composites for the non-solar heat flux anomalies, a high degree of agreement between the patterns can be observed, but with opposite signs. This suggests that the variations of the non-penetrative part of the heat flux are probably mainly caused by the latent heat component, with lesser contributions from the sensible heat and the net longwave radiation.

The similarities between both fields are also apparent when computing the pattern correlation coefficients between the MJO composites and the EOF modes. Thus, the EOF1 mode of the non-penetrative part of the heat flux (Figure 3.15) and the EOF1 mode of evaporation (Figure 3.21) both resemble the same two phases of their corresponding MJO composites. From Table 3.2, MJO phase 3 and phase 7 show maximum correlation values of opposed signs, and the pattern correlation coefficients are as high as 0.9 and -0.9 for non-solar heat flux and -0.8 and 0.9 for evaporation, respectively. For the EOF2 modes, these have the maximum correlations with the MJO phase 1 non-solar and MJO phase 1 evaporation composite of r ~ 0.6 and r ~ -0.5, respectively.

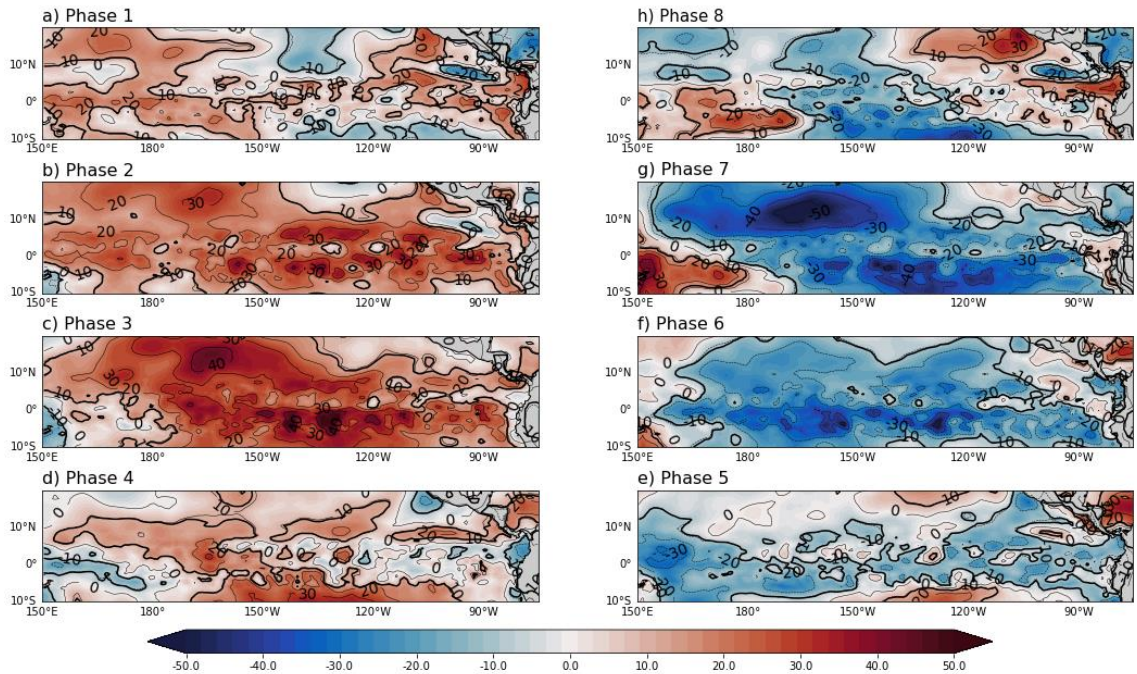

Figure 3.33. MJO composites of the evaporation anomalies from the entire dataset (as a percent change from standard deviation sea surface zonal velocity). The thick black lines show 95% significance.

The composites for the SSS anomalies that are associated with the MJO cycle are presented in Figure 3.34. As expected, the surface salinity anomalies are closely related to precipitation anomalies (Figure 3.35). During phases 1, 2 and 3 of the MJO, significant SSS negative anomalies are observed in the central and eastern Pacific regions. It is to be noted that in phase 3 a minimum of SSS negative anomalies of approximately -30% of the STD is reached. Conversely, in the opposite half of the MJO cycle (phases 5→8), SSS positive anomalies are recorded of up to 35% of the STD. Phases 5, 6, 7 and 8 show a pattern consisting of those that were observed in the corresponding precipitation composites, thus an increase in precipitation leads to negative salinity anomalies in the central and eastern Pacific regions (Figure 3.35e-h). However, the salinity anomalies that develop in the western Pacific do not follow this pattern, suggesting that other ocean processes may play a role. Another important aspect is the meridional distribution of the SSS anomalies, which seems to be modulated by the migration of the ITCZ (Delcroix and Hénin, 1991).

Patterns of precipitation anomalies can be observed that are in agreement with the mean position of the ITCZ in almost all phases of the MJO cycle (Figure 3.35). Over the eastern Pacific warm pool region, changes in precipitation are consistent with wind anomalies (Figure 3.32). In phases 8, 1 and 2, relatively wetter conditions can be observed, this is due to the presence of westerly anomalies that tend to weaken the trade winds. Conversely, enhanced easterlies in phases 4, 5 and 6 tend to strengthen the trade winds thus resulting in drier conditions. In the Central Pacific, precipitation anomalies have values of up to 20% in phase 2 and conversely down to -22% in phase7, variations whose patterns coincide quite well with those of the SST anomalies (Figure 3.29). Active convection occurs in regions where warm SST anomalies are observed. While when the convention is suppressed negative SST, anomalies are present.

The pattern correlation between the EOF1 mode of salinity (Figure 3.9) and MJO phase 8 is -0.4, while the pattern correlation between the EOF2 mode and MJO phase 3 is -0.6. For precipitation, MJO phase 5 ($r \sim -0.6$) and MJO phase 4 ($r \sim 0.5$) displays maximum pattern correlations with EOF1 and EOF2 (Figure 3.24), respectively.

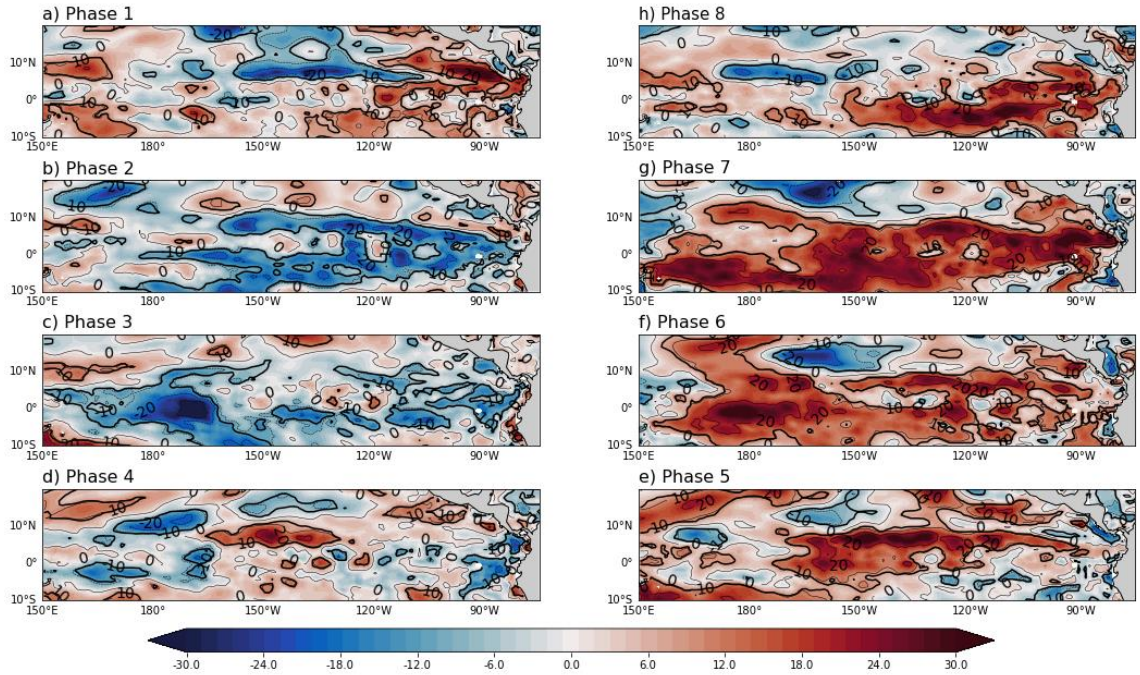

Figure 3.34. MJO composites of the SSS anomalies from the entire dataset (as a percent change from standard deviation SSS). The thick black lines show 95% significance.

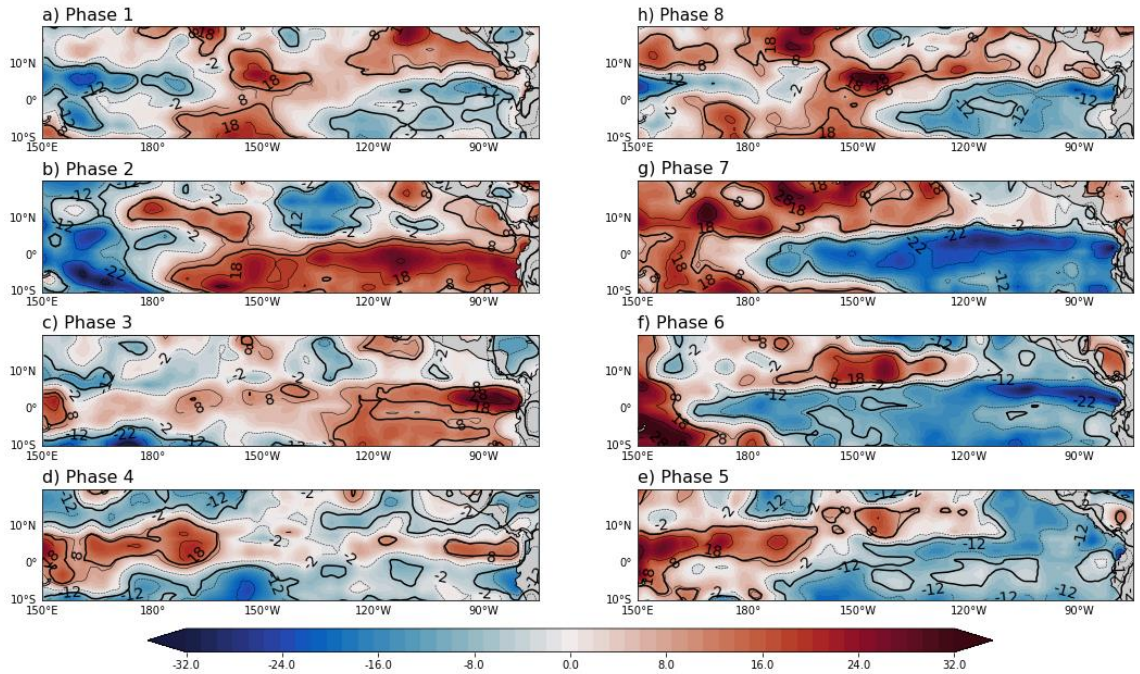

Figure 3.35. MJO composites of the precipitation anomalies from the entire dataset (as a percent change from standard deviation sea surface zonal velocity). The thick black lines show 95% significance.

3.5 Lagged linear regression and Granger causality analysis

As presented in the previous sections, each of the eight variables discussed shows some degree of relationship with the MJO cycle. However, the MJO is not the only known phenomenon that develops in the tropical Pacific on intraseasonal timescales. This section aims to examine more specifically the contribution of the MJO to the characteristics of the ocean surface. To achieve this, each of the variables was examined using two statistical models, namely, lagged linear regression and Granger causality. These statistical models and the methodology used in the results of this section are detailed in Chapter 2.

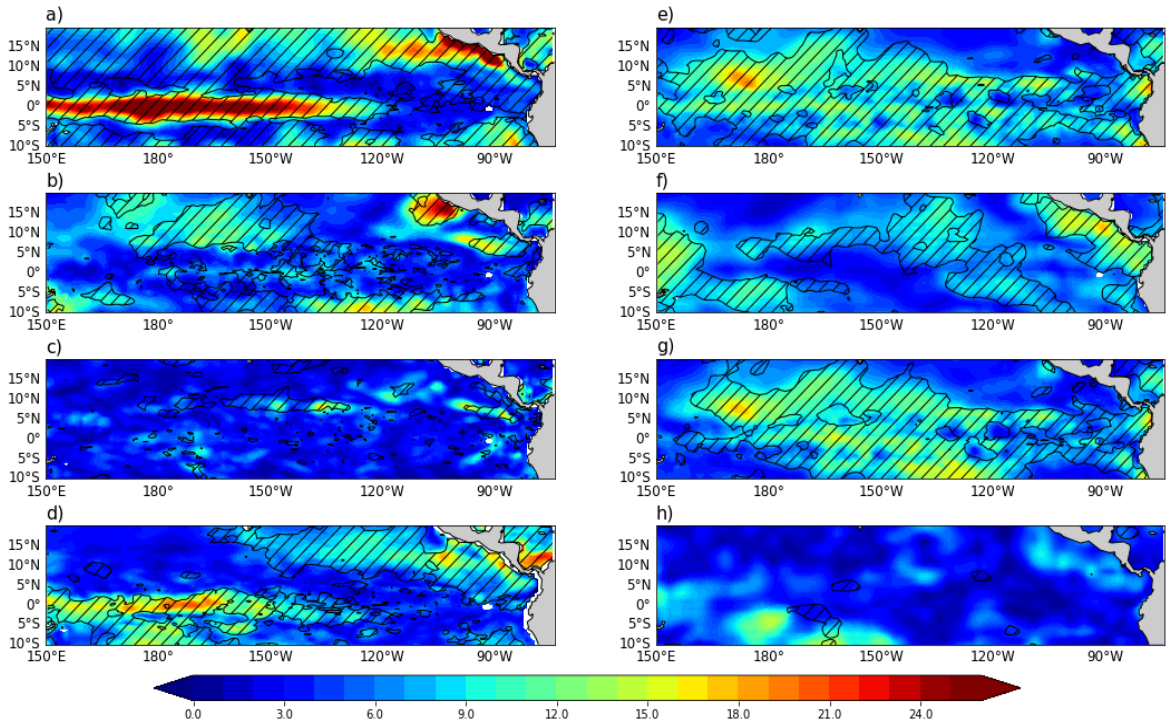

Figure 3.36. Variance (%) explained by lagged linear regression model for filtered anomalies of a) SSH, b) SST, c) SSS, d) sea surface zonal current, e) non-solar heat flux, f) solar heat flux, g) evaporation and h) precipitation, regressed against RMM1 and RMM2. The hatched regions are those where Granger causality is significant at a 99% confidence level.

For example, Figure 3.36a shows the variance map from the lagged regression of the SSH upon the MJO index. At an average lag of approximately 28 days (see Appendix B), two regions were identified where the variance percentages are in the order of 30%. The first one is in the equatorial band of the central Pacific and the other region is near the Pacific coast of Central America extending to southwestern Mexico. These regions match where the MJO is seen to have a Granger causal effect on the SSH in a statistical sense. Similarly, the corresponding analysis for SSTs (Figure 3.36b) indicates that the Pacific region off the

Mexican southwest coast shows the highest correlation at an average lag of 28 days. Therefore, we can say that MJO index variability Granger causes SST variability in this area. However, this is not the case for the SSS (Figure 3.36c), for which there is little evidence of Granger causality by the MJO. The variance, as explained by the lagged regression model, reaches its maximum (17%) at an average lag of 28 days in this same region. Figure 3.36d shows the two main regions of the Granger causality link between zonal currents and the RMM index. These are located in the equatorial band of the western and central Pacific regions, where the variance rises to about 20%, and also over the eastern Pacific warm pool. In the latter region, the MJO Granger causes solar heat flux variations, presumably through changes in cloud cover (Figure 3.36f), with a maximum variance of 18% calculated by the lagged regression with a lag average of 27 days.

Figures 3.36e, and g show that there is a Granger causal effect on the non-solar heat flux and the evaporation by the MJO over most of the domain. The maximum variance values are around 20% for both variables, with an average lag of approximately 29 days. Finally, the precipitation, despite showing values of 15% of explained variance in the region (190°W-50°W, 10°S-0) and 10% in the eastern Pacific warm pool, does not seem to be Granger caused by the MJO.

3.6 Summary

In this chapter, the impact of the MJO on the ocean surface characteristics in the eastern tropical Pacific region has been studied based on the results of the II simulation for the time period from 1990 to 2000. Although some of the results discussed above are corroborated by previous literature, particularly for variables such as SST or SSH, the novel results of this chapter are:

- The quantification and location of intraseasonal variability in terms of percentages. For each variable, the regions with the highest levels of intraseasonal variability (10-120 days) were identified, and the relative contribution of the said variability to the total variance was calculated. The highest relative variabilities hover around 20 to 60% of the total variance and largest values are typically located or centred on the equatorial band.
- Two spatial-temporal techniques have been used to analyse the model results. First, EOF analysis has allowed us to identify the two leading patterns of variability in

each field. The first two modes represented more than 60% of the intraseasonal variance in all of the eight variables studied. Second, the use of a wavelet analysis showed how this variability is distributed throughout the study period and allowed us to detect the behaviour of intraseasonal variability in the different phases of ENSO. The power spectrum representation of the two PCs helped to identify the main periodicity for both time series.

- The response patterns of the oceanic surface to the MJO and the quantification of this response with respect to the standard deviation of each variable. The composites of all the MJO phases for each variable have shown a clear oscillatory behaviour between large positive and negative anomalies (up to 50% of the standard deviation of the entire time series). It was also possible to quantify the relationship between each EOF mode and each MJO phase by computing the associated pattern correlation coefficients.
- In the last section of this chapter, the lagged linear regression and Granger causality analyses identified the regions in which variability can be said to be "Granger caused" by the MJO and the associated variance percentages relative to the total filtered variance were calculated. To the best of the author's knowledge, this is the first time that Granger causality analysis has been used to relate intraseasonal variability to the MJO.
- Essentially, the MJO acts as a Granger cause in two main regions, namely, over the equatorial band and the eastern Pacific warm pool. Variables such as SSH, SST and zonal currents are Granger caused in the equatorial band because of their dynamic connection with the propagation of intraseasonal equatorial Kelvin waves. Non-solar heat fluxes, solar heat fluxes and evaporation are related to changes in cloud cover generated by the MJO and, therefore, are Granger caused not only along the equator but also over the eastern Pacific warm pool. According to our analysis, salinity and precipitation do not show a Granger causal relationship with the MJO.

The results presented here help to identify key features of the intraseasonal upper-ocean variability and its relationship with the MJO cycle. However, a study of the impact of the MJO on the ocean should not be limited to the ocean surface layer. Therefore, we next analyse the dynamic response of the ocean to the MJO below the surface.

Chapter 4

The Madden-Julian Oscillation's impact below the ocean surface in the central and eastern regions of the tropical Pacific

4.1 Introduction

In the previous chapter, the connection of the MJO with different ocean surface variables in the tropical Pacific was studied. However, the dynamics of the upper, tropical Pacific Ocean cannot be fully examined by looking exclusive at surface processes. Therefore, the aim of this chapter is to investigate the role of the MJO in controlling changes in temperature, salinity, and currents at depth. This study will identify the intraseasonal variations in the mixed layer depth (MLD), the thermocline, the halocline, and the pycnocline and their relationships with the MJO. As in the previous chapter, output from the four-dimensional II simulation will be used for the time period from 1990 to 2000.

This chapter is structured as follows: spatial and vertical distributions of time means are discussed in Section 4.2. Section 4.3 in which the regions having the highest percentages of intraseasonal variability are identified. The vertical structures of the ocean variables are described in Section 4.4. The connections with the MJO are investigated in Section 4.5. Section 4.6 discusses results of a lagged linear regression analysis, including Granger causality analysis. To conclude this chapter, Section 4.7 presents a summary of the results and a few observations and reflections based on them.

4.2 Upper ocean vertical structure

The general hydrographic characteristics of the tropical Pacific are shown in Figure 4.1, which depicts the simulated time-mean temperature, salinity and currents in the top 260 m. The minimum temperatures are located on the far east of the domain, while the maxima are located towards the west (Figure 4.1a, b). The trade winds in the western Pacific cause meridional divergent near-surface flows and equatorial upwelling in the eastern Pacific. As a result of intense precipitation along the equator, salinity exhibits a local minimum in the

equatorial band. A strong equatorial jet corresponding to the South Equatorial Current is the leading feature of the mean zonal currents and the location of this jet coincides with the area of largest equatorial upwelling (Figure 4.1e and i).

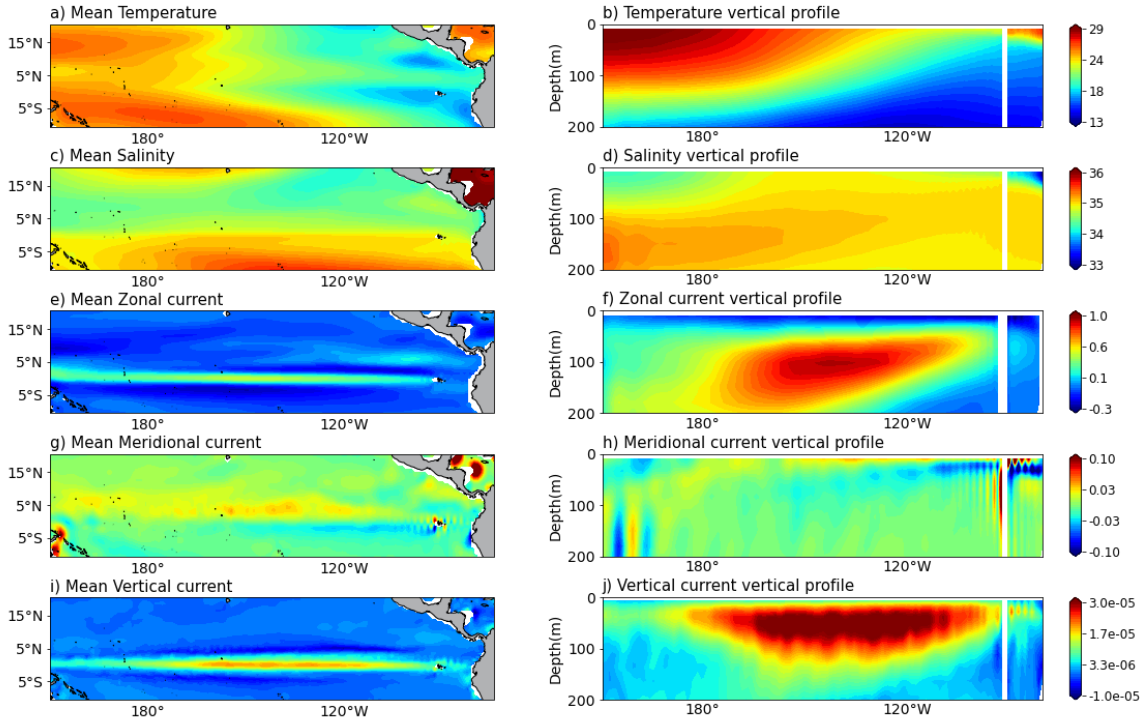

Figure 4.1. Time means of vertically averaged (between 10 and 260 m) **a)** temperature (˚C), **c)** salinity (psu), **e)** zonal current (m/s), **d)** meridional current (m/s) and **e)** vertical current (m/s). Longitude-depth sections of the same time means of **b)** temperature (˚C), **d)** salinity (psu), **f)** zonal current (m/s), **g)** meridional current (m/s) and **h)** vertical current (m/s).

In this work, the MLD was calculated based on a density threshold criterion. In other words, the MLD was defined as the depth at which the local, potential density has increased relative to the surface by an amount that is equivalent to the increase in density that would be caused by a 0.3˚C decrease in local, potential temperature relative to the surface value. The depth of the maximum vertical temperature gradient (dT/dz) is known as the thermocline depth. Although, the depth of the 20˚C isotherm has been commonly used as the thermocline depth in the tropical Pacific region (Kessler, 1990), it has been shown that this isotherm does not correctly represent the seasonal variability of the thermocline (Fiedler and Talley, 2006). In the same way, the halocline depth is defined, as the depth of the maximum vertical salinity gradient (dS/dz). Similarly, the pycnocline depth is defined here as the depth of the maximum (in absolute value) density gradient ($d\rho/dz$). The spatial distributions of mean mixed layer, thermocline, halocline and pycnocline depths are shown in Figure 4.2. Pronounced east-to-west depth gradients are obvious in all four variables.

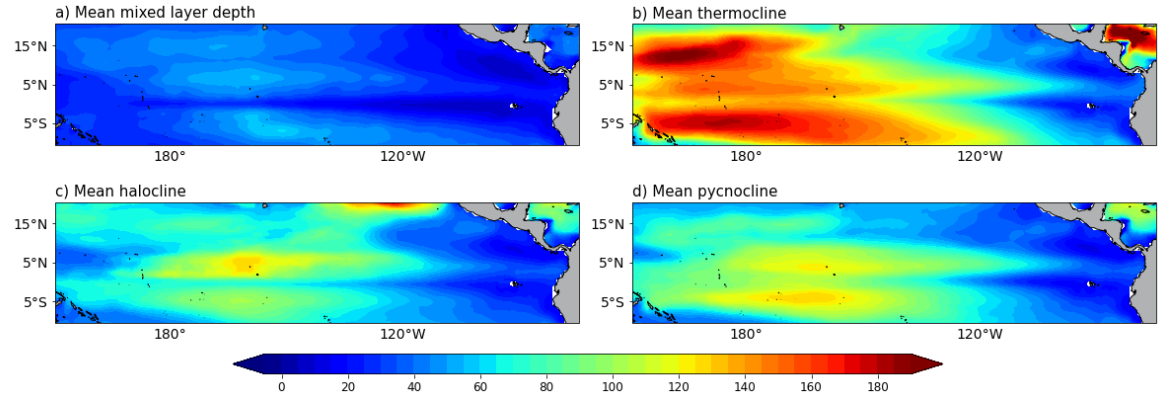

Figure 4.2. Time means of a) mixed layer depth (m), b) thermocline depth (m), c) halocline depth (m) and d) pycnocline depth (m).

4.3 Spatial patterns of intraseasonal variability

The same methodology that was used earlier in Section 3.2 was followed here in the calculation of the statistical variability of the different fields in units of the standard deviation of their unfiltered, long-term values. However, while in Section 3.2 this was done using solely surface values, here we use the averaged values of temperatures, salinities and ocean currents between 10 m and 260 m. The lower limit of 260 m was chosen because it was observed that the intraseasonal variations (Section 4.3) are relatively small below this depth.

The total variance of the subsurface temperature is shown in Figure 4.3a. Two regions of greater variability can be identified, with variations that are close to 1.5°C. Both are upwelling regions: the equatorial band of the central and eastern Pacific, and the Costa Rica Dome. However, the highest percentages of intraseasonal variability do not coincide with these two aforementioned regions. In the Central Pacific region centred on 5°N, 40% of total variability corresponds to the intraseasonal time scale. In the case of the subsurface salinity (Figure 4.3b), the equatorial region of the central and eastern Pacific displays the highest percentages of intraseasonal variance. In particular, the region that is located between 100°W and 140°W (which accounts for 60% of the whole region examined) has been mainly related to tropical instability waves (TIWs) in the sea surface salinity signal (Lee *et al.*, 2012).

Both the subsurface zonal and meridional currents show maximum variations that are close to 22 cm/s and 18 cm/s respectively, located in the equatorial region (Figure 4.3c and d). The intraseasonal variance can explain up to 60% of the total variation of the subsurface zonal currents and this variability is believed to be partly related to the propagation of intraseasonal Kelvin waves (ISKw) (Rydbeck *et al.*, 2019). But it is also influenced by the presence of TIWs and these come to represent up to 90% of the total variance north of the equatorial region between 100°W and 150°W. The maximum percentage of the intraseasonal variance of subsurface vertical currents is located between 130°W and the dateline at the equator with a value of 60% (Figure 4.3e).

The total variance of the MLD reaches maximum values of 24 m in several different regions of the Pacific Ocean. However, when these are compared with maximums of the relative intraseasonal variance, the regions do not match. For example, the region located in the eastern Pacific whose relative variance is above 60% is a region where the total variations are relatively small, in the range of 2-10 m. These regions of low total variability are consistent with the observations of Fiedler *et al.* (2012).

Figure 4.3f shows that the standard deviation values of the thermocline depth are greater in the western Pacific region than in the eastern Pacific region. The latter region is characterized by having a permanent thermocline that is both strong and shallow (Fiedler and Talley, 2006). Intraseasonal variations of the thermocline can represent up to 60% of the total variance north of the equatorial Pacific region between 110°W and 160°W. Not by coincidence, this region of the Pacific is also the region where the greatest intraseasonal subsurface temperature variation is found in Figure 4.3a. Meanwhile, the highest percentages of the intraseasonal variance of both the halocline and the pycnocline can reach values of 60% and both are located in the equatorial zone between 90° W and 120°W.

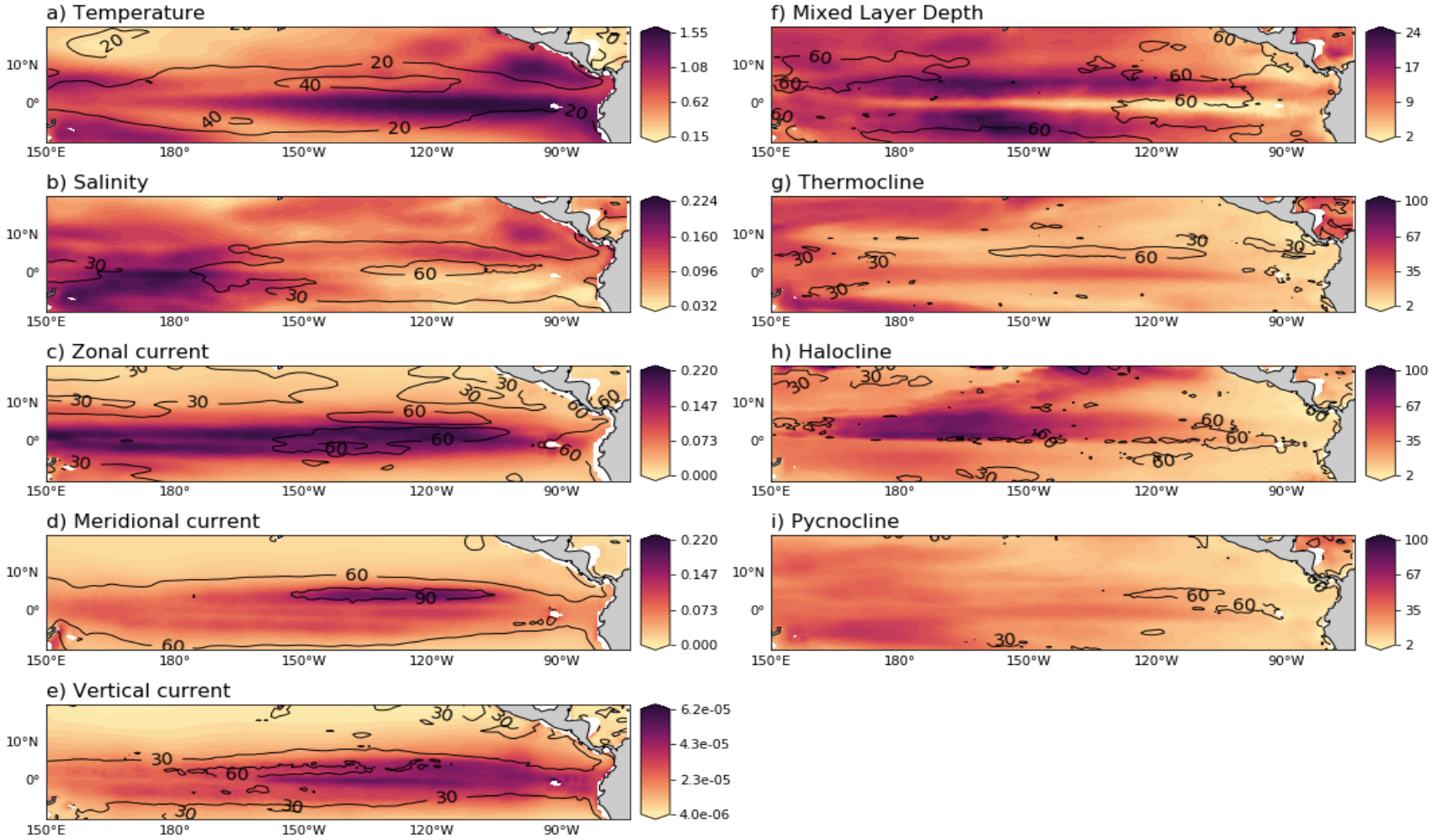

Figure 4.3. Shaded regions denote the total variance and the black contour lines are the fraction of the intraseasonal (10-120 day) variance to the total variance of a) temperature (°C), b) salinity (psu), c) zonal current (m/s), d) meridional current (m/s), e) vertical current (m/s), where each are averaged between 10-260 m. And f) mixed layer depth (m), g) thermocline depth (m), h) halocline depth (m) and i) pycnocline depth (m) where each is expressed in units of standard deviation. Percent contours are plotted every 30, starting at 0 except for temperature where contours are plotted every 20, starting at 0.

4.4 Intraseasonal oceanography vertical structure

The study of zonal sections of temperature, salinity, and currents provides knowledge about their vertical distribution on an intraseasonal period. The zonal sections display the standard deviation of the filtered variables in the period from 1990 to 2000. Six sections located at 5°S, 2°S, 0°, 2°N, 5°N and 7°N were chosen. We focus on the upper 300 m of the water column and we also display the mean thermocline, halocline, and pycnocline depths in each of these latitudes.

4.4.1 Temperature

Most of the intraseasonal temperature variability is seen to be concentrated around latitude 5°N (Figure 4.4b). This notable variation in temperature reaches values that are higher than 1.5°C and it spreads throughout the central and eastern Pacific region just below the mean thermocline depth. This intraseasonal variation can also be observed in all other latitudes, although occurring in a smaller range (0.5-1°C). This variability could be attributed to various phenomena within the intraseasonal time scale; therefore, a spectral analysis was undertaken. This analysis was performed at five different longitudes, uniformly spaced every 20 degrees and for each of the six latitudes, with the depth selection being based on the point of greatest variability and for each corresponding latitude and longitude grid location (Figure 4.4).

Figure 4.5 shows that the time series that is located further west, 160°E, predominantly displays maximum peaks around the period 60-80 days. Also, it is worth noting that the trend is also present at the points of latitudes 2°N and 5°N, with the peaks shifting towards increasingly shorter periods eastward. This suggests that intraseasonal variability of the subsurface temperature is being modulated mainly by two processes, namely, the ISKw and TIWs, whose typical periods and amplitudes are consistent with those of the spectral peaks, the western Pacific region being the most influenced by the ISKw while the eastern Pacific region is dominated by TIWs. These observations are consistent with earlier studies (e.g., McPhaden, 2002; Jochum *et al.*, 2007). This is not, however, the general case, for example, for latitudes such as the equator or 2°S, where according to the power spectrum analysis, the same period of 60-80 days is identified for all longitudes. Although these

changes in peaks cannot probably be interpreted solely as resulting from ISKw activity, these waves are known to be one of the largest contributors (e.g., Zhang, 2001).

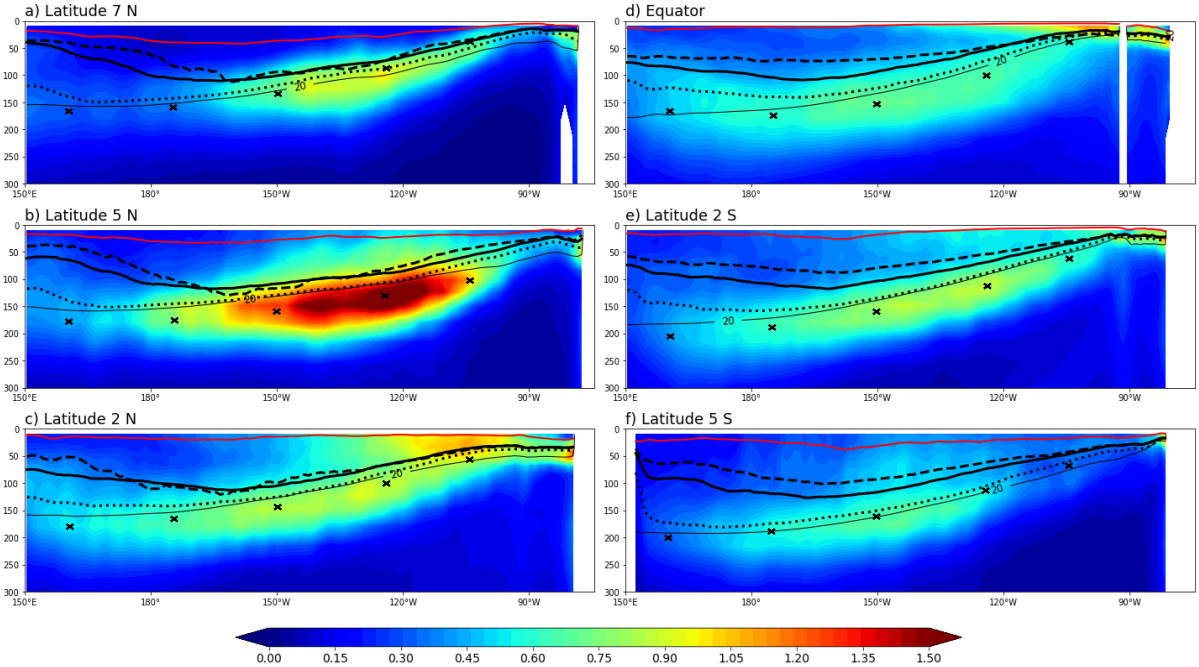

Figure 4.4. Longitude-depth vertical sections of standard deviation filtered temperature (˚C) at a) 7˚N, b) 5˚N, c) 2˚N, d) equator, e) 2˚S and f) 5˚S, from the coast (right edge) to 150˚E in the upper 300 m. Dotted, dashed, solid black and solid red lines denote the corresponding mean thermocline, mean halocline, mean pycnocline and mean mixed layer depths, respectively. The thin black line denotes the 20˚C isotherm. Crosses denote the locations for which power spectra were computed and are presented in Figure 4.5.

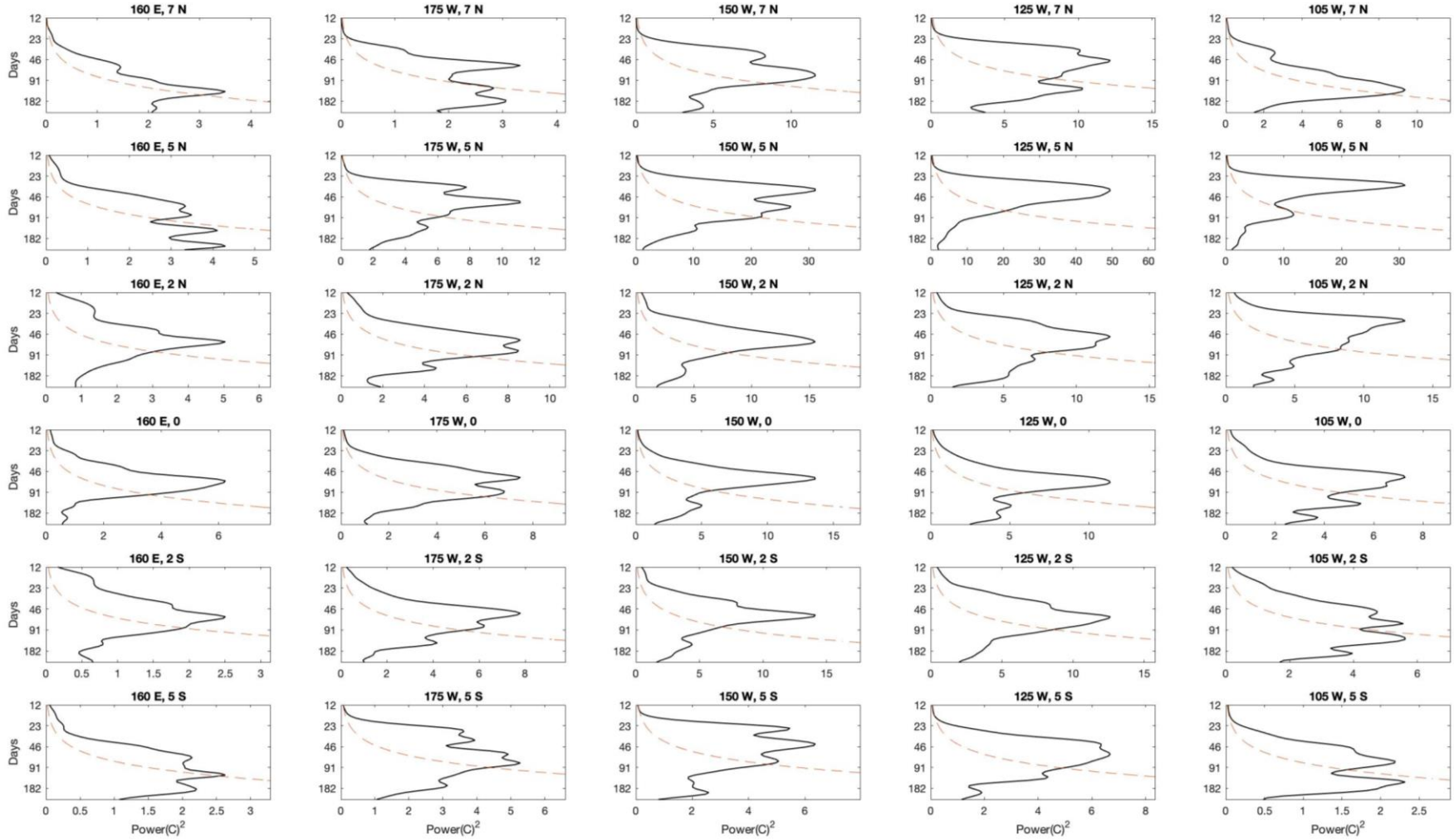

Figure 4.5. Power spectrums for intraseasonal temperature time series for depths indicated in Figure 4.4 at latitudes 7˚N, 5˚N, 2˚N, equator, 2˚S and 5˚S and longitudes 160˚E, 175˚W, 150˚W, 125˚W and 105˚W. The dashed curves denote the 95% significance level.

In order to better understand the individual roles of the various processes that modulate intraseasonal subsurface temperatures, the magnitude of temperature balance was examined (see Appendix A for details). Figure 4.6 shows the standard deviation of the bandpass filtered (10-120 days) temperature time derivative $\left(\frac{\partial T}{\partial t}\right)$ and zonal $\left(u\frac{\partial T}{\partial x}\right)$, meridional $\left(v\frac{\partial T}{\partial y}\right)$ and vertical $\left(w\frac{\partial T}{\partial z}\right)$ advection of temperature. The standard deviation terms are considered of increasing importance as they approach the standard deviation of $\frac{\partial T}{\partial t}$.

We observe that the zonal advection has a significant effect in the central and eastern Pacific regions at latitude 2°N. This relatively high variation is located in the first 100 m of depth and it is also observed at the equator and 2°S regions, possibly being forced by the ISKw (Mosquera-Vásquez *et al.*, 2013). Figure 4.6j, for example, shows the second region of the high variability of zonal advection at the equator, which is located below the mean thermocline depth and that could be related to the dynamic processes of the EUC (Zhang *et al.*, 2010).

Another significant term that contributes to intraseasonal temperature variation in the 2°N region is the meridional advection. The highest standard deviation values are located along the thermocline in the eastern Pacific region. Previous studies (Waliser *et al.*, 2003; Lucas *et al.*, 2010) have pointed out that the dominant factor of the change in intraseasonal temperature is meridional advection that is forced by MJO-generated Kelvin waves. However, in this study, vertical advection is seen to play a major role in the intraseasonal variation of the subsurface temperature, more so than do meridional or zonal advection in the eastern Pacific region (Figure 4.6). This is consistent with what has been reported by McPhaden (2002), who, using mooring data showed that a combination of vertical advection and entrainment are the largest contributors to intraseasonal variability of the eastern Pacific SST.

Variations in vertical advection of temperature are seen to be more prominent below the mean thermocline depth, as was also observed in variations in subsurface temperatures (Figure 4.4). Except for the 7°N region, the influence of vertical advection seems to be

spread throughout the Pacific region. Therefore, it could be associated mainly with both TIWs and the ISKw (Waliser *et al.*, 2003).

In this subsection, attention has only focused on the contributions of the horizontal and vertical advection components. However, other mechanisms, notably diapycnal mixing and entrainment, are potentially relevant to the development of subsurface temperature variations. Here, lateral diffusion and vertical diffusion were calculated, but their terms were insignificant and were therefore excluded from the analysis.

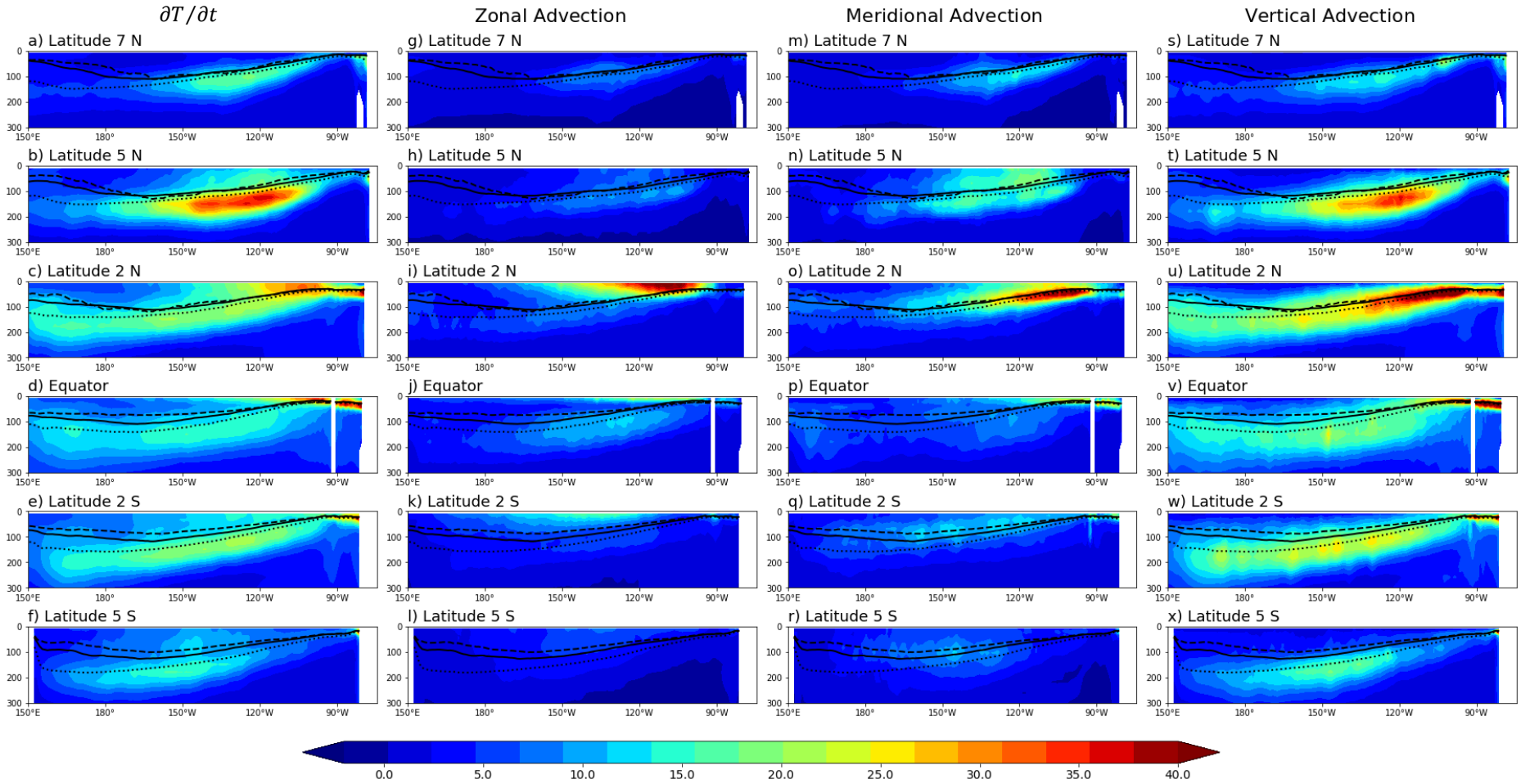

Figure 4.6. Longitude-depth vertical sections of standard deviation (in 10^{-7} ˚C/s) of temperature time derivative, zonal advection, meridional advection, and vertical advection of temperature at latitudes 7˚N, 5˚N, 2˚N, equator, 2˚S and 5˚S from the coast (right edge) to 150˚E in the upper 300 m. Dotted, dashed and solid black lines denote the corresponding mean thermocline, mean halocline and mean pycnocline, respectively.

4.4.2 Salinity

The standard deviation values of the intraseasonal subsurface salinity levels are in the range of 0 to 0.3 psu as shown in Figure 4.7. The maximum standard deviation values are located in the Gulf of Panama. As previously mentioned, this region is characterized by low overall salinity (<33 psu) (Fiedler and Talley, 2006), which is largely explained by precipitation rates that exceed evaporation rates and by freshwater discharges from adjacent rivers (Amador *et al.*, 2006).

A relatively large variation of up to 0.2 psu is also found in the eastern Pacific region mainly at latitude 2°N and the equator, but can also be distinguished with, however, less intensity, at 5°N and 7°N above the mean thermocline depth. In considering the power spectrum in this region (the two rightmost columns of Figure 4.8) it is not possible to identify a single dominant peak. Hence these results suggest that the intraseasonal variation of salinity could be influenced by both the MJO and TIWs (Li *et al.*, 2015).

Another region of significant intraseasonal variability is found in the western Pacific. In this case, the spectral peak period (Figure 4.8) is seen to be concentrated in the 60–90-day band. This is consistent with the findings of Matthews *et al.* (2010), who identified the MJO phenomenon as a driving mechanism for the variability of salinity in the upper Indo-Pacific Ocean region from Argo float data.

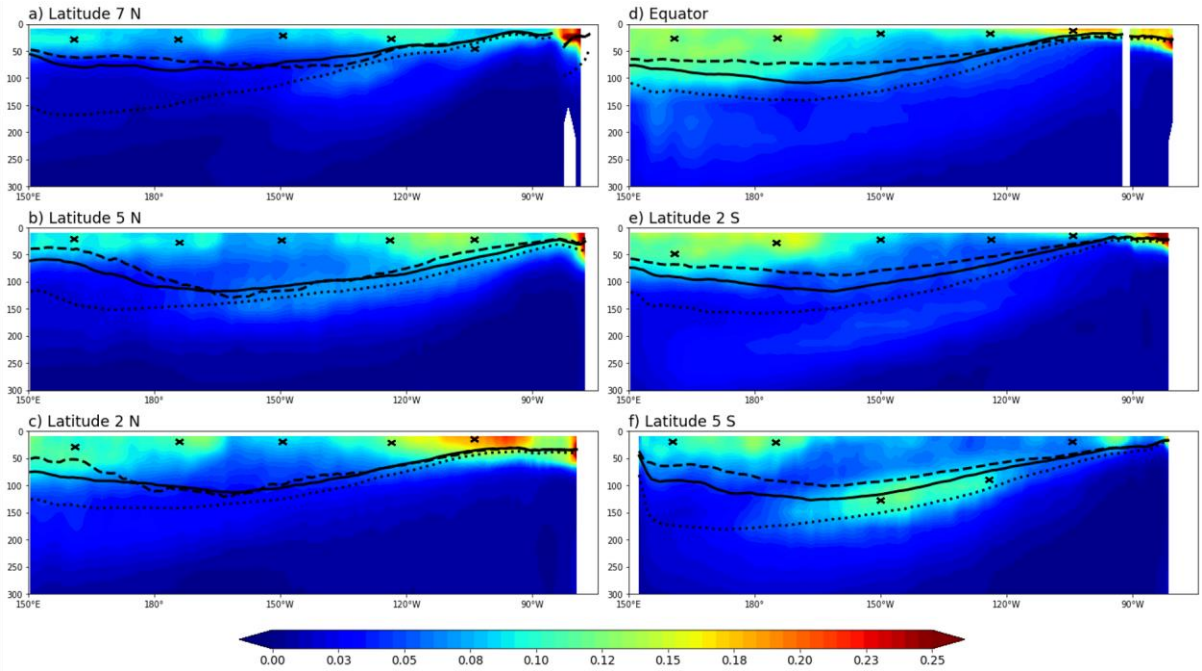

Figure 4.7. Longitude-depth vertical sections of standard deviation filtered salinity (psu) at a) 7˚N, b) 5˚N, c) 2˚N, d) equator, e) 2˚S and f) 5˚S, from the coast (right edge) to 150˚E in the upper 300 m. Dotted, dashed and solid black lines denote the corresponding mean thermocline, mean halocline and mean pycnocline depths, respectively. Crosses denote the locations for which power spectra were computed and are presented in Figure 4.8.

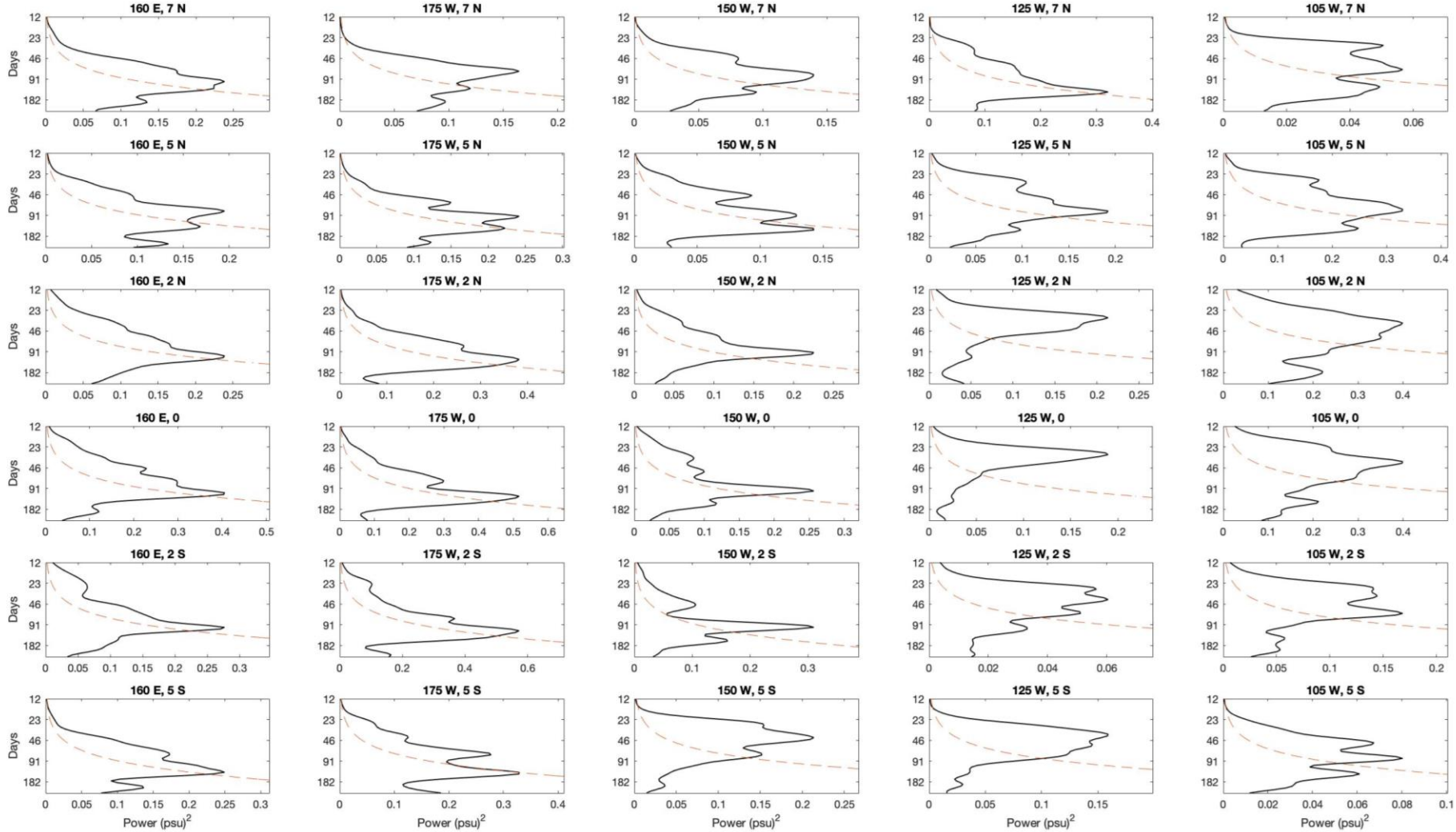

Figure 4.8. Power spectrums for intraseasonal salinity time series for depths indicated in Figure 4.7 at latitudes 7˚N, 5˚N, 2˚N, equator, 2˚S and 5˚S and longitudes 160˚E, 175˚W, 150˚W, 125˚W and 105˚W. The dashed curves denote the 95% significance level.

4.4.3 Zonal Currents

The vertical distribution of the intraseasonal variance of zonal currents is shown for various locations in Figure 4.9. The largest amplitudes of variability occur in the upper 150 m above the mean thermocline depth and only in the western Pacific. The variance is the strongest near the equator at latitudes of the EUC and the SEC (jointly between 3°N and 18°S) and decreases toward higher latitudes at the NECC (between 3°N and 8°N) (Kessler, 2006). Maximum values of intraseasonal variance (standard deviation > 0.25 m/s) are seen to be concentrated mainly in two regions: western and eastern Pacific.

The distribution of the intraseasonal variance in the frequency space allows us to identify the possible mechanisms that may cause this variability (Figure 4.10). The time series in the western Pacific area shows clear power peaks at 45-90 days, particularly those near to the equator. At these low latitudes, the MJO is the most likely candidate to explain this well-defined peak, which is consistent with the conclusions of Zhang *et al.* (2010) and Wang *et al.* (2016b). On the other hand, the points that are located in the central and eastern Pacific areas show pronounced peaks at between 23 to 46 days, notably at 2°N, 5°N, and 7°N. These peaks are likely associated with TIWs (Liu *et al.*, 2019).

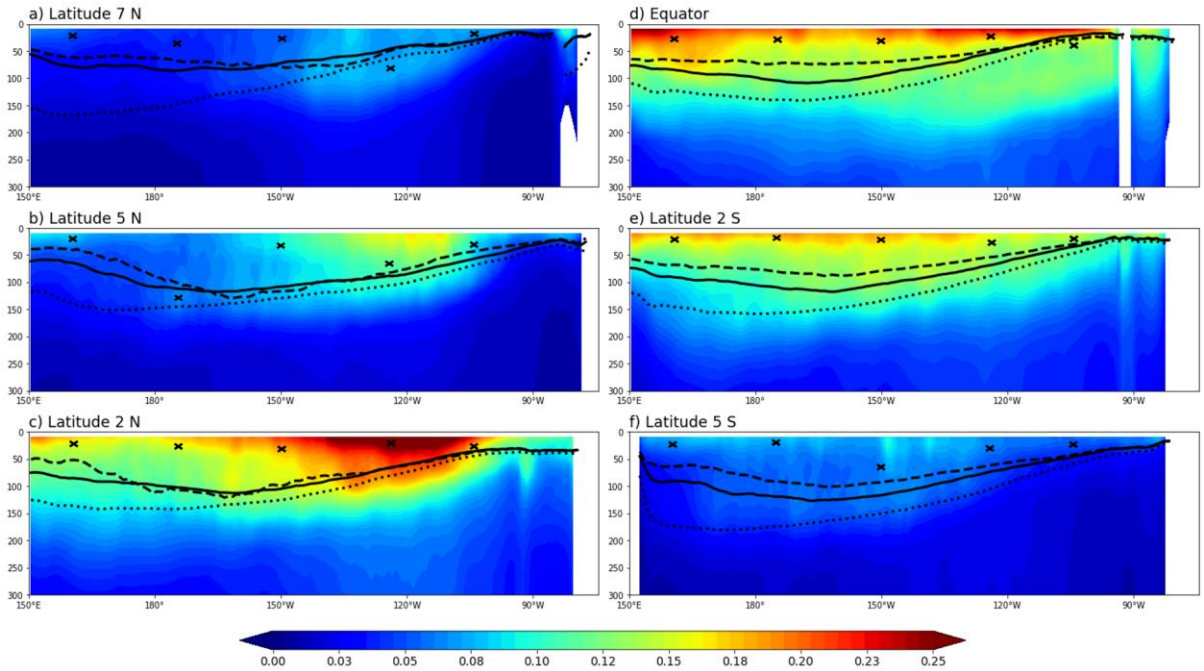

Figure 4.9. Longitude-depth vertical sections of standard deviation filtered zonal currents (m/s) at a) 7˚N, b) 5˚N, c) 2˚N, d) equator, e) 2˚S and f) 5˚S, from the coast (right edge) to 150˚E in the upper 300 m. Dotted, dashed and solid black lines denote the corresponding mean thermocline, mean halocline and mean pycnocline depths, respectively. Crosses denote the locations for which power spectra were computed and are presented in Figure 4.10.

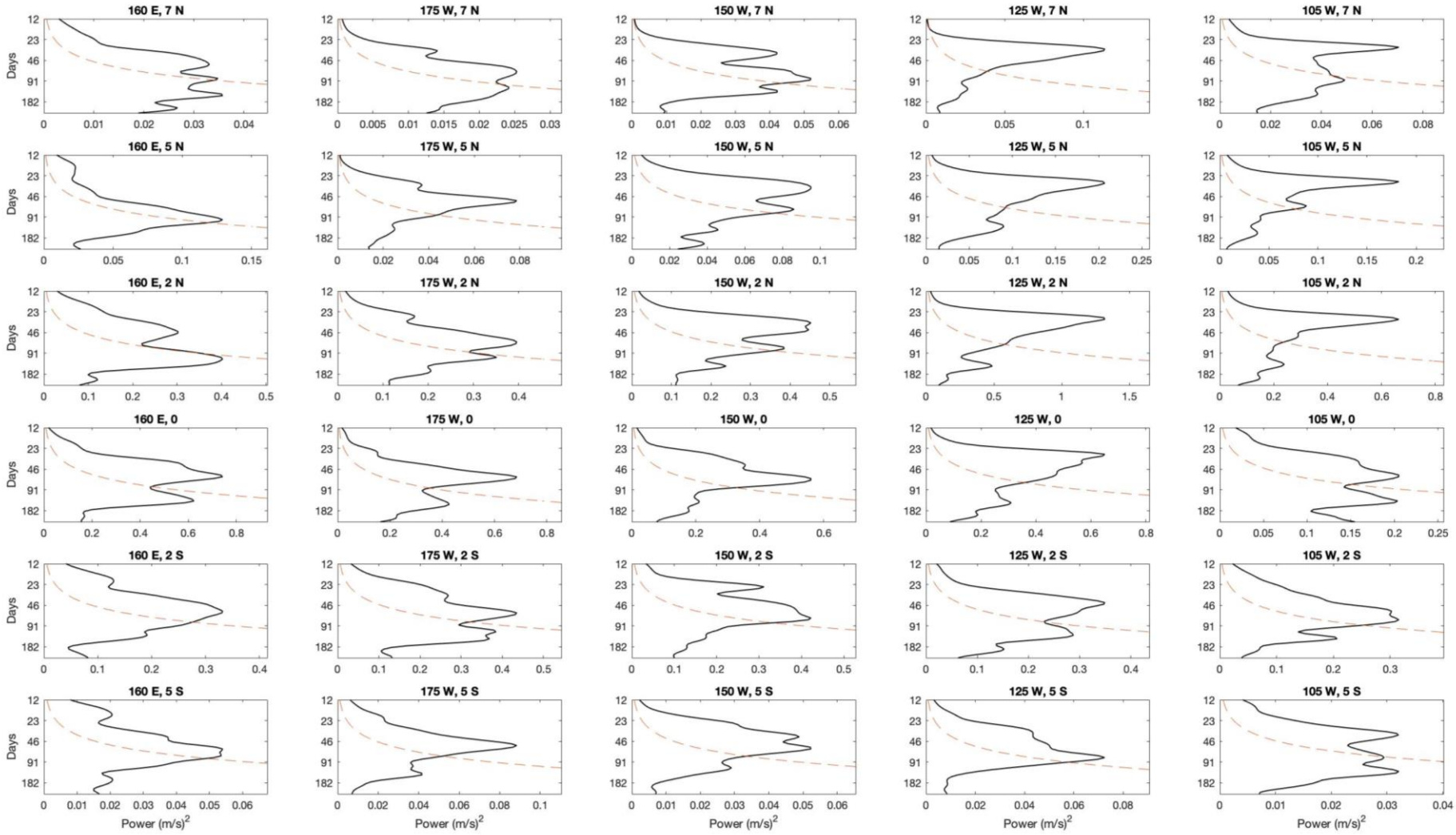

Figure 4.10. Power spectrums for intraseasonal zonal currents time series for depths indicated in Figure 4.9 at latitudes 7°N, 5°N, 2°N, equator, 2°S and 5°S and longitudes 160°E, 175°W, 150°W, 125°W and 105°W. The dashed curves denote the 95% significance level.

4.4.4 Meridional Currents

The spatial patterns of the intraseasonal variability of meridional currents are shown in Figure 4.11. The largest amplitudes, of up to 0.3 m/s, are encountered at latitudes 2°N and 5°N and between 100°W to 150°W. Another relatively high variability region, with standard deviation values that do not exceed 0.2 m/s, extends through essentially the entire Pacific at the equator and 2°S. In both cases, variances are contained in the first 200 m of depth.

In terms of spectral properties, the variance of meridional currents clearly shows spectral peaks of around 30 days (Figure 4.12). Points located in the central and eastern Pacific regions can be individually identified as a single sharp peak for all latitudes. While the westernmost region also displays several prominent and wider peaks but with, however, periods that are no longer than 50 days. The sharpness of the eastern peaks has been mainly associated with TIWs. Computer model simulations and data analysis made by Im *et al.* (2012) showed that 80% of the climatological variability of meridional currents are explained by TIWs around the equator between 110°W and 150°W. More recently, Inoue *et al.* (2019) using moored observations identified that the disturbances in the meridional currents in the first 80 m of depth were related to TIWs in the central equatorial Pacific during 2008.

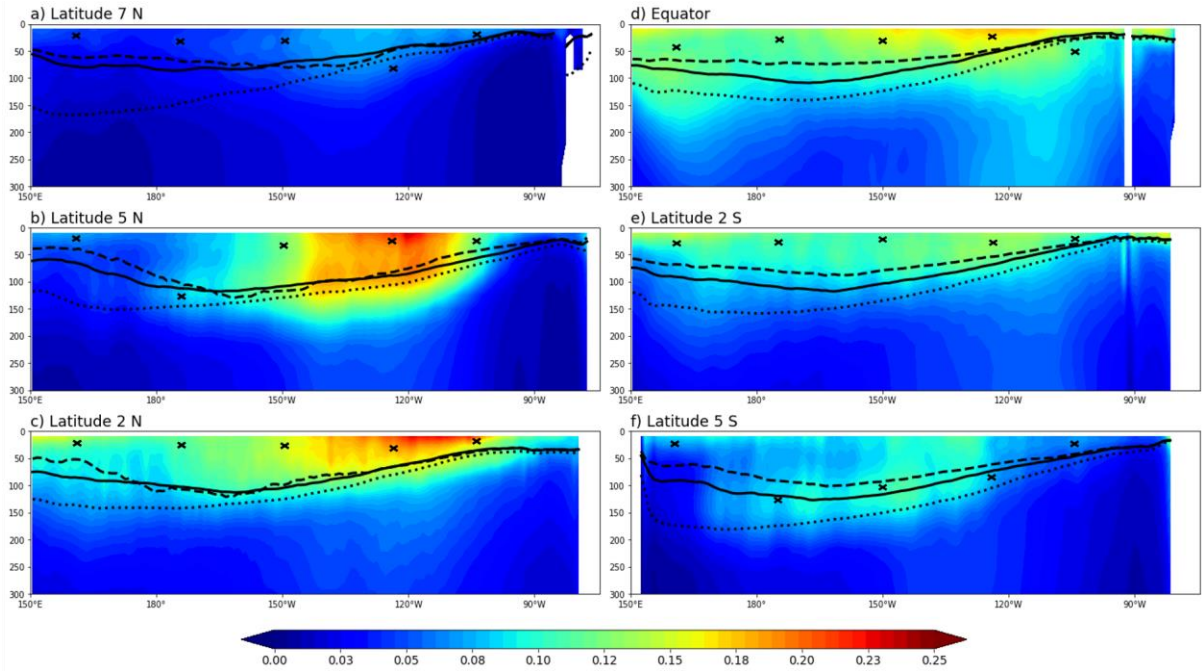

Figure 4.11. Longitude-depth vertical sections of standard deviation filtered meridional currents (m/s) at a) 7˚N, b) 5˚N, c) 2˚N, d) equator, e) 2˚S and f) 5˚S, from the coast (right edge) to 150˚E in the upper 300 m. Dotted, dashed and solid black lines denote the corresponding mean thermocline, mean halocline and mean pycnocline depths, respectively. Crosses denote the locations for which power spectra were computed and are presented in Figure 4.12.

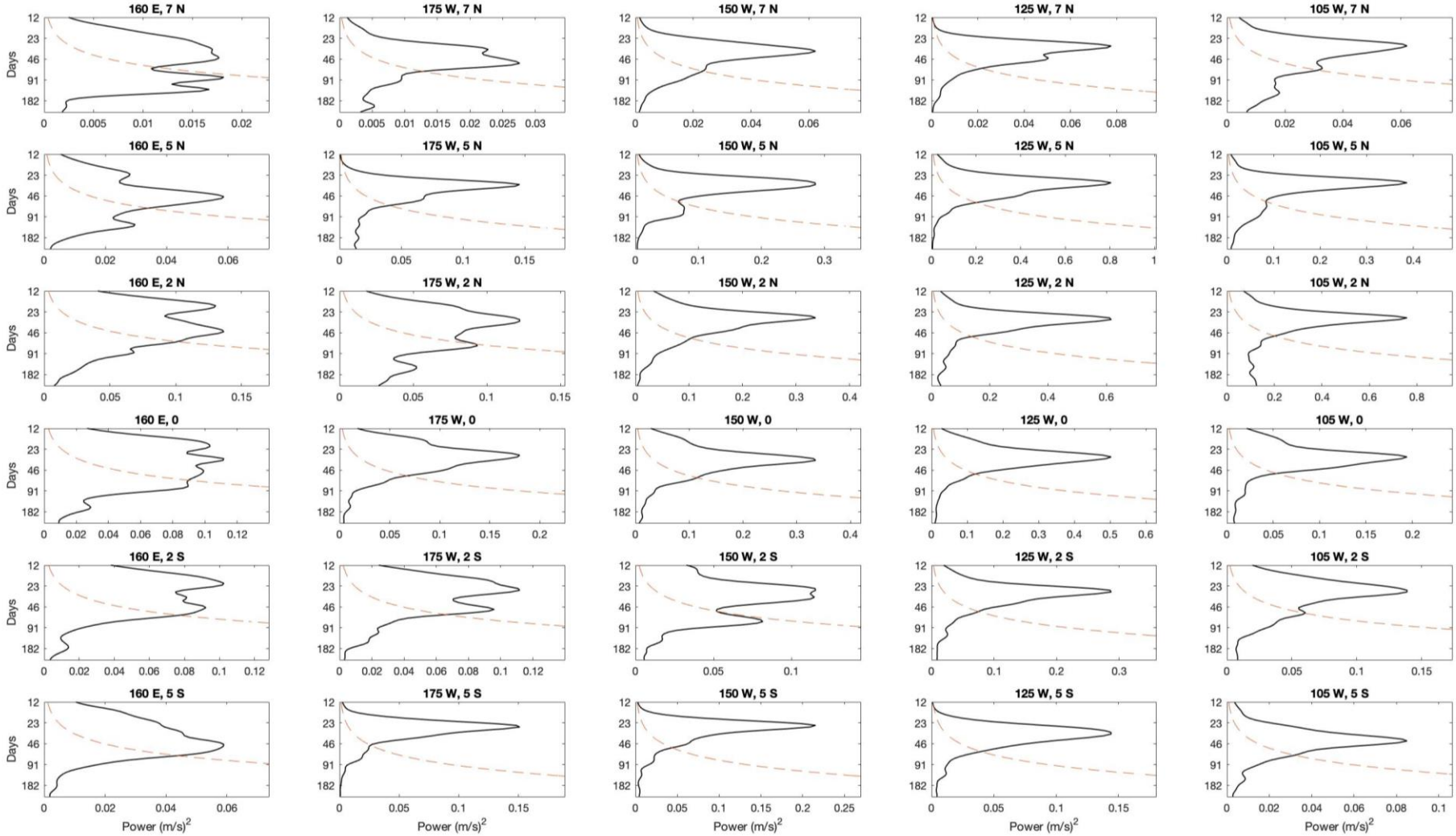

Figure 4.12. Power spectrums for intraseasonal meridional currents time series for depths indicated in Figure 4.11 at latitudes 7°N, 5°N, 2°N, equator, 2°S and 5°S and longitudes 160°E, 175°W, 150°W, 125°W and 105°W. The dashed curves denote the 95% significance level.

4.4.5 Vertical Currents

Variations in the velocities of vertical currents are illustrated by the standard deviation in vertical profiles at different latitudes (Figure 4.13). The maximum standard deviation value of approximately 4.5 x 10^{-5} m/s (about 4 m per day) occurred between 50 and 100 m of depth at latitudes 2°N and 5°N. Relatively high variability is also observed at the equator with standard deviation values up to 4 x 10^{-5} m/s, and these variations are both above and below the depth of the maximum EUC core speed, i.e. 125 m (Halpern *et al.*, 2015) between 90°W and 150°W. Past studies (e.g., Weisberg and Qiao, 2000; Johnson *et al.*, 2001) have estimated similar values of a few metres per day of the vertical circulation in the equatorial Pacific.

Intraseasonal variability in vertical currents has been associated with numerous factors, including variations of local zonal winds, the ISKw (Zhang *et al.*, 2010), and TIWs (Qiao and Weisberg, 1998). These links are also suggested by the results of the dominant period in the power spectrum plots (Figure 4.14). The power spectra show a single prominent signal that is in the range of 23 to 46 days when the time series relates to the north-eastern quadrant, while some of the coordinates that are located south of the equator and in the western Pacific show two separate peaks of around 23 and 46 days.

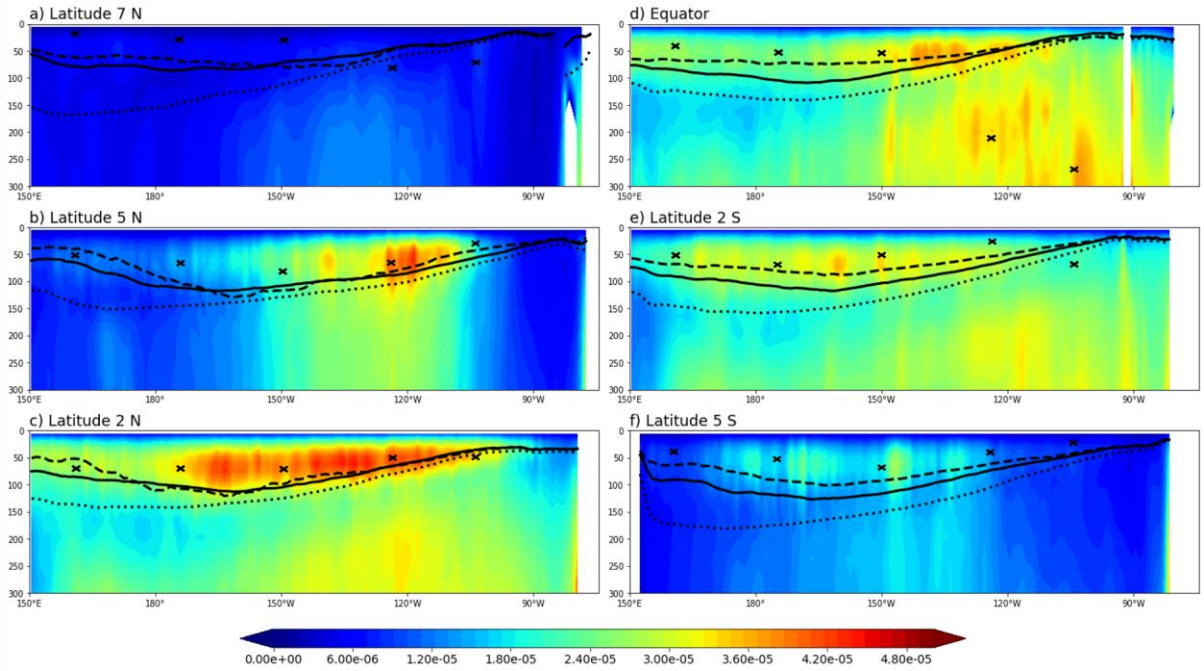

Figure 4.13. Longitude-depth vertical sections of standard deviation filtered vertical currents (m/s) at a) 7˚N, b) 5˚N, c) 2˚N, d) equator, e) 2˚S and f) 5˚S, from the coast (right edge) to 150˚E in the upper 300 m. Dotted, dashed and solid black lines denote the corresponding mean thermocline, mean halocline and mean pycnocline depths, respectively. Crosses denote the locations for which power spectra were computed and are presented in Figure 4.14.

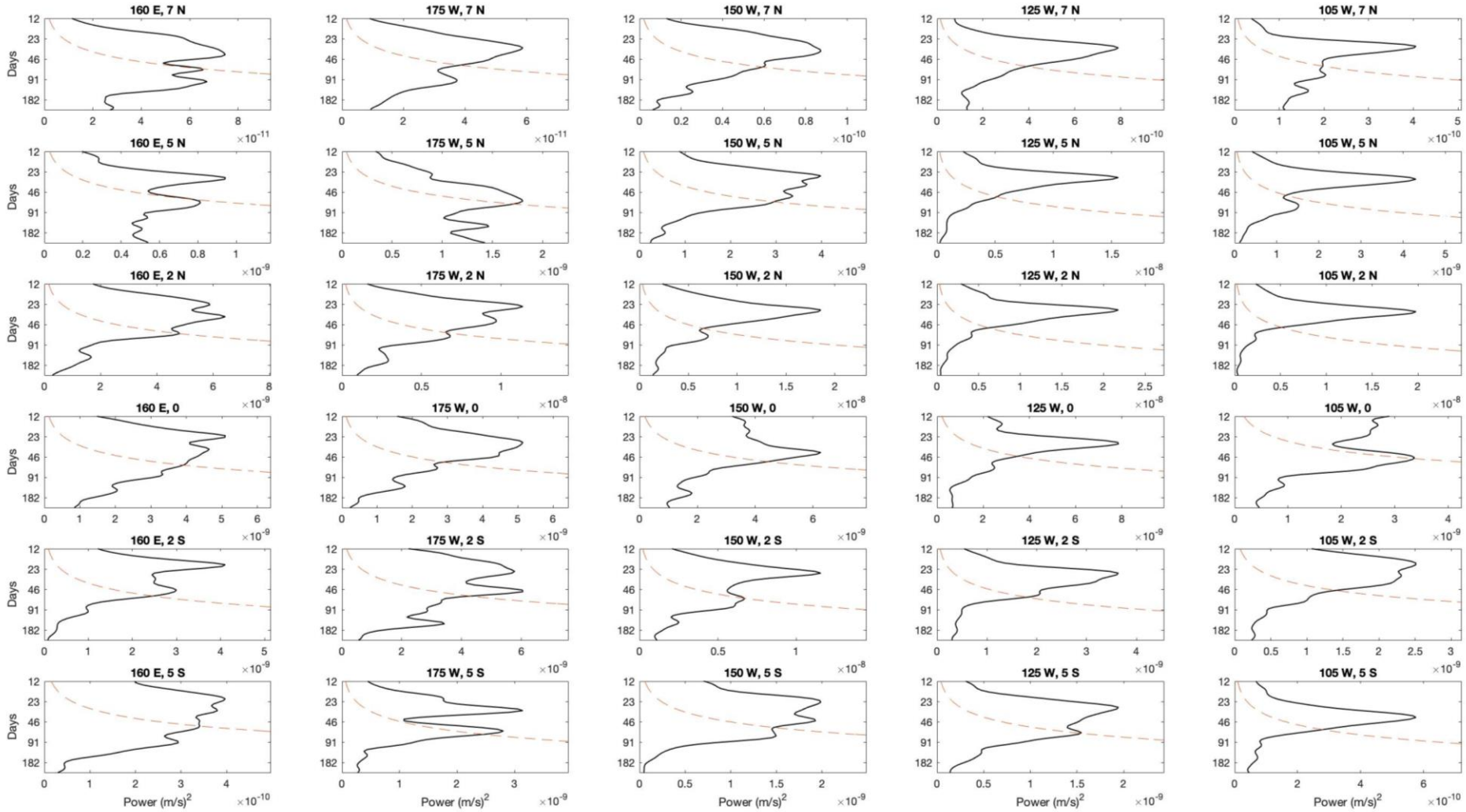

Figure 4.14. Power spectrums for intraseasonal vertical currents time series for depths indicated in Figure 4.13 at latitudes 7˚N, 5˚N, 2˚N, equator, 2˚S and 5˚S and longitudes 160˚E, 175˚W, 150˚W, 125˚W and 105˚W. The dashed curves denote the 95% significance level.

4.5 Potential links with the MJO

In this section, the individual relationships between temperature, salinity, and currents with the MJO are explored through the application of the compositing technique (see Chapter 2). In order to track the MJO activity, the Wheeler-Hendon index (Wheeler and Hendon, 2004) is used (see Chapter 1). A composite is constructed for each phase of the MJO by averaging all days having an MJO amplitude that is greater than one according to the Wheeler-Hendon index. This threshold in amplitude is a criterion that is generally used as an ocean researcher's community standard (Lafleur *et al.*, 2015). Table 3.1, presented earlier, details the number of days per phase in the time period 1990 to 2000. As in the previous chapter, the MJO composites serve to illustrate possible anomalies that may occur in percentages of change from the standard deviation of the entire time series, from now on we refer to this standard deviation as STD. The significance of these composites has been tested by a Student's t-test at the 95% confidence level.

The composite temperature anomalies of all of the eight MJO phases at 2°N, the equator, and 2°S in the top 300 m below the surface are presented in Figure 4.15. The significant maximum negative anomalies for each phase can be seen below the mean thermocline depth. These propagate from the west (phase 1) to the east (phase 8), reaching their greatest values in phase 6. The occurrence of warm subsurface anomalies is found in phases 5 and 6 in the western Pacific. During phase 7, positive anomalies reach up to 40% above of the STD. These anomalies then gradually weaken in the subsequent phases until arriving in the eastern Pacific (phase 3).

These subsurface temperature anomalies have been identified previously as being the product of upwelling and downwelling Kelvin waves (e.g., Kessler *et al.*, 1995; Hendon *et al.*, 1998). From the successive temperature MJO composites (Figure 4.15) the phase velocity of the waves can be estimated at around 2.1 m/s, which is consistent with the typical value of the average phase velocity of Kelvin waves of approximately 2.5 m/s (Rydbeck *et al.*, 2019). Oscillation patterns that we speculate could be related to the presence of TIWs can be observed below the mean thermocline depth, especially during phases 2-3 and 6-7. These interactions will be examined in more detail in the next chapter.

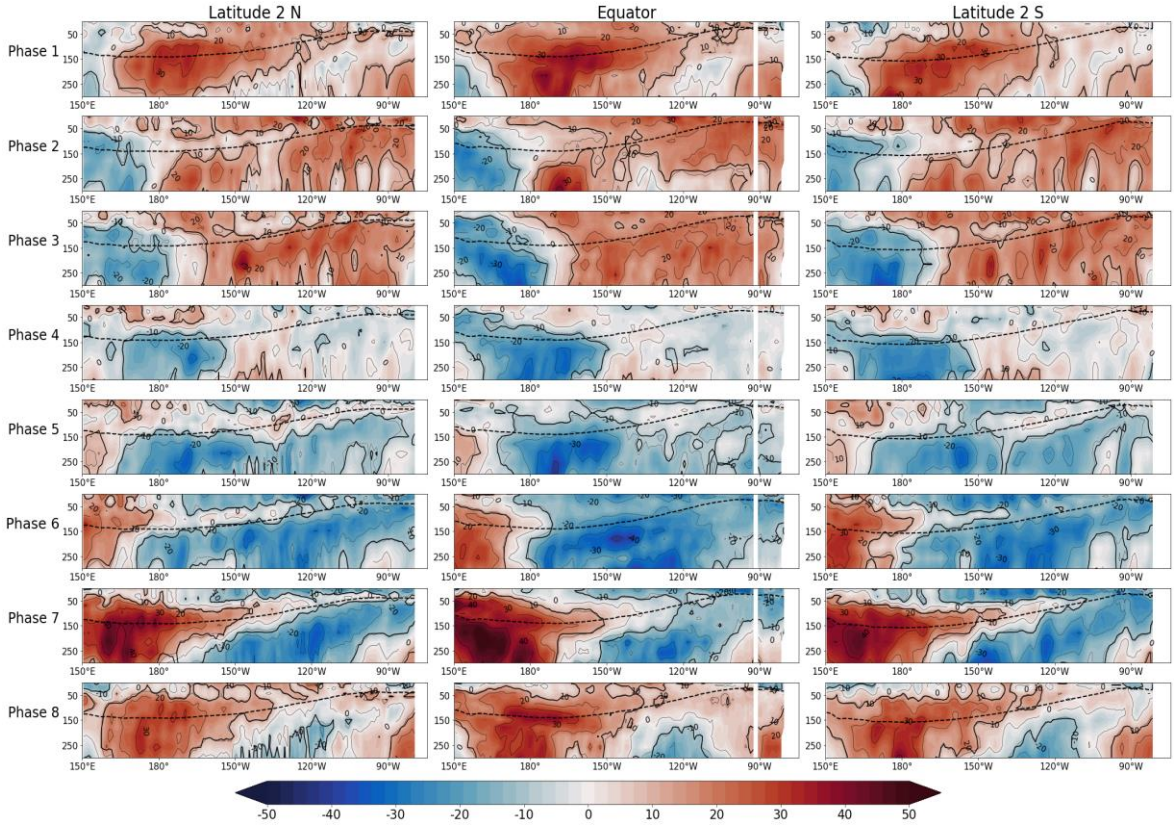

Figure 4.15. Longitude-depth sections showing MJO composites of temperature anomalies relative to total standard deviation (in %) at 2˚N, the equator, and 2˚S, from the coast (right edge) to 150˚E in the upper 300 m. The thick black lines show 95% significance. The dashed lines indicate the corresponding mean thermocline depth.

The signature of the MJO on the subsurface salinity is presented in Figure 4.16. A clear separation between anomalies of different sign either side of the mean thermocline depth can be observed, mainly at the equator and also at 2˚S. During phases 1, 2, and 3 the negative anomalies are above the mean thermocline depth while the positive anomalies are below it. Subsequently, in phases 4, 5, and 6, the converse is the case, with positive anomalies located above the mean thermocline depth and negative anomalies below it. During phases 6 and 7 the anomalies attain maximum values of around ±30% at the equator and 2˚S. The structure at 2˚N is, however, more complex. Here, there is a clear separation of positive and negative anomalies across the mean thermocline depth only in phases 5, 6, and 7, and this is observed mainly in the western and central Pacific regions.

Significant anomalies below the mean thermocline depth appear to be modulated by Kelvin waves through vertical advection (Matthews *et al.*, 2010). For example, at the equator

(Figure 4.16) negative anomalies below the mean thermocline depth seem to propagate eastward from phase 1 to eventually disappear in phase 8. This mechanism resembles the upwelling component of the Kelvin waves, in which fresh cold water rises from below. And this is consistent with what was previously observed in the subsurface temperature anomalies for the same phases (Figure 4.15). The opposite occurs for the downwelling portion of the Kelvin waves, with positive anomalies travelling east from phase 5 in the western Pacific and reaching the eastern Pacific in phase 3. Above the mean thermocline depth, the anomalies are associated with both the zonal displacements of the western Pacific warm pool and horizontal advection (Li *et al.*, 2015).

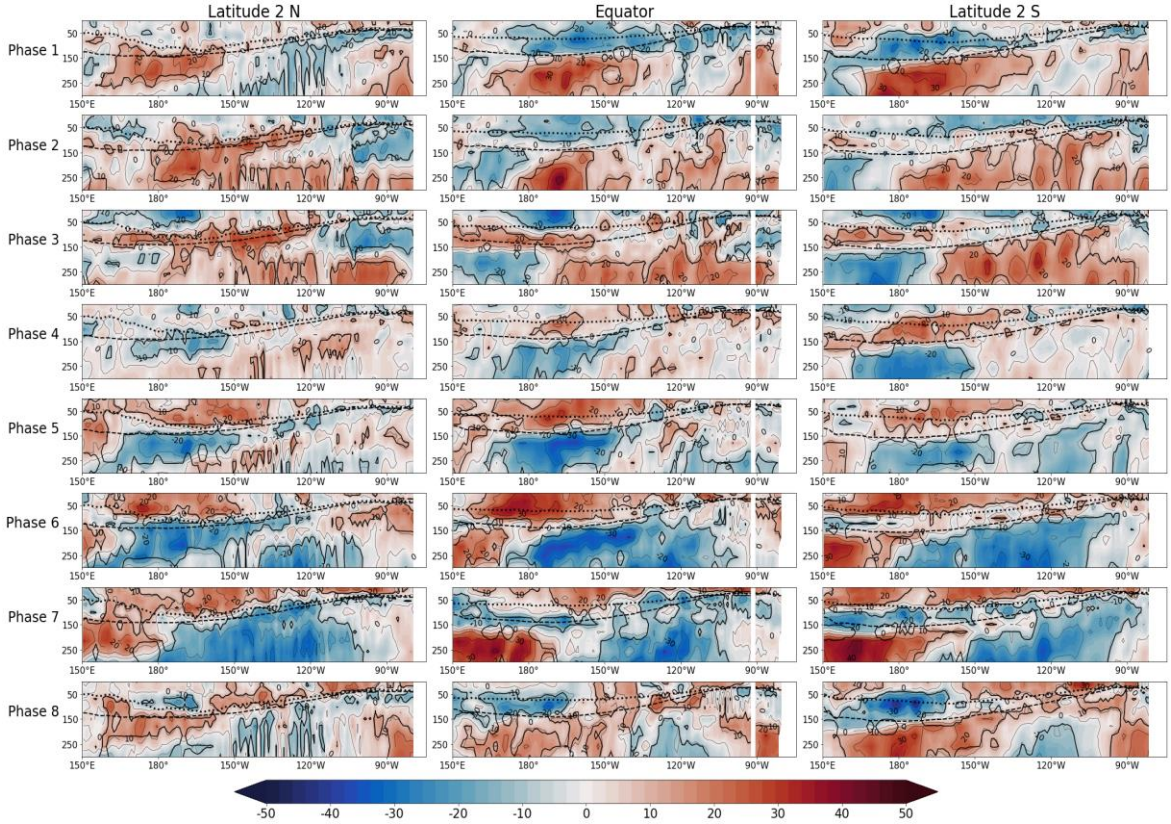

Figure 4.16. Longitude-depth sections showing MJO composites of salinity anomalies relative to total standard deviation (in %) at 2°N, the equator, and 2°S, from the coast (right edge) to 150°E in the upper 300 m. The thick black lines show 95% significance. The dotted and dashed lines indicate the corresponding mean halocline and thermocline, respectively.

The MJO composite for zonal currents is displayed in Figure 4.17. The propagation behaviour of anomalous zonal currents seems again to be associated with Kelvin waves that are induced by MJO wind anomalies (Kessler *et al.*, 1995). The eastward propagation of negative (positive) zonal current anomalies begins in phase 1 (phase 4) in the western Pacific and moves through the Pacific basin until it arrives at the eastern Pacific in phase 8

(phase 3). Although this behaviour is particularly evident at latitudes 2˚N and 2˚S, the signature of the TIWs is also observed in the eastern Pacific. The maximum and minimum anomaly values (around +/- 40% from the average annual STD) are reached in phases 7 and 6 respectively. These results show that not only is the SEC influenced by the MJO cycle, as it had already been pointed out by Wang *et al.* (2016b), but also the EUC, whose core is located at around 100 m below the surface. It is also evident in the MJO composite that when one wave eventually reaches the eastern Pacific another wave is forming in the western Pacific region. This is illustrated, for example at the equator during phases 1 and 4, and this behaviour results from the fact that the MJO has a faster travel speed (~ 5 m/s) than does the Kelvin waves (~ 2.5 m/s) (Wang *et al.*, 2016b).

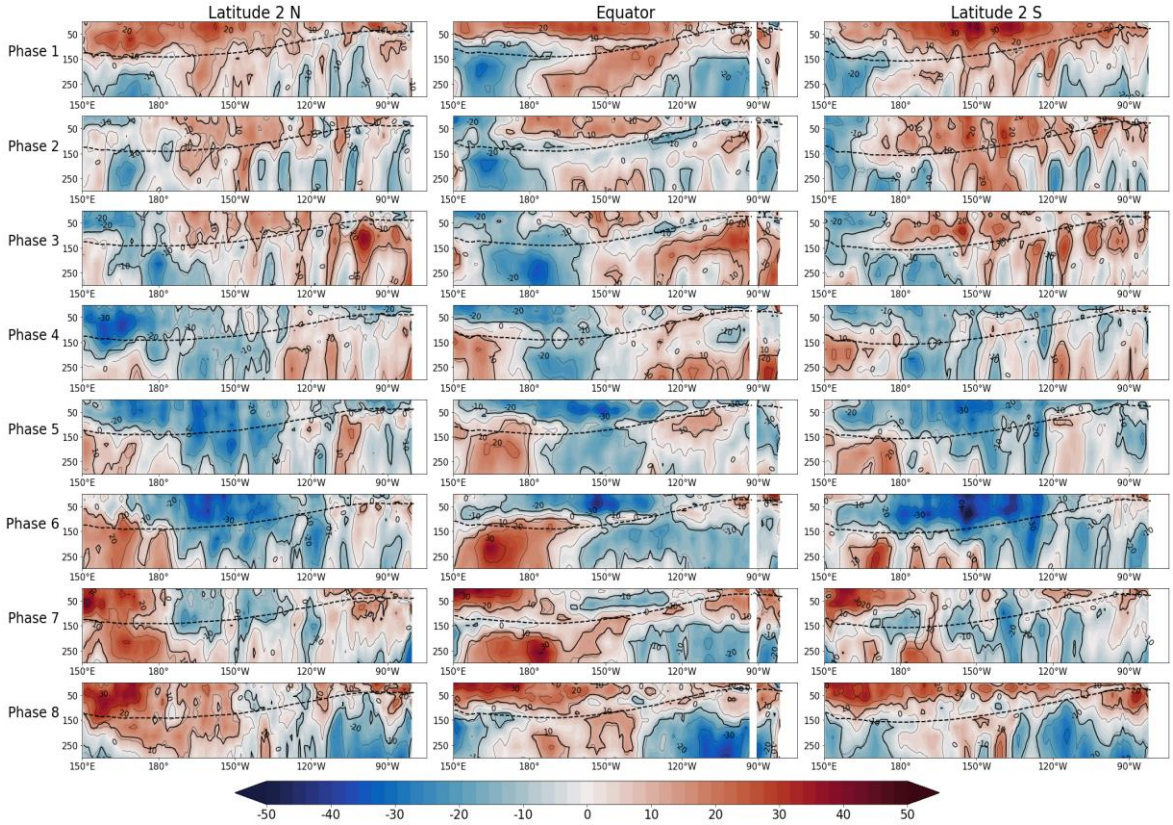

Figure 4.17. Longitude-depth sections showing MJO composites of zonal current anomalies relative to total standard deviation (in %) at 2˚N, the equator, and 2˚S, from the coast (right edge) to 150˚E in the upper 300 m. The thick black lines show 95% significance. The dashed lines indicate the corresponding mean thermocline depth.

In contrast to the zonal current anomalies, the MJO composite of the meridional current anomalies does not reveal a pattern consistent with the propagation of Kelvin waves (Figure 4.18). As mentioned above, meridional velocity intraseasonal anomalies have energy peaks at periods that are not longer than 45 days (Figure 4.12). This is in agreement with the study

by Johnson and McPhaden (1993), who showed that there is no coherence between the meridional current and the equatorial Kelvin wave train.

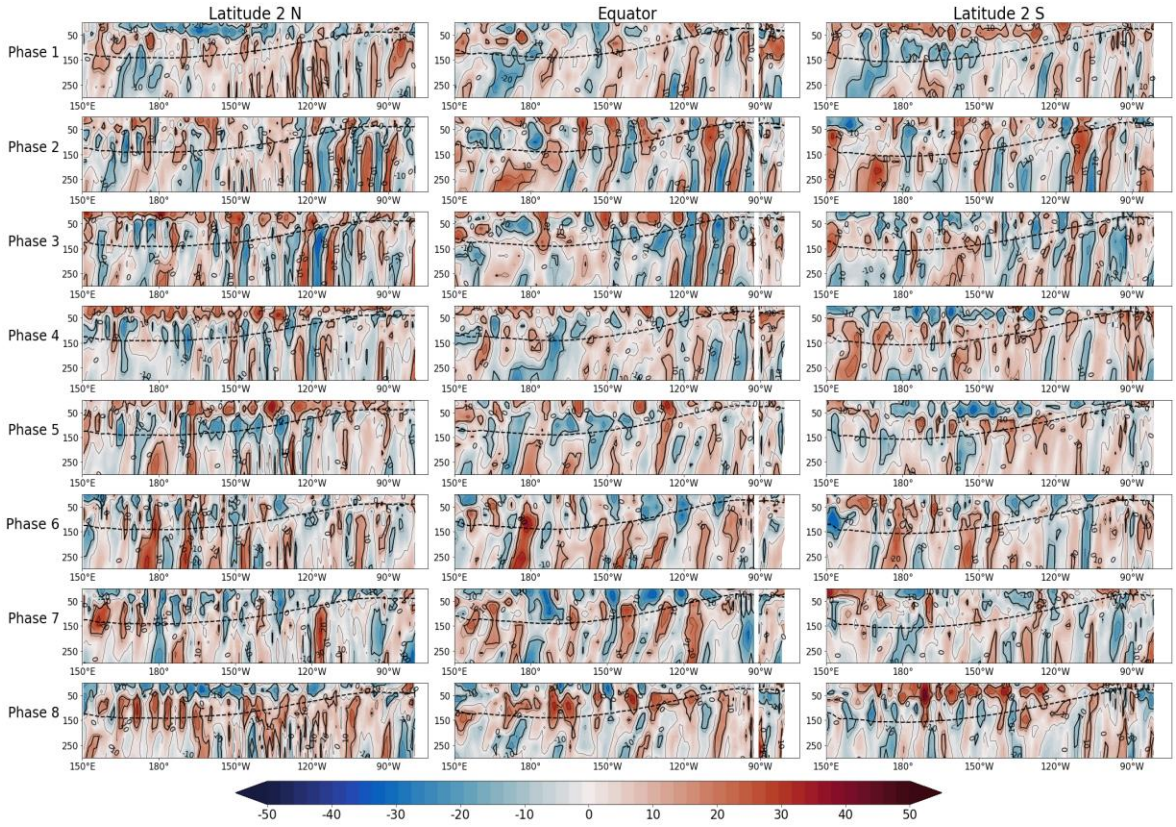

Figure 4.18. Longitude-depth sections showing MJO composites of meridional currents anomalies relative to total standard deviation (in %) at 2˚N, the equator, and 2˚S, from the coast (right edge) to 150˚E in the upper 300 m. The thick black lines show 95% significance. The dashed lines indicate the corresponding mean thermocline depth.

The composite cycle of MJO vertical current anomalies is shown in Figure 4.19. Values that are significantly different from zero at the 95% confidence level are confined to the western and central Pacific regions. At the equator, negative anomalies appear in the western Pacific in phases 3→4 and then travel towards the east in subsequent phases while decreasing in amplitude. Positive anomalies are also seen travelling eastward from phases 8 to 6. The highest anomalies occur in phase 6→7 with values that are 30% below of the STD and phases 3→4 with values that are around 25% above of the STD. The propagation of vertical current anomalies in the 2˚N and 2˚S band exhibits a less clear, perhaps more complex, behaviour. However, the MJO signature can still be observed.

A Granger causality analysis was thus undertaken to identify the regions of the tropical Pacific that are the most affected by the MJO phenomenon, and this is discussed in the following section.

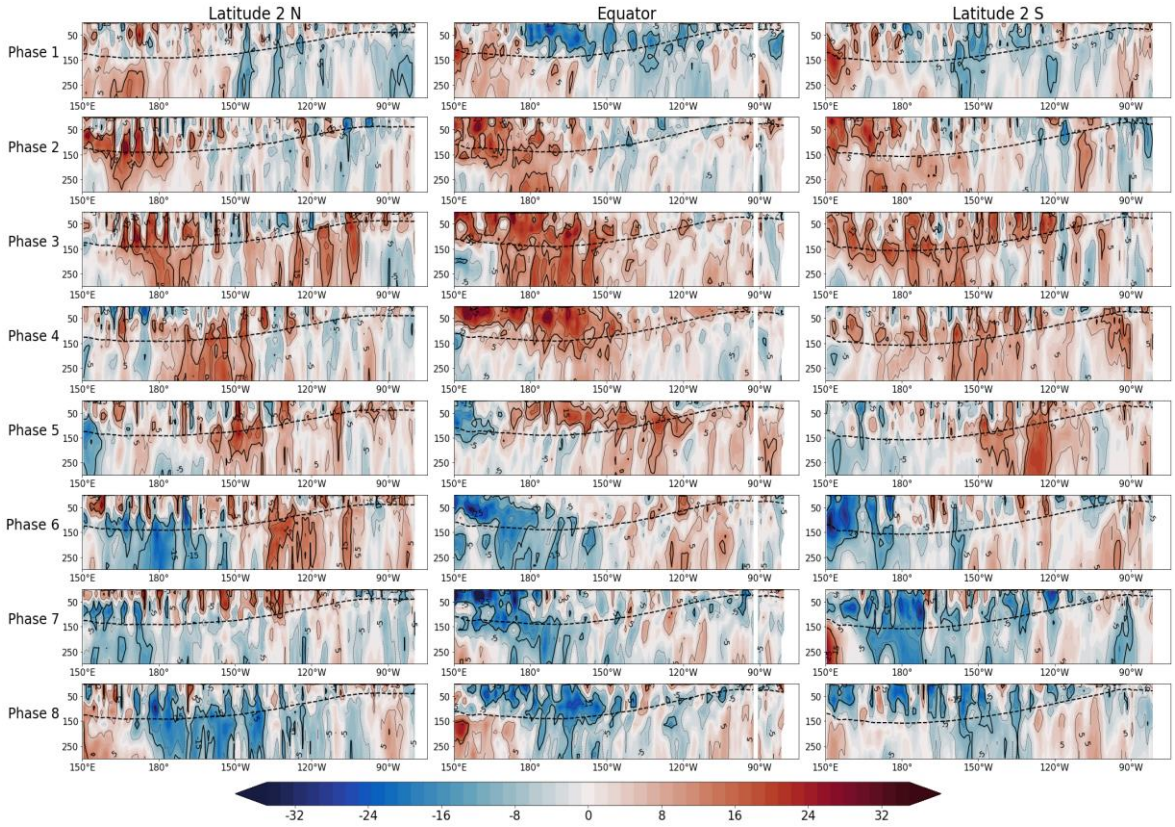

Figure 4.19. Longitude-depth sections showing MJO composites of vertical currents anomalies relative to total standard deviation (in %) at 2˚N, the equator, and 2˚S, from the coast (right edge) to 150˚E in the upper 300 m. The thick black lines show 95% significance. The dashed lines indicate the corresponding mean thermocline depth.

4.6 Lagged linear regression and Granger causality analysis

To establish a more detailed evaluation of the MJO's impact on the subsurface ocean in the tropical Pacific region, a Granger causality analysis and lagged linear regression were carried out. These analyses were applied at four different depths, namely, at the mean mixed, mean thermocline, mean halocline, and mean pycnocline depth. The same methodology employed in the previous chapter (Section 3.5) was followed to establish the Granger causality and to calculate the associated variance. Three simulations were analysed in this way. The first simulation is the one labelled II, in which the II interannual atmospheric forcing is used. The second experiment is labelled IN and is basically the same

as II except that the input of the wind stress comes from the NYF. Finally, the third run is NI, in which the same interannual wind forcing as in II is adopted, but the other forcing fields come from the NYF. For more details on sensitive simulations and associated forcings, see Chapter 2, Section 2.2.

In Figure 4.20, we map the regions where the MJO has a Granger causal effect on ocean temperature variability at different depths. In both the II and the NI runs the mean thermocline is the depth at which the MJO has a greater influence on the intraseasonal temperature variability. Over the equatorial band of the western and central Pacific regions where Granger causality is significant, the intraseasonal variance explained by the linear regression model attains values of up to 28% at an average lag of approximately 24 days (Figures 4.20b and j). At pycnocline and halocline depths we also observe relatively high values of explained intraseasonal variance over this tropical Pacific region for both runs, but weaker for the halocline compared to the pycnocline. This is to be expected considering that the mean pycnocline is closer to the mean thermocline than it is to the mean halocline in this region (Figure 4.4). The output from IN indicates that, at the mixed layer depth, that the MJO Granger-causes temperature variability over the Pacific coast of Central America and the southwestern Mexican coast with a lag average of 23 days. Especially in the former region, this means that intraseasonal wind stress forcing is not the main factor to explain surface temperature variability. This finding is consistent with results discussed in the previous chapter (Section 3.4) and with the study by Maloney and Kiehl (2002), who suggest that the intraseasonal variability of the temperature of this region is mainly regulated by latent heat fluxes and shortwave radiation.

Figure 4.21 shows the numerical results for the potential of the MJO to drive the intraseasonal variability of salinity. In both the II and the NI runs, the Granger causality of the MJO on salinity at halocline and pycnocline depths falls into two main ocean regions. The first is located in the equatorial band of the western Pacific and the second south of the Isthmus of Tehuantepec and the Central American Pacific coast with an average lag of approximately 23 days. The Granger causal link is also observed in the latter region at mean thermocline depth. Thus, these results suggest that the intraseasonal variability associated with the MJO is primarily induced by intraseasonal wind stress effects.

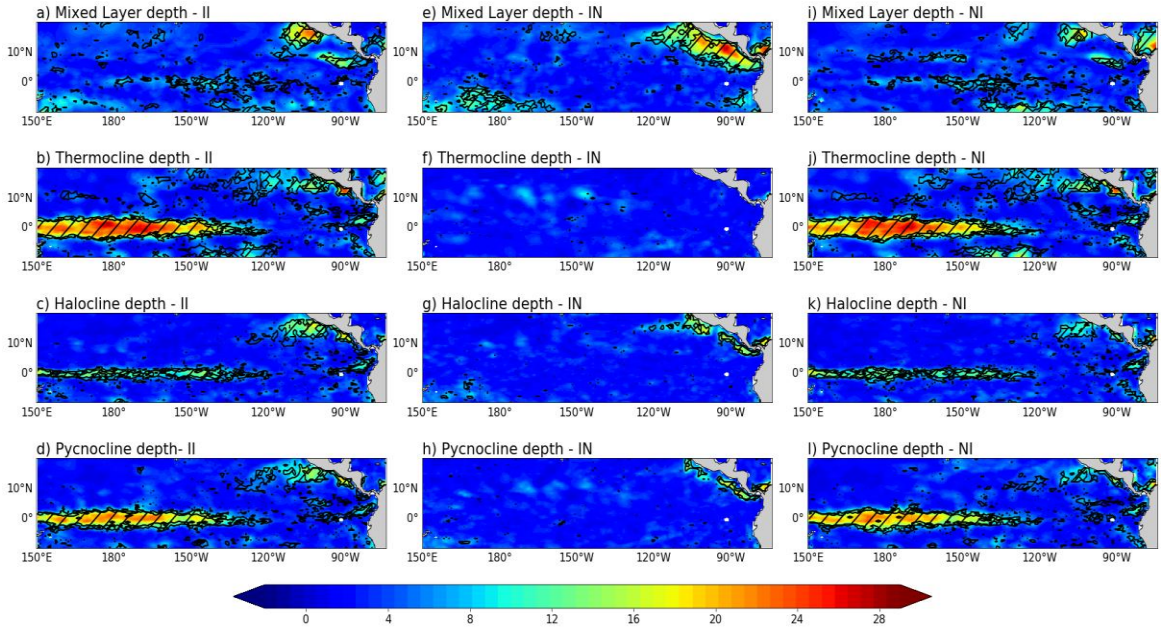

Figure 4.20. Variance (%) explained by the lagged linear regression model for filtered temperature anomalies at the mixed layer depth (a, e, and i), the mean thermocline depth (b, f, and j), the mean halocline depth (c, g, and k) and the mean pycnocline depth (d, h, and l) regressed against RMM1 and RMM2, based on II (left), IN (centre) and NI (right) output. The hatched regions indicate a significant Granger causality test. Significance is assessed at a 99% confidence level.

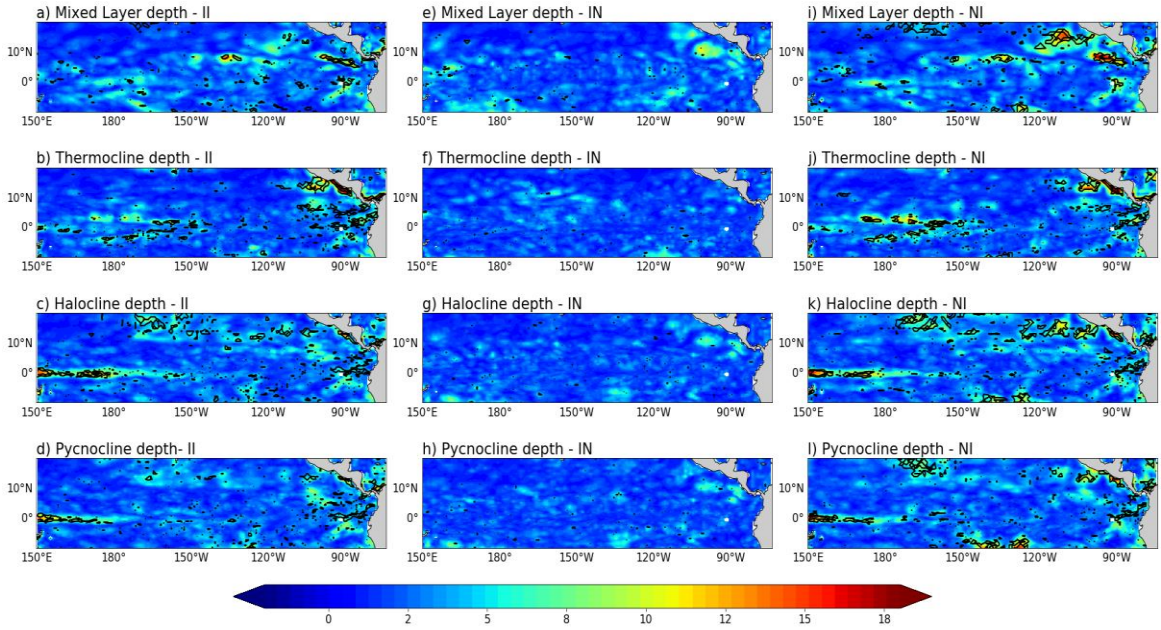

Figure 4.21. Variance (%) explained by the lagged linear regression model for filtered salinity anomalies at the mixed layer depth (a, e, and i), the mean thermocline depth (b, f, and j), the mean halocline depth (c, g, and k) and the mean pycnocline depth (d, h, and l) regressed against RMM1 and RMM2, based on II (left), IN (centre) and NI (right) output. The hatched regions indicate a significant Granger causality test. Significance is assessed at a 99% confidence level.

The Granger causality analysis for the intraseasonal zonal current is shown in Figure 4.22. The maximum variance (20%) explained by the lagged regression model is found in the MLD with a lag average of 23 days, in both the II and the NI numerical studies. At this level, the MJO Granger causality of the zonal current is significant over a region that extends throughout the eastern and central Pacific regions north the equator and over an equatorial band spanning the central and western Pacific (Figures 4.22a and i). The influence of the MJO on zonal currents can also be observed in the mean thermocline, the mean halocline, and in the mean pycnocline over the western and central equatorial Pacific, but the pattern is very discontinuous. Clearly, the dominant forcing accounting for the MJO influence on zonal current intraseasonal variability is the wind stress.

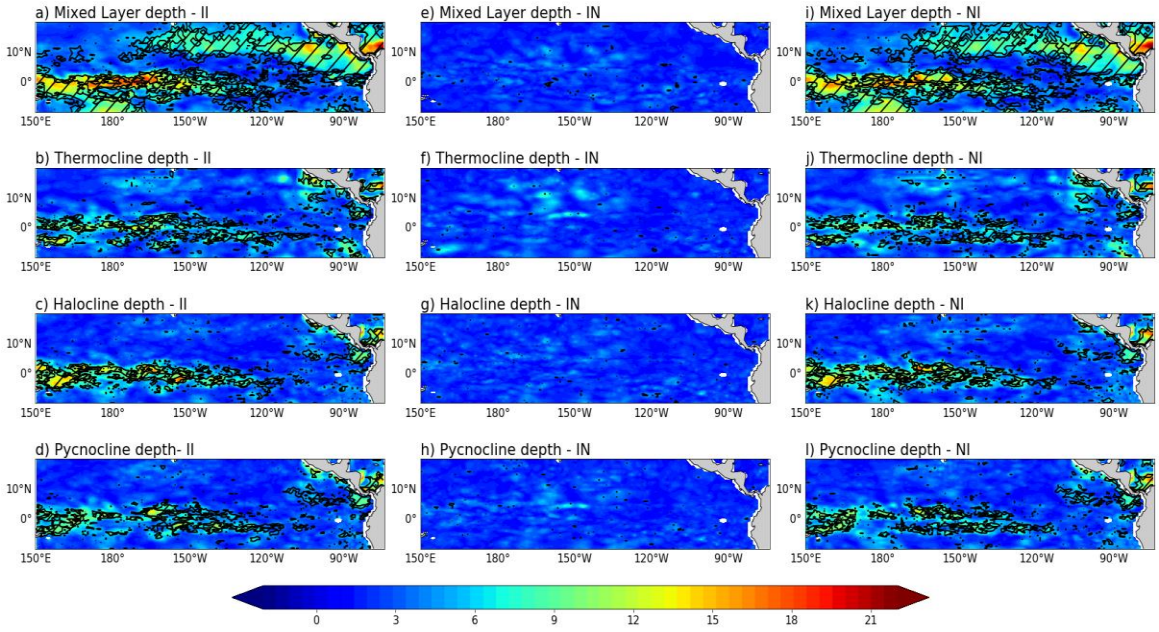

Figure 4.22. Variance (%) explained by the lagged linear regression model for filtered zonal current anomalies at the mixed layer depth (a, e, and i), the mean thermocline depth (b, f, and j), the mean halocline depth (c, g, and k) and the mean pycnocline depth (d, h, and l) regressed against RMM1 and RMM2, based on II (left), IN (centre) and NI (right) output. The hatched regions indicate a significant Granger causality test. Significance is assessed at a 99% confidence level.

Figure 4.23 shows the results of the Granger causality analysis on the meridional currents. Granger causality can be identified at the MLD depth outside the equatorial band, in the region north of 5°N, showing the highest percentage of variance (> 20%) in the eastern Pacific, with a lag average of 23 days, for both the II and NI experiments. For these experiments, the previously noted causal relationship can also be observed at the halocline and pycnocline depths, although weaker and in a smaller region of the ocean. Thus, the

variance explained in these northern latitudes is predominantly the manifestation of intraseasonal wind stress forcing.

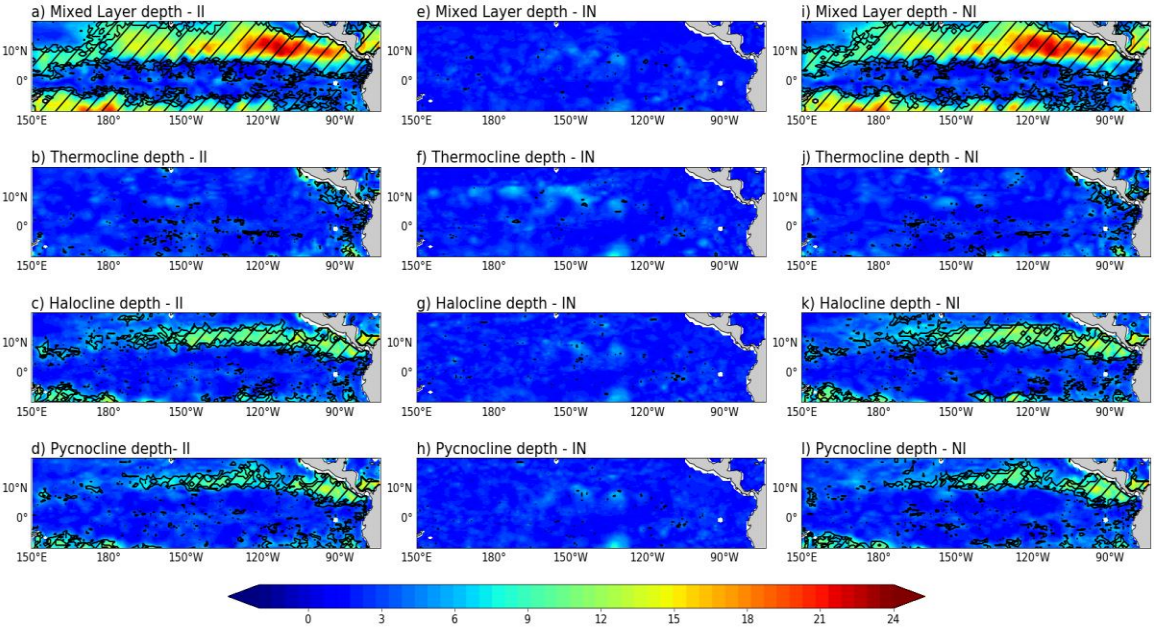

Figure 4.23. Variance (%) explained by the lagged linear regression model for filtered meridional current anomalies at the mixed layer depth (a, e, and i), the mean thermocline depth (b, f, and j), the mean halocline depth (c, g, and k) and the mean pycnocline depth (d, h, and l) regressed against RMM1 and RMM2, based on II (left), IN (centre) and NI (right) output. The hatched regions indicate a significant Granger causality test. Significance is assessed at a 99% confidence level.

Finally, the analysis of the Granger causal relationship between the MJO and vertical currents is summarised in Figure 4.24. The Granger causality shows a significant response in the mean thermocline, mean halocline, and mean pycnocline depths over relatively narrow equatorial bands of the western and central Pacific and over the eastern Pacific warm pool region, with an average lag of 23 to 24 days in experiments II and NI. The eastern Pacific warm pool is typically characterized by high nutrient concentration levels supplied by both vertical mixing and upwelling associated with local wind jets forcing (Fiedler and Talley, 2006). The variability of the Intertropical Convergence Zone, which modulates these wind jets, is affected by the MJO (Raymond *et al.*, 2006).

It is perhaps remarkable that all the hydrographic variables we have investigated have a highest correlation with the MJO index at a lag of about 23-24 days, which clearly indicates they are all responding almost in unison to the MJO forcing. Explaining this synchronised

behaviour is beyond the scope of this work but this is, no doubt, behaviour that calls for a dynamic explanation.

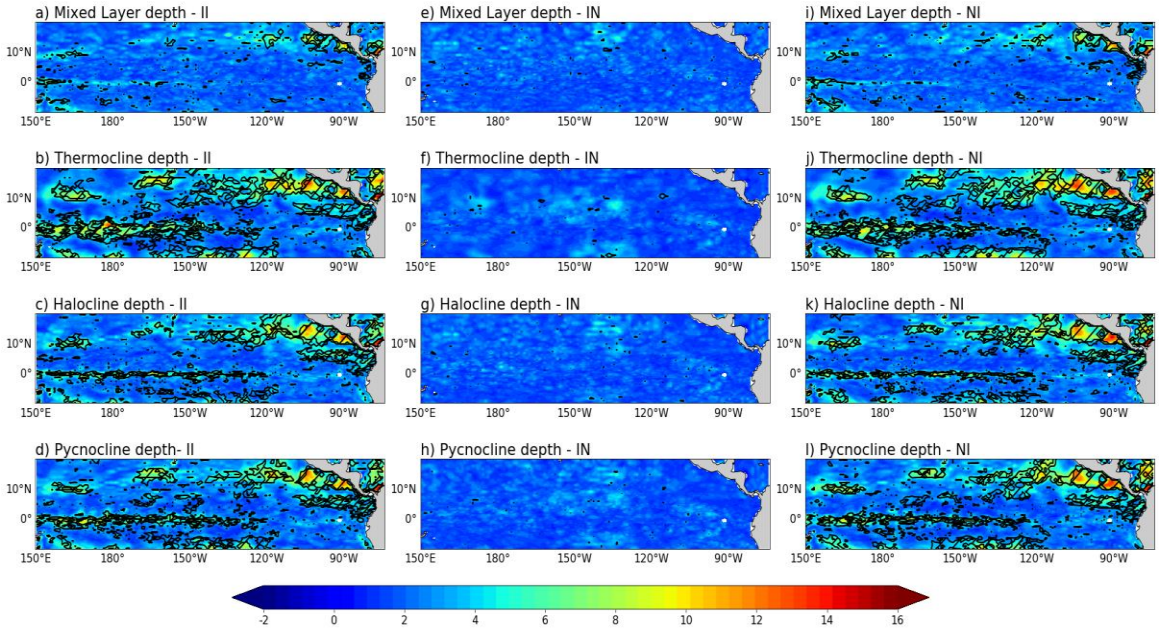

Figure 4.24. Variance (%) explained by the lagged linear regression model for filtered vertical current anomalies at the mixed layer depth (a, e, and i), the mean thermocline depth (b, f, and j), the mean halocline depth (c, g, and k) and the mean pycnocline depth (d, h, and l) regressed against RMM1 and RMM2, based on II (left), IN (centre) and NI (right) output. The hatched regions indicate a significant Granger causality test. Significance is assessed at a 99% confidence level.

4.7 Summary

The effects of the MJO on the vertical structure of the upper ocean (the first 300 m below the surface) in the tropical Pacific have been examined in this chapter. The salient contributions of this chapter are:

- The intraseasonal variability (averaged between 10-260 m) of temperature, salinity, and ocean currents is mainly found in zonal regions located about five degrees north and south of the equator. In these regions, the intraseasonal variance of these fields can represent up to 90% of the total variance (in the case of meridional currents). The MLD, the mean thermocline, the mean halocline, and the mean pycnocline depths all show the highest percentages of intraseasonal variance (of around 60% of the total variance) in the eastern and central equatorial Pacific regions (Figure 4.3).
- The analysis of vertical sections at six selected latitudes allowed us to establish the regions with the highest intraseasonal variability, and the corresponding power

spectrum was also calculated in order to identify the dominant periods within the said intraseasonal timescale. Thus, for example, for the subsurface temperature, the region of greatest variance is located at 5°N below the mean thermocline depth in the central Pacific region, with spectral peaks of between 23-46 days (Figures 4.4 and 4.5). For the subsurface salinity, the highest STD values are encountered in the top 50 m in the eastern Pacific region (Figure 4.7). Similarly, the greatest variance in the velocities of ocean currents occurs above the mean thermocline depth, and mainly at the equator, and also at 2°N and 5°N (Figures 4.9, 4.11 and 4.13).

- An examination of the longitude-depth composites shows a strong influence of the MJO on temperature, salinity, zonal current and vertical current in the first 300 m of depth, particularly at the equator. Figure 4.15 illustrates, for example, that positive temperature anomalies can reach values of up to 50% of the total STD of temperature during phase 7 of the MJO. This MJO cycle for ocean currents is presented here for the first time.
- Granger causality was used to determine the spatial patterns of the influence of the MJO on the intraseasonal variability of the tropical Pacific. In addition to the control simulation (II), two other experiments using variations of the original atmospheric forcing were carried out to separate the dynamic and thermodynamic forcing associated with the MJO. In NI interannual winds are used (as in II) but the thermodynamic forcing (heat and freshwater fluxes) has no interannual variability. In contrast, in IN, the interannual variability of the wind, dynamic forcing is supressed, while that of the thermodynamic forcing is retained. In the two simulations with interannual wind forcing, II and NI, MJO Granger causality is evident mainly over the equatorial band and north of 5°N with a lag average of 23-24 days, thus demonstrating that the intraseasonal variability of the wind is the key control of the MJO's impact on the tropical Pacific Ocean. In the absence of interannual winds, that is, in the IN simulation, MJO Granger causality is detected only within the mixed layer depth off the Central American and southwestern Mexican coasts.

The results obtained and reviewed in this chapter and in the previous chapter have helped us to identify several mechanisms that are potentially responsible for the intraseasonal ocean variability in the region.

Chapter 5

The influence of the Madden-Julian Oscillation on Tropical Instability Waves in the eastern tropical Pacific

5.1 Introduction

The impact on the upper ocean of the dominant mode of intraseasonal variability in the tropical atmosphere, the MJO, has been examined in earlier chapters. However, the ocean itself has its own complex modes of intraseasonal variability. This internal oceanic variability also has a large amount of latent power at the intraseasonal scale that manifests itself in various phenomena such as mesoscales eddies, gyres, meanders of ocean jets, submesoscale filaments and tropical instabilities waves (TIWs) (Willett *et al.*, 2006). In the tropical Pacific Ocean, the TIWs are considered to be one of the more prominent of the mesoscale features (e.g., Legeckis, 1986).

The purpose of this chapter is thus to identify and then quantify the possible influence of the MJO on TIWs. The data chosen for this comes from the daily output obtained from six different numerical simulations. The numeric experiments used are II, IN, NN, NI, NN+, and NN- as summarized earlier in Table 2.4. More information on these numerical experiments can be found in Chapter 2 (Section 2.2), with Table 2.4 repeated below for the reader's convenience.

Table 2.4 Characteristics of the numerical experiments.

Name	Atmospheric forcing excluding winds	Winds stress forcing
NN	**N**YF	**N**YF
II	**I**AF	**I**AF
IN	**I**AF	**N**YF
NI	**N**YF	**I**AF
NN+	**N**YF	**N**YF +50%
NN-	**N**YF	**N**YF -50%

The contents of this chapter are organized as follows: Section 2 presents the results of sensitivity simulations in which TIWs are identified and their meridional related variations

are discussed. The spatial and vertical distributions of the source of the TIWs are given in Section 3, and the influence of the MJO on these is then examined in Section 4. The various observations and findings are summarized in Section 5.

5.2 Identification of TIWs

In order to assess the ocean model's ability to capture the characteristics of TIW activity and how this activity varies with different atmospheric forcings, the eddy kinetic energy (EKE) was computed from the results of each of four selected simulations, as follows. The II experiment covers the period between 1990 and 2000. Each of the other three simulations, NN, NN+ and NN-, are forced with NYF fields and, like II, span 11 years of integration. To identify EKE disturbances due to TIW dynamics, a 10-120-day intraseasonal band-pass filter was applied to the velocity field and then the EKE computed as

$$EKE = \frac{1}{2}\left(u'^2 + v'^2\right) \tag{5.1}$$

where u' and v' are the filtered zonal and meridional velocity components respectively. The resulting EKE values regionally averaged over the band 0–5°N, (the latitudes that are observed to be spanned by the most energetic TIWs, Figure 5.3) are shown in Figure 5.1 as longitude-time, Hovmöller plots. In each of the four simulations, the TIWs can be clearly identified. Their eastwards propagation and characteristic seasonal behaviour (from July to December) are evident. From this figure, the typical phase velocity and wavelength of the TIWs can be calculated as 0.55 m/s and ~ 1100 km respectively. These values are consistent with recorded observations, such as those from the Tropical Instability Wave Experiment (TIWE) (Qiao and Weisberg, 1995).

In the output from the II run, Figure 5.1, which uses interannual atmospheric forcing, it is also possible to observe the influence of the El Niño–Southern Oscillation (ENSO) on the TIWs. The TIW signal intensifies during La Niña events (blue boxes) and, conversely, the signal is weaker during El Niño events (red boxes). These observed variations have been studied by other researchers in the past, e.g., An (2008), who suggested the existence of a negative feedback on ENSO by TIWs. In other words, the TIWs partially contribute to ENSO's Niño-Niña asymmetry, and it appears that the TIWs, possibly due to thermal

advection, induce warming during La Niña years and correspondingly cooling during El Niño years.

The other three simulations allow us to gauge the contribution that different strengths of wind stress from NYF can make on the intensity of the EKE. In the NN+ run the EKE reaches values that are greater than 1 m^2/s^2, while in the NN- run the maximum values of EKE are approximately 0.4 m^2/s^2. The maximum EKE values are either doubled or decreased by 50% in simulations NN+ and NN- respectively, with respect to the highest values of the NN experiment. This is to be expected in an ocean region where wind stress is the dominant factor in oceanic circulation (Kessler, 2006). Furthermore, it can be seen that the enhanced EKE signal obtained in NN+ extends considerably further west than the corresponding signals from both the NN and the NN- simulations.

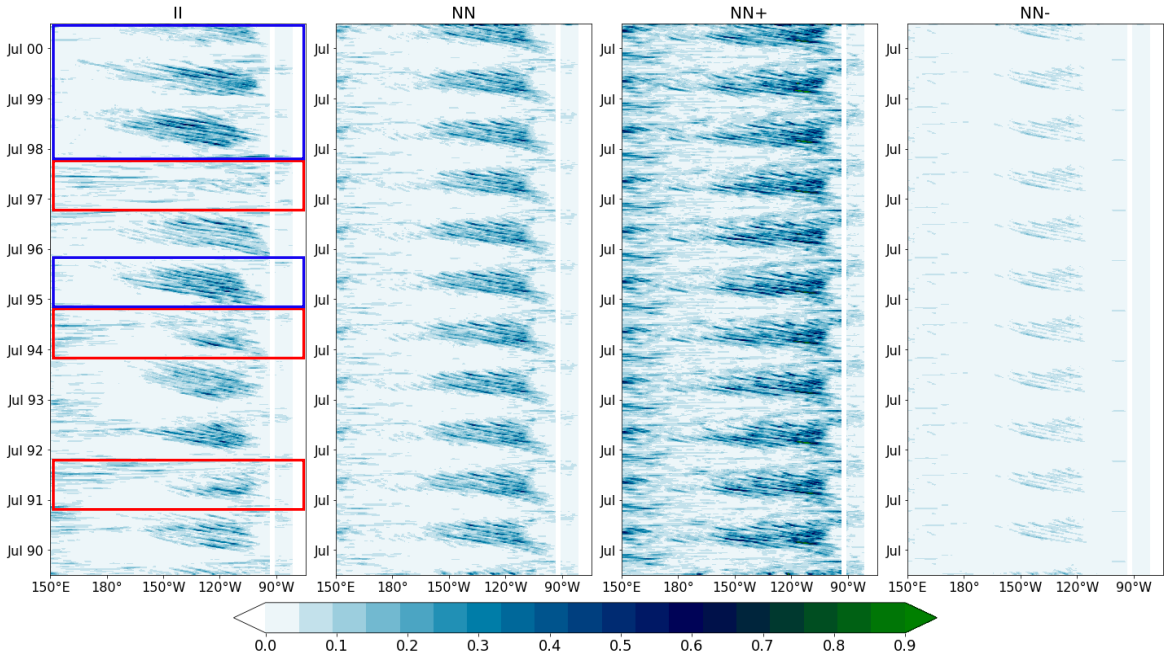

Figure 5.1. Hovmöller diagrams of 0 to 5°N averaged, filtered EKE [m^2/s^2] from the II, NFY1, NN+ and NN- simulations. The x-axis is longitude, and the y-axis is time. The red and blue boxes correspond to the occurrence of the Niño and Niña events, respectively.

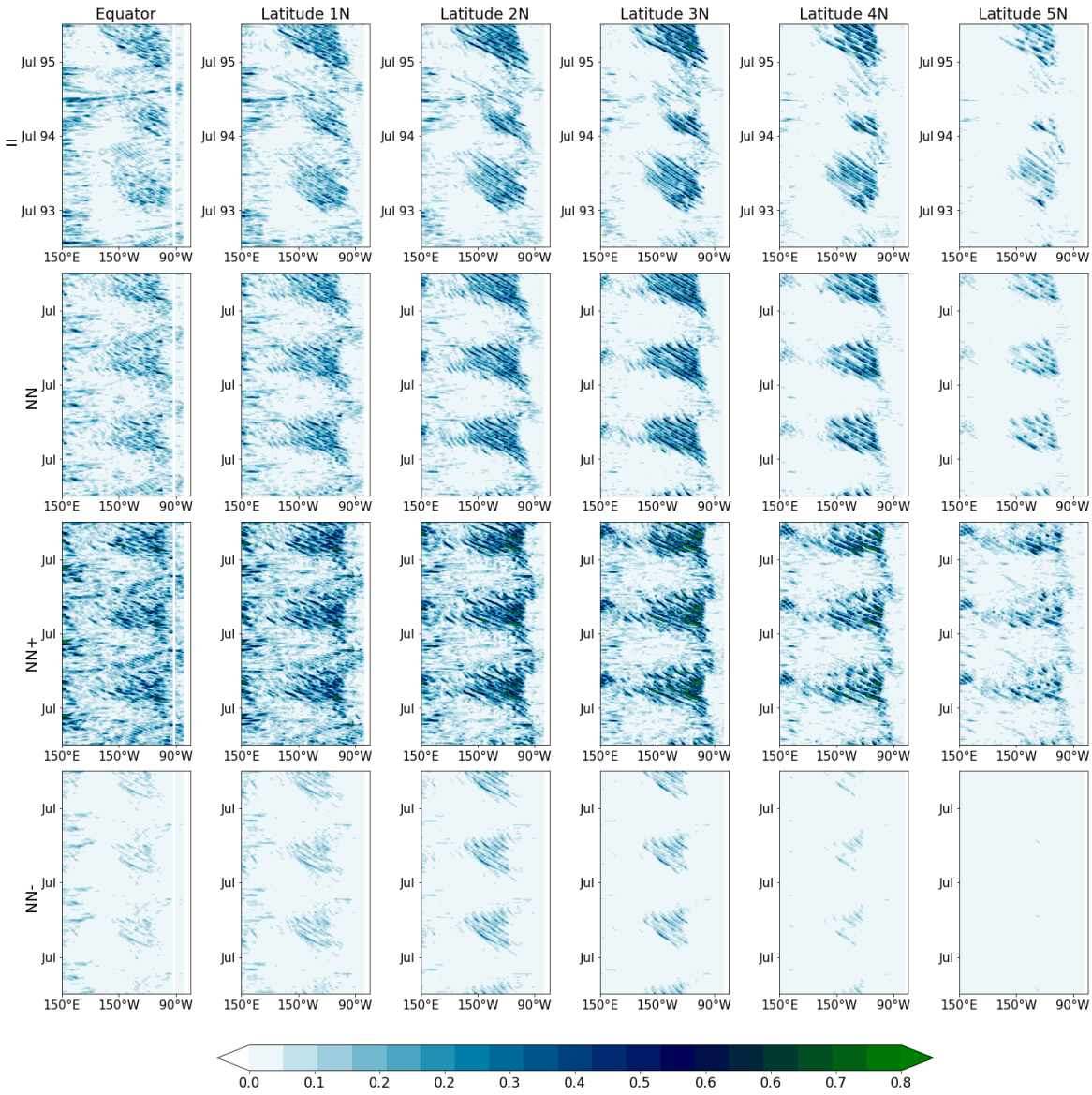

Figure 5.2. Hovmöller diagrams of filtered EKE [m^2/s^2] at 0, 1˚N, 2˚N, 3˚N, 4˚N and 5˚N from II, NFY1, NN+ and NN- simulations. The x-axis is longitude, and the y-axis is time in for 11 years.

Figure 5.2 shows the EKE but for each incremental degree of latitude, from the equator to 5˚N, and in a shorter period of only for three years. The maximum amplitudes of the EKE are seen to be located within latitudes 2˚N-3˚N for all four simulations. This is consistent with earlier studies that have found the highest amplitudes of the anomalies of SSH, SST and meridional currents to be in the vicinity to the equator. For example, Jochum *et al.* (2007) estimated variations in SST of up to 0.7˚C/month at 2˚N from May 2004 through to February 2005. Shinoda *et al.* (2009) identified maximum variations in SSH anomalies to occur at 5˚N, and similarly Im *et al.* (2012) observed peak amplitudes in meridional currents occurring at 4˚N. It is important, however, to note that the TIW signal is relatively weak or

indeed almost imperceptible at the latitude of 5°N, either in an actual El Niño event, such as the 1994-1995 in the II simulation, or in the NN- run, with very weak trade winds. This is partly due to the fact that during El Niño episodes the meridional temperature gradient is reduced and therefore the TIWs are suppressed (An, 2008).

In addition to the Hovmöller plots, the time mean EKE was also computed over the top 100 m of the water column to study its horizontal and vertical spatial patterns, and these are shown in Figure 5.3 and 5.4 respectively. In the four simulations, relatively large EKE values are found in the eastern Pacific region just a few degrees north of the equator (Figure 5.3). Maximum values of up to 0.15 m^2/s^2 are displayed in the NN+ run results. Significant EKE values can also be observed in the western Pacific, which could be related to the NECC activity (e.g., Chen *et al.*, 2015). These horizontal patterns and their associated values agree with those that have been obtained by Marchesiello *et al.* (2011) using 1° resolution outputs from the ROMS model.

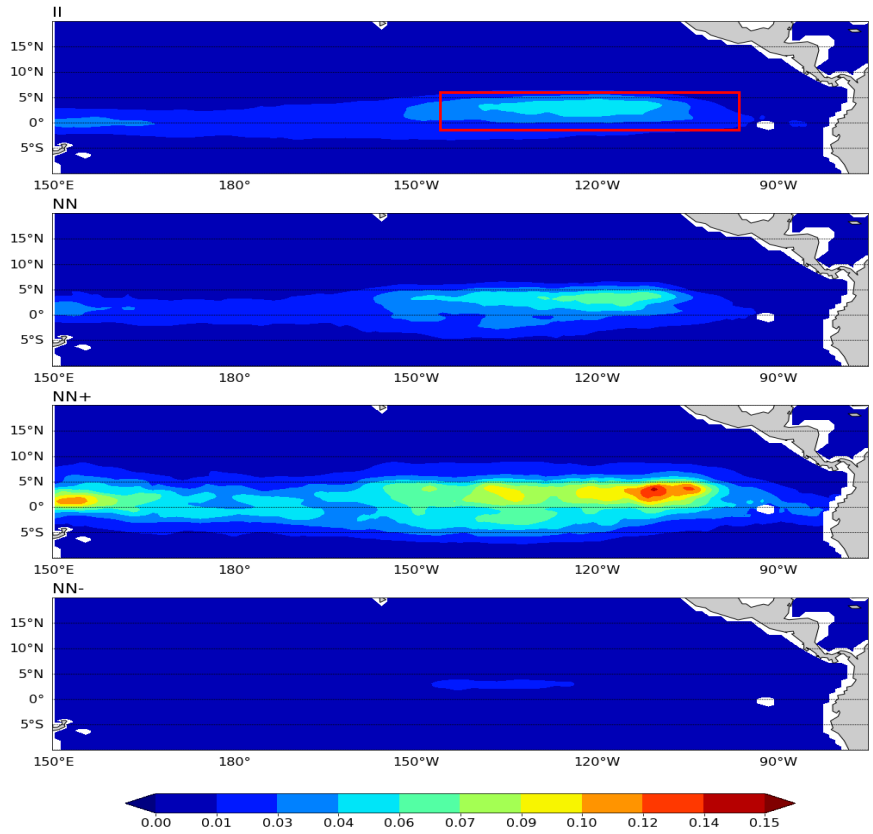

Figure 5.3. Time mean EKE [m^2/s^2] averaged in the upper 100 m in the II, NN, NN+ and NN- simulations between 1990 to 2000. The red box (2°S-6°N, 100°W-150°W) represents the region where the EKE data density is relatively high in II.

In the vertical section plots (Figure 5.4) it can be seen that the distributions of the most energetic values of the EKE are confined to the upper tens of metres (thus being above the thermocline) and decreasing in magnitude with increasing depth (Figure 5.4). When comparing the II and NN runs, the results confirm that the EKE intensity is predominantly modulated by internal variability and that the interannual atmospheric forcing fields have corresponding less effect on it.

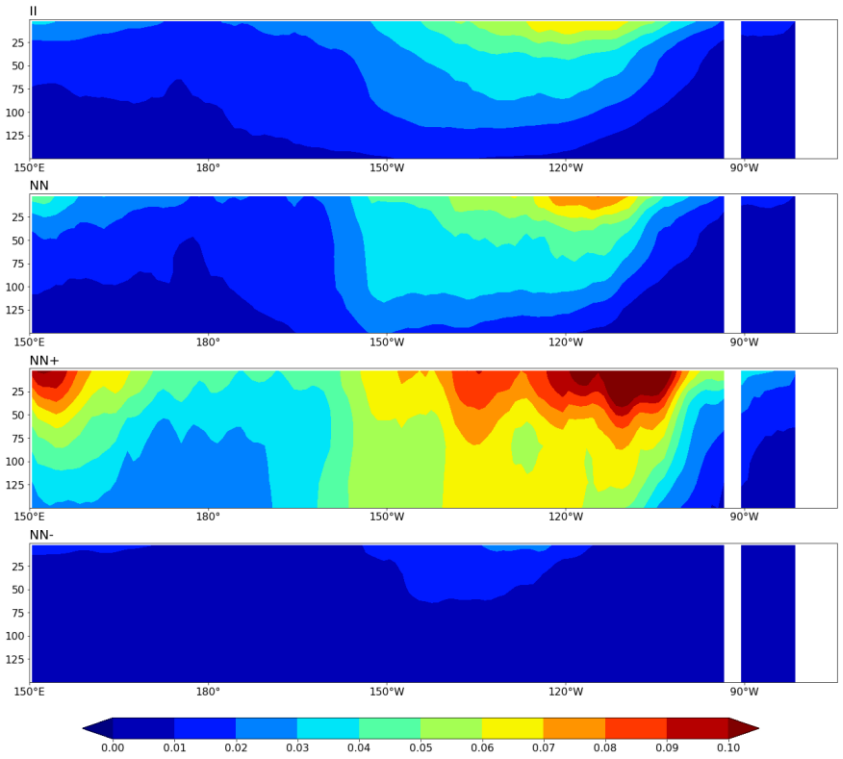

Figure 5.4. Longitude-depth vertical sections of mean filtered EKE [m^2/s^2] averaged between 0 to 5°N in the II, NN, NN+ and NN- simulations between 1990 to 2000, from the coast (right edge) to 150°E in the upper 150 m.

According to Figure 5.5, the amplitudes of the EKE in the first 150 m of depth in the eastern Pacific region can be up to 4 times greater than NN (NN+) when the wind forcing factor is increased, or conversely it can reach values close to 0 when the wind forcing decreases (NN-). The central Pacific (120°W-150°W) appears to be the region where the wind forcing effect is lower than in the rest of the tropical Pacific. In the central Pacific, the EKE values increase by two to three times in the NN+ simulation and, conversely, decrease by one fifth to one third in the NN- simulation.

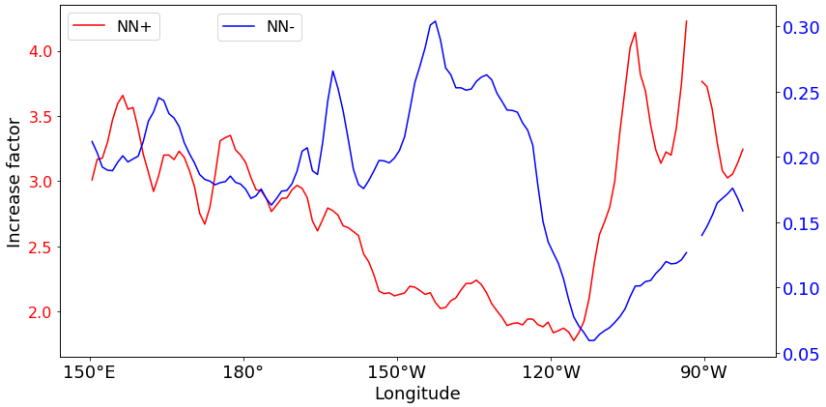

Figure 5.5. Increase factor in mean filtered EKE [m^2/s^2] in the NN+ (red) and the NN- (blue) simulations regionally averaged between 0 to 5°N and in the upper 150 m, from the coast (right edge) to 150°E.

Overall, the TIWs features are reasonably well represented in the model simulations, therefore their interactions and dynamic processes can be investigated with some degree of confidence.

5.3 Dominant factors in the TIW energy transformation process

TIWs are physically generated by the combined influence of barotropic, Kelvin-Helmholtz and baroclinic instability mechanisms. Barotropic and Kelvin-Helmholtz instabilities, resulting from the horizontal and the vertical shear components of the mean equatorial current system respectively, have been identified from observational studies e.g., Qiao and Weisberg (1995) and Qiao and Weisberg (1998) and by data modelling studies e.g., Cox (1980). Similarly, baroclinic instabilities have been associated with the meridional gradient of the SST, e.g., Luther and Johnson (1990) and Yu *et al.* (1995). In this section, these TIWs energy sources are analysed for four different simulations.

Following the work of Masina *et al.* (1999), the two main sources of the EKE are the conversion of mean kinetic energy to EKE (BTR-KH) and the conversion of mean potential energy to EKE (BCL), and which are given by (5.2) and (5.3) respectively:

$$BTR - KH = -\overline{u'u'}\frac{\partial U}{\partial x} - \overline{u'v'}\frac{\partial V}{\partial x} - \overline{u'v'}\frac{\partial U}{\partial y} - \overline{v'v'}\frac{\partial V}{\partial y} - \overline{u'w'}\frac{\partial U}{\partial z} - \overline{v'w'}\frac{\partial V}{\partial z} \quad (5.2)$$

$$BCL = -\frac{g}{\rho_0}\overline{\rho'w'} \quad (5.3)$$

where the primes denote the 10-120-day bandpass filtered variables, the overbars (or uppercase) indicate the background ocean state calculated with a 120-day moving average

filter, $g = 9.81$ m/s^2 is the acceleration of gravity and $p_0 = 1025$ kg/m^3 is a reference value for the density of sea water.

5.3.1 BRT-KH

The BTR-KH term represents the conversion of mean kinetic energy into EKE through horizontal and vertical deformation work. The first four terms on the right-hand side in (5.2) express the horizontal strain work, which involves horizontal Reynolds forces acting on horizontal current shear and known as 'barotropic conversion'. The remaining two terms in (5.2) represent the vertical deformation work known as the 'Kelvin-Helmholtz conversion', which is associated with the vertical Reynolds stresses acting on the vertical shear of the current (Masina *et al.*, 1999).

The contributions of each of the six-terms in (5.2) obtained from each of the four different simulations are given in Table 5.1. The first upper half of the table are the values corresponding to the ocean surface, and the other four rows, the lower half, corresponding to the average values of the terms over the first 100 m of depth. In all cases, the term $-\overline{u'v'}\frac{\partial U}{\partial y}$ is the largest (>1). The terms $-\overline{u'u'}\frac{\partial U}{\partial x}$ and $-\overline{u'v'}\frac{\partial V}{\partial x}$ in (5.2) have relatively small magnitudes (typically < 0.1). Therefore, their contribution will not be further considered in the calculations of the BTR-KH term. Furthermore, since barotropic instabilities represent the largest contribution to the term BTR-KH, for simplicity we will subsequently refer to this as the 'barotropic conversion' term.

Table 5.1. Time mean of each of the barotropic terms and the baroclinic term [10^{-8} m^2/s^3] averaged over 2°S-6°N and 100°W-150°W (red box Figure 5.3) at the surface.

Simulation	$-\overline{u'u'}\frac{\partial U}{\partial x}$	$-\overline{u'v'}\frac{\partial V}{\partial x}$	$-\overline{u'v'}\frac{\partial U}{\partial y}$	$-\overline{v'v'}\frac{\partial V}{\partial y}$	$-\overline{u'w'}\frac{\partial U}{\partial z}$	$-\overline{v'w'}\frac{\partial V}{\partial z}$	$-\frac{g}{p_0}\overline{p'w'}$
II	0.10	-0.03	3.15	-0.35	-1.6 x 10^{-4}	2.4 x 10^{-4}	0.001
NN	0.11	-0.04	3.85	-0.22	-1.7x 10^{-4}	2.3 x 10^{-4}	0.001
NI	0.08	-0.03	3.13	-0.27	-1.3 x 10^{-5}	2.2 x 10^{-4}	0.001
IN	0.14	-0.04	3.99	-0.12	4.8 x 10^{-6}	1.2 x 10^{-4}	0.001
II*	0.007	-0.01	1.73	-0.19	-0.33	0.25	1.35
NN*	1 x 10^{-4}	-0.02	2.22	-0.20	-0.38	0.41	1.47
NI*	0.004	-0.01	1.74	-0.17	-0.29	0.24	1.24
IN*	0.001	-0.02	2.21	-0.16	-0.09	0.21	1.33

* averaged in the upper 100 m

Thus Figure 5.6 shows the mean barotropic conversion term as the sum of the $-\overline{u'u'}\frac{\partial U}{\partial y}$, $-\overline{v'v'}\frac{\partial V}{\partial y}$, $-\overline{u'w'}\frac{\partial U}{\partial z}$ and $-\overline{v'w'}\frac{\partial V}{\partial z}$ components. Positive values of BTR-KH imply energy transfer from background flow to the EKE. The maximum positive BTR-KH values are located in a narrow band, as obtained in each of the four simulations. The most prominent band is located between latitudes 2˚N-5˚N and is probably related to meridional shear instability between the NECC and the SEC. The maximum secondary energy that is located nearer to the equator is produced by the shear between the EUC and the northern branch of the SEC (Flament *et al.*, 1996). Regions with small negative BTR-KH values indicate energy transfer from the eddy field to the mean flow. These results are consistent with those presented by Qiao and Weisberg (1998). In particular, the approximate 3/2 relationship between barotropic ($-\overline{u'v'}\frac{\partial U}{\partial y}$) and baroclinic conversion that was identified by Masina *et al.* (1999) in a simulation using normal year forcing is approximately satisfied in our NN and IN simulations (Table 5.1).

The simulations NN and IN, undertaken using wind forcing from the NYF, show the highest BTR-KH values. In simulations with interannual wind variability, episodes such as El Niño, in which the strength of the trade winds is reduced, time-averaged BTR-KH values are accordingly reduced. In this study period of 1990-2000, three El Niño events were experienced (Figure 5.1).

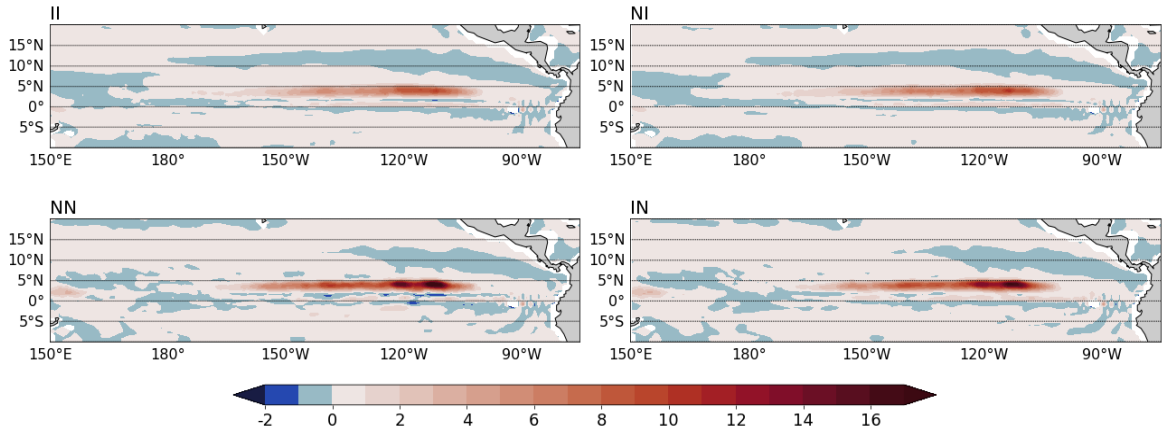

Figure 5.6. Time mean barotropic conversion term [10^{-8} m^2/s^3] averaged in the upper 100 m in the II, NN, NI and IN simulations.

The vertical distribution of the BTR-KH term is illustrated in Figure 5.7. The largest BTR-KH values are confined to the first 50 m below the surface, and in the zonal band between 100˚W to 120˚W centred around 4˚N. In this region, the maximum BTR-KH values can effectively double in the simulations using the NYF wind forcing. The meridional sections

(the lower part of Figure 5.7) show a clear match between the positions of the tropical Pacific currents and the location of the greatest BTR-KH amplitudes. The positive maximum BTR-KH values (around 4˚N) are located in the meeting region between the westward SEC and the eastward NECC (see Chapter 2). It is also possible to distinguish two other regions with positive BTR-KH values at the depth of the EUC core, that come about because of the horizontal shear instability between the EUC and the SEC. There is an extended region of complex geometry in which BTR-KH values are negative. Near the surface, it straddles the equator and north of the equator it plunges down to around 125 m at 4˚N. The largest terms contributing to this transfer of energy from the waves to the mean flow are the Kelvin-Helmholtz terms in (5.2). These regions, therefore, act as energy sinks and thus weakening the TIWs.

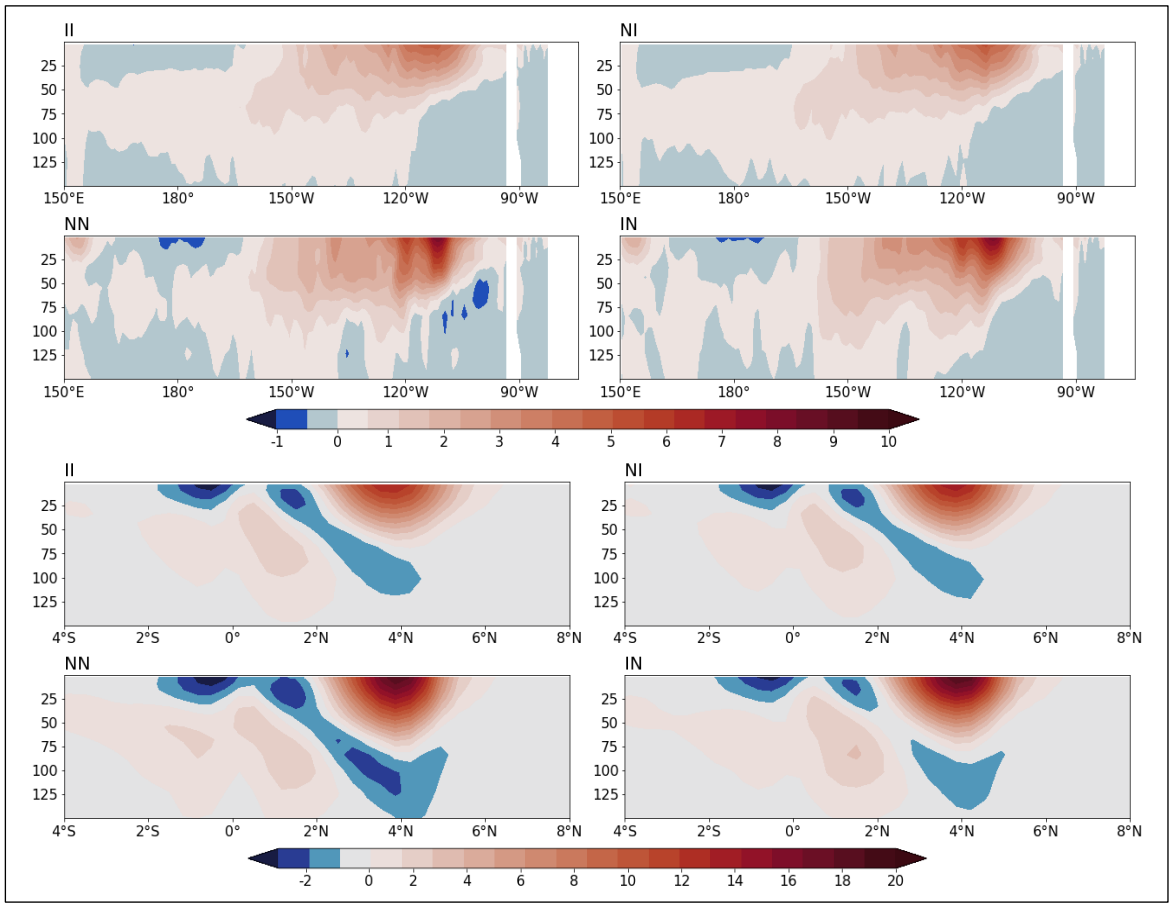

Figure 5.7. Time mean barotropic conversion term [10^{-8} m^2/s^3]. Top group: longitude-depth vertical sections averaged between 2˚S to 6˚N. Bottom group: latitude-depth vertical sections averaged between 100˚W to 150˚W in the II, NN, NI and IN simulations in the upper 150 m.

5.3.2 BCL

The BCL component represents the energy conversion that takes place between the EKE and the eddy potential energy (EPE) caused through vertical Reynolds density fluxes (5.3) (Masina *et al.*, 1999). In Table 5.1 the seventh column represents the baroclinic term, which is relatively weak near the surface but can be quite significant at depth. The corresponding time mean baroclinic conversion terms that have been obtained from each simulation are shown in Figure 5.8. The horizontal distributions are quite similar in all four simulations. The main area of EKE generation is located between 0 and 5°N extending along the eastern and central Pacific regions. A second region with relatively modest positive BCL values is located south of the equator, between 0 to 5°S. Similar to the barotropic term, the differences in the strengths of the baroclinic term obtained from each of the four simulations can be easily perceived. Those simulations, that are the result of using the same wind forcing from NYF, show not only higher positive values but also that the EKE production region extends further westwards.

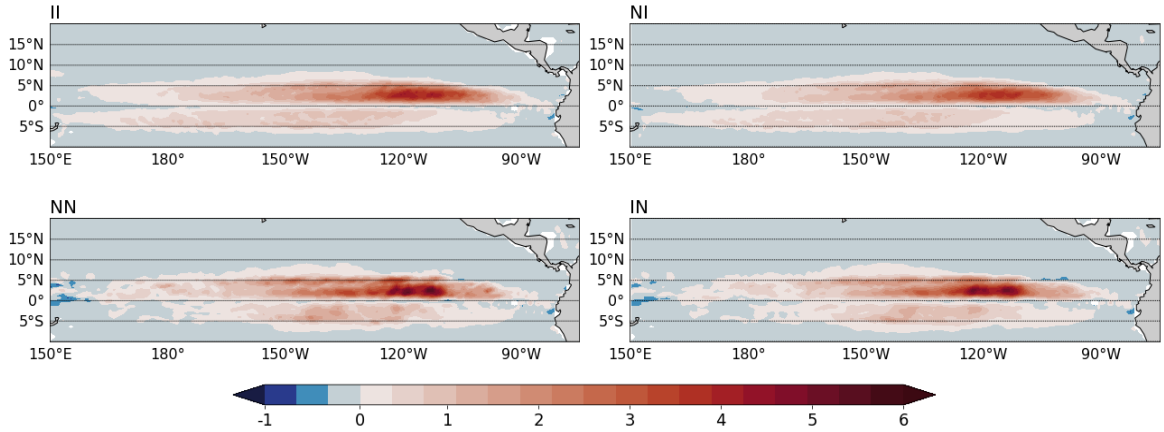

Figure 5.8. Time mean baroclinic conversion term [10^{-8} m^2/s^3] averaged in the upper 100 m in the II, NN, NI and IN simulations.

Figure 5.9 shows vertical sections of the mean baroclinic conversion. The absolute maximum values are located just below the surface, between 25 and 50 m of depth and occur mainly in the eastern Pacific (Figure 5.9, top panels). In the western Pacific, the conversion from EPE to EKE is lower.

In the meridional sections, a degree of symmetry is observed between both sides of the equator as regards the general distribution of the BCL term, although baroclinic conversion is manifestly more intense on the Northern Hemisphere (Figure 5.9, bottom panels). This symmetry is related to meridional temperature gradients, represents the main source of

available EPE (Yu *et al.*, 1995). In the equatorial region, the presence of a weakly stratified mixed layer together with a strong meridional temperature gradient results in an EPE reservoir (Masina *et al.*, 1999). The highest values of the BCL are located north of the equator and are divided into two maxima, one between 1°N to 2°N and a second one between 4°N to 6°N. This intensity in the positive values north of the equator is due to the strength of the northern branch of the SEC (Masina *et al.*, 1999). The negative BCL values representing the conversion from EKE to EPE are below a depth of 75 m and are located between 4°N and 6°N.

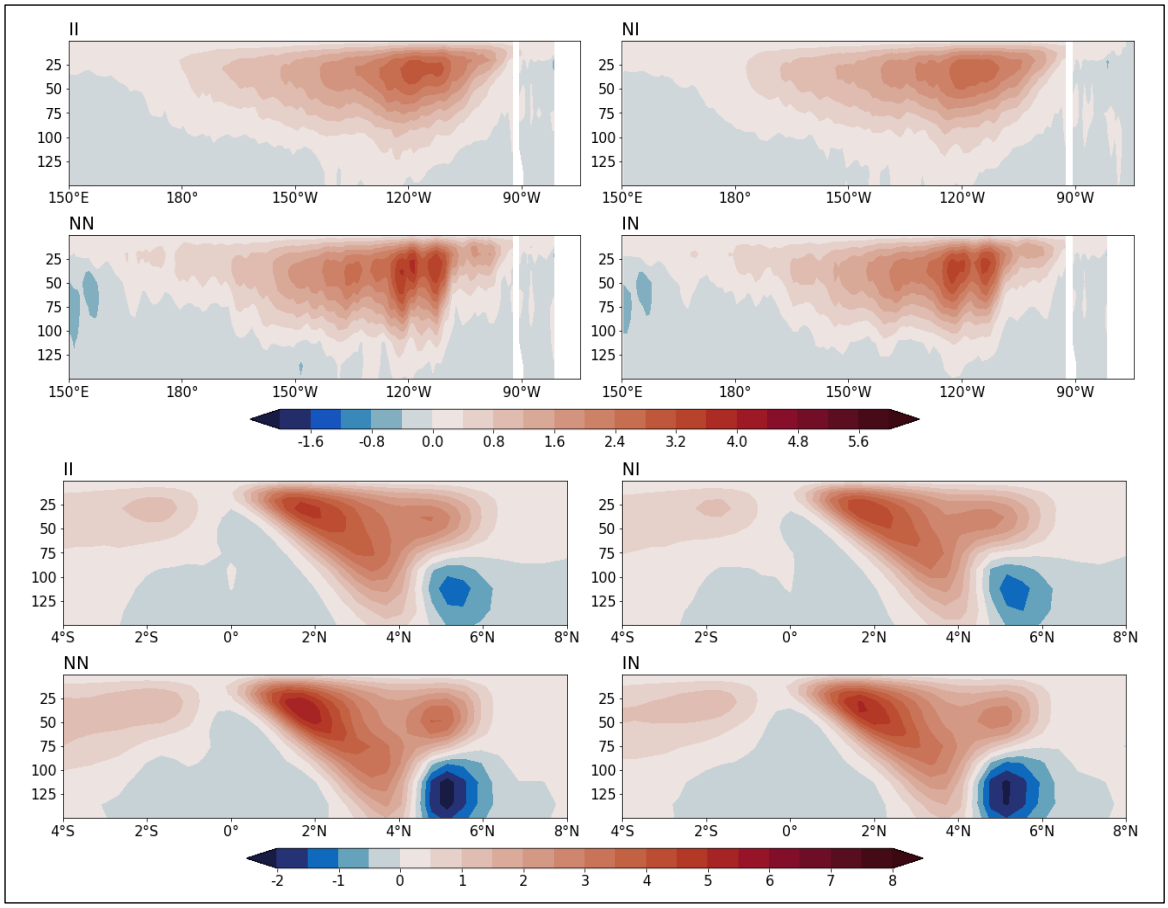

Figure 5.9. Time mean baroclinic conversion term [10^{-8} m^2/s^3]. Top: longitude-depth vertical sections averaged between 2°S to 6°N. Bottom: latitude-depth vertical sections averaged between 100°W to 150°W in the II, NN, NI and IN simulations in the upper 150 m.

The time series of both the BTR-KH and the BCL terms averaged over the region bounded by 2°S-6°N and 100°W- 150°W (the red box in Figure 5.3 for the II simulation) are shown in Figure 5.10. Both terms demonstrate a clear seasonal variability, reaching their maximums in the second half of each year. This seasonality appears to remain unchanged

regardless of the applied atmospheric forcing. In each of the four simulations, the contribution of the barotropic term is greater than the contribution of the baroclinic term, even in El Niño years when a notable decrease in the values is generally observed when compared to the other years. For both the BTR-KH and the BCL, the simulations with NYF wind forcing show higher values in all years except for episodes of La Niña in 95-96 and 99-00. A closer examination of the effects of intraseasonal winds on TIWs, specifically the MJO cycle effect, is undertaken in the following section.

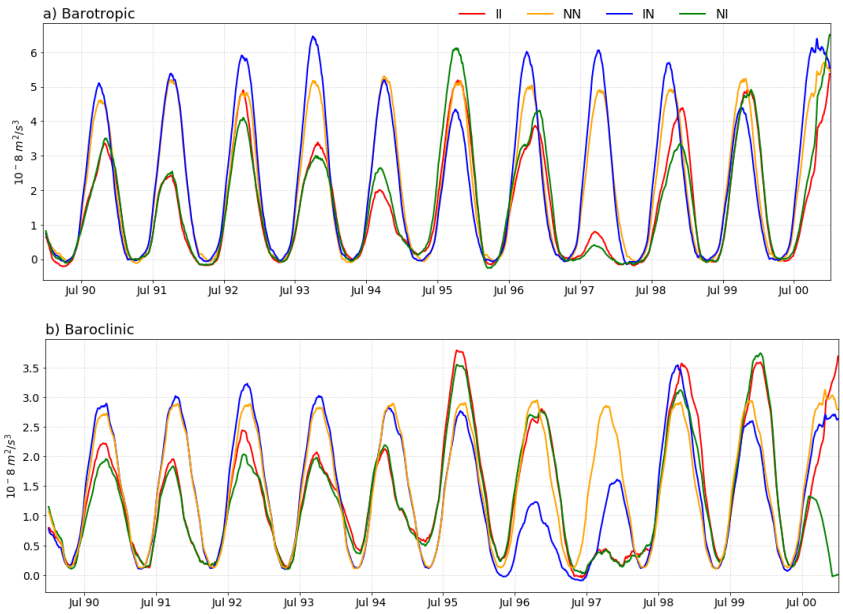

Figure 5.10. Time series of a) barotropic [10^{-8} m^2/s^3] and b) baroclinic conversion term [10^{-8} m^2/s^3] averaged between 2˚S to 7˚N and 100˚W to 150˚W over 0-100 m, from the II (red), NN (yellow), IN (blue) and NI (green) simulations.

5.4 Connection with the MJO

In order to establish how the MJO influences the EKE budget, the main energy sources of the TIWs have been selectively analysed for days of active MJO. In the discussion of Section 5.3, the BTR-KH and BCL terms were calculated using a 120-day moving average. Obviously, this approach is not suitable for the investigation of the effect of the MJO, which has a duration of between 30 and 90 days, on the eddy energetics. Therefore, a shorter 10-day moving average was applied here for the recalculation of BTR-KH and BCL in (5.2) and (5.3). The reader is reminded that the MJO analysis carried out here uses the Wheeler-Hendon index (Wheeler and Hendon, 2004), as described in Chapter 1. As in the earlier chapters, only the days with amplitudes that are greater than 1 are considered, since it is

only in those particular days that larger atmospheric disturbances are generally related to the active MJO. Considering that the TIWs and their energy sources are particularly active in the second half of the year, the individual MJO events selected for further study were only those occurring from July to December inclusive. Table 5.2 shows the number of days that have been selected per the MJO phase.

Table 5.2. Number of days for MJO composite analysis from the TIWs season (July to December) for years 1990 to 2000.

MJO phase		**1**	**2**	**3**	**4**	**5**	**6**	**7**	**8**	**MJO all**	**%**
Number of days	Active	183	149	112	109	198	158	127	119	1155	57
	Inactive	121	113	125	120	97	88	120	85	869	43

In the MJO composite plots of Figures 5.11, 5.12, the y-axis represents time in terms of the phases of the MJO and the same composite is repeated twice in order to show the oscillatory behaviour through the MJO and to better visualize the evolution from phase 1 through to phase 8. Figure 5.11 (5.12) display the composite of the BTR-KH (BCL) in each phase of the MJO during the period 1990 through to 2000. Strong BTR-KH values, with maxima that are close to 6 $x10^{-8}$ m^2/s^3, are identified in MJO phases 4→7 in both the II and the NI simulations (Figure 5.11). These BTR-KH values and the corresponding zonal winds show statistically the highest correlation ($r \sim -0.82$) when the MJO zonal winds lead the BTR-KH values by 8 days (roughly the duration of a phase) in the II simulation.

Since the behaviour of the mean flow (U, V) is essential in the calculation of the barotropic term, it is useful to revisit the changes in the currents caused by the MJO, which we described in Chapter 4. Figure 4.15 shows that during phases 5→7 the zonal currents presented the most negative values of anomalies found in the central and eastern Pacific regions above the depth of 100 m. That is, when the zonal currents are relatively stronger, therefore larger BTR-KH values are to be expected during these phases. Similarly, during phases 7→1 westerly wind anomalies tend to prevail, and the zonal currents are hence correspondingly weakened, thus resulting in smaller BTR-KH anomalies throughout the central and eastern Pacific regions. On the other hand, in the absence of interannual wind forcing (as in the IN run) the BTR-KH values increase up to 11 $x10^{-8}$ m^2/s^3 in the region between 110°-115°W. In this latter region, the BTR-KH values increase by more than 50%

when comparing the same phases 7→1 between the IN run and with those of the II and the NI runs.

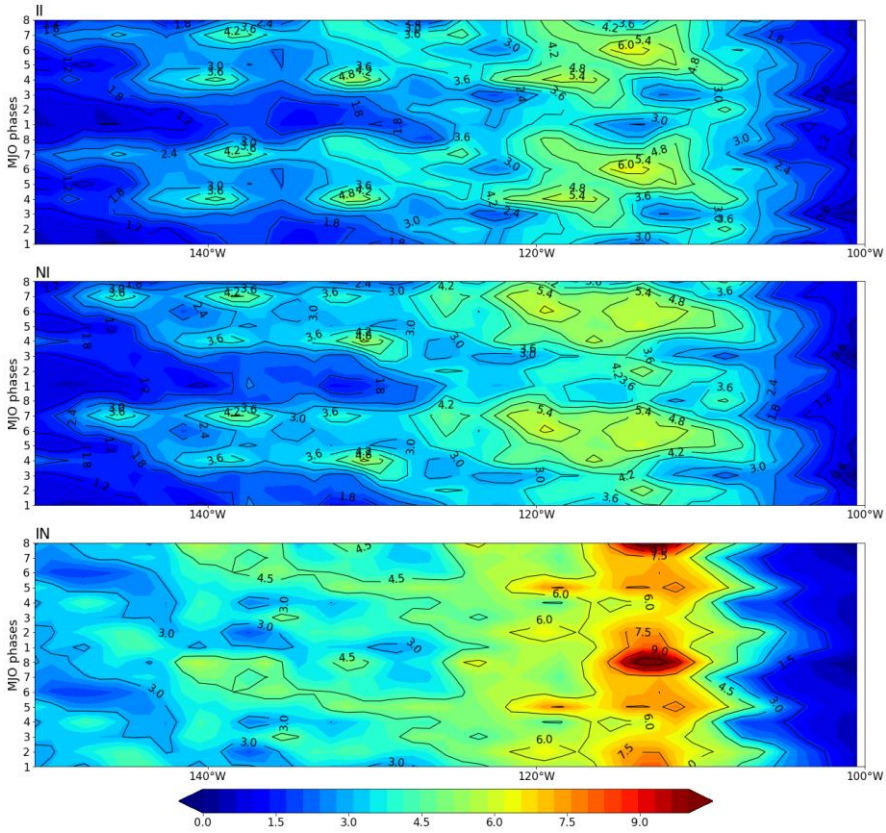

Figure 5.11. MJO composites of barotropic conversion term [10^{-8} m^2/s^3] averaged between 2˚S to 7˚N and over 0-100 m, from the II, NI, and IN simulations.

The meridional distribution of BCL term, Figure 5.12, has maximum anomalies of up to 4 x10^{-8} m^2/s^3 located between 110˚W -125˚W in both the II and the NI simulations. These BCL maximum values are reached in MJO phases 4→7. As in the barotropic term, a negative correlation occurs between the MJO zonal winds and the BCL. This maximum correlation (r ~ -0.88) is found when the zonal winds lead the BCL anomalies by 8 days. Noting that the BCL term is related to changes in temperature, these higher BCL anomalies are thus consistent with that which was observed in Figure 4.11 (Chapter 4) where the maximum negative temperature anomalies occur in phases 5→7. Negative temperature anomalies indicate a strong SST front that potentially provides an available energy source for initiating baroclinic instabilities (Masina *et al.*, 1999).

Otherwise, in the MJO phases 7→2 that are typically characterized by westerly wind anomalies, weak anomalies of BCL appear. The BCL anomalies that are developed in the

IN simulation are relatively less organized although they are stronger than observed in the other simulations. The results reveal that under MJO conditions the variations in BTR-KH anomalies are greater than those observed in BCL.

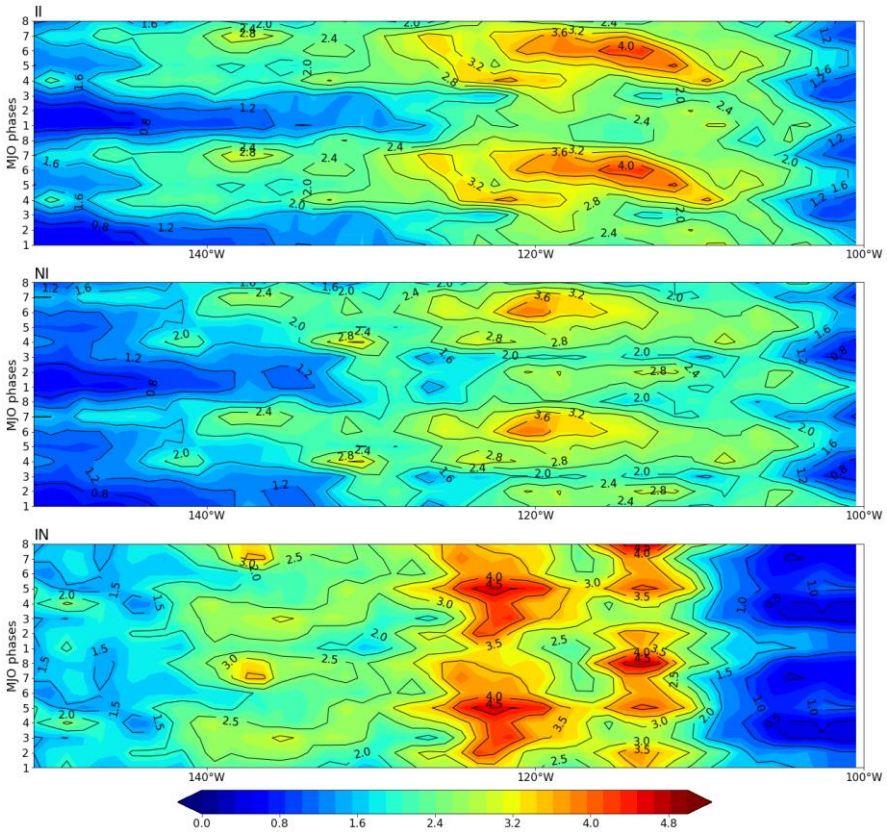

Figure 5.12. MJO composites of baroclinic conversion term [10^{-8} m^2/s^3] averaged between 2˚S to 7˚N and over 0-100 m, from the II, NI, and IN simulations.

We have so far investigated the impact of the MJO on the barotropic conversion term and shown it to be significant (Figure 5.11). However, BTR-KH is a complex function of the many stress terms and it is pertinent to ask which of these terms contributes more significantly to the overall conversion. Of the terms contributing to BTR-KH in (5.2) the first two terms were found to be negligible and, therefore, will not be investigated here further. Below we show depth-time panels for each of the individual contributions to BTR-KH, select those terms that have a substantial contribution (Figure 5.13), and then display panels for the corresponding Reynolds stress and mean flow gradients (Figures 5.14 and 5.15) specifically for the 1993 TIW season (July to December). This year (1993) was deliberately chosen for being a neutral year, with neither El Niño nor La Niña events developing in these specific months. The depth of the EUC core, which is defined as the

depth of maximum eastward velocity, has also been plotted (black solid line). It is noteworthy that the average value of the EUC core depth modelled in the absence of interannual winds (IN) is deeper when compared to II or NI simulations. As shown in for example Figure 5.13 this difference is more noticeable in the months of October and December.

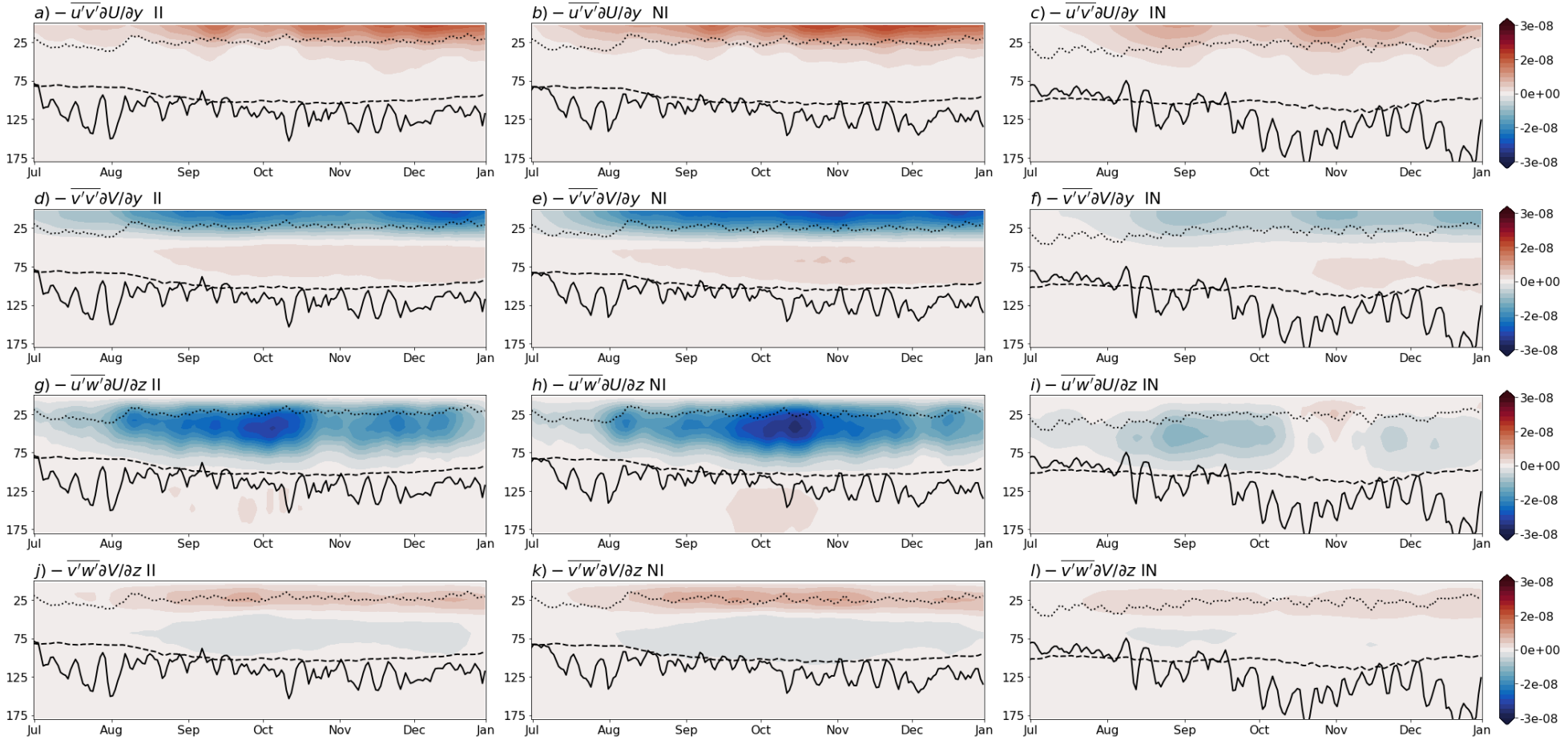

Figure 5.13. Depth-time plots of BTR-KH components a-c) $-\overline{u'v'}\,\partial U/\partial y$ (m^2/s^3), d-f) $-\overline{v'v'}\,\partial V/\partial y$ (m^2/s^3), g-i) $-\overline{u'w'}\,\partial U/\partial z$ (m^2/s^3) and j-l) $-\overline{v'w'}\,\partial V/\partial z$ (m^2/s^3) averaged between 2˚S to 7˚N and 100˚W to 150˚W in the upper 180 m, from the II (left panel), the NI (centre panel) and the IN (right panel) simulations. The three dotted, dashed and solid lines indicate the corresponding mixed layer depth, 20˚C isotherm and the depth of the EUC core, respectively.

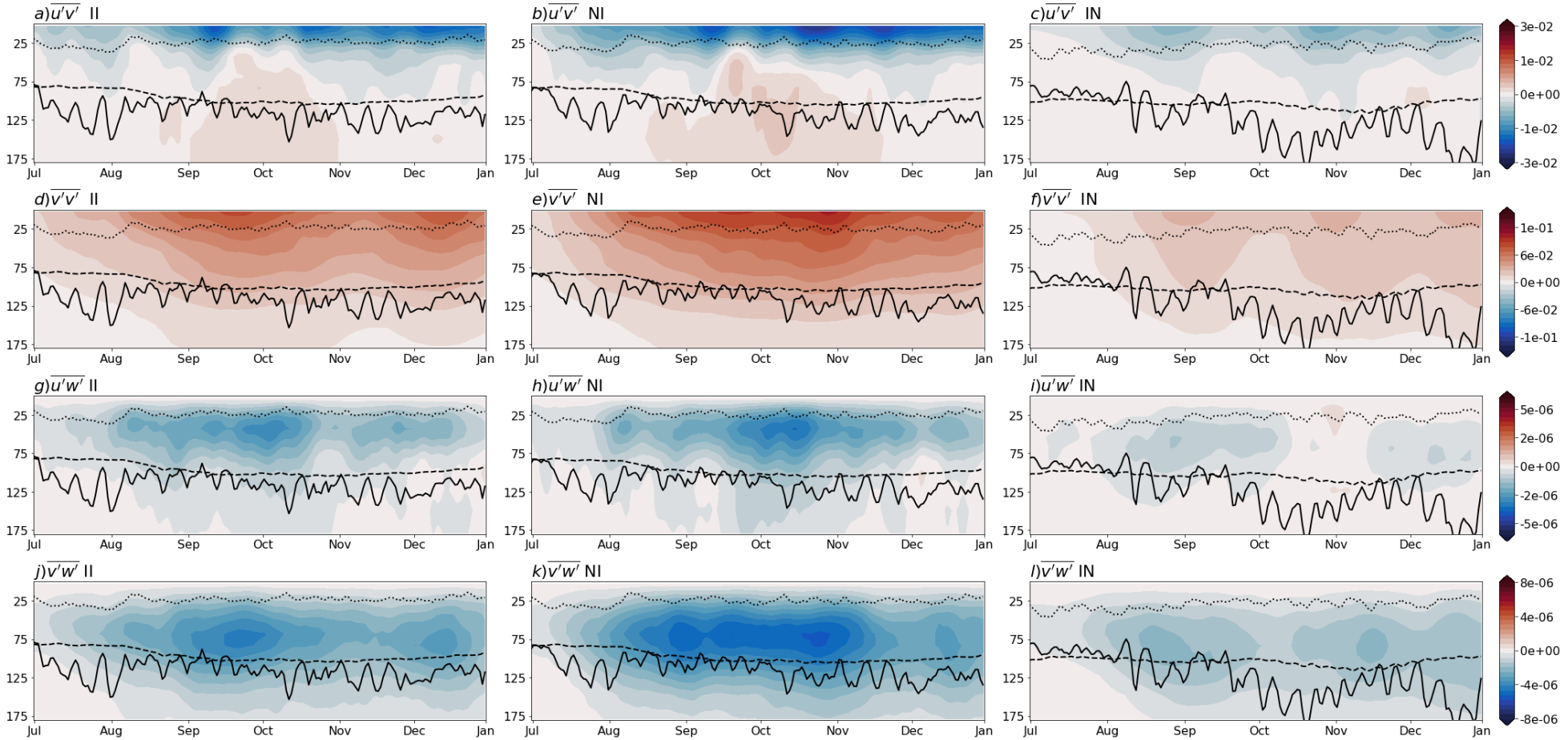

Figure 5.14. Depth-time plots of Reynolds stress components a-c) $\overline{u'v'}$ (m^2/s^2), d-f) $\overline{v'v'}$ (m^2/s^2), g-i) $\overline{u'w'}$ (m^2/s^2) and j-l) $\overline{v'w'}$ (m^2/s^2) averaged between 2˚S to 7˚N and 100˚W to 150˚W in the upper 180 m, from the II (left panel), the NI (centre panel) and the IN (right panel) simulations. The three dotted, dashed and solid lines indicate the corresponding mixed layer depth, 20˚C isotherm and the depth of the EUC core, respectively. Note the colorbar for each row of panels is different.

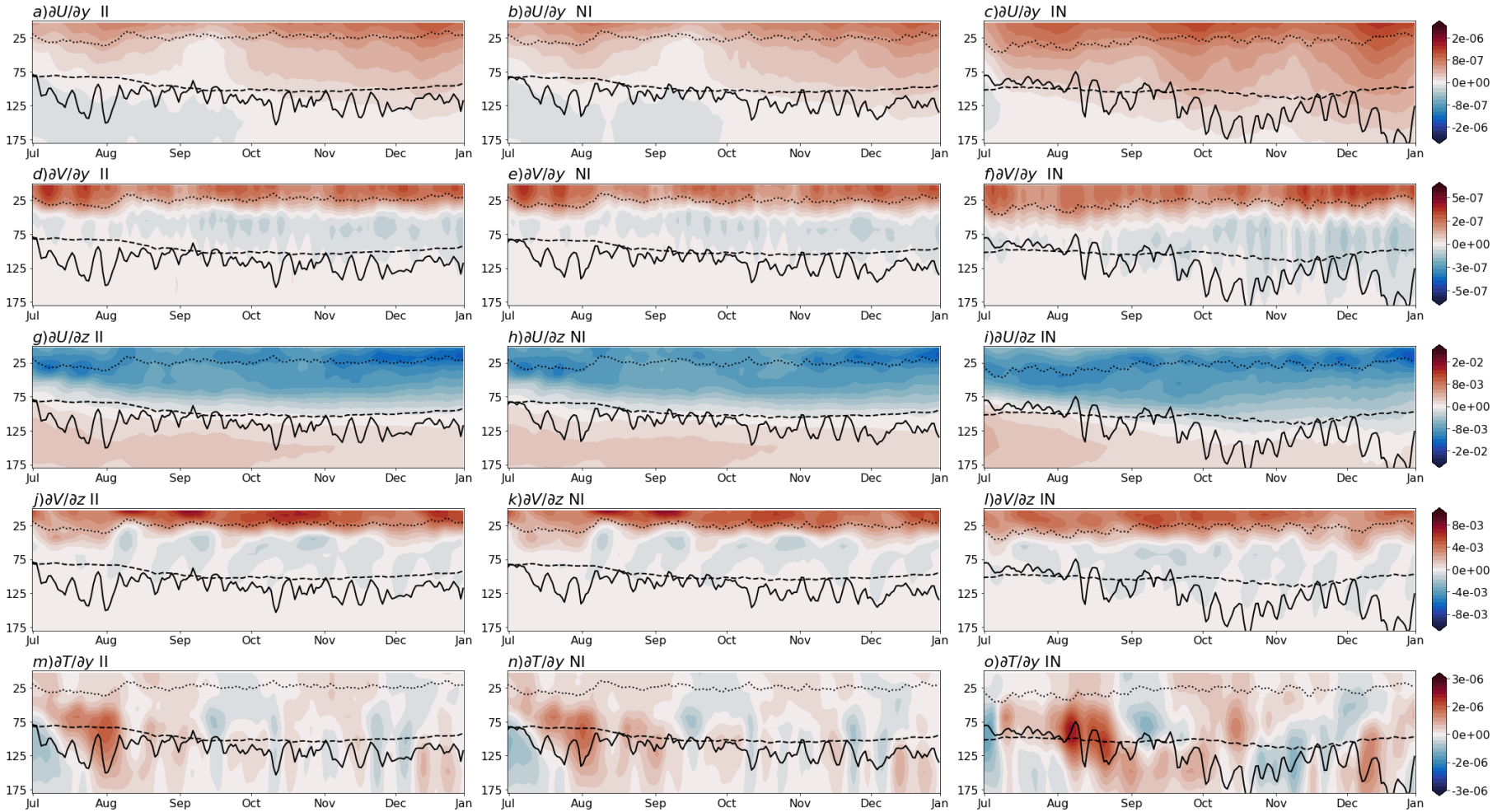

Figure 5.15. Depth-time plots of a-c) meridional shear of the zonal velocity (s^{-1}), d-f) meridional shear of the meridional velocity (s^{-1}), g-i) vertical shear of the zonal velocity (s^{-1}), j-l) vertical shear of the meridional velocity (s^{-1}), and m-o) meridional gradient of temperature (Cm^{-1}) averaged between 2˚S to 7˚N and 100˚W to 150˚W in the upper 180 m, from the II (left panel), the NI (centre panel) and the IN (right panel) simulations. The three dotted, dashed and solid lines indicate the corresponding mixed layer depth, 20˚C isotherm and the depth of the EUC core, respectively. Note the colorbar for each row of panels is different.

The off-diagonal Reynolds stress component $\overline{u'v'}$ shows relatively large negative values above the MLD in all three simulations (Figure 5.14 a-c). These values are most prominent in the II and the NI simulations. In these two experiments, positive values can also be observed with relatively small magnitudes below the MLD in the months of September and October. The diagonal component $\overline{v'v'}$ displays large positive values located above the EUC core depth (Figure 5.14 d-f). These absolute maximum values of the Reynolds stress term $\overline{v'v'}$ (~ 0.1 m^2/s^2) are much larger than those of the off-diagonal Reynolds stress components.

The vertical Reynolds stresses $\overline{u'w'}$ and $\overline{v'w'}$ show similar temporal variations (Figure 5.14 g-l). Both terms show large negative values from August to December. The largest values are confined to regions below the MLD and above the EUC core. The sign of the Reynold stress, or the eddy moment flux in a fluid, and the sign of the mean shear sign are important in order to infer the direction of the transfer taking place between mean and eddy energies and of the possible origins of this transfer mechanism.

The meridional shear of the zonal velocity, $\partial U/\partial y$, exhibits the largest positive values above the MLD, although positive values are observed down to the MLD core depth (Figure 5.15 a-c). The term $\partial U/\partial y$ tends to be greater in the IN simulation. Thus, because $\overline{u'v'}$ is mostly negative, it could be reasonably inferred that $-\overline{u'u'}\frac{\partial U}{\partial y}$ is mostly positive (Figure 5.13), thus resulting in a conversion of energy from the mean flow to the EKE. This is consistent with what can be seen in Figure 5.7, since $-\overline{u'u'}\frac{\partial U}{\partial y}$ is the largest contributor to the BRT term (Table 5.1).

The term $\partial V/\partial y$ displays positive values in the first 50 m, and then changes to weak negative values down to above the EUC core in all three simulations (Figure 5.15 d-f). Thus, taking into account the results of $\overline{v'v'}$, it could be postulated that the sign of $-\overline{v'v'}\frac{\partial V}{\partial y}$ is negative in the first 50 m of depth (Figure 5.13). This wave energy sink, that serves to weaken the TIWs, is identified between 2°N and 2°S in the latitude-depth vertical sections shown in Figure 5.7.

The results of the vertical shear of the zonal velocity $\partial U/\partial z$ show negative values as large as 1.3 $x10^{-2}$ s^{-1} above the 20°C isotherm (Figure 5.15 g-h). Below this isotherm, $\partial U/\partial z$

reverses its sign and tends to show weak positive values. However, the vertical shear of the meridional velocity $\partial V/\partial z$ is positive only in the first 30 m, thus, the contribution of both terms of the Kelvin-Helmholtz conversion is negative approximately below the MLD (Figure 5.13). This indicates a transfer of kinetic energy from the instability waves to the background mean flow.

The meridional temperature gradient shows the largest positive anomalies during July and August, which are the TIW's peak months (Liu *et al.*, 2016) (Figure 5.15 m-o). This is consistent with what is observed in Figure 5.10b, where baroclinic instabilities were the greatest in the period from July to October. However, it has been previously identified that the baroclinic component is not always the main source of energy of the TIWs (e.g., Qiao and Weisberg, 1998). Nevertheless, the meridional temperature gradient has been used to define the absence or presence of TIW activity (e.g., Liu *et al.*, 2016). In the absence of interannual winds (the IN run) $\partial T/\partial y$ is enhanced, the amplitudes are greater, and the vertical penetration is deeper.

In order to further evaluate the response of each of the contributory fields discussed above during the evolution of the MJO in the TIWs normal season, an MJO composite analysis has been conducted (Figure 5.16). In the Reynolds stress component $\overline{u'v'}$ (Figure 5.16a) the values in the II and the NI simulations are greater than the values in the IN run in MJO phases 8→3 and smaller in phases 4→7. During anomalous MJO easterlies winds the term $\overline{u'v'}$ in the II and NI simulations increases relative to the same term in IN by up to 30%, while, conversely, it decreases by up to 30% in response to anomalous MJO westerlies winds.

In the case of the diagonal Reynolds stress component, $\overline{v'v'}$, the experiments II and NI show higher values throughout the MJO cycle (Figure 5.16). Given that the greatest differences occur in phases 4→7 when easterlies are intensified, it could be assumed that this increase is the result of Ekman and zonal geostrophic transport driven by the anomalous zonal winds.

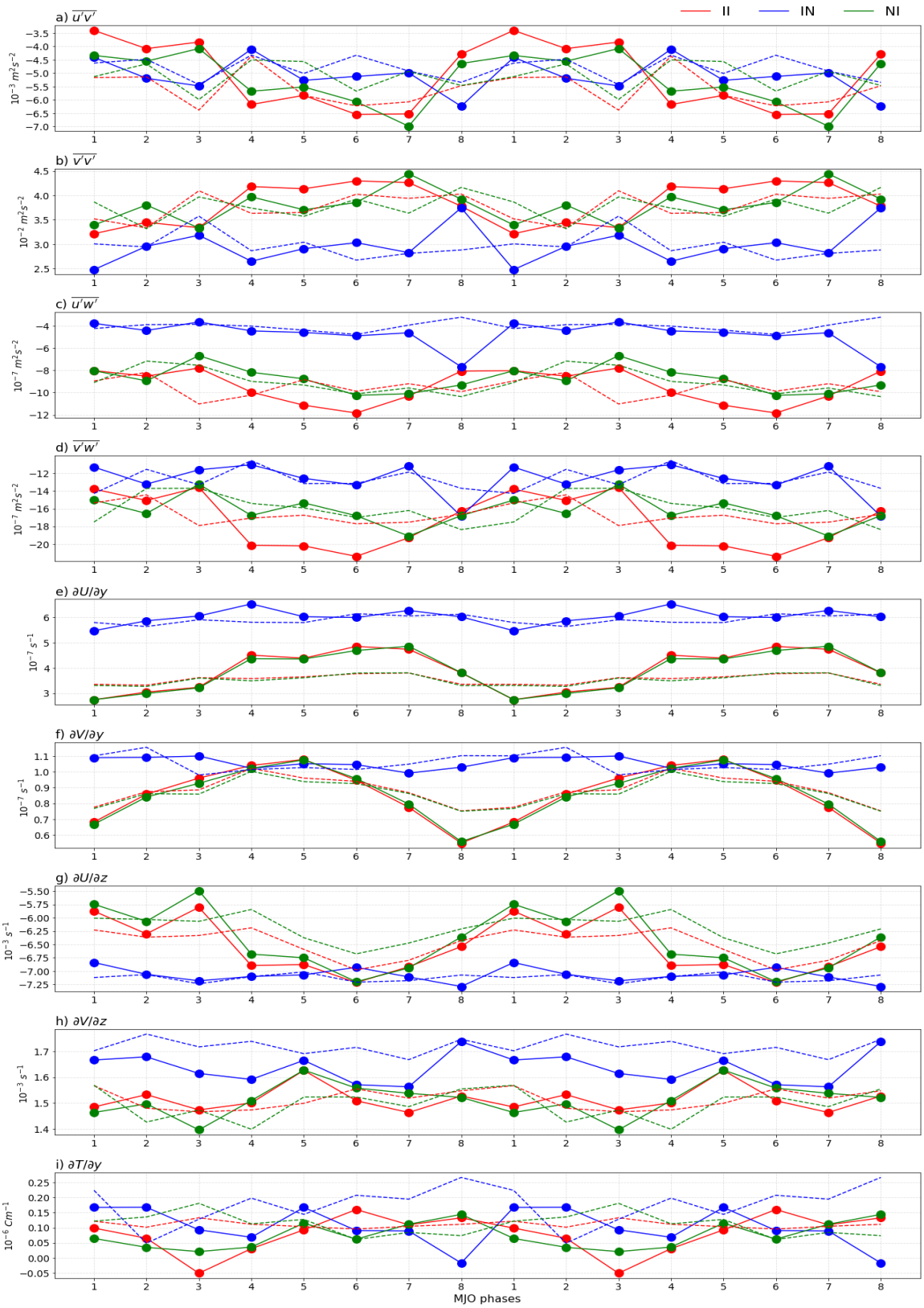

Figure 5.16. MJO composites of Reynolds stress components a) $\overline{u'v'}$, b) $\overline{v'v'}$, c) $\overline{u'w'}$, d) $\overline{v'w'}$, and e) meridional shear of the zonal velocity, f) meridional shear of the meridional velocity, g) vertical shear of the zonal velocity, h) vertical shear of the meridional velocity and i) meridional gradient of temperature averaged between 2˚S to 7˚N and 100˚W to 150˚W in the upper 100 m for MJO active (solid) and MJO inactive (dashed), from the II (red), NI (green) and IN (blue) simulations. Note the different vertical scale.

The resulting vertical Reynolds stress $\overline{u'w'}$ amplitudes from the II and the NI simulations can be up to 2-3 times smaller than the amplitudes from the IN run (Figure 5.16c). The values of $\overline{v'w'}$ exhibit a similar pattern to those of $\overline{u'w'}$ (Figure 5.16d). Furthermore, in the composite cycles of $\overline{v'w'}$ the differences in phases 4→6 between the NI and IN runs are comparable to those between the NI and the II runs. Therefore, in phases 4→6, the effect on $\overline{v'w'}$ of MJO atmospheric fields other than the wind stress (e.g., heat fluxes and freshwater fluxes) is comparable to that of the wind.

The impact of the active MJO on the meridional derivatives of the mean flow is visible in Figure 5.16 e-f. For both $\partial U/\partial y$ and $\partial V/\partial y$ the results from the NI and the II simulations are almost indistinguishable, and the two have a pronounced MJO cycle. In general, both meridional shears present higher magnitudes during easterlies winds (phases 4→6) compared to westerlies winds (phases 8→1). In the presence of interannual winds, the term $\partial U/\partial y$ is smaller by between 15% to 65% relative to the IN simulation, while $\partial V/\partial y$ is reduced by up to 50%. In contrast, in the vertical shears $\partial U/\partial z$ and $\partial V/\partial z$, only $\partial U/\partial z$ shows a pronounced cycle of the MJO (Figure 5.16g-h). For the three simulations, the magnitudes are comparable in phases 4→7 for $\partial U/\partial z$ and in phases 5→7 for $\partial V/\partial z$.

The variations in the amplitudes of $\partial T/\partial y$ are minimal in the absence of interannual wind stress forcing (Figure 5.16i). In general, the NI and II simulations show smaller meridional temperature gradients than does the IN in phases 1→5. Phase 8 particularly stands out, showing differences of around 15% between the values from the NI and the II and the values from IN run.

5.5 Summary

In this chapter, the response of TIWs to the MJO in the tropical Pacific has been investigated. The main findings of this chapter were:

- Strong EKE signals that map well on the known characteristics and mechanisms of TIWs were detected in the model simulations during 1990-2000 (Figure 5.1). The intensity of TIWs that is observed in the three sensitivity experiments is directly related to the type of wind stress forcing that is used. The greatest amplitudes of

EKE are located between 100°W to 150°W and 2°S to 7°N and in the top 100 metres of depth.

- In the creation of TIWs, barotropic and baroclinic instabilities have on average similar contributions, but their distributions in latitude and depth are different. For example, the conversion of the kinetic energy from mean flow to EKE is greater near 4°N and at the surface (Figure 5.7). In contrast, the conversion of the potential energy to EKE is at the strongest just below the surface at 2°N (Figure 5.9).
- The three simulations were undertaken in order to isolate the effects of different forcing factors, especially wind stress. The control simulation, II, the NI experiment, forced with interannual winds but the thermodynamic forcing that has no interannual variability (NYF) and the IN experiment, with interannual thermodynamic forcing and wind forcing from the NYF. The simulations with interannual winds are the ones that show a greater impact of the MJO on the ocean, indicating that it is the wind variability that predominantly drives the intraseasonal response of the ocean. Considering in particular TIW wave dynamics, the baroclinic and barotropic conversion terms tend to be weaker in the simulations with interannual wind variability when compared to simulation IN (Figure 5.12 and Figure 5.13). Nevertheless, the strongest barotropic and baroclinic energy values in the II and NI simulations occur in the MJO phases with predominantly easterly zonal wind anomalies.
- When the MJO is active, Reynolds stresses are clearly different depending on whether the anomalous MJO winds are from the east or from the west (Figure 5.16). We also note that both the meridional shear of the zonal current and the divergence of the meridional current are both stronger when a normal year wind forcing (IN run) is used. In experiments II and NI, both undergo a noticeable MJO cycle, with low (high) values during westerly (easterly) wind anomalies, and this is reflected in Figure 5.16.

Chapter 6

General Discussion

6.1 Oceanographic surface variability and its response to the MJO

The main characteristics of the intraseasonal variability and in particular the response to the Madden-Julian Oscillation (MJO) of the climate variables sea surface height (SSH), sea surface temperature (SST), sea surface salinity (SSS), surface zonal currents, non-solar part of the surface heat flux, solar heat flux, evaporation and precipitation in the tropical Pacific have been examined in detail based on ocean model simulations covering the period 1990-2000. In the present study the intraseasonal variability (10-120 days) of the SST, the surface zonal current, the non-solar surface heat flux, the evaporation and the precipitation, represents between 40 and 60% of the total variability over the simulation period (Figure 3.2). These maximum percentages occur in the equatorial band, which is also the region where the largest values of total variance are found. These intraseasonal variations in the oceanic surface fields are consistent with those obtained by several previous studies that have related these variations to two phenomena, namely the MJO and tropical instability waves (TIWs) (Maloney and Kiehl, 2002; Zhang *et al.*, 2010; Rydbeck *et al.*, 2013).

6.1.1 Dominant patterns of the surface intraseasonal variability

The possible mechanisms that govern the intraseasonal variability of these variables were analysed by identifying the two leading EOF (Empirical Orthogonal Function) modes and their respective power spectra. The results show that the SSH, SST, and zonal velocity anomalies gradually propagate eastward within and along the equatorial region, suggesting there is a common cause for these variations, presumably equatorial Kelvin wave dynamics (see Section 3.3). In addition, the two principal components (PCs) of the SSH exhibit a relatively high lag correlation (0.71 and 0.72) with those of the zonal velocity at lag 11 and 9 days, respectively. However, this is not the case for the PCs of the SST, which, in contrast, show correlations of less than 0.2 with those of the SSH and the zonal velocity, which indicates that the variability of the SST have sources other than those of the SSH and the zonal velocity. The dominant patterns of variability of the SSH, SST, and zonal velocity resemble the typical propagation of the intraseasonal Kelvin waves that are induced by

MJO wind anomalies (Rydbeck *et al.*, 2019). Spectral analyses of the PCs of the SSH, SST, and zonal velocity reveal additional evidence, each showing a similar significant spectral peak from 45 to 90 days that is consistent with the typical intraseasonal Kelvin wave period (Kessler *et al.*, 1995). The variability of the SST, however, seems to be also affected by processes other than intraseasonal, equatorial Kelvin waves. The peak energy of the SST PC1 is wider, with a range of 30 to 90 days, suggesting that TIWs (period 20-40 days) are probably also playing a role in supporting SST variability (Jochum *et al.*, 2007). Additionally, the SST EOF2 mode (Figure 3.6) shows an area of relatively high SST variability in the Costa Rica Dome region, where Maloney *et al.* (2008) have documented that variations in both latent heat flux and shortwave radiation contribute to the intraseasonal SST variability.

Intraseasonal SSH and zonal velocity variations have also been related to TIWs (Shinoda *et al.*, 2009). Indeed, the analysis of the intraseasonal variability of these two fields shows that they can contribute as much as 60% of the total variance in the region of the eastern equatorial Pacific where TIWs are most active (Figure 3.2). TIWs were captured in higher order EOF modes of these two variables. However, we decided to present only the first two leading modes in this study, since these first two modes are the most physically interpretable, and in many cases, higher order modes appear to be degenerate (North *et al.*, 1982).

In contrast, the EOF dominant patterns of the non-solar part of the surface heat flux, the solar heat flux, the evaporation and the precipitation are not located around the equator. Rather, the greatest amplitudes are generally located in the western Pacific and north of the equator, north of 5°N. A comparison with earlier studies shows our results to be generally consistent with previous research (e.g., Grodsky *et al.*, 2009; Pariyar *et al.*, 2019). Considering that the MJO is the dominant mode of atmospheric intraseasonal variability in the region and that the previous four fields show similar spectral characteristics to the MJO, with peaks in the range of 40 to 70 days, it is natural to conclude that their intraseasonal variability is largely governed by the MJO.

Thanks to the wavelet analyses it is also possible to observe the interannual behaviour of the intraseasonal variability and therefore its response to interannual phenomena such as El Niño Southern Oscillation (ENSO). The SSH and the zonal velocity signals are more

intense during El Niño of 1992-1993 and even more prominently during the 1997-1998 event. These results are consistent with the previous studies of the relationship between intraseasonal Kelvin wave propagation and ENSO (e.g., Benestad *et al.*, 2002; Rydbeck *et al.*, 2019). For example, Rydbeck *et al.* (2019) found a 20-40% reduction in SSH anomalies during La Niña events when compared to El Niño events.

6.1.2 MJO surface composites

The variability of the oceanic surface fields has been related to the eight phases of the MJO through MJO composites. A pattern correlation analyses found similar patterns but with opposite signs between pairs of phases, namely 1-5, 2-6, 3-7 and 4-8 (e.g., Figure 3.27), which corresponds to the known oscillatory nature of the MJO. Succinctly, the simulated ocean response to the MJO can be described as follows. Anomalous westerly winds are present in phases 6-7 in the western Pacific. These generate a downwelling equatorial Kelvin wave. This train of waves was identified in the simulation by significant positive anomalies of both the zonal velocity and the SSH during the same phases (see Section 3.4). These waves propagate eastwards during the subsequent MJO phases until eventually reaching the American continent. This descending portion of the Kelvin waves releases relatively warm water thus resulting in the development of positive SST anomalies (Figure 3.29). In addition to Kelvin wave dynamics, advective processes contribute as well to the development of intraseasonal temperature anomalies. This contribution will be further examined in Section 6.2.

The presence of positive SST anomalies favours the development of active atmospheric convection (Jones *et al.*, 1998). The increase (decrease) in evaporation was consistent with regions with positive (negative) SST anomalies, except phases 4 and 8 (Figure 3.33). A correspondence between precipitation anomalies and SST was also observed, except for within the eastern Pacific warm pool area (Figure 3.35). The reader is reminded that precipitation in the model is a forcing field and therefore it does not respond to SST. Maloney and Kiehl (2002) also noticed a mismatch between SST and precipitation in the eastern Pacific warm pool region, they documented a difference of between 10-15 days in the occurrence of both variables.

Over the general equatorial region, the patterns of the rainfall anomalies occupied the mean position of the Intertropical Convergence Zone (ITCZ). Because of this behaviour, the associated system of suppression and conversely enhanced evaporation was considered to be in agreement with the intraseasonal SSS variations. Therefore, regions of maximum positive SSS anomalies coincided well with the regions of negative precipitation anomalies.

In addition, it is evident that SST anomalies also respond to variations in the heat surface fluxes. Over the central and eastern equatorial Pacific an increase (decrease) in non-solar flux (latent heat flux being its greatest contributor) and a reduction (increase) in surface shortwave radiation flux results in cooling (warming) of the SST. In particular, in the eastern Pacific warm pool area, the shortwave radiation plays a significant role in SST anomalies, as previously suggested by Maloney and Kiehl (2002). The results presented here provide further evidence of the MJO's response over the tropical Pacific, in particular by the existence of a statistically significant cycle in the anomalies of the surface variables.

6.1.3 Lagged linear regression and Granger causality analysis

This study has also rigorously estimated the causal relation between the MJO and each of the eight chosen ocean surface variables through the use of Granger causality analyses. The results show that the two regions in which the MJO is a Granger-cause of the intraseasonal variability of the SSH and the zonal current fields are almost coincident (see Section 3.5). The first region is the area centred on the equator, which is consistent with the location of the MJO-induced intraseasonal Kelvin waves and consequently quite similar to the EOF modes of these variables. The second region is located near the Pacific coast of Central America where coastal Kelvin waves are propagating poleward. In the latter region, it can also be observed that the MJO Granger causes intraseasonal variations in the SST, presumably also due to coastal Kelvin wave propagation.

The explained variance of the intraseasonal anomalies of each field was calculated using the RMM MJO index as a predictor (Wheeler and Hendon, 2004) (see Section 2.3). Although the patterns of maximum variance are not always clearly indicative of MJO Granger causality, these patterns generally match. Interestingly, the MJO contributes more to the intraseasonal variance of the SSH than it does to any other variable, with maximum percentages of explained variance of up to 30% (Figure 3.36).

The MJO has a Granger causal effect on surfaces fluxes[1]. As expected, the regions that are influenced by MJO Granger-caused variability on the non-solar heat flux and evaporation are practically the same, extending over the equatorial band of the central and eastern Pacific. Conversely, the anomalies of the shortwave solar radiation[1] that are shown to be Granger caused by the MJO are in the south of Mexico and in the Central America regions. These variations of the surface fluxes could be related to the anomalies in the prevailing cloud cover and on the speed and direction of the winds due to the presence of the MJO (Grodsky *et al.*, 2009).

It is also interesting to note that the results do not appear to indicate a Granger causal relationship between the MJO and the intraseasonal anomalies of salinity or of between the MJO and the intraseasonal anomalies of precipitation[1]. Other studies have also demonstrated that the effects on salinity and precipitation induced by the MJO are much weaker in central and eastern Pacific regions when compared to those in the Indian Ocean and the western Pacific (e.g., Waliser *et al.*, 2003; Zhang, 2005; Li *et al.*, 2015; Li and Han, 2016).

6.2 Oceanographic subsurface variability and its response to the MJO

In the analyses of the intraseasonal subsurface variability of temperature, salinity and currents, the regions with the highest percentages of intraseasonal variability relative to the total, unfiltered variability were located at depths between 10 m and 260 m. The largest total variability of both the temperature and the zonal currents is encountered in the equatorial band, which can be explained mainly by the effects of the Kelvin waves (Zhang, 2001). However, the region that is to the north of the equator is the area that develops the highest percentages of relative intraseasonal variability. This behaviour is displayed not only by temperatures and zonal currents but also by thermocline depths, and meridional and vertical currents, with maximums of up to 90% of the total variance in the intraseasonal band (see Section 4.3). This region, located between 100°W and 160°W, is where the TIWs activity has been generally located (Contreras, 2002).

[1] We remind the reader that downwelling shortwave radiation and precipitation are forcing fields of the ocean model, rather than a prognostic field.

Although the equatorial region did not demonstrate the maximum percentages of 10-120 days variance, it continues to be a region of great importance for the intraseasonal variability. Its relative amplitude is considerable, with percentages between 20% to 60% of the total variance, and in the case of salinity, the maximum intraseasonal variability (60%) was located in this region of intraseasonal Kelvin wave's influence. The results then, being consistent with earlier studies (e.g., Matthews *et al.*, 2010; Lee *et al.*, 2012; Rydbeck *et al.*, 2019), suggest that the two main processes that modulate the oceanic intraseasonal variability in the tropical Pacific are the intraseasonal Kelvin wave (ISKw) and the TIWs. This raises two important questions: how deep below the surface reaches the influence of these mechanisms, and what is the latitudinal distribution of this variability, questions that will be addressed and analysed below.

6.2.1 Vertical sections of intraseasonal variability

The intraseasonal temperature variability was found to be highest in the vicinity of the thermocline, typically between 50 m and 200 m, and concentrated in the eastern and central Pacific (see Section 4.4.1). The causal mechanisms that are responsible for these anomalies appear to vary with geographic location. For example, according to a power spectrum analysis, the variations observed at 5°N showed dominant periods that are consistent with the ISKw towards the western region of the Pacific Basin, while towards the east the spectral peaks agree mostly with the TIWs. This is in agreement with the observations of McPhaden (2002).

The individual contributions of several different physical processes that are potentially involved in the generation of temperature variability have been the subject of several studies with different conclusions. For example, Zhang (2001) suggested that forced ISKw modulate the depth of the thermocline which causes, in turn, changes in the vertical temperature gradient. Subsequently, McPhaden (2002) estimated that zonal advection has a dominant role in the central Pacific while a combination of vertical advection and entrainment predominate in the eastern Pacific. In contrast, Lucas *et al.* (2010) identified meridional advection as being the component making the major contribution. But Halkides and Lee (2009) attributed the discrepancies in the various results to the use of different methodologies being employed between the studies. For example, the calculations differ if they are taken at a spatial point using mooring buoys, or if they are averaged over a specific

region. Some of the differences could also be related to the various time periods that are represented (Halkides and Lee, 2009). Our results show that the variations in the net tendency of intraseasonal temperature occurring in most latitudes are caused mainly by the vertical advection. However, at latitude 2°N, the contributions of the zonal advection and the meridional advection are significant in the eastern Pacific region. The role of diffusion, both lateral and vertical, was considered in this study. However, these processes have been shown to make a much lower contribution to the temperature variability.

The power spectra of the points of maximum intraseasonal variability of both salinity and zonal currents have revealed a similar behaviour to the variations in temperature. The points that are located in the eastern Pacific show spectral peaks that correspond to the typical period of the TIWs, while points in the western Pacific were shown to be associated with the Kelvin waves. In some points located in the central Pacific, it is possible to distinguish two separate power peaks that are likely related to the spatial meeting of two previous phenomena. These associations are in agreement with previous research (see Section 4.4.2 and 4.4.3). The results also suggest that in both salinity and the zonal currents the Kelvin waves exert a greater influence between latitudes 2°N to 2°S, while the TIWs generate more variability within the latitudes of 2°N and 5°N.

The intraseasonal variability of the meridional and vertical currents seems to respond mainly to the TIWs. The spectral analyses showed that most of the points that are located in high variance regions presented well-defined peaks with a period within the range of TIWs activity (Inoue *et al.*, 2019).

We have also shown that the regions of greater intraseasonal variability of both salinity and currents are located above the mean thermocline depth, with the exception of temperature, as discussed above.

6.2.2 MJO related subsurface composites

Similar to the ocean surface treatment, the structure of the vertical response of key ocean variable to the MJO was studied through the use of MJO composites. We include here ocean current composites, which, to the best of our knowledge, have not been shown in previous literature. The analysis was focused on sections along 2°N, 0° and 2°S and in the

upper 300 m. During an MJO, the temperature and zonal current anomalies were observed in phase. This phase alignment was most clearly shown at the equator. At this latitude, the maximum and minimum temperature anomalies tend to propagate along the slope of the mean thermocline depth, gradually ascending towards the east while also reducing in their intensity. The maximum temperature anomalies (phases 7 and 8) are located in the western Pacific and have been related to the anomalies in zonal winds in this region (Matthews *et al.*, 2010). It is in these phases, 7 and 8, when the active atmospheric convection is located over the western Pacific. While, as discussed earlier, the intraseasonal temperature variations seen in the central and eastern Pacific regions from latitudes 2°N to 2°S are primarily caused by temperature advection.

The zonal current sections show large significant anomalies occurring at different depths during the MJO cycle, pointing at the possible modulation of the South Equatorial Current (SEC) and the Equatorial Undercurrent (EUC) by the MJO, as also suggested by Wang *et al.* (2016b), in the western Pacific region.

Salinity anomalies were also shown to be related to the ISKw particularly at the equator and at 2°S. In contrast to the temperature and the zonal current behaviours, this influence appears to be confined to below the mean thermocline depth. The salinity variations above the mean thermocline depth are probably related to the movement of fresher water either by upwelling or by horizontal advection (Matthews *et al.*, 2010; Li *et al.*, 2015).

In the MJO composite for vertical currents, it was also possible to observe the ISKw signature, although with less clarity in the corresponding anomalies if these are compared with those of temperature, salinity or zonal currents. The variations in the vertical current during an MJO cycle resemble those of the anomalies of zonal currents but with the opposite sign. The vertical velocity profiles are thus consistent with ISKw's upwelling/downwelling movements.

Importantly, the variations shown in these MJO composites are not small when compared to the standard deviation of the entire time series (STD). The maximum amplitudes in temperature variability, for example, can reach up to 50% of the STD. In the case of both the salinity and the zonal current, variations of up to +/- 40% of the STD are seen and for the vertical currents, their anomalies can be up to +/- 30% of the STD.

The present study also examined the response of the meridional currents to the MJO cycle. However, it was not possible to identify a visible pattern in the anomalies. This is consistent with the vertical structures of the intraseasonal variation of the meridional currents discussed above, where spectral peaks were located in different periods rather than in the MJO range (see Section 4.4). It must be taken into consideration, nevertheless, that these MJO composites were limited to the vicinity of the equator and, according to the Granger causality analysis that was performed in Section 4.5, there is an influence of the MJO in the meridional currents north of 5°N.

6.2.3 Lagged linear regression and Granger causality analysis

The influence of the MJO on the subsurface of the tropical Pacific was assessed within the framework of Granger causality. Overall, the equatorial band was found to be the region with the greatest influence of the MJO on temperature, salinity, and both zonal and vertical currents when intraseasonal wind stress forcing is present. These results were to be expected since the ISKw propagates directionally along the equator (Rydbeck *et al.*, 2019). However, the Granger causal relationship was not located at the same depths for all the four variables mentioned. In the case of temperature, the regions around the mean thermocline and the mean pycnocline revealed significant Granger causality related to the MJO, with a relatively higher percentage of the intraseasonal variance observed over the western and central Pacific. This was anticipated considering that the ISKw not only propagates through the thermocline but is also modified by the thermocline structure (Kessler *et al.*, 1995). On the other hand, it is also not surprising that the pycnocline showed MJO Granger-causes temperature variability, given the vertical proximity between the thermocline and the pycnocline at the equator. Variations in the depth of the tropical pycnocline are mainly determined by temperature (Fiedler *et al.*, 2012).

At mixed layer depth (MLD), the Granger causal relationship between the MJO and temperature, zonal and meridional currents over the eastern Pacific warm pool was also identified. Although the Granger causality of the MJO on zonal and meridional currents was only observed in those simulations that used intraseasonal wind stress forcing. This response could be attributed to large anomalies of the zonal winds during the MJO cycle present in this area (see Figure 3.32). At pycnocline and halocline depths, the Granger-causal link between MJO and the variability of meridional currents was also observed.

Contrarily, the MJO Granger causality of the temperature at MLD is significant in the absence of intraseasonal wind stress forcing, as temperature variability in the MLD is most sensitive to latent heat and shortwave radiation fluxes (Maloney and Kiehl, 2002).

We conclude that the MJO Granger-caused subsurface variability at different depths is mainly induced by variable wind stress forcing. Except for the temperature variations over the eastern Pacific warm pool at MLD that showed significant MJO Granger causality related to surface heat fluxes.

6.3 TIWs and their response to MJO

The model captures well the dynamics and structure of the TIWs. A Hovmöller diagram clearly revealed the eastward propagation of these waves. We were able to identify their typical seasonality (July to December), phase velocity (~ 0.55 m/s) and wavelength (~ 1100 km) (Qiao and Weisberg, 1995) (see Section 5.2). Additionally, through this Hovmöller diagram, the behaviour of the TIWs during ENSO events was also made evident. In the El Niño years (1991-1992, 1994-1995, 1997-1998) a near suppression of the TIWs was shown while in the La Niña years (1995-1996, 1998-1999, 1999-2000) the TIWs were stronger. These results are consistent with previous studies where a negative feedback between ENSO and TIWs is proposed (e.g., An, 2008) (see Section 5.2).

The intensity of the intraseasonal eddy kinetic energy (EKE) variability is strongly controlled by the intensity of the surface winds. The EKE can be 4 times larger when using 1.5 times higher wind speed forcing. The maximum amplitudes of EKE were located in the central and eastern Pacific averaged in the upper 100 m, with values of up to 0.15 m^2/s^2. The associated filtered velocities are then on the order of 0.5 m/s. The results from the simulation with an increase of 50% in the surface wind forcing also showed relatively high EKE values in deeper water, a more extended EKE signal both east and west, and a higher TIW phase velocity compared to the control simulation (II) (see Section 5.2). Although these strong responses were mostly confined between 100°W to 150°W, TIWs' region of activity.

This intraseasonal EKE response to wind speed forcings is not surprising, since ocean circulation in the tropical Pacific is largely driven by wind stress (Kessler, 2006), and particularly the intensification of southerly winds present in the second half of the year

allows a greater production of EKE as already discussed by Wang *et al.* (2019). Although to the best of the author's knowledge, the changes in the phase speed of TIWs caused by the changes in wind speed which we have shown in the sensitivity experiments, have not been presented in the literature before.

6.3.1 TIWs energy transformation

The main sources of TIWs were quantified following Masina *et al.* (1999). The two main processes controlling changes in EKE are the conversion of mean kinetic energy to EKE (barotropic instabilities and Kelvin-Helmholtz instabilities, which actually do not operate in a decoupled way) and the energy transfer from the available potential energy to EKE (baroclinic instabilities). The current study found that the maximum contributions of these dominant terms to the production of EKE vary both meridional and in depth (see Table 5.1), although, on average in the entire region, barotropic instabilities are the greatest. These results are consistent with those registered by Wang *et al.* (2017) for the tropical Pacific region, although they did not take into account the contribution of Kelvin-Helmholtz terms.

These diverse instabilities, caused primarily by seasonal southerly winds, generate variations in the zonal currents and SST fronts. For example, the maximum contributions from barotropic instabilities were concentrated at the surface around 4°N. This energy transfer from the mean flow to EKE is the product of the meridional shear between the EUC and the NECC. The Kelvin-Helmholtz instabilities were located below the surface acting as an energy sink (negative values) for EKE. The baroclinic instabilities were negligible on the surface and significant below it, with positive values on both sides of the equator that indicate a contribution towards EKE production. These positive baroclinic disturbances are related to SST fronts which are intensified by the encounter of cold upwelled water with warm surface water (de Szoeke *et al.*, 2007). Although, the values of the baroclinic conversion term were shown to be larger north than south of the equator. This difference between hemispheres comes about because in the Southern Hemisphere the SST front is weaker due to the continuous cold waters advected there from the Peru Current (de Szoeke *et al.*, 2007). The results also showed negative values of the baroclinic conversion term located between 80 and 150 m around 4-5°N. This was in agreement with

Qiao and Weisberg (1998) who showed that the conversion of kinetic energy into potential energy is achieved through an upward buoyancy force.

Overall, these EKE production mechanisms were shown to be modulated by wind speed. Both the barotropic conversion term (BTR-KH) and baroclinic conversion term (BCL) exhibited higher values when winds coming from Normal Year Forcing (NYF) were used. Therefore, it can be concluded that those simulations with interannual wind variability, that allow the development of phenomena such as El Niño, reduce the barotropic and baroclinic conversion terms.

6.3.2 MJO composites

Neither the currents nor the temperature were significantly influenced by the MJO in the simulation without interannual winds (see Section 4.5). To try to understand better this response, it was decided to contrast the behaviour of BTR-KH and BCL in the MJO phases, expecting changes in these terms to depend on the sign of the wind anomalies in a particular phase. The results showed high correlations between zonal wind and EKE conversion terms when the wind leads BTR-KH and BCL by 8 days. In those MJO phases with negative (positive) zonal wind anomalies, stronger (weaker) zonal currents and larger (smaller) BTR-KH values were observed. This is expected by the modification of the background velocity field, which leads to an increase (or decrease) in barotropic instabilities through horizontal shear intensification between the EUC and the SEC, and the EUC and the NECC (Masina *et al.*, 1999).

Similarly, a correspondence was observed between those MJO phases with negative (positive) anomalies of zonal winds, negative (positive) temperature anomalies and larger (smaller) BCL values. Since the water density changes in this tropical region are controlled mainly by temperature changes (Fiedler and Talley, 2006), variations in baroclinic instabilities are closely related to perturbations in temperature fronts. SST fronts are intensified by anticyclonic wind curls produced by strong southeast winds in the eastern Pacific (Wang *et al.*, 2019).

In addition, the impact of the MJO was analysed on each of the significant components responsible for the production of BTR-KH and BCL. Overall, the Reynolds components,

$\overline{u'v'}, \overline{v'v'}, \overline{u'w'}$ and $\overline{v'w'}$ showed a clear difference between the MJO phases with anomalous easterlies winds and the MJO phases with anomalous westerlies winds. In the simulations forced with interannual winds, an intensification of the magnitudes of all the Reynolds components was observed during the easterlies wind anomalies when compared to the results from the simulation forced with NYF winds.

Similarly, the meridional derivatives of the currents showed a clear response to the different phases of the MJO. These variations can attain values in the range of 15% to 65% between simulations with different wind forcing. In the case of the vertical shear of the zonal velocity, it is also possible to observe a pronounced MJO cycle. These results reinforce what was previously shown in Section 5.3, namely, that the MJO cycle decreases the intensity of the TIWs production sources in phases 7→1, and this attenuation results from the presence of anomalous westerly winds.

6.4 Limitations

Although this thesis presents results that were carefully and rigorously analysed as well as its subsequent conclusions, certainly, this research contains several limitations that should be addressed in future work.

6.4.1 Statistical Methods

The statistical tools used in this study, particularly Empirical orthogonal functions (EOFs) and Granger causality, are frequently used to address problems related to climate variability (e.g., McGraw and Barnes, 2018; Pariyar *et al.*, 2019). However, although powerful, both methods must be used with caution to avoid misinterpretations.

A great strength of the EOF analysis is that it projects the climatic data onto mutually orthogonal spatial patterns (von Storch and Zwiers, 2001). In addition, it provides a measure of variance associated with each EOF mode. Despite these advantages, this method is limited by a number of factors, including:

- The number of EOF modes corresponds to the length of the data.
- Sometimes, many modes need to be retained in order to explain a certain amount of the total variance.

- A symmetry between positive and negative phases in the spatial patterns is assumed.
- There is no guarantee that individual EOF modes can be physically interpreted. For example, in the case of propagation phenomena, such as travelling waves, at least two modes are needed to represent a single phenomenon.

The Granger causality method, meanwhile, stands out because it helps to infer causal influences between signals based on temporal precedence. However, this method requires the selection of a particular variable, or field, as the causal predictor, and this selection is not always free of arbitrariness (Granger, 1969). Furthermore, there are also limitations associated with the possible existence of hidden common causes. For example, if both X and Y are caused by Z, X would appear to Granger cause Y. Granger causality does not include intermediate variables and ignores the fact that X can cause Y through of Z, therefore it is then possible to incorrectly designate X as the causal influence. Finally, Granger causality requires assumptions of linear and stationary processes (McGraw and Barnes, 2018).

6.4.2 Model Resolution

In this study, the chosen 1° horizontal global model resolution is a response to limitations in computational resources. Although our model is of about eddy permitting resolution in the equatorial region, since the zonal resolution is 1° and has a meridional refinement around the equator of up to $1/3^{\circ}$, still it is not able to resolve properly mesoscale processes. According to Graham (2014), if the resolution of the model is improved using 0.25° in the tropical Pacific there is a better simulation of the TIWs, but also the meridional heat advection by TIWs increases by 37% compared to 1° model resolution. In the present work, an attempt was made to improve the resolution of the model through multiple grid nesting focused on the tropical Pacific, however, it was not successfully achieved.

6.4.3 Coupled Model

Currently simulating the MJO still represents a challenge (Shoup *et al.*, 2020). Both global atmospheric general circulation models (AGCM) and coupled general circulation models (CGCM) have shown several deficiencies in an accurate representation of the MJO, mainly as regards its amplitude, propagation speed and seasonality (Inness and Slingo, 2003),

although current research has led to improvements in the MJO simulation in AGCM using different approaches, among them being the use of higher frequencies of prescribed SST from monthly to daily (Kim *et al.*, 2008) or using a better vertical resolution for the ocean mixing layer (Woolnough *et al.*, 2007; Klingaman and Woolnough, 2014). However, as the MJO is strongly coupled there is a consensus that the implementation of a coupled model favours the representation of the MJO (Shoup *et al.*, 2020).

Chapter 7

Conclusions and future work

7.1 Synthesis of key findings

We have completed a modelling study of the intraseasonal variability of the equatorial Pacific Ocean and its response to the Madden-Julian Oscillation (MJO). Chapter 3 focused on surface variability using the following techniques: EOF, spectral, composites, Granger causality, etc. The main results were:

- Maximum intraseasonal variations of sea surface height (SSH), sea surface temperature (SST) and surface zonal currents are located in the equatorial band. This variability is generated mainly by equatorial Kelvin waves induced by MJO wind anomalies and tropical instability waves (TIWs).
- The dominant patterns of intraseasonal variability of the non-solar part of the surface heat flux, solar heat flux, evaporation and precipitation[2] are located in the western Pacific and north of the equator and are largely controlled by the MJO.
- During the MJO cycle, positive (negative) SST anomalies are associated with downwelling (upwelling) equatorial Kelvin waves that also generate positive (negative) anomalies in SSH and zonal currents during their propagation eastwards.
- The evolution of SST anomalies also shows a direct relationship with variations in heat surface fluxes and evaporation through the MJO phases.
- The equatorial band and the eastern Pacific warm pool are the regions where the MJO is a Granger-cause of the intraseasonal variability in most of the surface variables, except for sea surface salinity and precipitation.

The role of the MJO in controlling intraseasonal variations in temperature, salinity, and currents at depth was examined in Chapter 4. The key findings of this chapter are as follows.

- Most of the intraseasonal temperature variability is concentrated around latitude 5°N below the mean thermocline depth, with maximum variations of 1.5°C.

[2] We remind the reader that precipitation is a forcing of the ocean model, rather than a prognostic field.

- Vertical advection of temperature is the main contributor to variations in the net tendency of intraseasonal temperature.
- Changes in intraseasonal subsurface variability of salinity and zonal currents are mainly related to the intraseasonal Kelvin waves (ISKw) in the western Pacific and to TIWs in the central and eastern Pacific.
- TIWs are the main mechanism responsible for the maximum intraseasonal variations of the meridional and vertical currents, which are located above the mean thermocline depth between 2°S and 7°N.
- Large, statistically significant anomalies of the temperature, salinity, zonal current and vertical current occur during the MJO cycle predominantly at the equator, where the ISKw signature can be also observed.
- The intraseasonal wind variability is the key forcing factor that modulates the impact of the MJO on the tropical Pacific Ocean.

In Chapter 5 the influence of the MJO on the dynamics of TIWs was identified and quantified using various sensitivity model simulations. The main contributions of this chapter were:

- Mechanisms of EKE production are modulated by wind variability. The barotropic and Kelvin-Helmholtz conversion term, as well as the baroclinic conversion term, were stronger when a normal year wind forcing is used.
- The Reynolds components of the barotropic and Kelvin-Helmholtz conversion term are intensified during MJO easterly wind anomalies compared to phases with predominantly westerly anomalies.
- The meridional shear of the zonal current, the divergence of the meridional current and the vertical shear of the zonal current show a pronounced MJO cycle.
- In the presence of interannual winds, the term $\partial U/\partial y$, $\partial V/\partial y$ and $\partial U/\partial y$ can be considerably smaller than in the IN simulation particularly during westerly wind anomalies.

The results outlined above contribute to a better understanding of the physical processes involved in the dynamics of intraseasonal variability in the equatorial Pacific Ocean and, in particular, its response to the MJO. This is of primary importance to our ability to make more reliable short and mid-range oceanic climate forecasts for the region.

7.2 Opportunities for future research

The work presented in this thesis also points in several directions in terms of potential future developments. From the point of view of methodology, using a coupled climate model with higher temporal and spatial resolution would allow us not only to improve the simulation of the distribution of intraseasonal oceanic variability but also to represent the interaction between the ocean and the atmosphere during an MJO cycle, in particular, the feedback of TIWs on the surface intraseasonal winds (Seo *et al.*, 2016). Another line of investigation related to TIWs would be to focus on the separate contribution of temperature and salinity to density anomalies that play a key role in baroclinic conversion in the tropical Pacific Ocean (Lee *et al.*, 2014). Regarding the MJO, future research should include the examination of the impact of interannual variability of the MJO on the ocean dynamics. Additionally, the role of the MJO in regional circulation in areas such as the Costa Rica Dome should be studied. Experiments aiming at differentiating between the roles of local and remote forcing in the oceanic variability would also be valuable.

References

Alory, G., Maes, C., Delcroix, T., Reul, N. and Illig, S. (2012) 'Seasonal dynamics of sea surface salinity off Panama: The far eastern Pacific Fresh Pool', *Journal of Geophysical Research: Oceans*, 117(4).

Amador, J.A., Alfaro, E.J., Lizano, O.G. and Magaña, V.O. (2006) 'Atmospheric forcing of the eastern tropical Pacific: A review', *Progress in Oceanography*, 69(2–4), pp. 101-142.

Amante, C. and Eakins, B.W. (2009) 'ETOPO1 Global Relief Model converted to PanMap layer format'. PANGAEA. Available at: https://doi.org/10.1594/PANGAEA.769615.

An, S.-I. (2008) 'Interannual Variations of the Tropical Ocean Instability Wave and ENSO', *Journal of Climate*, 21(15), pp. 3680-3686.

Balmaseda, M.A., Mogensen, K. and Weaver, A.T. (2013) 'Evaluation of the ECMWF ocean reanalysis system ORAS4', *Quarterly Journal of the Royal Meteorological Society*, 139(674), pp. 1132-1161.

Barlow, M. and Salstein, D. (2006) 'Summertime influence of the Madden-Julian Oscillation on daily rainfall over Mexico and Central America', *Geophysical Research Letters*, 33(21).

Batstone, C.P., Matthews, A.J. and Stevens, D.P. (2005) 'Coupled Ocean–Atmosphere Interactions between the Madden–Julian Oscillation and Synoptic-Scale Variability over the Warm Pool', *Journal of Climate*, 18(12), pp. 2004-2020.

Benestad, R.E., Sutton, R.T. and Anderson, D.L.T. (2002) 'The effect of El Niño on intraseasonal Kelvin waves', *Quarterly Journal of the Royal Meteorological Society*, 128(582), pp. 1277-1291.

Brown, J.R., Power, S.B., Delage, F.P., Colman, R.A., Moise, A.F. and Murphy, B.F. (2011) 'Evaluation of the South Pacific Convergence Zone in IPCC AR4 Climate Model Simulations of the Twentieth Century', *Journal of Climate*, 24(6), pp. 1565-1582.

Butterworth, S. (1930) 'On the Theory of Filter Amplifiers', *Experimental Wireless and the Wireless Engineer*, 7, pp. 536-541.

Carton, J.A. and Giese, B.S. (2008) 'A Reanalysis of Ocean Climate Using Simple Ocean Data Assimilation (SODA)', *Monthly Weather Review*, 136(8), pp. 2999-3017.

Charney, J.G. and Eliassen, A. (1964) 'On the Growth of the Hurricane Depression', *Journal of the Atmospheric Sciences*, 21(1), pp. 68-75.

Chelton, D.B., Wentz, F.J., Gentemann, C.L., de Szoeke, R.A. and Schlax, M.G. (2000) 'Satellite microwave SST observations of transequatorial tropical instability waves', *Geophysical Research Letters*, 27(9), pp. 1239-1242.

Chen, X., Qiu, B., Chen, S., Qi, Y. and Du, Y. (2015) 'Seasonal eddy kinetic energy modulations along the North Equatorial Countercurrent in the western Pacific', *Journal of Geophysical Research: Oceans*, 120(9), pp. 6351-6362.

Church, J.A. and White, N.J. (2011) 'Sea-Level Rise from the Late 19th to the Early 21st Century', *Surveys in Geophysics*, 32(4), pp. 585-602.

Compo, G.P., Whitaker, J.S. and Sardeshmukh, P.D. (2006) 'Feasibility of a 100-Year Reanalysis Using Only Surface Pressure Data', *Bulletin of the American Meteorological Society*, 87(2), pp. 175-190.

Compo, G.P., Whitaker, J.S., Sardeshmukh, P.D., Matsui, N., Allan, R.J., Yin, X., Gleason, B.E., Vose, R.S., Rutledge, G., Bessemoulin, P., Brönnimann, S., Brunet, M., Crouthamel, R.I., Grant, A.N., Groisman, P.Y., Jones, P.D., Kruk, M.C., Kruger, A.C., Marshall, G.J., Maugeri, M., Mok, H.Y., Nordli, Ø., Ross, T.F., Trigo, R.M., Wang, X.L., Woodruff, S.D. and Worley, S.J. (2011) 'The Twentieth Century Reanalysis Project', *Quarterly Journal of the Royal Meteorological Society*, 137(654), pp. 1-28.

Contreras, R.F. (2002) 'Long-Term Observations of Tropical Instability Waves', *Journal of Physical Oceanography*, 32(9), pp. 2715-2722.

Cox, M.D. (1980) 'Generation and Propagation of 30-Day Waves in a Numerical Model of the Pacific', *Journal of Physical Oceanography*, 10(8), pp. 1168-1186.

Crueger, T., Stevens, B. and Brokopf, R. (2013) 'The Madden–Julian Oscillation in ECHAM6 and the Introduction of an Objective MJO Metric', *Journal of Climate*, 26(10), pp. 3241-3257.

Cushman-Roisin, B. and Beckers, J.-M. (2011) *Introduction to geophysical fluid dynamics: physical and numerical aspects*. Academic Press.

Dai, A., Qian, T., Trenberth, K.E. and Milliman, J.D. (2009) 'Changes in Continental Freshwater Discharge from 1948 to 2004', *Journal of Climate*, 22(10), pp. 2773-2792.

de Szoeke, S.P., Xie, S.-P., Miyama, T., Richards, K.J. and Small, R.J.O. (2007) 'What Maintains the SST Front North of the Eastern Pacific Equatorial Cold Tongue?*', *Journal of Climate*, 20(11), pp. 2500-2514.

Dee, D.P., Uppala, S.M., Simmons, A.J., Berrisford, P., Poli, P., Kobayashi, S., Andrae, U., Balmaseda, M.A., Balsamo, G., Bauer, P., Bechtold, P., Beljaars, A.C.M., van de Berg, L., Bidlot, J., Bormann, N., Delsol, C., Dragani, R., Fuentes, M., Geer, A.J., Haimberger, L., Healy, S.B., Hersbach, H., Hólm, E.V., Isaksen, L., Kållberg, P., Köhler, M., Matricardi, M., McNally, A.P., Monge-Sanz, B.M., Morcrette, J.J., Park, B.K., Peubey, C., de Rosnay, P., Tavolato, C., Thépaut, J.N. and Vitart, F. (2011) 'The ERA-Interim reanalysis: configuration and performance of the data assimilation system', *Quarterly Journal of the Royal Meteorological Society*, 137(656), pp. 553-597.

Delcroix, T. and Hénin, C. (1991) 'Seasonal and interannual variations of sea surface salinity in the tropical Pacific Ocean', *Journal of Geophysical Research: Oceans*, 96(C12), pp. 22135-22150.

Dobricic, S. and Pinardi, N. (2008) 'An oceanographic three-dimensional variational data assimilation scheme', *Ocean Modelling*, 22(3), pp. 89-105.

Düing, W., Hisard, P., Katz, E., Meincke, J., Miller, L., Moroshkin, K.V., Philander, G., Ribnikov, A.A., Voigt, K. and Weisberg, R. (1975) 'Meanders and long waves in the equatorial Atlantic', *Nature*, 257(5524), pp. 280-284.

Eden, C. and Timmermann, A. (2004) 'The influence of the Galápagos Islands on tropical temperatures, currents and the generation of tropical instability waves', *Geophysical Research Letters*, 31(15), p. L15308.

Emanuel, K.A. (1987) 'An Air-Sea Interaction Model of Intraseasonal Oscillations in the Tropics', *Journal of the Atmospheric Sciences*, 44(16), pp. 2324-2340.

Fedorov, A.V. and Brown, J.N. (2009) 'Equatorial Waves', in Steele, J.H. (ed.) *Encyclopedia of Ocean Sciences (Second Edition)*. Oxford: Academic Press, pp. 271-287.

Fiedler, P.C. (2002) 'The annual cycle and biological effects of the Costa Rica Dome', *Deep Sea Research Part I: Oceanographic Research Papers*, 49(2), pp. 321-338.

Fiedler, P.C. and Lavín, M.F. (2006) 'Introduction: A review of eastern tropical Pacific oceanography', *Progress in Oceanography*, 69(2–4), pp. 94-100.

Fiedler, P.C., Mendelssohn, R., Palacios, D.M. and Bograd, S.J. (2012) 'Pycnocline Variations in the Eastern Tropical and North Pacific, 1958–2008', *Journal of Climate*, 26(2), pp. 583-599.

Fiedler, P.C. and Talley, L.D. (2006) 'Hydrography of the eastern tropical Pacific: A review', *Progress in Oceanography*, 69(2–4), pp. 143-180.

Flament, P.J., Kennan, S.C., Knox, R.A., Niiler, P.P. and Bernstein, R.L. (1996) 'The three-dimensional structure of an upper ocean vortex in the tropical Pacific Ocean', *Nature*, 383(6601), pp. 610-613.

Flatau, M., Flatau, P.J., Phoebus, P. and Niiler, P.P. (1997) 'The Feedback between Equatorial Convection and Local Radiative and Evaporative Processes: The Implications for Intraseasonal Oscillations', *Journal of the Atmospheric Sciences*, 54(19), pp. 2373-2386.

Frederiksen, J. and Frederiksen, C. (1997) 'Mechanisms of the formation of intraseasonal oscillations and Australian monsoon disturbances: The roles of convection, barotropic and baroclinic instability', *Contributions to atmospheric physics*, 70, pp. 39-56.

Gaspar, P., Grégoris, Y. and Lefevre, J.-M. (1990) 'A simple eddy kinetic energy model for simulations of the oceanic vertical mixing: Tests at station Papa and long-term upper ocean study site', *Journal of Geophysical Research: Oceans*, 95(C9), pp. 16179-16193.

Geweke, J., Meese, R. and Dent, W. (1983) 'Comparing alternative tests of causality in temporal systems: Analytic results and experimental evidence', *Journal of Econometrics*, 21(2), pp. 161-194.

Graham, T. (2014) 'The importance of eddy permitting model resolution for simulation of the heat budget of tropical instability waves', *Ocean Modelling*, 79, pp. 21-32.

Granger, C.W.J. (1969) 'Investigating Causal Relations by Econometric Models and Cross-spectral Methods', *Econometrica*, 37(3), pp. 424-438.

Griffies, S., Yin, J., Durack, P., Goddard, P., Bates, S., Behrens, E., Bentsen, M., Bi, D., Biastoch, A., Böning, C., Bozec, A., Chassignet, E., Danabasoglu, G., Danilov, S., Domingues, C., Drange, H., Farneti, R., Fernandez, E., Greatbatch, R. and Zhang, X. (2014) 'An assessment of global and regional sea level for years 1993–2007 in a suite of interannual CORE-II simulations', *Ocean Modelling*, 78, pp. 35-89.

Grodsky, S.A., Bentamy, A., Carton, J.A. and Pinker, R.T. (2009) 'Intraseasonal Latent Heat Flux Based on Satellite Observations', *Journal of Climate*, 22(17), pp. 4539-4556.

Haffke, C. and Magnusdottir, G. (2013) 'The South Pacific Convergence Zone in three decades of satellite images', *Journal of Geophysical Research: Atmospheres*, 118(19), pp. 10,839-10,849.

Halkides, D.J. and Lee, T. (2009) 'Mechanisms controlling seasonal-to-interannual mixed layer temperature variability in the southeastern tropical Indian Ocean', *Journal of Geophysical Research: Oceans*, 114(C2).

Halpern, D., Menemenlis, D. and Wang, X. (2015) 'Impact of Data Assimilation on ECCO2 Equatorial Undercurrent and North Equatorial Countercurrent in the Pacific Ocean', *Journal of Atmospheric and Oceanic Technology*, 32(1), pp. 131-143.

Hayashi, M. and Itoh, H. (2017) 'A New Mechanism of the Slow Eastward Propagation of Unstable Disturbances with Convection in the Tropics: Implications for the MJO', *Journal of the Atmospheric Sciences*, 74(11), pp. 3749-3769.

Hayashi, Y. and Golder, D.G. (1986) 'Tropical Intraseasonal Oscilations Appearing in a GFDL General Circulation Model and FGGE Data. Part I: Phase Propagation', *Journal of the Atmospheric Sciences*, 43(24), pp. 3058-3067.

Hendon, H.H. (2000) 'Impact of Air–Sea Coupling on the Madden–Julian Oscillation in a General Circulation Model', *Journal of the Atmospheric Sciences*, 57(24), pp. 3939-3952.

Hendon, H.H., Liebmann, B. and Glick, J.D. (1998) 'Oceanic Kelvin Waves and the Madden–Julian Oscillation', *Journal of the Atmospheric Sciences*, 55(1), pp. 88-101.

Hendon, H.H. and Salby, M.L. (1994) 'The Life Cycle of the Madden–Julian Oscillation', *Journal of the Atmospheric Sciences*, 51(15), pp. 2225-2237.

Hu, Q. and Randall, D.A. (1995) 'Low-Frequency Oscillations In Radiative-Convective Systems. Part II: An Idealized Model', *Journal of the Atmospheric Sciences*, 52(4), pp. 478-490.

Hung, M.-P., Lin, J.-L., Wang, W., Kim, D., Shinoda, T. and Weaver, S.J. (2013) 'MJO and Convectively Coupled Equatorial Waves Simulated by CMIP5 Climate Models', *Journal of Climate*, 26(17), pp. 6185-6214.

Im, S.-H., An, S.-I., Lengaigne, M. and Noh, Y. (2012) 'Seasonality of Tropical Instability Waves and Its Feedback to the Seasonal Cycle in the Tropical Eastern Pacific', *The Scientific World Journal*, 2012, p. 612048.

Inness, P.M. and Slingo, J.M. (2003) 'Simulation of the Madden–Julian Oscillation in a Coupled General Circulation Model. Part I: Comparison with Observations and an Atmosphere-Only GCM', *Journal of Climate*, 16(3), pp. 345-364.

Inoue, R., Lien, R.-C., Moum, J.N., Perez, R.C. and Gregg, M.C. (2019) 'Variations of Equatorial Shear, Stratification, and Turbulence Within a Tropical Instability Wave Cycle', *Journal of Geophysical Research: Oceans*, 124(3), pp. 1858-1875.

Jiang, X., Adames, Á.F., Kim, D., Maloney, E.D., Lin, H., Kim, H., Zhang, C., DeMott, C.A. and Klingaman, N.P. (2020) 'Fifty Years of Research on the Madden-Julian Oscillation: Recent Progress, Challenges, and Perspectives', *Journal of Geophysical Research: Atmospheres*, 125(17), p. e2019JD030911.

Jochum, M., Cronin, M.F., Kessler, W.S. and Shea, D. (2007) 'Observed horizontal temperature advection by tropical instability waves', *Geophysical Research Letters*, 34(9).

Johnson, E.S. and McPhaden, M.J. (1993) 'Effects of a three-dimensional mean flow on intraseasonal Kelvin waves in the equatorial Pacific Ocean', *Journal of Geophysical Research: Oceans*, 98(C6), pp. 10185-10194.

Johnson, G.C., McPhaden, M.J. and Firing, E. (2001) 'Equatorial Pacific Ocean Horizontal Velocity, Divergence, and Upwelling*', *Journal of Physical Oceanography*, 31(3), pp. 839-849.

Jones, C., Waliser, D.E. and Gautier, C. (1998) 'The Influence of the Madden–Julian Oscillation on Ocean Surface Heat Fluxes and Sea Surface Temperature', *Journal of Climate*, 11(5), pp. 1057-1072.

Kessler, W.S. (1990) 'Observations of long Rossby waves in the northern tropical Pacific', *Journal of Geophysical Research: Oceans*, 95(C4), pp. 5183-5217.

Kessler, W.S. (2006) 'The circulation of the eastern tropical Pacific: A review', *Progress in Oceanography*, 69(2–4), pp. 181-217.

Kessler, W.S., McPhaden, M.J. and Weickmann, K.M. (1995) 'Forcing of intraseasonal Kelvin waves in the equatorial Pacific', *Journal of Geophysical Research: Oceans*, 100(C6), pp. 10613-10631.

Kim, H.-M., Hoyos, C.D., Webster, P.J. and Kang, I.-S. (2008) 'Sensitivity of MJO Simulation and Predictability to Sea Surface Temperature Variability', *Journal of Climate*, 21(20), pp. 5304-5317.

Kim, H.-M., Hoyos, C.D., Webster, P.J. and Kang, I.-S. (2010) 'Ocean–atmosphere coupling and the boreal winter MJO', *Climate Dynamics*, 35(5), pp. 771-784.

Klingaman, N.P. and Woolnough, S.J. (2014) 'Using a case-study approach to improve the Madden–Julian oscillation in the Hadley Centre model', *Quarterly Journal of the Royal Meteorological Society*, 140(685), pp. 2491-2505.

Lafleur, D.M., Barrett, B.S. and Henderson, G.R. (2015) 'Some Climatological Aspects of the Madden–Julian Oscillation (MJO)', *Journal of Climate*, 28(15), pp. 6039-6053.

Large, W.G. and Yeager, S.G. (2004) 'Diurnal to decadal global forcing for ocean and sea-ice models: the data sets and flux climatologies'.

Large, W.G. and Yeager, S.G. (2008) 'The global climatology of an interannually varying air–sea flux data set', *Climate Dynamics*, 33(2), pp. 341-364.

Lau, N.-C. and Lau, K.-M. (1986) 'The Structure and Propagation of Intraseasonal Oscillations Appearing in a GFDL General Circulation Model', *Journal of the Atmospheric Sciences*, 43(19), pp. 2023-2047.

Lau, W.K.M., Waliser, D.E. and Wang, B. (2012) 'Theories', in Lau, W.K.M. and Waliser, D.E. (eds.) *Intraseasonal Variability in the Atmosphere-Ocean Climate System*. Berlin, Heidelberg: Springer Berlin Heidelberg, pp. 335-398.

Lee, T., Lagerloef, G., Gierach, M.M., Kao, H.-Y., Yueh, S. and Dohan, K. (2012) 'Aquarius reveals salinity structure of tropical instability waves', *Geophysical Research Letters*, 39(12).

Lee, T., Lagerloef, G., Kao, H.-Y., McPhaden, M.J., Willis, J. and Gierach, M.M. (2014) 'The influence of salinity on tropical Atlantic instability waves', *Journal of Geophysical Research: Oceans*, 119(12), pp. 8375-8394.

Legeckis, R. (1977) 'Long Waves in the Eastern Equatorial Pacific Ocean: A View from a Geostationary Satellite', *Science*, 197(4309), pp. 1179-1181.

Legeckis, R. (1986) 'A satellite time series of sea surface temperatures in the eastern equatorial Pacific Ocean, 1982–1986', *Journal of Geophysical Research: Oceans*, 91(C11), pp. 12879-12886.

Li, Y. and Han, W. (2016) 'Causes for intraseasonal sea surface salinity variability in the western tropical Pacific Ocean and its seasonality', *Journal of Geophysical Research: Oceans*, 121(1), pp. 85-103.

Li, Y., Han, W. and Lee, T. (2015) 'Intraseasonal sea surface salinity variability in the equatorial Indo-Pacific Ocean induced by Madden-Julian oscillations', *Journal of Geophysical Research: Oceans*, 120(3), pp. 2233-2258.

Liess, S. and Bengtsson, L. (2004) 'The intraseasonal oscillation in ECHAM4 Part II: sensitivity studies', *Climate Dynamics*, 22(6), pp. 671-688.

Lin, J.-L. (2007) 'The Double-ITCZ Problem in IPCC AR4 Coupled GCMs: Ocean–Atmosphere Feedback Analysis', *Journal of Climate*, 20(18), pp. 4497-4525.

Lindzen, R.S. (1974) 'Wave-CISK in the Tropics', *Journal of the Atmospheric Sciences*, 31(1), pp. 156-179.

Liu, C., Fang, L., Köhl, A., Liu, Z., Smyth, W.D. and Wang, F. (2019) 'The Subsurface Mode Tropical Instability Waves in the Equatorial Pacific Ocean and Their Impacts on Shear and Mixing', *Geophysical Research Letters*, 46(21), pp. 12270-12278.

Liu, C., Köhl, A., Liu, Z., Wang, F. and Stammer, D. (2016) 'Deep-reaching thermocline mixing in the equatorial pacific cold tongue', *Nature Communications*, 7(1), p. 11576.

Locarnini, R.A., Mishonov, A.V., Antonov, J.I., Boyer, T.P., Garcia, H.E., Baranova, O.K., Zweng, M.M., Paver, C.R., Reagan, J.R. and Johnson, D.R. (2013) 'World ocean atlas 2013, Volume 1: Temperature', *S. Levitus, Ed.; A. Mishonov, Technical Ed NOAA Atlas NESDIS*, 73, p. 40.

Lucas, L.E., Waliser, D.E. and Murtugudde, R. (2010) 'Mechanisms governing sea surface temperature anomalies in the eastern tropical Pacific Ocean associated with the boreal winter Madden-Julian Oscillation', *Journal of Geophysical Research: Oceans*, 115(C5).

Luther, D.S. and Johnson, E.S. (1990) 'Eddy Energetics in the Upper Equatorial Pacific during the Hawaii-to-Tahiti Shuttle Experiment', *Journal of Physical Oceanography*, 20(7), pp. 913-944.

Madden, R.A. and Julian, P.R. (1971) 'Detection of a 40–50 Day Oscillation in the Zonal Wind in the Tropical Pacific', *Journal of the Atmospheric Sciences*, 28(5), pp. 702-708.

Madden, R.A. and Julian, P.R. (1972) 'Description of Global-Scale Circulation Cells in the Tropics with a 40–50 Day Period', *Journal of the Atmospheric Sciences*, 29(6), pp. 1109-1123.

Madec, G., Delecluse, P., Imbard, M. and Levy, C. (1997) 'Ocean general circulation model reference manual', *LODYC, Paris*, 91.

Madec, G. and NEMO-team (2016) 'NEMO ocean engine, version 3.6 stable', *Note du Pôle de modélisation, Institut Pierre-Simon Laplace*, No. 27.

Majda, A.J. and Stechmann, S.N. (2009) 'A Simple Dynamical Model with Features of Convective Momentum Transport', *Journal of the Atmospheric Sciences*, 66(2), pp. 373-392.

Maloney, E.D., Chelton, D.B. and Esbensen, S.K. (2008) 'Subseasonal SST Variability in the Tropical Eastern North Pacific during Boreal Summer', *Journal of Climate*, 21(17), pp. 4149-4167.

Maloney, E.D. and Hartmann, D.L. (2000) 'Modulation of Eastern North Pacific Hurricanes by the Madden–Julian Oscillation', *Journal of Climate*, 13(9), pp. 1451-1460.

Maloney, E.D. and Kiehl, J.T. (2002) 'MJO-Related SST Variations over the Tropical Eastern Pacific during Northern Hemisphere Summer', *Journal of Climate*, 15(6), pp. 675-689.

Marchesiello, P., Capet, X., Menkes, C. and Kennan, S.C. (2011) 'Submesoscale dynamics in tropical instability waves', *Ocean Modelling*, 39(1), pp. 31-46.

Masina, S. and Philander, S.G.H. (1999) 'An analysis of tropical instability waves in a numerical model of the Pacific Ocean: 1. Spatial variability of the waves', *Journal of Geophysical Research: Oceans*, 104(C12), pp. 29613-29635.

Masina, S., Philander, S.G.H. and Bush, A.B.G. (1999) 'An analysis of tropical instability waves in a numerical model of the Pacific Ocean: 2. Generation and energetics of the waves', *Journal of Geophysical Research: Oceans*, 104(C12), pp. 29637-29661.

Matsuno, T. (1966) 'Quasi-Geostrophic Motions in the Equatorial Area', *Journal of the Meteorological Society of Japan. Ser. II*, 44(1), pp. 25-43.

Matthews, A.J. (2008) 'Primary and successive events in the Madden–Julian Oscillation', *Quarterly Journal of the Royal Meteorological Society*, 134(631), pp. 439-453.

Matthews, A.J., Singhruck, P. and Heywood, K.J. (2010) 'Ocean temperature and salinity components of the Madden–Julian oscillation observed by Argo floats', *Climate Dynamics*, 35(7), pp. 1149-1168.

McGraw, M.C. and Barnes, E.A. (2018) 'Memory Matters: A Case for Granger Causality in Climate Variability Studies', *Journal of Climate*, 31(8), pp. 3289-3300.

McPhaden, M.J. (2002) 'Mixed Layer Temperature Balance on Intraseasonal Timescales in the Equatorial Pacific Ocean*', *Journal of Climate*, 15(18), pp. 2632-2647.

Mestas-Nuñez, A.M. and Miller, A.J. (2006) 'Interdecadal variability and climate change in the eastern tropical Pacific: A review', *Progress in Oceanography*, 69(2), pp. 267-284.

Miyakawa, T., Yashiro, H., Suzuki, T., Tatebe, H. and Satoh, M. (2017) 'A Madden-Julian Oscillation event remotely accelerates ocean upwelling to abruptly terminate the 1997/1998 super El Niño', *Geophysical Research Letters*, 44(18), pp. 9489-9495.

Mogensen, K., Balmaseda, M.A. and Weaver, A. (2012) 'The NEMOVAR ocean data assimilation system as implemented in the ECMWF ocean analysis for System 4'. ECMWF. Available at: https://www.ecmwf.int/node/11174.

Mosquera-Vásquez, K., Dewitte, B. and Illig, S. (2014) 'The Central Pacific El Niño intraseasonal Kelvin wave', *Journal of Geophysical Research: Oceans*, 119(10), pp. 6605-6621.

Mosquera-Vásquez, K., Dewitte, B., Illig, S., Takahashi, K. and Garric, G. (2013) 'The 2002/2003 El Niño: Equatorial waves sequence and their impact on sea surface temperature', *Journal of Geophysical Research: Oceans*, 118(1), pp. 346-357.

Moum, J.N., Pujiana, K., Lien, R.-C. and Smyth, W.D. (2016) 'Ocean feedback to pulses of the Madden–Julian Oscillation in the equatorial Indian Ocean', *Nature Communications*, 7(1), p. 13203.

Nakazawa, T. (1988) 'Tropical Super Clusters within Intraseasonal Variations over the Western Pacific', *Journal of the Meteorological Society of Japan. Ser. II*, 66(6), pp. 823-839.

Neelin, J.D., Held, I.M. and Cook, K.H. (1987) 'Evaporation-Wind Feedback and Low-Frequency Variability in the Tropical Atmosphere', *Journal of the Atmospheric Sciences*, 44(16), pp. 2341-2348.

North, G.R., Bell, T.L., Cahalan, R.F. and Moeng, F.J. (1982) 'Sampling Errors in the Estimation of Empirical Orthogonal Functions', *Monthly Weather Review*, 110(7), pp. 699-706.

Pariyar, S.K., Keenlyside, N., Bhatt, B.C. and Omrani, N.-E. (2019) 'The Dominant Patterns of Intraseasonal Rainfall Variability in May–October and November–April over the Tropical Western Pacific', *Monthly Weather Review*, 147(8), pp. 2941-2960.

Pedlosky, J. (1996) *Ocean circulation theory*. 1 edn. Springer-Verlag Berlin Heidelberg.

Philander, S.G.H. (1990) *El Niño, La Niña, and the Southern Oscillation*.

Qiao, L. and Weisberg, R.H. (1995) 'Tropical instability wave kinematics: Observations from the Tropical Instability Wave Experiment', *Journal of Geophysical Research: Oceans*, 100(C5), pp. 8677-8693.

Qiao, L. and Weisberg, R.H. (1998) 'Tropical Instability Wave Energetics: Observations from the Tropical Instability Wave Experiment', *Journal of Physical Oceanography*, 28(2), pp. 345-360.

Raymond, D.J., Bretherton, C.S. and Molinari, J. (2006) 'Dynamics of the Intertropical Convergence Zone of the East Pacific', *Journal of the Atmospheric Sciences*, 63(2), pp. 582-597.

Redi, M.H. (1982) 'Oceanic Isopycnal Mixing by Coordinate Rotation', *Journal of Physical Oceanography*, 12(10), pp. 1154-1158.

Rydbeck, A.V., Jensen, T.G. and Flatau, M. (2019) 'Characterization of Intraseasonal Kelvin Waves in the Equatorial Pacific Ocean', *Journal of Geophysical Research: Oceans*, 124(3), pp. 2028-2053.

Rydbeck, A.V., Maloney, E.D., Xie, S.-P., Hafner, J. and Shaman, J. (2013) 'Remote Forcing versus Local Feedback of East Pacific Intraseasonal Variability during Boreal Summer', *Journal of Climate*, 26(11), pp. 3575-3596.

Salby, M.L. and Garcia, R.R. (1987) 'Transient Response to Localized Episodic Heating in the Tropics. Part I: Excitation and Short-Time Near-Field Behavior', *Journal of the Atmospheric Sciences*, 44(2), pp. 458-498.

Schwarz, G. (1978) 'Estimating the Dimension of a Model', *Ann. Statist.*, 6(2), pp. 461-464.

Seo, H., Miller, A.J. and Norris, J.R. (2016) 'Eddy–Wind Interaction in the California Current System: Dynamics and Impacts', *Journal of Physical Oceanography*, 46(2), pp. 439-459.

Shchepetkin, A.F. and McWilliams, J.C. (2005) 'The regional oceanic modeling system (ROMS): a split-explicit, free-surface, topography-following-coordinate oceanic model', *Ocean Modelling*, 9(4), pp. 347-404.

Shinoda, T. and Hendon, H.H. (1998) 'Mixed Layer Modeling of Intraseasonal Variability in the Tropical Western Pacific and Indian Oceans', *Journal of Climate*, 11(10), pp. 2668-2685.

Shinoda, T., Kiladis, G.N. and Roundy, P.E. (2009) 'Statistical representation of equatorial waves and tropical instability waves in the Pacific Ocean', *Atmospheric Research*, 94(1), pp. 37-44.

Shoup, C.G., Roman-Stork, H.L. and Subrahmanyam, B. (2020) 'Analysis of Coupled Oceanic and Atmospheric Preconditioning for Primary Madden-Julian Oscillation Events Across ENSO Phases', *Journal of Geophysical Research: Oceans*, 125(9), p. e2020JC016358.

Slingo, J.M., Sperber, K.R., Boyle, J.S., Ceron, J.P., Dix, M., Dugas, B., Ebisuzaki, W., Fyfe, J., Gregory, D., Gueremy, J.F., Hack, J., Harzallah, A., Inness, P., Kitoh, A., Lau, W.K.M., McAvaney, B., Madden, R., Matthews, A., Palmer, T.N., Parkas, C.K., Randall, D. and Renno, N. (1996) 'Intraseasonal oscillations in 15 atmospheric general circulation models: results from an AMIP diagnostic subproject', *Climate Dynamics*, 12(5), pp. 325-357.

Small, R.J., Xie, S.-P., Maloney, E.D., de Szoeke, S.P. and Miyama, T. (2011) 'Intraseasonal variability in the far-east pacific: investigation of the role of air–sea coupling in a regional coupled model', *Climate Dynamics*, 36(5), pp. 867-890.

Smith, R.D., Dukowicz, J.K. and Malone, R.C. (1992) 'Parallel ocean general circulation modeling', *Phys. D*, 60(1-4), pp. 38-61.

Stewart, R. (2008) *Introduction To Physical Oceanography*.

Stocker, T. (2011) *Introduction to Climate Modelling*.

Storto, A. and Masina, S. (2016) 'C-GLORSv5: an improved multi-purpose global ocean eddy-permitting physical reanalysis', *Earth System Science Data Discussions*, pp. 1-29.

Swinbank, R., Palmer, T.N. and Davey, M.K. (1988) 'Numerical Simulations of the Madden and Julian Oscillation', *Journal of the Atmospheric Sciences*, 45(5), pp. 774-788.

Thandlam, V. and Rahaman, H. (2019) 'Evaluation of surface shortwave and longwave downwelling radiations over the global tropical oceans', *SN Applied Sciences*, 1(10), p. 1171.

Tian, B. and Ramanathan, V. (2002) 'Role of Tropical Clouds in Surface and Atmospheric Energy Budget', *Journal of Climate*, 15(3), pp. 296-305.

Toda, H.Y. and Yamamoto, T. (1995) 'Statistical inference in vector autoregressions with possibly integrated processes', *Journal of Econometrics*, 66(1), pp. 225-250.

Tomczak, M. and Godfrey, J.S. (1994) 'CHAPTER 8 - The Pacific Ocean', in Tomczak, M. and Godfrey, J.S. (eds.) *Regional Oceanography*. Amsterdam: Pergamon, pp. 113-147.

Torrence, C. and Compo, G.P. (1998) 'A practical guide to wavelet analysis', *Bulletin of the American Meteorological society*, 79(1), pp. 61-78.

Uppala, S.M., KÅllberg, P.W., Simmons, A.J., Andrae, U., Bechtold, V.D.C., Fiorino, M., Gibson, J.K., Haseler, J., Hernandez, A., Kelly, G.A., Li, X., Onogi, K., Saarinen, S., Sokka, N., Allan, R.P., Andersson, E., Arpe, K., Balmaseda, M.A., Beljaars, A.C.M., Berg, L.V.D., Bidlot, J., Bormann, N., Caires, S., Chevallier, F., Dethof, A., Dragosavac, M., Fisher, M., Fuentes, M., Hagemann, S., Hólm, E., Hoskins, B.J., Isaksen, L., Janssen, P.A.E.M., Jenne, R., Mcnally, A.P., Mahfouf, J.-F., Morcrette, J.-J., Rayner, N.A., Saunders, R.W., Simon, P., Sterl, A., Trenberth, K.E., Untch, A., Vasiljevic, D., Viterbo, P. and Woollen, J. (2005) 'The ERA-40 re-analysis', *Quarterly Journal of the Royal Meteorological Society*, 131(612), pp. 2961-3012.

Vannière, B., Guilyardi, E., Madec, G., Doblas-Reyes, F.J. and Woolnough, S. (2013) 'Using seasonal hindcasts to understand the origin of the equatorial cold tongue bias in CGCMs and its impact on ENSO', *Climate Dynamics*, 40(3), pp. 963-981.

von Storch, H. and Frankignoul, C. (1998) 'Empirical modal decomposition in coastal oceanography', *The global coastal ocean: processes and methods*, 10, p. 419.

von Storch, H. and Zwiers, F.W. (2001) *Statistical analysis in climate research*. Cambridge university press.

Waliser, D.E., Murtugudde, R. and Lucas, L.E. (2003) 'Indo-Pacific Ocean response to atmospheric intraseasonal variability: 1. Austral summer and the Madden-Julian Oscillation', *Journal of Geophysical Research: Oceans*, 108(C5).

Wang, B., Liu, F. and Chen, G. (2016a) 'A trio-interaction theory for Madden–Julian oscillation', *Geoscience Letters*, 3(1), p. 34.

Wang, C. and Enfield, D.B. (2001) 'The Tropical Western Hemisphere Warm Pool', *Geophysical Research Letters*, 28(8), pp. 1635-1638.

Wang, C. and Fiedler, P.C. (2006) 'ENSO variability and the eastern tropical Pacific: A review', *Progress in Oceanography*, 69(2–4), pp. 239-266.

Wang, F., Li, Y. and Wang, J. (2016b) 'Intraseasonal Variability of the Surface Zonal Currents in the Western Tropical Pacific Ocean: Characteristics and Mechanisms', *Journal of Physical Oceanography*, 46(12), pp. 3639-3660.

Wang, M., Du, Y., Qiu, B., Cheng, X., Luo, Y., Chen, X. and Feng, M. (2017) 'Mechanism of seasonal eddy kinetic energy variability in the eastern equatorial Pacific Ocean', *Journal of Geophysical Research: Oceans*, 122(4), pp. 3240-3252.

Wang, M., Du, Y., Qiu, B., Xie, S.-P. and Feng, M. (2019) 'Dynamics on Seasonal Variability of EKE Associated with TIWs in the Eastern Equatorial Pacific Ocean', *Journal of Physical Oceanography*, 49(6), pp. 1503-1519.

Weisberg, R.H. and Qiao, L. (2000) 'Equatorial Upwelling in the Central Pacific Estimated from Moored Velocity Profilers', *Journal of Physical Oceanography*, 30(1), pp. 105-124.

Wheeler, M.C. and Hendon, H.H. (2004) 'An All-Season Real-Time Multivariate MJO Index: Development of an Index for Monitoring and Prediction', *Monthly Weather Review*, 132(8), pp. 1917-1932.

Whitaker, J.S., Compo, G.P., Wei, X. and Hamill, T.M. (2004) 'Reanalysis without Radiosondes Using Ensemble Data Assimilation', *Monthly Weather Review*, 132(5), pp. 1190-1200.

Willett, C.S., Leben, R.R. and Lavín, M.F. (2006) 'Eddies and Tropical Instability Waves in the eastern tropical Pacific: A review', *Progress in Oceanography*, 69(2–4), pp. 218-238.

Woodworth, P.L. and Player, R. (2003) 'The permanent service for mean sea level: an update to the 21stCentury', *Journal of Coastal Research*, pp. 287-295.

Woolnough, S.J., Vitart, F. and Balmaseda, M.A. (2007) 'The role of the ocean in the Madden–Julian Oscillation: Implications for MJO prediction', *Quarterly Journal of the Royal Meteorological Society*, 133(622), pp. 117-128.

Xie, S.-P., Xu, H., Kessler, W.S. and Nonaka, M. (2005) 'Air–Sea Interaction over the Eastern Pacific Warm Pool: Gap Winds, Thermocline Dome, and Atmospheric Convection', *Journal of Climate*, 18(1), pp. 5-20.

Yang, D. and Ingersoll, A.P. (2013) 'Triggered Convection, Gravity Waves, and the MJO: A Shallow-Water Model', *Journal of the Atmospheric Sciences*, 70(8), pp. 2476-2486.

Yano, J.-I. and Tribbia, J.J. (2017) 'Tropical Atmospheric Madden–Julian Oscillation: A Strongly Nonlinear Free Solitary Rossby Wave?', *Journal of the Atmospheric Sciences*, 74(10), pp. 3473-3489.

Yoo, C. and Cho, E. (2018) 'Comparison of GCM Precipitation Predictions with Their RMSEs and Pattern Correlation Coefficients', *Water*, 10(1), p. 28.

Yu, Z., McCreary, J.P., Jr. and Proehl, J.A. (1995) 'Meridional Asymmetry and Energetics of Tropical Instability Waves', *Journal of Physical Oceanography*, 25(12), pp. 2997-3007.

Zalesak, S.T. (1979) 'Fully multidimensional flux-corrected transport algorithms for fluids', *Journal of Computational Physics*, 31(3), pp. 335-362.

Zhang, C. (2001) 'Intraseasonal Perturbations in Sea Surface Temperatures of the Equatorial Eastern Pacific and Their Association with the Madden–Julian Oscillation', *Journal of Climate*, 14(6), pp. 1309-1322.

Zhang, C. (2005) 'Madden-Julian Oscillation', *Reviews of Geophysics*, 43(2).

Zhang, C., Dong, M., Gualdi, S., Hendon, H.H., Maloney, E.D., Marshall, A., Sperber, K.R. and Wang, W. (2006) 'Simulations of the Madden–Julian oscillation in four pairs of coupled and uncoupled global models', *Climate Dynamics*, 27(6), pp. 573-592.

Zhang, X., Lu, Y. and Thompson, K.R. (2009) 'Sea Level Variations in the Tropical Pacific Ocean and the Madden–Julian Oscillation', *Journal of Physical Oceanography*, 39(8), pp. 1984-1992.

Zhang, X., Lu, Y., Thompson, K.R., Jiang, J. and Ritchie, H. (2010) 'Tropical Pacific Ocean and the Madden-Julian Oscillation: Role of wind and buoyancy forcing', *Journal of Geophysical Research: Oceans*, 115(C5).

Zhou, H., Liu, X. and Xu, P. (2019) 'Sensitivity of Sverdrup transport to surface wind products over the tropical North Pacific Ocean', *Ocean Dynamics*, 69(5), pp. 529-542.

Zweng, M.M., Reagan, J.R., Antonov, J.I., Locarnini, R.A., Mishonov, A.V., Boyer, T.P., Garcia, H.E., Baranova, O.K., Johnson, D.R. and Seidov, D. (2013) 'World Ocean Atlas 2013, Volume 2: Salinity', *S. Levitus, Ed.; A. Mishonov, Technical Ed NOAA Atlas NESDIS*, 74, p. 39.

Appendices

Appendix A

The advection-diffusion equation for a tracer, T, is in Cartesian coordinates:

$$\partial_t T = -\boldsymbol{\nabla} \cdot (\boldsymbol{u}T) + \boldsymbol{\nabla} \cdot (\kappa \boldsymbol{\nabla} T), \qquad (A.1)$$

where $\boldsymbol{\nabla}$ is the divergence operator, subscripts denote the partial derivative with respect to the corresponding variable, κ is a diffusion coefficient and $\boldsymbol{u}$ is the velocity 3D field (Stocker, 2011). Equation (A.1) can be expanded as:

$$\partial_t T = -u\partial_x T - v\partial_y T - w\partial_z T + \partial_x(\kappa \partial_x T) + \partial_y\big(\kappa \partial_y T\big) + \partial_z(\kappa \partial_z T), \qquad (A.2)$$

Now, let us assume that the solution of this equation, $T(x, y, z, t)$, has a constant long-term average, $\bar{T}$, namely,

$$\partial_t \bar{T} = \frac{1}{t_f - t_0} \int_{t_0}^{t_f} T(x, y, z, t)\ \mathrm{d}t, \qquad (A.3)$$

where $\big(t_0, t_f\big)$ is a suitable time interval for averaging, and

$$\partial_t \bar{T} = 0. \qquad (A.4)$$

The advection-diffusion equation that results from taking the time average of (A.2) is, therefore:

$$0 = -\overline{\mathrm{u}\,\partial_\mathrm{x}\mathrm{T}} - \overline{\mathrm{v}\,\partial_\mathrm{y}\mathrm{T}} - \overline{\mathrm{w}\,\partial_\mathrm{z}\mathrm{T}} + \overline{\partial_\mathrm{x}(\kappa\,\partial_\mathrm{x}\mathrm{T})} + \overline{\partial_\mathrm{y}\big(\kappa\,\partial_\mathrm{y}\mathrm{T}\big)} + \overline{\partial_\mathrm{z}(\kappa\,\partial_\mathrm{z}\mathrm{T})}. \qquad (A.5)$$

And then, the corresponding equation for the anomalies $\mathrm{T}' = T - \bar{T}$ is

$$\begin{aligned}\partial_\mathrm{t}\mathrm{T}' = {} & \big[\mathrm{u}\,\partial_\mathrm{x}\mathrm{T} - \overline{\mathrm{u}\,\partial_\mathrm{x}\mathrm{T}}\big] + \big[\mathrm{v}\,\partial_\mathrm{y}\mathrm{T} - \overline{\mathrm{v}\,\partial_\mathrm{y}\mathrm{T}}\big] + \big[\mathrm{w}\,\partial_\mathrm{z}\mathrm{T} - \overline{\mathrm{w}\,\partial_\mathrm{z}\mathrm{T}}\big] + \big[\partial_\mathrm{x}(\kappa\,\partial_\mathrm{x}\mathrm{T}) - \overline{\partial_\mathrm{x}(\kappa\,\partial_\mathrm{x}\mathrm{T})}\big] + \\ & \Big[\partial_\mathrm{y}\big(\kappa\,\partial_\mathrm{y}\mathrm{T}\big) - \overline{\partial_\mathrm{y}\big(\kappa\,\partial_\mathrm{y}\mathrm{T}\big)}\Big] + \Big[\partial_\mathrm{y}\big(\kappa\,\partial_\mathrm{y}\mathrm{T}\big) - \overline{\partial_\mathrm{y}\big(\kappa\,\partial_\mathrm{y}\mathrm{T}\big)}\Big] + \big[\partial_\mathrm{z}(\kappa\,\partial_\mathrm{z}\mathrm{T}) - \overline{\partial_\mathrm{z}(\kappa\,\partial_\mathrm{z}\mathrm{T})}\big]. \qquad (A.6)\end{aligned}$$

For convenience, let us condense (A.6) into

$$\partial_\mathrm{t}\mathrm{T}' = A_1' + A_2' + A_3' + D_1' + D_2' + D_3'. \qquad (A.7)$$

In (A.7), A_1' stands for $\big[\mathrm{u}\,\partial_\mathrm{x}\mathrm{T} - \overline{\mathrm{u}\,\partial_\mathrm{x}\mathrm{T}}\big]$, and similarly for the other terms on the right-hand side of the equation. The variance of the anomaly tendency is then

$$\overline{\partial_t T' \, \partial_t T'} = \overline{(A_1' + A_2' + A_3' + D_1' + D_2' + D_3')(A_1' + A_2' + A_3' + D_1' + D_2' + D_3')}, \quad (A.8)$$

which contains not only terms such as $\overline{A_1' A_1'}$ but also cross-terms, such as, for example, $\overline{A_1' D_1'}$. In the discussion of intraseasonal temperature variability (section 4.3.1), only those terms with a significant contribution are presented.

Appendix B

Table B.1. Lag order selection by Schwarz information criterion for sea surface height at different locations in the equatorial Pacific.

Lag / Point	2°S, 204°W	5°S, 175°W	0°, 156°W	3°N, 150°W	5°N, 127°W	9°N, 96°W
0	-0.87	-0.79	-0.97	-0.81	-0.77	-0.80
1	-12.03	-12.35	-12.58	-11.92	-12.16	-12.31
2	-17.66	-18.22	-17.98	-17.64	-18.72	-17.87
3	-20.64	-20.98	-20.75	-20.49	-21.39	-20.52
4	-22.02	-22.38	-22.53	-21.87	-22.91	-21.7
5	-22.97	-23.26	-23.46	-22.86	-23.84	-22.54
6	-23.55	-23.87	-24.06	-23.58	-24.49	-23.16
7	-23.87	-24.31	-24.5	-23.96	-24.94	-23.56
8	-24.18	-24.65	-24.74	-24.3	-25.22	-23.82
9	-24.45	-24.87	-24.94	-24.5	-25.48	-24.07
10	-24.6	-25.05	-25.18	-24.66	-25.66	-24.26
11	-24.73	-25.21	-25.27	-24.8	-25.77	-24.39
12	-24.84	-25.29	-25.38	-24.89	-25.85	-24.48
13	-24.9	-25.4	-25.51	-24.98	-25.95	-24.57
14	-24.97	-25.43	-25.57	-25.04	-26	-24.62
15	-25.03	-25.48	-25.64	-25.13	-26.06	-24.67
16	-25.08	-25.54	-25.7	-25.17	-26.1	-24.72
17	-25.11	-25.57	-25.73	-25.2	-26.13	-24.76
18	-25.14	-25.58	-25.76	-25.22	-26.18	-24.8
19	-25.16	-25.6	-25.8	-25.25	-26.21	-24.82
20	-25.18	-25.64	-25.82	-25.27	-26.23	-24.84
21	-25.19	-25.66	-25.83	-25.29	-26.24	-24.86
22	-25.21	-25.69	-25.85	-25.31	-26.26	-24.88
23	-25.22	-25.7	-25.87	-25.31	-26.27	-24.89
24	-25.23	-25.69	-25.87	-25.32	-26.28	-24.89
25	-25.24	-25.7	-25.88	-25.33	-26.29	-24.89
26	-25.24	-25.72	-25.9	-25.34	-26.3	-24.91
27	-25.25	-25.73*	-25.91	-25.35	-26.32	-24.92
28	-25.26*	-25.73	-25.91	-25.36	-26.33*	-24.92*
29	-25.25	-25.72	-25.92*	-25.36*	-26.33	-24.91
30	-25.25	-25.72	-25.92	-25.36	-26.33	-24.91
31	-25.25	-25.72	-25.92	-25.35	-26.33	-24.91
32	-25.24	-25.72	-25.92	-25.36	-26.32	-24.9
33	-25.24	-25.71	-25.92	-25.36	-26.32	-24.9
34	-25.23	-25.71	-25.91	-25.35	-26.32	-24.9
35	-25.23	-25.71	-25.91	-25.35	-26.32	-24.89
36	-25.22	-25.7	-25.9	-25.35	-26.32	-24.89
37	-25.22	-25.69	-25.89	-25.34	-26.31	-24.88
38	-25.21	-25.69	-25.89	-25.33	-26.3	-24.88
39	-25.2	-25.68	-25.88	-25.32	-26.29	-24.87
40	-25.2	-25.68	-25.87	-25.32	-26.29	-24.86

*indicates lag order selected

Table B.2. Lag order selection by Schwarz information criterion for temperature at thermocline at different locations in the equatorial Pacific.

Lag / Point	2˚S, 204˚W	5˚S, 175˚W	0˚, 156˚W	3˚N, 150˚W	5˚N, 127˚W	9˚N, 96˚W
0	-0.91	-0.79	-0.90	-0.81	-0.79	-0.77
1	-11.03	-11.86	-11.49	-11.41	-11.47	-11.12
2	-15.08	-16.3	-15.56	-15.5	-15.57	-15.15
3	-17.35	-18.58	-17.81	-17.81	-17.86	-17.39
4	-18.38	-19.61	-18.83	-18.85	-18.93	-18.44
5	-19.05	-20.28	-19.51	-19.52	-19.64	-19.13
6	-19.43	-20.68	-19.9	-19.91	-20.04	-19.51
7	-19.66	-20.91	-20.14	-20.14	-20.28	-19.74
8	-19.83	-21.08	-20.31	-20.3	-20.44	-19.9
9	-19.96	-21.21	-20.44	-20.44	-20.58	-20.04
10	-20.07	-21.32	-20.54	-20.55	-20.68	-20.15
11	-20.13	-21.39	-20.61	-20.62	-20.75	-20.22
12	-20.18	-21.45	-20.67	-20.67	-20.8	-20.26
13	-20.24	-21.5	-20.73	-20.73	-20.85	-20.32
14	-20.27	-21.53	-20.75	-20.75	-20.88	-20.35
15	-20.3	-21.57	-20.78	-20.78	-20.91	-20.38
16	-20.32	-21.58	-20.8	-20.8	-20.93	-20.4
17	-20.34	-21.6	-20.83	-20.83	-20.95	-20.42
18	-20.36	-21.62	-20.84	-20.84	-20.96	-20.43
19	-20.36	-21.63	-20.85	-20.85	-20.97	-20.44
20	-20.37	-21.64	-20.85	-20.85	-20.98	-20.45
21	-20.37	-21.65	-20.86	-20.86	-20.98	-20.46
22	-20.38	-21.65	-20.87	-20.86	-20.99	-20.46
23	-20.38	-21.65	-20.87	-20.88	-20.99	-20.47
24	-20.38	-21.65	-20.87	-20.87	-20.99	-20.46
25	-20.38	-21.66	-20.87	-20.87	-21	-20.47
26	-20.38	-21.65	-20.87	-20.87	-20.99	-20.46
27	-20.38*	-21.66*	-20.87*	-20.88*	-21.00*	-20.47*
28	-20.38	-21.65	-20.87	-20.88	-21	-20.47
29	-20.37	-21.65	-20.86	-20.87	-20.99	-20.46
30	-20.37	-21.64	-20.85	-20.86	-20.98	-20.45
31	-20.37	-21.64	-20.85	-20.86	-20.98	-20.45
32	-20.35	-21.63	-20.84	-20.85	-20.96	-20.44
33	-20.35	-21.62	-20.84	-20.85	-20.96	-20.44
34	-20.34	-21.61	-20.82	-20.84	-20.95	-20.42
35	-20.34	-21.61	-20.82	-20.83	-20.94	-20.42
36	-20.33	-21.6	-20.81	-20.83	-20.94	-20.41
37	-20.32	-21.59	-20.8	-20.81	-20.92	-20.4
38	-20.31	-21.58	-20.79	-20.8	-20.91	-20.39
39	-20.3	-21.57	-20.78	-20.8	-20.9	-20.38
40	-20.29	-21.56	-20.77	-20.79	-20.89	-20.37

*indicates lag order selected